2011 SUMMER RESEARCH PROGRAM FOR HIGH SCHOOL JUNIORS

AT THE

UNIVERSITY OF ROCHESTER'S

LABORATORY FOR LASER ENERGETICS

STUDENT RESEARCH REPORTS

PROGRAM COORDINATOR

Dr. R. Stephen Craxton

June 2012 **Laboratory Report 372**

2011 SUMMER RESEARCH PROGRAM FOR HIGH SCHOOL JUNIORS

AT THE

UNIVERSITY OF ROCHESTER'S

LABORATORY FOR LASER ENERGETICS

STUDENT RESEARCH REPORTS

PROGRAM COORDINATOR

Dr. R. Stephen Craxton

LABORATORY FOR LASER ENERGETICS
University of Rochester
250 East River Road
Rochester, NY 14623-1299

During the summer of 2011, 16 students from Rochester-area high schools participated in the Laboratory for Laser Energetics' Summer High School Research Program. The goal of this program is to excite a group of high school students about careers in the areas of science and technology by exposing them to research in a state-of-the-art environment. Too often, students are exposed to "research" only through classroom laboratories, which have prescribed procedures and predictable results. In LLE's summer program, the students experience many of the trials, tribulations, and

rewards of scientific research. By participating in research in a real environment, the students often become more excited about careers in science and technology. In addition, LLE gains from the contributions of the many highly talented students who are attracted to the program.

The students spent most of their time working on their individual research projects with members of LLE's scientific staff. The projects were related to current research activities at LLE and covered a broad range of areas of interest including experimental systems and diagnostic development, computational modeling of implosion physics, chemistry, materials science, laser system development and diagnostics, and database development. The students, their high schools, their LLE supervisors, and their project titles are listed in the table. Their written reports are collected in this volume.

The students attended weekly seminars on technical topics associated with LLE's research. Topics this year included laser physics, fusion, holography, nonlinear optics, atomic force microscopy, glass and glass fracture, and electronic paper. The students also received safety training, learned how to give scientific presentations, and were introduced to LLE's resources, especially the computational facilities.

The program culminated on 24 August with the "High School Student Summer Research Symposium," at which the students presented the results of their research to an audience including parents, teachers, and LLE staff. Each student spoke for approximately ten minutes and answered questions. At the symposium the 15th annual William D. Ryan Inspirational Teacher Award was presented to Mrs. Deborah Reynolds, a chemistry teacher at Brighton High School. This award honors a teacher, nominated by alumni of the LLE program, who has inspired outstanding students in the areas of

science, mathematics, and technology. Mrs. Reynolds was nominated by Andrew Chun and Connie Jiang, participants in the 2010 Summer Program.

A total of 281 high school students have participated in the program since it began in 1989. The students this year were selected from over 50 applicants. Each applicant submitted an essay describing their interests in science and technology, a copy of their transcript, and a letter of recommendation from a science or math teacher.

In the past, several participants of this program have gone on to become semifinalists and finalists in the prestigious, nationwide Intel Science Talent Search. This tradition of success continued this year with the selection of Patricia Olson as one of the 300 semifinalists nationwide in this competition.

LLE plans to continue this program in future years. The program is strictly for students from Rochester-area high schools who have just completed their junior year. Application information is mailed to schools and placed on the LLE website in early February with an application deadline near the end of March. For more information about the program, please contact Dr. R. Stephen Craxton at LLE.

This program was supported by the U.S. Department of Energy Office of Inertial Confinement Fusion under Cooperative Agreement No. DE-FC52-08NA28302.

High School Students and Projects (Summer 2011)

Name	High School	Supervisor	Project Title
Brandon Avila	Allendale Columbia	R. W. Kidder	Optimizing LLE Information Operations Through Natural Language Processing
Andrew Boyce	McQuaid	W. T. Shmayda	Water-Stimulated Tritium Release from Metals
Matthew DeCross	Pittsford Sutherland	L. D. Lund	Characterization of Cryogenic Deuterium–Tritium Target Motion
Avery Gnolek	Webster Thomas	K. L. Marshall	Photoaligned Liquid Crystal Wave Plate
Dana Gretton	Honeoye Falls Lima	R. G. Peck and E. Druszkiewicz	Design of a New Master Timing Generator
Sean Hamlin	Fairport	R. Epstein	X-Ray Fluorescence as an Imploded-Shell Diagnostic
Felix Jin	Brighton	G. Fiksel	Characterization and Design of Magnetic Coils for the Magneto-Inertial Fusion Electrical Discharge System (MIFEDS)
Jefferson Lee	Canandaigua Academy	W. T. Shmayda	Modeling Tritium Removal from Metal Surfaces
Kevin Mizes	Pittsford Sutherland	R. Boni, D. H. Froula, and S. Ivancic	Modeling and Testing Array Generation Techniques for Grid Image Refractometry on OMEGA EP*
Patricia Olson	Brighton	R. S. Craxton	Optimization of Beam Configurations for Shock Ignition Experiments on the NIF and OMEGA
Sean Reid	Fairport	M. Burke, R. Boni, and S. D. Jacobs	The Use of Surface Grinding and Polishing to Remove Etch Induced Noise Pitting in CR-39 Samples
Madeline Rutan	Penfield	K. L. Marshall	Abrasion Resistant Anti-Reflective Sol-Gel Coatings
Michael Statt	School of the Arts	C. Dorrer and K. L. Marshall	Generation of Radially Polarized Beams Using Optically Patterned Liquid Crystals
Troy Thomas	Webster Thomas	B. E. Kruschwitz	Optical Time-Domain Reflectometry for the Transport Spatial Filter on the OMEGA Extended Performance Laser
Harrison Xiao	Pittsford Sutherland	P. A. Jaanimagi	Dynamic Defocusing in Streak Tubes
Andrew Zhao	Webster Thomas	R. Boni, D. H. Froula, and S. Ivancic	Modeling and Testing Array Generation Techniques for Grid Image Refractometry on OMEGA EP*

*Joint report between Kevin Mizes and Andrew Zhao.

Optimizing LLE Information Operations through Natural Language Processing

Brandon E. Avila
Allendale Columbia School
Advisor: Rick Kidder
Summer 2011

Abstract:

Research in natural language processing (NLP) was conducted to determine the feasibility of its use in optimizing information processing for large scale laser facility operations at the Laboratory for Laser Energetics (LLE). NLP was used to extract and link the information from several sources used to house operational knowledge. A vocabulary of common terms found in LLE's documentation, including diagnostic system documents and LLE staff records, was created and used for developing increasingly complex data relationships among the data in the decentralized knowledge base. Extensible Markup Language (XML) data serialization was chosen to store portable information. Using XML, expansion by NLP provided a method for faster knowledge-base construction than any previously implemented technique at LLE.

Introduction:

Benefits of NLP

In recent years, an effort has been made to centralize the information within the LLE systems, creating large repositories of relationally linked information gathered from the databases and tables within the inherently disorganized server system. Methods of creation of these knowledge bases have required manual work in adding object data and explicitly defined descriptions of relationships rather than automatic inference through table and document reading. Adding object data to these repositories has relied upon time-consuming manual information look-up, searching through internal and external documentation and phonebooks to complete entries on associated scientists and engineers as well as laser and lab components.

Furthermore, a manual centralization can never be entirely exhaustive. Data exist in documentation in hundreds of directories throughout many servers that would be impractical to manually read, discern, and enter into a central location, such as the ontology created in a separate project [1]. In addition, some information is hard to gather, as it is not included in the easily accessible databases. Multiple levels of permissions are required to find any kind of information when reading through newly added documentation, and it is often difficult to keep track of which directories have been read through and entered into the centralized system. Moreover, directories are dynamic, and their contents may be modified or removed, making a record of completed directories impossible.

To assist in the process of recording and analyzing this information, NLP is designed to read, interpret, and understand these data on a more abstract level than a simple database parse, simulating a human reader in discerning the meaning of English statements within the LLE documentation. NLP algorithms are designed to be a system of cumulative learning as demonstrated in Figure 1, taking information from previously scanned documents (a), searching for more in-depth information (b), storing the data in a dynamic vocabulary of terms (c), and using newly learned information to repeat the cycle with a greater knowledge of the meaning of words.

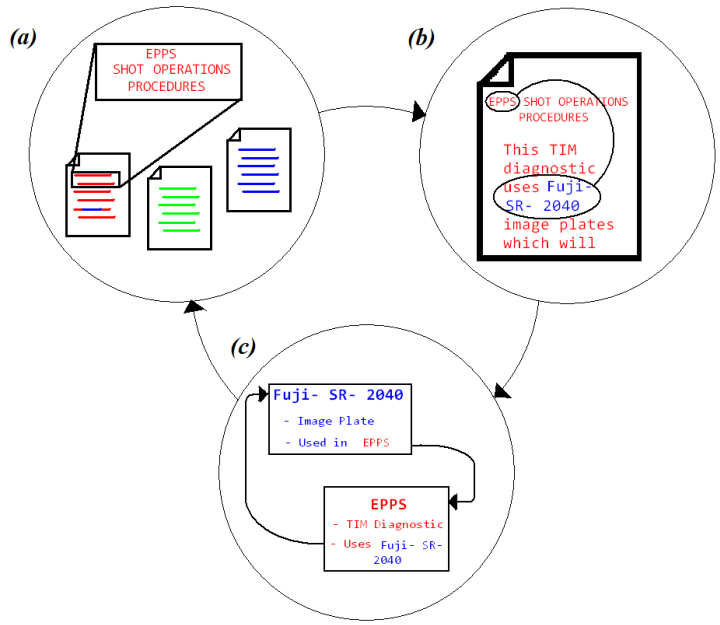

Figure 1: The NLP model. Relevant information is (a) extracted based on search parameters, (b) classified, and (c) inserted into the vocabulary's web of relationships. This information can be (a) reused to extend future searches.

NLP eliminates several major problems involved in the process of manually scanning documentation. First, scanning a directory for documents containing relevant information only takes a few seconds, while a human reading a single operations manual or procedural checklist may take several minutes or longer to find no information at all. Automatic parsing decreases time spent searching by orders of magnitude. Second, the efficiency of the program depends on how much it knows. No time scanning documents is wasted, because even in scanning the same document twice, new information can be inferred based on what was learned during the last parse. It takes a significant number of scans to cease finding new data to gather. Finally, a well-constructed program does not have to know what specific data are being sought, but can register any and all new information in its vocabulary. While a human may search for the phone number of an employee on a page containing his information, a NLP-based algorithm may be able to infer his room number, job title, and team without any additional effort. A perfectly constructed algorithm is able to search any document, and learn all knowledge directly connected to any information it already knows.

Foundations of NLP Algorithms

An algorithm for parsing and interpreting documents through NLP is based on the recognition, classification, and definition of certain words, as well as the inference of their relationships with other terms within a vocabulary [2]. At the base of an algorithm using NLP is word recognition, shown in Figure 2. To recognize a word by type or shape, the particle is compared to a set of regular expressions that provides a format for any meaningful categorization (e.g. name, number, email). Based on character matches between the examined word and the templates, a word may be categorized under one of these types and saved for further context processing. Once a phrase or group of words is complete, a higher-level matching algorithm may

search the context, recognizing the structure of the phrase in terms of its previously defined categories, and infer more perceptive information about the meaning of the word.

When words are recognized in context, and can be related to information already known, they are added to a web of terms, or relational vocabulary, that is capable of explaining these terms in relation to the others. It is the analog of an English dictionary. Terms can be accessed by the NLP algorithms or third party programs, but they mean nothing alone, and the relationships by which they are defined must be understood in order to find any intelligible meaning within them. For this reason, a search through a relational vocabulary is able to provide a more comprehensive explanation of an object by providing partial definitions of related terms that can be used to recursively search. Figure 3 shows how upon searching for a term, one may find its

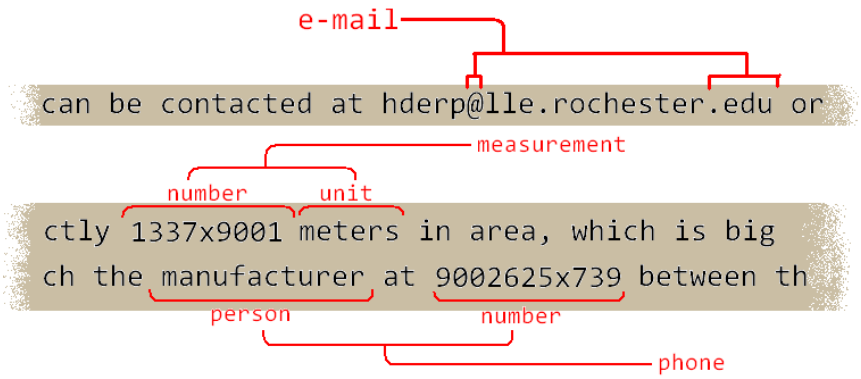

Figure 2: Demonstration of NLP parsing techniques. Words are tagged by examining their character composition and comparing them to regular expressions. These words are given meaning based on the context in which they are found.

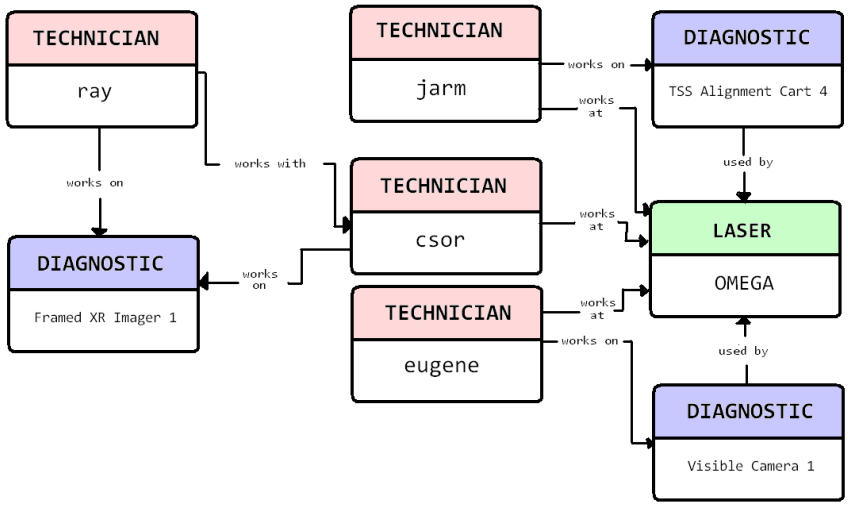

Figure 3: An example relational vocabulary. Known terms share relationships that link the vocabulary into a network. When a program queries the knowledge base, these relationships can be used to provide a large amount of relevant information.

type, as well as the objects to which it is related. A query whose search term includes any specific technician will provide information on his project team as well as the diagnostics and lasers with which they work.

Research and Development:

Creating and Storing the Vocabulary

To begin seeding the vocabulary to be used at the LLE, many databases and tables were first parsed manually to retrieve some information to which newly added terms could be related. Through a combination of manual definition of data-types such as people, diagnostics, and laboratories, and a simplistic automatic scan of these tables, approximately 200 terms were linked with about 900 relationships among them. This initial seed was used to further accumulate terms by parsing through a large directory of presentations and reports containing information about certain diagnostics, projects, and the scientists and engineers maintaining them. The vocabulary was continually being manually seeded from other sources while information was extracted automatically to accelerate the data acquisition. A total of five major parsing algorithms were completed, each consisting of several phases of extraction of different sets of data from a major directory. Data and relationships extracted included, but were not limited to, Project Assistants, Principal Investigators, System Engineers, experts, and specialists, and were extracted from procedural checklists, Operational Readiness Reviews, and project reports, among other sources of information.

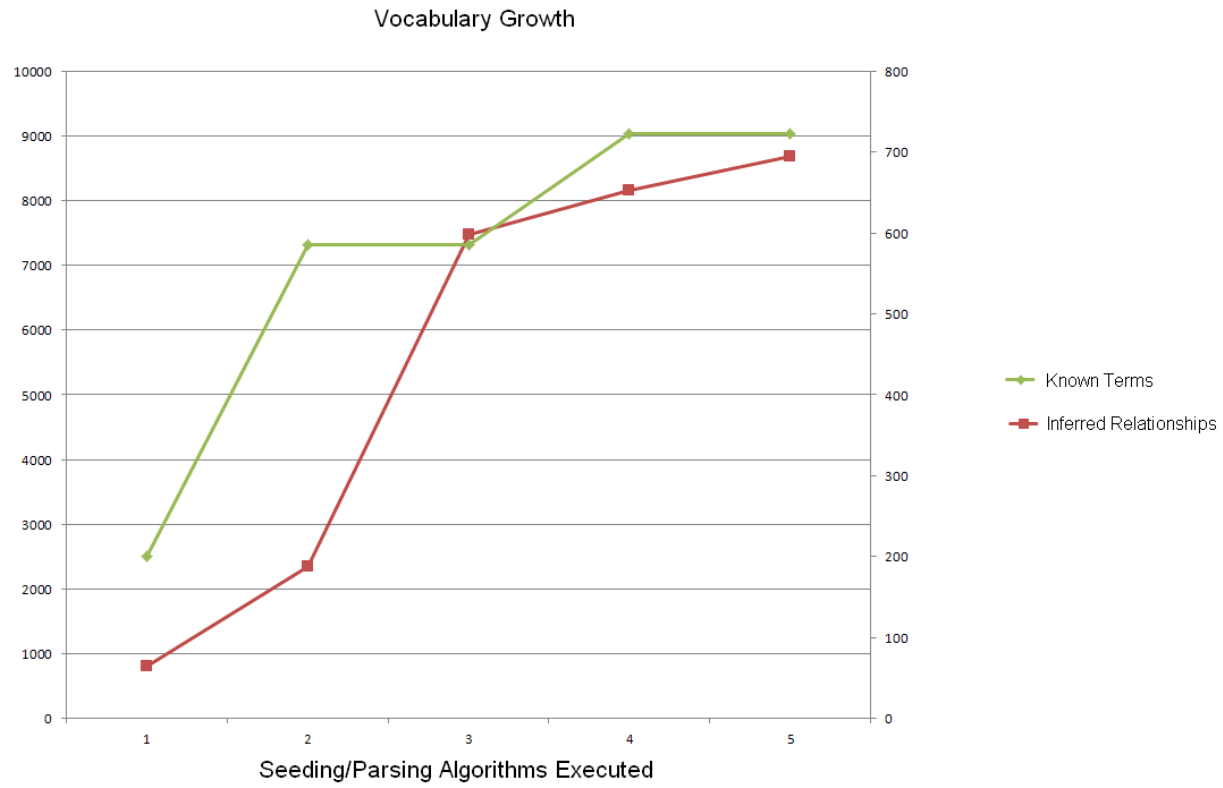

Figure 4: Growth of the established vocabulary. After initial seeding, the vocabulary contained approximately 200 terms and is seen to have grown to over 700 by the end of the project. This was achieved through both continuous seeding and relationship inference. The right and left axes correspond to the number of Known Terms and Inferred Relationships respectively.

As seen in Figure 4, the algorithms developed eventually reached a point where each algorithm run on a directory brought fewer inferred relationships. While the graph demonstrates only a portion of all documentation available for parsing, the concept applies to larger sets of documentation. Without more sophisticated algorithms or a larger pool of information available to organize, the amount of knowledge not yet gathered continues to decrease until every logical relationship has been inferred.

To make the vocabulary available for reuse by the NLP algorithms and other programs dependent on LLE terms and relationships, it was stored in portable, accessible files. XML was chosen to serialize the information in an easy-to-read format that could quickly be searched and

altered through simple programs and scripts. While XML was efficiently updated and read by the NLP algorithms, it was also effective in serving as the knowledge base of a newly designed ontology, fabricated in a separate project.

Problems Faced in Reading Documentation

Many LLE documents include signatures, forms, or other hand-written information. When these documents are signed or filled out, they are scanned and uploaded to the servers in Portable Document Format (PDF) files. These can be easier to use than simple image files, and most PDF readers contain a built-in feature that attempts to convert these hand-written lines into machine-readable text. These programs, however, are certainly not comprehensive, and often fail to accurately read any sort of information: errors like the one in Figure 5 occur frequently. It is thus quite difficult to extract anything valuable from the handwritten forms.

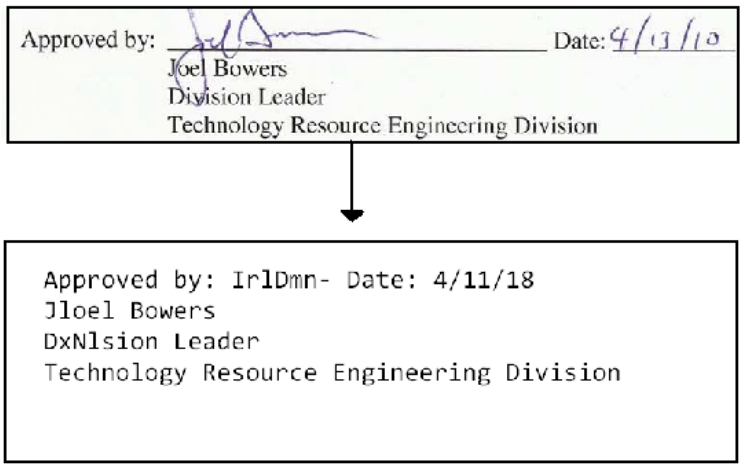

Figure 5: Inaccurate document reading. Current technologies are incapable of accurately reading hand-written or scanned documents.

In addition to the scanned documents, the majority of other documentation at LLE is also stored in PDF files. These files are effective in providing users with a comprehensive view of diagnostics and procedures at the lab, as they elegantly integrate text, graphics, and checklists. Often it is simple to read the text within these files through the use of external programs, but sometimes this information is jumbled or concatenated, making it difficult to extract coherent sentences, or even words, from the text. The most common cause of the problem proved to be

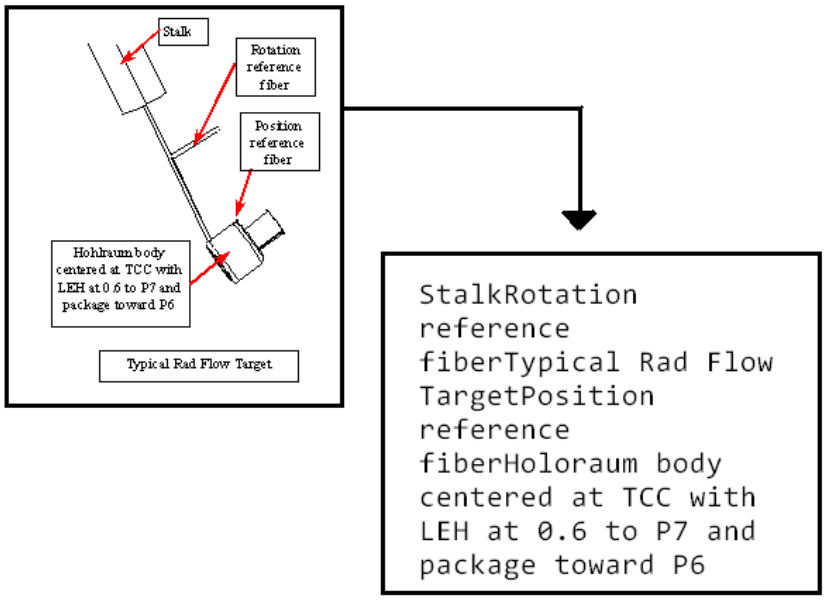

Figure 6: PDF reading errors. When trying to parse a figure with discernable text, the result is often jumbled and concatenated captions.

graphics labeled with spatially formatted blocks of text. As seen in Figure 6, words were present, but incoherent in the formatting retrieved from reading the documents.

Future Work

Work on this project was primarily in determining the feasibility of NLP algorithms as the primary method of knowledge base construction and information compilation. For this reason, many of the algorithms written were simplistic, and meant to test only for efficiency in scanning, reading, and extracting simple information from a relatively small collection of documents. A large-scale version of the project would involve creating programs capable of performing more complex operations on larger collections of information. Extending the project should be aided by the vocabulary now installed within the LLE systems.

Further work involves the creation or use of more effective document-reading programs. Much information was lost in inaccurate readings of text or hand-written information. The project would benefit most from a program granting the ability to accurately read these obfuscated documents.

Acknowledgments:

I thank Mr. Rick Kidder and Dr. Stephen Craxton for granting me the opportunity to spend my summer at the Laboratory for Laser Energetics. I further extend my gratitude to Mr. Kidder for his advice and support in designing and carrying out this project. Additionally, I thank Rob Cooper and Dustin Axman for their previous work on related projects, as well as their assistance and support in integrating this project into the established system at the LLE.

References:

1. R. Cooper, "Development of an Ontology for the OMEGA EP Laser System," 2010 Summer High School Research Program at the University of Rochester's Laboratory for Laser Energetics
2. S. Bird, E. Klein, E. Loper, *Natural Language Processing with Python* (O'Reilly Media, 2009).

Water-Stimulated Tritium Release from Metals

Andrew M. Boyce

McQuaid Jesuit High School

Advisor: Dr. Walter Shmayda

Oct 2011

Abstract

Experiments have been carried out to understand how tritium, a radioactive isotope of hydrogen, desorbs from, or leaves, metal surfaces. In the experiment, a tritium-contaminated metal coupon is exposed to a gas stream and the radioactivity removed from the coupon is carried by the gas stream and bubbled into a liquid scintillation cocktail for counting. From this measurement, the rate of tritium outgassing is calculated and plotted as a function of time. The outgassing rate was measured as a function of the humidity of the gas stream, the temperature of the oven in which the coupon is held, and the chemical composition of the metal coupon used. A goal of the experiments was to measure the steady desorption rates at a given temperature and humidity. Specifically, the present experimental purpose was to measure how tritium desorption is affected at modest temperatures (40˚C→130˚C) and relative humidity (0-40%RH). These experiments demonstrated that the rate of tritium desorption increases with increasing temperature and humidity. It was also concluded that the tritium removed at these temperatures emanated from only the near-surface layers of the metal. The results of these experiments were found to be reproducible.

Introduction

Tritium is a radioactive isotope of hydrogen that has applications in nuclear fusion. Tritium contaminates metal surfaces found in the area in which it is being used. Through a process called adsorption, tritium forms a chemical bond with a surface in a process known as chemisorption or is held to the surface by weaker inter-molecular attractive forces in a process known as physisorption. The accumulation of adsorbed tritium creates one or more monolayers on a surface. The first monolayer of tritium is often chemisorbed, while subsequent layers are physisorbed.

Tritium contamination poses a health hazard to radiation workers. Tritium can adsorb onto and desorb from surfaces as a pure gas (T_2); however, it is more commonly found in the place of a protium molecule in water, such as in HTO. More generally, the adsorption and desorption of water have numerous other applications. For one, water desorption off metals can act as a contaminant in ultra-pure gas streams used in industrial settings. Water can desorb off the inner surfaces of process lines into streams used in the fabrication of semi-conductor chips. The water can then adsorb onto the surface of these chips and reduce their lifespan and reliability[1,2,3]. Another application of note is water adsorption onto metal surfaces as a cause of corrosion. Building metal can be corroded through the adsorption of water layers onto the metal surface. These water layers can then absorb contaminants such as hydrogen sulfide (H_2S), causing the formation of acidic water, which can corrode the metal. Research has been performed examining ways to prevent water adsorption onto metal surfaces, such as the use of copper (I) sulfide to prevent adsorption onto a copper surface. The adsorption of water layers on the cryogenic targets used in the Omega Laser System can reduce the neutron yield of inertial confinement fusion implosions. Previous reports [4,5] have examined the dependence of tritium outgassing rates on humidity at higher temperatures.

The present experiments studied tritium desorption off copper and stainless steel coupons at temperatures below 130˚C and RH below 40% by heating and exposing the samples to water vapor simultaneously. The dependence of desorption rates on low temperatures for a range of humidities was measured.

Experimental Setup

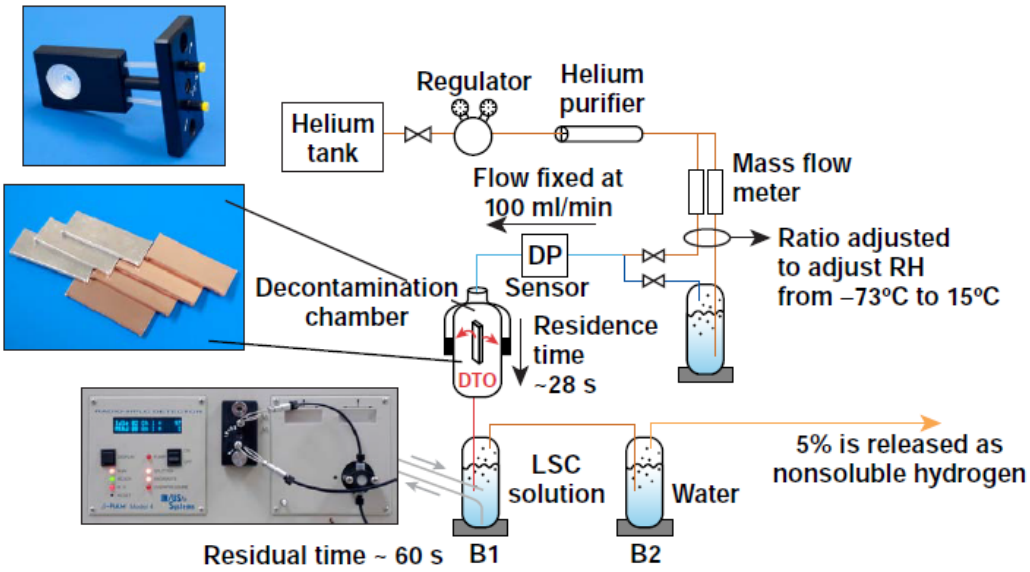

Fig 1: A representation of the experimental setup. The decontamination chamber also serves as an oven.

A schematic of the experiment is shown in Fig. 1. The experiment begins with a tank of compressed helium gas. Gas passes from a line beginning at the tank to a regulator, through which the pressure of the gas stream is reduced to about 20 psi. The gas stream then passes through a helium purifier, which removes any initial humidity or other contaminants that may exist in the stream. The stream is then split and passed to two mass flow meters. One of the mass flow meters passes helium to a humidifier allowing water to enter the stream; the other meter does not pass the stream to a humidifier, ensuring that this portion of the gas stream remains dry. The meters allow the amount of gas passed through each respective stream to be controlled. The total flow rate used in the experiment is always 100 mL/min; however, this total flow can be split in different ratios between the humidified and dry streams.

Following splitting and passing through the mass flow meters, the streams are rejoined and run through a digital dew point (DP) sensor, allowing the humidity to be monitored. The gas stream is then passed under a fume hood and into an oven where the temperature of the stream can be varied. Thermocouples are used to measure the temperature inside the oven. Also inside the oven is a metal coupon that has been exposed to tritium. Exposure of the gas stream to the coupon inside the oven allows tritium to desorb off the coupon and into the gas stream. Plastic tubing then runs the gas stream through two consecutive bubblers each containing liquid scintillation cocktail. The efficiency of each bubbler in collecting tritium is 90% and, thus, their combined efficiency is 99%. Therefore, the gas can then be safely emitted into the fume hood.

The cocktail is continuously sampled using the β-Ram system. When tritium decays to emit a β particle, the cocktail emits a photon, causing a flash of light which can be counted to provide a measure of the activity of the cocktail sampled and, therefore, the tritium that desorbed from the metal into the gas stream. Through the Scint Flow program, the number of fluoresces is recorded in a Microsoft Excel spreadsheet. The Oven Control program written in LabView controls the flow rate of the gas stream and the temperature of the oven. Tritium desorption rates are understood to be affected by three factors: the rate of diffusion from the bulk of the metal to the oxide layer, the rate of diffusion through the oxide layer and the rate of desorption from the surface oxide layer. Modeling of tritium desorption was performed by Jefferson Lee.[6]

Data Processing

From the activity reading recorded in an Excel spreadsheet, a number of conversions are used including the counting efficiency of the β-Ram system, which is measured through the use of a calibrated liquid scintillation counter (LSC). The LSC gives the activity of the cocktail in

both CPM and decays per minute (DPM) by counting the number of fluoresces made by the cocktail over a certain time interval. One-milliliter samples of cocktail were collected from each of the two bubblers for processing in the LSC. Once these conversions are completed, the activity is given in a more conventional unit: microcuries (μCi). The data are then differentiated with respect to time to give the outgassing rate of tritium from the metal coupon in $nCi/cm^2/s$.

Data were then entered into the Mathcad function Supsmooth, which removes much of the experimental noise from the data. Noise is found within all data collected. It is not merely a consequence of the limitations of measurement taking; in actuality, the decay of tritium is statistical, occurring at inherently inconsistent rates, causing a large amount of the noise in the data. Tritium decay can occur in bursts, followed by periods of fewer decays afterwards. This causes fluctuations in the data, even though the activity of the LSC should only increase because activity is added only and not removed. Consequently, Supsmooth provides an essential function to the data processing of the experiment because the fluctuations recorded in the activity measure are amplified when a derivative is applied to give the outgassing rate. It is noted, however, that Supsmooth can remove some of the sharp inclines and declines that represent real data. This, in turn, can skew the perceived timing of changes made in the experimental system. Additionally, Supsmooth on some occasions removes data peaks. Because of this, some runs are processed using a boxcar smoothing method. This method works by averaging the value of every point on the graph with respect to a specified number of surrounding points. The typical number of points used in the averaging process is 5, two on either side of the data point being averaged. An example of boxcar smoothing is shown in Fig. 2.

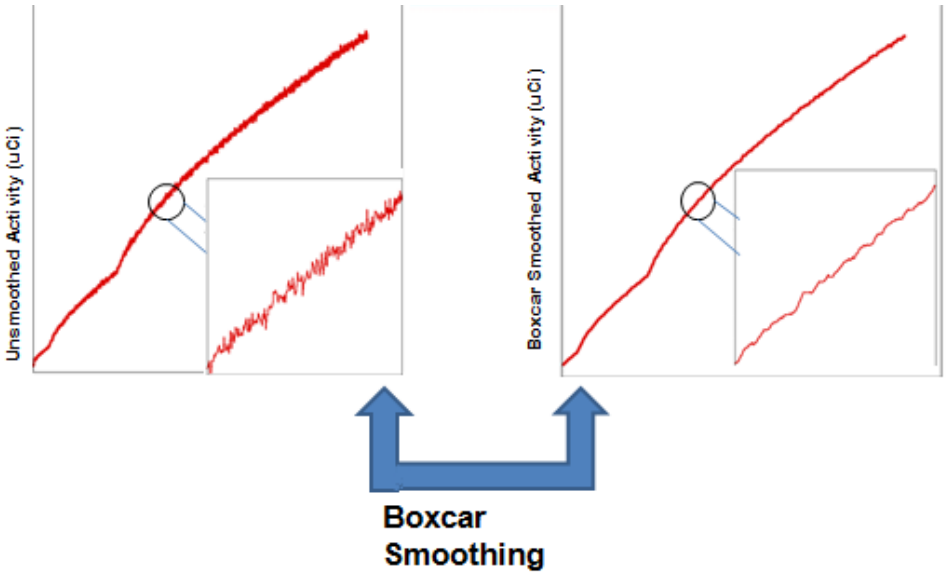

Fig 2: The effect of boxcar smoothing in removing data noise.

The noise of the resultant graphs is often greater for boxcar smoothed data compared to Supsmoothed data; however, this compromise is often necessary in order to preserve the information in the data.

In order to gain an accurate measure of the humidity in the system, the mass of the humidifying bubbler was recorded before and after experiments. The theoretical change in mass of the bubbler can be calculated using known experimental conditions through the use of the equation:

$$\frac{dm}{dt} = \frac{P_V F_{carrier}}{RT_S} * \frac{M_W}{\rho} \qquad (1)$$

where P_v is the water vapor pressure, $F_{carrier}$ is the flow rate of the humidified gas stream (liters/min), R is the universal gas constant, T_s, is the temperature of the gas, M_w is the molar mass of water and ρ is the density of water (g/mL).

Dependence of Outgassing Rate on Temperature

A run was conducted with the relative humidity being held constant, but with changes made to the temperature. The run was conducted using a relative humidity of 40% with temperatures ranging from 100°C-130°C and increasing in ten degree steps. This makes it possible to see the effect of increases in temperature with a fixed humidity. The supsmoothed outgassing rates of this run are shown in Fig. 3.

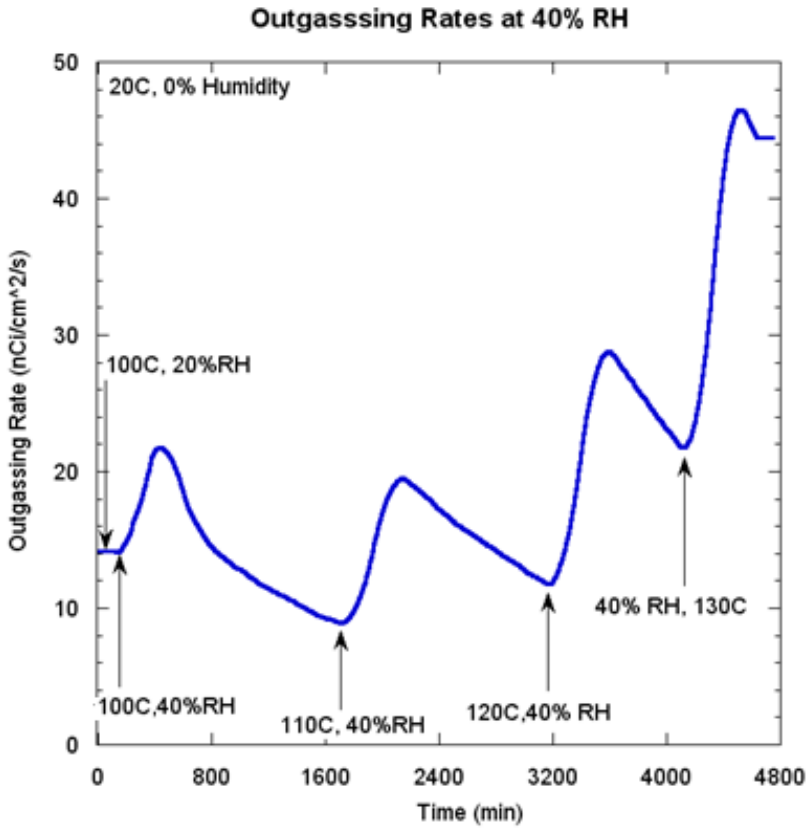

Fig 3: A plot of the supsmoothed outgassing rates at temperatures between 100 and 130°C at 40% relative humidity.

To compare the evolution of the curves for the three different temperatures, the individual curves were extracted from Figure 3, overlaid and plotted, such that the base of each peak was set to have an outgassing rate of zero. The results are shown in Fig. 4.

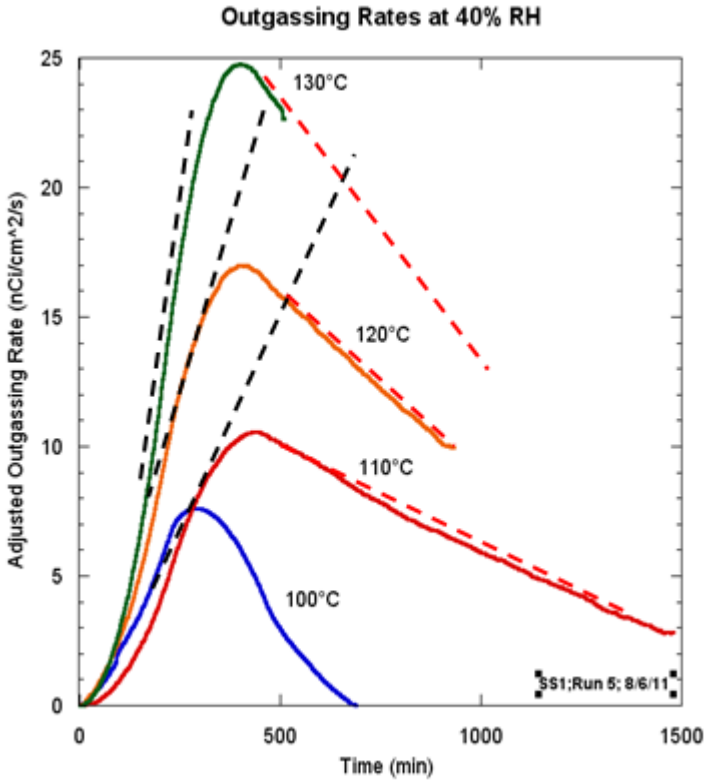

Fig 4: The normalized outgassing rate peaks over time for various temperatures at 40% relative humidity. This is derived from Fig. 3 by plotting the peaks for each temperature by shifting each peak such that the base of all peaks occur at time zero and with outgassing rate zero. Also shown are the approximate tangent lines for each curve.

This graph shows that the outgassing rate is dependent upon the temperature of the run. Not only does the peak outgassing rate increase with increased temperature, but the rate of the climb of the outgassing rate also increases (which can be seen from the tangent lines drawn along with the curves) with increasing temperature. Desorption is a thermally activated process.

The outgassing rate is observed to decline more rapidly after the peak with increasing temperature. This suggests that the store of water and tritium on the coupon surface participating in the desorption process is finite and dependent on the desorbing temperature.

The amount removed depends on the desorption temperature. The integral of the outgassing curves represents the quantity of water and tritium desorbed from the surface. The amount removed increases with increasing desorption temperature suggesting that a greater fraction of water and tritium bound to the surface is removed with increasing temperature.

Tritium residing in the metal bulk contributes negligibly to the quantity released from the surface. As tritium diffuses from a semi-infinite bulk to the surface, the tritium concentration profile in the metal will develop into an error function. The concentration at the oxide-metal interface will be a small value. The concentration deep in the bulk will be high. The maximum distance that a triton can travel at a given temperature and time will be given by:

$$\frac{z}{\sqrt{D * t}} = 1 \qquad (2)$$

where z is the maximum penetration depth that a trition can propagate to in time t and D is the diffusivity of tritium in metal. Substituting $1.2 * 10^{-9}$ cm^2/s for a typical triton diffusivity[7] in copper at 130°C and 30,000 s (500 min), the typical duration of an experiment, suggests that tritons beyond a depth of 65 microns into the metal cannot contribute to the desorption process. At 40°C, the diffusivity decreases to $1.3 * 10^{-11}$ cm^2/s and tritons beyond a depth of 0.4 microns will not contribute to the amount desorbed. The amount of tritium dissolved in stainless steel is:

$$S = S_o \sqrt{P} \exp(-\frac{E_a}{RT}) \quad (3)$$

where S_o = 1.9 scc of gas/cc of metal/atm$^{1/2}$ is a constant for hydrogen solubility in copper, P is the driving pressure used to charge the sample with tritium, 0.5 atm in this case, and E_a is the activation energy for dissolution of tritium in the metal, 9.1 kJ/mol[8]. At 40°C, the amount of tritium dissolved in 0.4 microns of copper will be 0.3 mCi. The total quantity of tritium collected in the 40°C run was 8 mCi. These calculations confirm that at temperatures below 130°C, tritium bound in the oxide layer dominates the desorption spectrum.

Dependence of Outgassing Rate on Humidity

A run was conducted using a stainless steel coupon. The run was begun with a dry purge of helium at room temperature. After 30 minutes, the temperature of the coupon was increased to 100°C. At 314 minutes, the humidity of the dry gas stream was increased to 20%RH. The dry gas stream contained approximately 10 ppm water. At 20%RH the water content in the gas stream is 1000 ppm. The activity data collected was then run through a boxcar smoothing program and differentiated with respect to time. The boxcar-smoothed outgassing rates are shown in Fig 5.

Two peaks are seen in this run. One is for the experimental condition of 100°C and 0% RH; the other is at the same temperature for a relative humidity of 20%. To compare the evolution of the outgassing dependence on humidity, the individual curves were extracted from Figure 5 and plotted such that the starting point of both curves was set to the same value at time zero. The plot of the two overlaid curves is provided in Fig. 6.

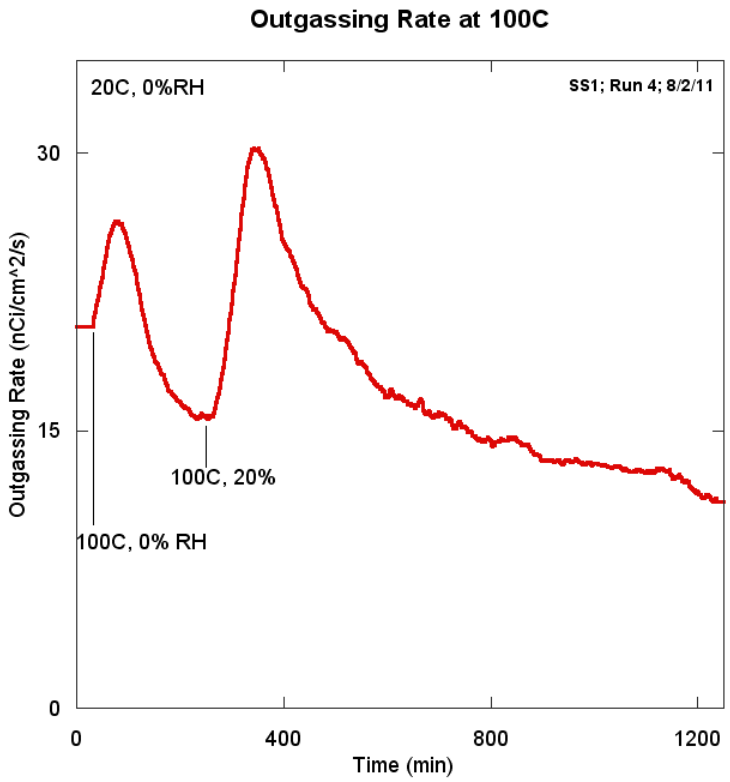

Fig 5: A plot of outgassing rate over time at 100°C; the humidity of the gas stream was changed from 0 to 20% RH at 314 min.

Figure 6 shows that outgassing rates for the two cases evolve in a similar manner, firstly increasing to a peak and then decreasing towards a steady state outgassing rate after a long time. This suggests that the rate-limiting step for desorbing tritium from the surface is determined by the arrival rate of water vapor to the surface. Tritium desorption from the sample decreases as the oxide layers closest to the gas stream are depleted of tritium. It appears that over the duration of the experiment, tritium located deep inside the oxide layer does not diffuse towards the surface rapidly and does not contribute to the emission.

The quantity of tritium removed increases in the presence of humidity. The quantity of tritium desorbed from the surface increased 216 fold when the humidity of the carrier increased

100 fold. This suggests that the number of monolayers contributing to the desorption process increased with the increase in humidity. It is also noteworthy that the duration of the outgassing process doubled, also suggesting that layers deeper in the oxide layer contributed to the emission.

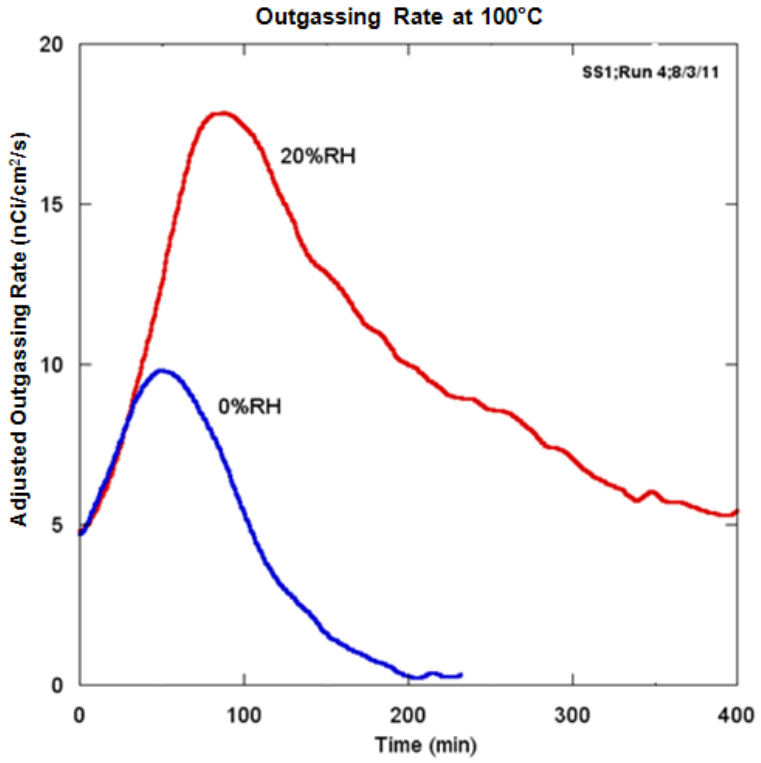

Fig 6: A plot of the normalized outgassing peaks over time for a run conducted at 100°C. The outgassing profiles for the runs at both humidities were adjusted to coincide at time zero to highlight the similarities and differences in the two profiles.

A second test was conducted to investigate the outgassing rate dependence on humidity at 40˚C. The humidity of the gas stream was changed to 20% RH and a resultant increase in the outgassing rate is shown. Fig. 7 shows the boxcar-smoothed outgassing rates of this experiment. The average outgassing rate into the dry stream is about 20 nCi/cm^2/s. When the humidity is increased to 20%RH, the average outgassing rate increases to about 150 nCi/cm^2/s. Returning to

dry purge stream conditions causes the outgassing rate to return to its previous level of about 20 nCi/cm^2/s. This figure illustrates that humidity in the purge stream stimulates desorption from the copper surface.

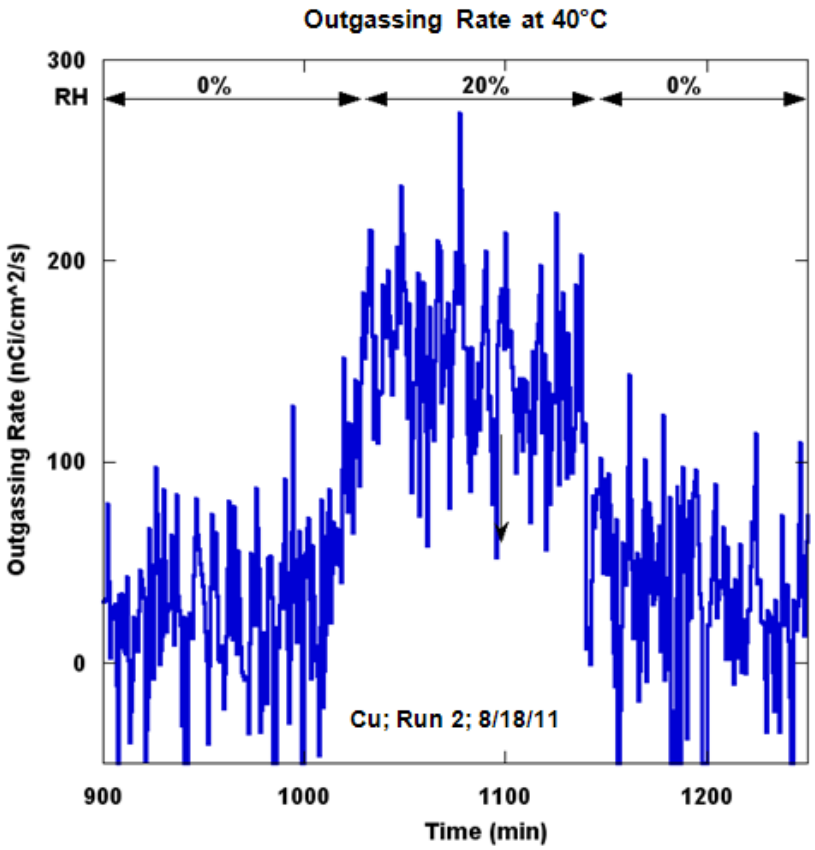

Fig 7: A plot of outgassing rate over time conducted at 40°C. The outgassing rate increases with increased humidity

At 40^{o}C, a 100 fold increase in water content in the purge stream resulted in an 8 fold increase in the outgassing rate. As discussed in the 100^{o}C run, the number of monolayers participating in the desorption process increases with increased humidity. However, the total number of layers involved appears to decrease as the metal temperature decreases. The

assumption in both the 40 and 100^{o}C runs is that tritium is uniformly distributed throughout the layers of oxide from the gas/oxide interface through to the oxide/metal interface.

Conclusions

Experiments have been conducted to measure the tritium outgassing rate from stainless steel and copper coupons. The outgassing rate is seen to depend on both the temperature of the metal and on the humidity of the purge stream. Increasing the metal temperature increases the outgassing rate from the surface. Increasing the humidity of the gas stream also increases the outgassing rate.

Increasing either the temperature or the humidity appears to increase the number of oxide monolayers that participate in the release of tritium. At temperatures below 130˚C, tritium dissolved in the metal bulk does not contribute to the outgassing profile.

References

1. Ohmi, Tadahiro. *Future Trends and Applications of Ultra-Clean Technology*. Tech. 1989. Print.
2. Ohmi, Tadahiro et al. *Trace Moisture Analysis in Specialty Gases*. Tech. 9th ed. Vol. 139. Electrochemical Society. Print.
3. Shirai, Yasuki, Tsutomu Kojima, Shinji Miyoshi, and Masaki Narazaki. "Introduction." *Specialty Gas Distribution System Free from Corrosion Gas Decomposition and Reaction*. Proc. of Microcontamination. 1. Print.
4. Ben Petroski, “Water Desorption from Metallic Surfaces at Room Temperature”, 2009 Summer Research Program at the University of Rochester’s Laboratory for Laser Energetics
5. Ryan Shea, “Tritium Desorption from Stainless Steel Surfaces at Variable Temperatures”, 2010 Summer Research Program at the University of Rochester’s Laboratory for Laser Energetics

6. Jefferson Lee, “Modeling Tritium Release in Metals”, 2011 Summer Research Program at the University of Rochester’s Laboratory for Laser Energetics
7. J. H Austin, T.S. Elleman, J. Nuc. Mater. 43, 119 (1972)
8. M.R.Louthan, R.G. Derrick, Corros. Sci. 15, 565 (1975)

Acknowledgments

I would like to thank Dr. Craxton for allowing me to participate in this truly rewarding program. I thank my advisor, Dr. Shmayda, for his expertise and support while I conducted this project. I would like to thank Ben Petroski, Jefferson Lee and Matt Sharpe for their assistance in the project. Lastly, I would like to thank all of my fellow high school students in the program for their support and advice.

Characterization of Cryogenic Deuterium-Tritium Target Motion

Matthew DeCross

Pittsford Sutherland High School

Pittsford, NY

Advisor: Mr. L.D. Lund

Laboratory for Laser Energetics

University of Rochester

Rochester, NY

August 2011

Abstract

Knowledge of target motion characteristics is important for maximizing the efficiency of cryogenic target implosions in internal confinement fusion. Target motion data from two high-speed video cameras situated inside the target chamber of the OMEGA laser system was analyzed using MATLAB. It was shown that targets follow elliptical paths through space. A time-domain parametric elliptical model of low frequency target motion was created that can predict the location of targets at the time of a shot. Using this model, vibration characteristics including resonance frequencies, amplitudes, and phase angles were extracted. Damping was estimated using the exponential decay method with the amplitudes of these ellipses. It was found that cryogenic targets typically damp within four seconds, meaning that it is possible to optimize timing of the retraction of the thermal shroud such that target motion at the time of a laser shot is minimized.

1 Introduction

The Laboratory for Laser Energetics of the University of Rochester operates the OMEGA laser system and is one of several large laboratories experimenting with internal confinement fusion using this facility. On OMEGA, a cryogenic spherical capsule containing the deuterium and tritium isotopes of hydrogen is compressed and heated by sixty ultraviolet laser beams to ignite the following reaction and produce energy [1]:

$$ {}_{1}^{2}H + {}_{1}^{3}H \rightarrow {}_{2}^{4}He + {}_{0}^{1}n + 17.59\ MeV. \qquad (1) $$

This capsule is a plastic shell 5 to 20 μm thick, with a layer of cryogenic deuterium and tritium under the surface approximately 100 μm thick [2].

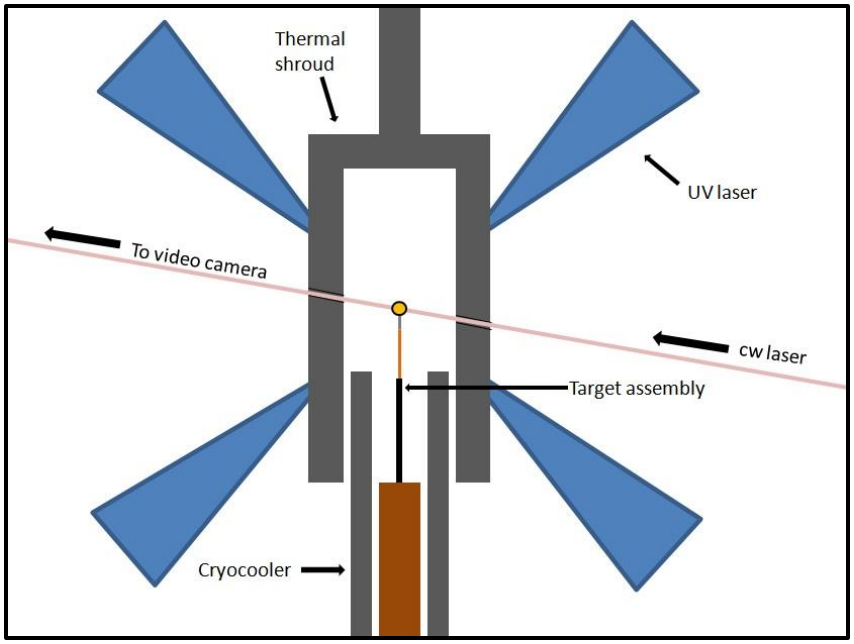

Fig. 1 The geometry of the OMEGA target chamber
For simplicity, four of the sixty ultraviolet lasers which irradiate a cryogenic target when fired on OMEGA are shown. Feedback from a cw laser which illuminates the target provides high-speed video cameras information about target position.

In order to compress the deuterium and tritium evenly and maximize the fusion energy produced, uniform distribution of the laser radiation on the surface of the capsule is necessary. This requires that the capsule be as close to target chamber center as possible, preferably less than or equal to 10 μm away. However, there are numerous sources of vibrational excitation present in the target chamber, as depicted in Fig. 1. Cryocoolers, necessary to keep the capsule below 20 K, create a steady state vibration observed to be around 4 Hz. The thermal shroud which insulates the target capsule from the surrounding environment transiently excites the target on all axes

when it is retracted prior to the laser shot [2]. Since off-center targets will not be shocked and compressed evenly by a laser pulse, knowledge of target vibration characteristics is important for providing information on target location and motion behavior at the time of a laser shot. Target damping, the rate of decay of vibration amplitude, is particularly important since targets with high damping will be closer to the target chamber center at shot time.

In the OMEGA target chamber, two high speed video cameras monitor the position of targets constantly during the time period before a laser shot. The most important data is visible in the 50-70 milliseconds after the retraction of the thermal shroud but before a shutter blocks each camera to prevent damage from laser shot debris, since the target is damping from vibrational excitation during this period. This data is returned as graphs of target location vs. time on each axis as well as radial distance. Using MATLAB, programs were written to model the path of target motion and extract vibration characteristics for various types of targets.

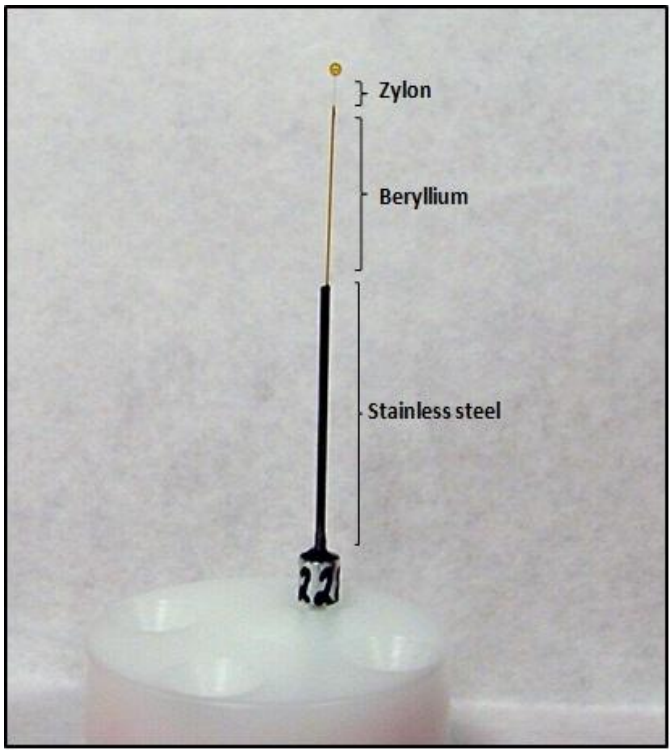

Fig. 2 Anatomy of a Type 1 mass equivalent fusion target
The highly flexible synthetic polymer Zylon permits excessive target vibration, reducing laser shot efficiency.

Fig. 2 displays a Type 1 mass equivalent fusion target assembly, one of several types used on OMEGA for laser fusion experiments. The base of the stalk is composed of stainless steel and beryllium, which are important for their strength and relative immunity to radiation. The tip of the stalk is made of Zylon, a highly flexible synthetic polymer. Though this flexibility

guards against the danger of having the capsule snap off from the stalk, it allows a greater range of vibrational motion for the target. Type 1 targets have a fairly low natural frequency in comparison with some other target types, which have different metals and polymers in their stalks and are less mobile but more fragile.

For the purposes of analyzing target motion, some targets were tested without a laser shot, yielding data on target motion during free vibration in the OMEGA target chamber. The mass of the deuterium-tritium fuel significantly affects target motion since it changes the natural frequency of targets. Therefore, targets with a mass equivalent of plastic at 20 K were used for laboratory testing in order to exactly simulate the conditions of a cryogenic target.

There are several methods for measuring the vibration characteristics of targets in the laboratory. One, called the half-power bandwidth method, uses a shaker test to convert the response acceleration to an applied force on an empty or mass equivalent target into a frequency-domain function, called a frequency response function. This method allows calculation of resonance frequency, response amplitude, and a damping estimate. Another method, called the logarithmic decrement or exponential decay method, excites a target at its known resonance frequency and uses the resultant oscillating damping curve to calculate damping (ζ) via the formula:

$$\zeta = \frac{\delta^2}{\sqrt{4\pi^2+\delta^2}} \qquad (2)$$

where δ, known as the logarithmic decrement, is described by:

$$\delta = \frac{1}{n}\ln\frac{x_0}{x_n} \qquad (3)$$

where x_0 is the maximum amplitude and x_n is the amplitude of the nth peak from the maximum amplitude of the oscillating damping curve [3].

Previously, the vibration characteristics of cryogenic fusion targets had never been characterized. As a result of this work, a time-domain parametric model of target motion was created by processing high-speed video camera data with MATLAB, allowing target location at the time of a laser shot to be calculated. Target damping during the time shortly before a laser shot was estimated for the first time using the exponential decay method, and it was shown that targets may damp to steady state motion within one to three seconds after thermal shroud retraction. A new routine for thermal shroud retraction allowing for minimum target motion at the time of a laser shot has been implemented as a result of this characterization. Another potential solution to excessive target motion concerning alternative target choices has also been considered based on models of the target motion path.

2 Research Methods

The target-stalk system is a viscoelastically damped multiple degree of freedom oscillator. However, motion at the capsule is more easily and still accurately modeled as a single degree of freedom oscillating system on each axis [4]. This means that the target can be treated as any other oscillating system with a restoring force proportional to displacement and a damping force proportional to velocity. Such systems are typically modeled by the homogeneous second-order linear differential equation on each axis:

$$\frac{d^2x}{dt^2} + \gamma\frac{dx}{dt} + {\omega_0}^2 x = 0 \qquad (4)$$

where *x(t)* is the position function on the respective axis of the capsule, γ is the damping constant for that axis, and ω_0 is the resonance frequency on that axis [2]. The solution to this equation gives both a real and complex term, which describes the amplitude, frequency, and phase angle of target oscillation.

By analyzing camera data of target motion, these parameters which characterize target vibration can be extracted. Position data from the two high-speed video cameras situated inside the OMEGA target chamber is sampled at 2000 Hz. The data is based in "OMEGA-space", a complicated linear basis for 3-space which is appropriate for the geometry of the cameras and target chamber, since the camera views are not perfectly orthogonal. Therefore, the data from these cameras is passed through a change-of-basis algorithm to convert it into a measurement of the coordinates X, Y, and Z relative to the origin, which is the center of the target chamber. The radial distance from the origin of the target is also measured.

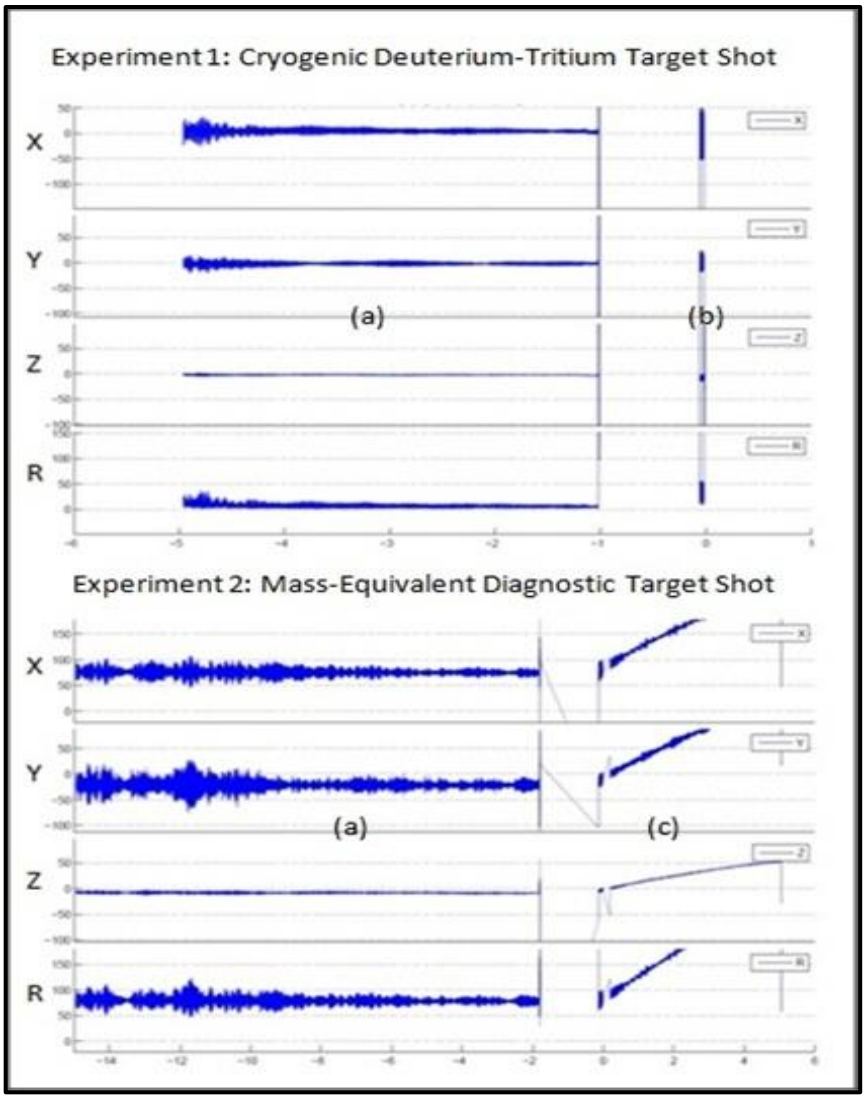

Fig. 3 Transient data taken by two high-speed video cameras situated inside the OMEGA laser system
Data from two different shots are displayed for all three standard axes as well as radius. In region (a), the target is experiencing steady state vibration caused by background machinery. In region (b), the thermal shroud has been lifted and the target is exposed to the video cameras. In region (c), the target has not been hit by a laser shot but instead its vibrations have been allowed to damp out.

Different target data is available depending on the general experiment that was performed at the time of the laser shot. Fig. 3 shows two different data printouts from different experiments. The data

show oscillation on all axes due to the various excitation sources previously discussed. When a laser shot is desired, the only data available is the steady state vibration of the target as well as target motion in the 50-70 ms window after the thermal shroud has been retracted but before the shot. In Experiment 1, the thermal shroud is retracted between Fig. 3 regions (a) and (b), resulting in the significantly increased amplitude of oscillation in region (b) which has not been able to damp down to the steady state amplitude of region (a). A shutter blocks the cameras at the time of the shot, that is, at the end of Fig. 3 region (b). The brevity of this time window illustrates the necessity to characterize target damping. Occasionally, as in Experiment 2, diagnostic tests are being performed which do not require a laser shot. Data from these tests are useful because they feature broad enough time windows to provide information about target damping on all axes.

Interestingly, as seen in Fig. 3 region (c), the measured target position drifts away from the origin, which in the case of this specific target, CRYO-ME-2Q11-01-42, is likely the result of thermal expansion. This presents a problem because targets should obey an oscillating damping curve according to their equation of motion, permitting use of the exponential decay method to estimate damping, but thermal expansion distorts this curve. Additionally, the measured position of the target is displaced from the origin from the beginning of the time record. A program was written in MATLAB to break down data into 50 ms segments, and the means of these data segments were subtracted out to standardize and normalize the data. The top three graphs of Fig. 4 show the raw data from the two high-speed video cameras which has been adjusted in the bottom three graphs. The periodic nature of these curves may not be immediately apparent due to the high volume of data in each graph. Fig. 5 displays a close-up view of target motion on one axis to confirm that targets are indeed oscillating about the origin. Since the data is periodic on

all axes, this indicates that target motion is characterized as revolution around the origin.

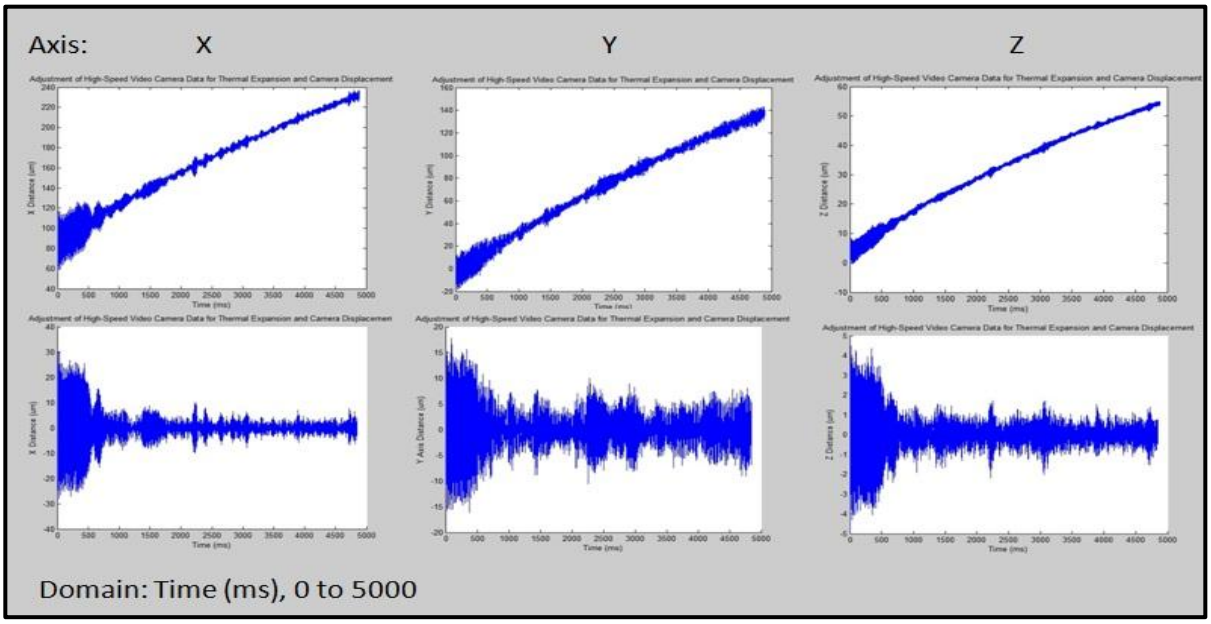

Fig. 4 Adjustment of high-speed video camera data to account for thermal expansion and camera displacement
By applying a MATLAB program, position data was adjusted from the raw data on the top three graphs to form the oscillating damping curves shown in the bottom three graphs. Position is measured in microns from the origin and is typically under 100 microns.

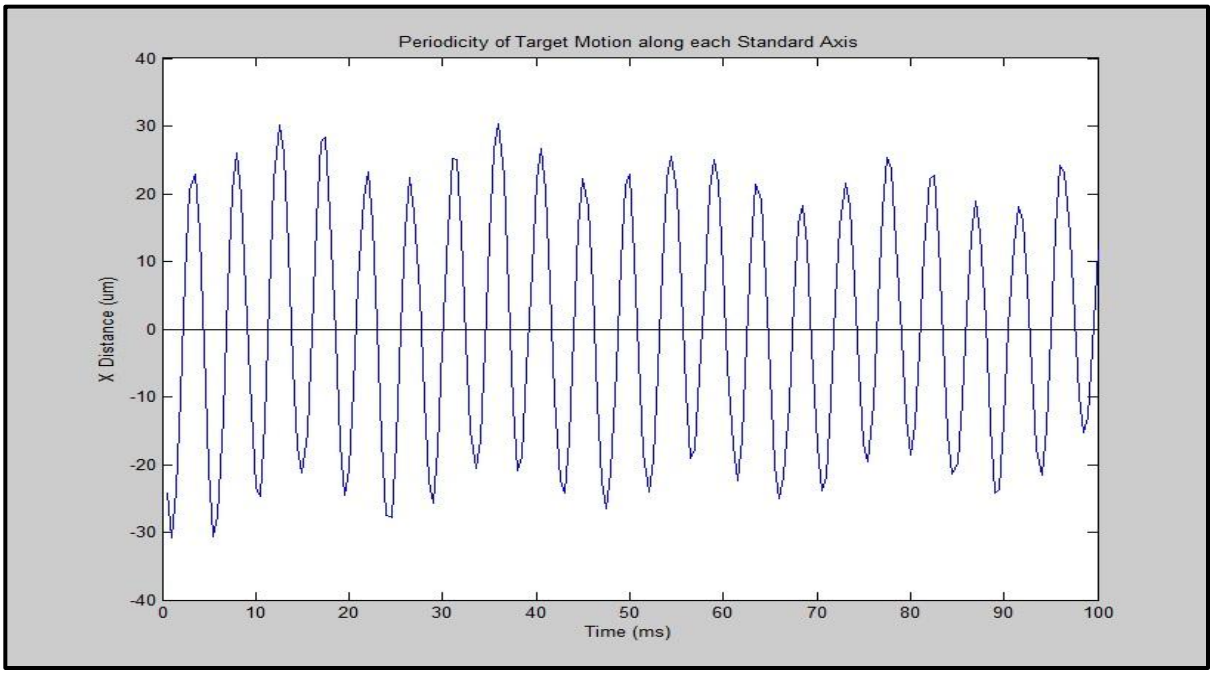

Fig. 5 A closer look at target position over time along an individual axis of motion
Targets oscillate with a frequency roughly corresponding to their fundamental resonance frequency along each axis. The amplitude of oscillation decreases slowly over time within the exponential damping envelope until reaching steady state vibration as shown in the bottom graphs of Fig. 4

3 Results and Analysis

3.1 3-dimensional transient cryogenic target motion modeling

As stated, position data from the two high-speed video cameras situated inside the OMEGA target chamber were imported into MATLAB for further analysis. Fast Fourier Transforms, a method of extracting frequency components from time-domain data, were performed to identify fundamental frequencies as shown in Fig. 6. Table 1 presents the results of this analysis for some targets which were used in laser shots and diagnostic tests.

Table 1 Analysis of frequency components of cryogenic fusion targets

Target Name	CRYO-2094-1830			CRYO-ME-2Q11-01-42		
Axis	X	Y	Z	X	Y	Z
Fundamental Resonance Frequency	156.3 Hz	148.4 Hz	437.5 Hz	215.2 Hz	215.6 Hz	215.7 Hz

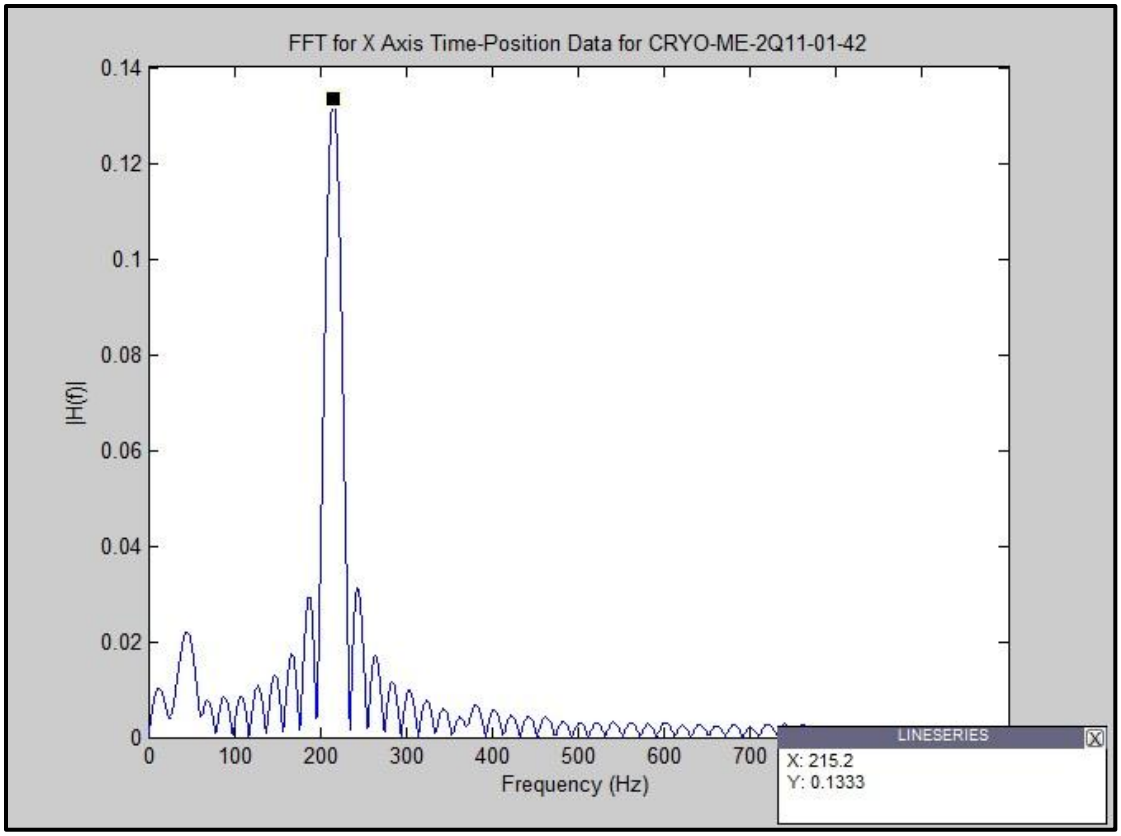

Fig. 6 Fast Fourier Transform of X axis position of CRYO-ME-2Q11-01-42
Position data is processed through the FFT algorithm to yield frequency components of target motion and thus fundamental resonance frequencies. The fundamental frequency of this target, CRYO-ME-2Q11-01-42, is seen to be approximately 215.2 Hz on the X axis.

The two targets in Table 1 are Type 1 and 1d targets, respectively. These targets have relatively low fundamental frequencies on their X and Y axes. Because the Z axis is oriented longitudinally along the stalk of the target, it is sometimes characterized by much higher frequencies, as in the case of CRYO-2094-1830. Because the video camera sampling frequency is 2000 Hz, the highest frequency level possible to measure, called the Nyquist frequency, is 1000 Hz. Some other types of targets such as Type 4 and Type 6 targets are made of different materials and have fundamental frequencies around 1000 Hz, so it is difficult to extract vibration characteristics for these as well.

Target oscillation on each axis is usually at approximately the same frequency, as shown in Table 1, but has different amplitudes and different phase angles. The target's path of motion as a result of these characteristics is that of an arbitrarily oriented ellipse in 3-dimensional space. Given that the standard ellipse is described by the parametric equations $x = a\cos t$, $y = b\sin t$, $z = 0$, one can use three rotation matrices to find the coordinates of any ellipse in 3-space:

If $a > b$:

$$\hat{x}''' = \begin{bmatrix} \cos\phi & \sin\phi & 0 \\ -\sin\phi & \cos\phi & 0 \\ 0 & 0 & 1 \end{bmatrix} \begin{bmatrix} \cos\theta & 0 & -\sin\theta \\ 0 & 1 & 0 \\ \sin\theta & 0 & \cos\theta \end{bmatrix} \begin{bmatrix} 1 & 0 & 0 \\ 0 & \cos\psi & \sin\psi \\ 0 & -\sin\psi & \cos\psi \end{bmatrix} \begin{bmatrix} a\cos t \\ b\sin t \\ 0 \end{bmatrix} \quad (5)$$

If $a < b$:

$$\hat{x}''' = \begin{bmatrix} \cos\phi & \sin\phi & 0 \\ -\sin\phi & \cos\phi & 0 \\ 0 & 0 & 1 \end{bmatrix} \begin{bmatrix} 1 & 0 & 0 \\ 0 & \cos\psi & \sin\psi \\ 0 & -\sin\psi & \cos\psi \end{bmatrix} \begin{bmatrix} \cos\theta & 0 & -\sin\theta \\ 0 & 1 & 0 \\ \sin\theta & 0 & \cos\theta \end{bmatrix} \begin{bmatrix} a\cos t \\ b\sin t \\ 0 \end{bmatrix} \quad (6)$$

where ϕ, θ, and ψ are the angles of rotation in space about the Z, Y, and X axes respectively, a and b are either the semimajor or semiminor axes, and t is time [5]. There are two possible equations as shown because the order in which the rotation matrices should be applied varies depending on the major axis of the ellipse.

With this in mind, a brute force algorithm was created to solve for the three spatial angles and semimajor/minor axes of the least-squares ellipse. However, such an algorithm was computationally intensive, slow to run, and of questionable precision. Therefore, a genetic algorithm called *TransformerEvolution* was created to solve for the same five ellipse parameters by evolving toward the minimum σ, where:

$$\sigma = \sqrt{\frac{\sum_{i=1}^{N}\sqrt{(x_i-x_2)^2+(y_i-y_2)^2+(z_i-z_2)^2}}{N}} \qquad (7)$$

where *N* is the number of position data points, (x_i, y_i, z_i) are the coordinates of a data point, and (x_2, y_2, z_2) are the coordinates of the closest point on an ellipse along the geodesic, that is, the shortest possible path, to the elliptical model. Essentially, this solves for the true least-squares ellipse by varying the parameters of potential elliptical models until the average distance from all data points on the model is minimized. This algorithm, the results of which are displayed in Fig. 7, both precisely and efficiently produces one of the ellipse equations *(5)* or *(6)* as a model of cryogenic deuterium-tritium target motion. These two similar equations are necessary because alignment along the correct axis is a required starting condition for this genetic algorithm to run

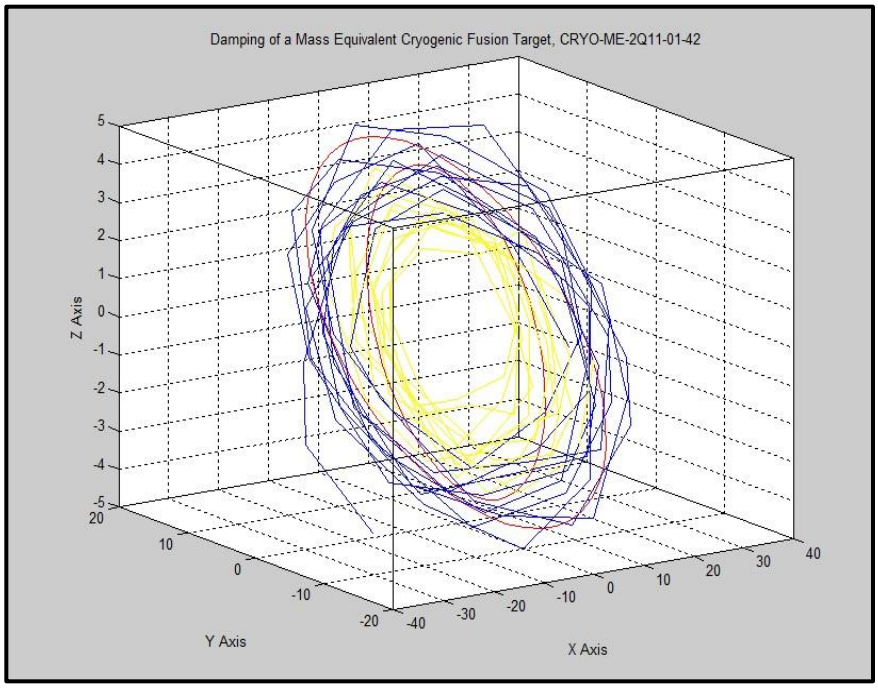

Fig. 7 3-dimensional visualization of the damping of a cryogenic target motion path
This path of motion of this target, CRYO-ME-2Q11-01-42, diminishes in size while rotating through space. Two elliptical models calculated at different points in time, depicted here in red, are accurate representations of target motion path, overlaid on the data shown in blue and yellow. Note that the magnitude of the scale on each axis varies.

accurately. This model is extremely useful because it is in the time domain, so one can extrapolate an accurate prediction of target location in the time regions where the high-speed video cameras in OMEGA are unable to record data simply by increasing or decreasing the value of *t* as given by the ellipse equations. As *t* increases, calculating new best-fit elliptical models shows that the values of *a* and *b* decrease while the values of ϕ,ψ, and θ also change. This describes the path's rotation on all coordinate axes as the size of the target motion path decreases, due to the variation of damping along each axis of the target.

When a mass equivalent target is used in an experiment without a laser shot, there is enough data to calculate a reliable damping estimate with the exponential decay method. The average radii of elliptical models for the target path were treated as peaks on a damping curve, as displayed in Fig. 8. The average radii of the elliptical models were used in place of the initial data for target radius because the models discretize the data and also eliminate the mathematical difficulties involved with oscillating damping curves. This model shows that it takes between one and three seconds for a typical target to damp to steady state

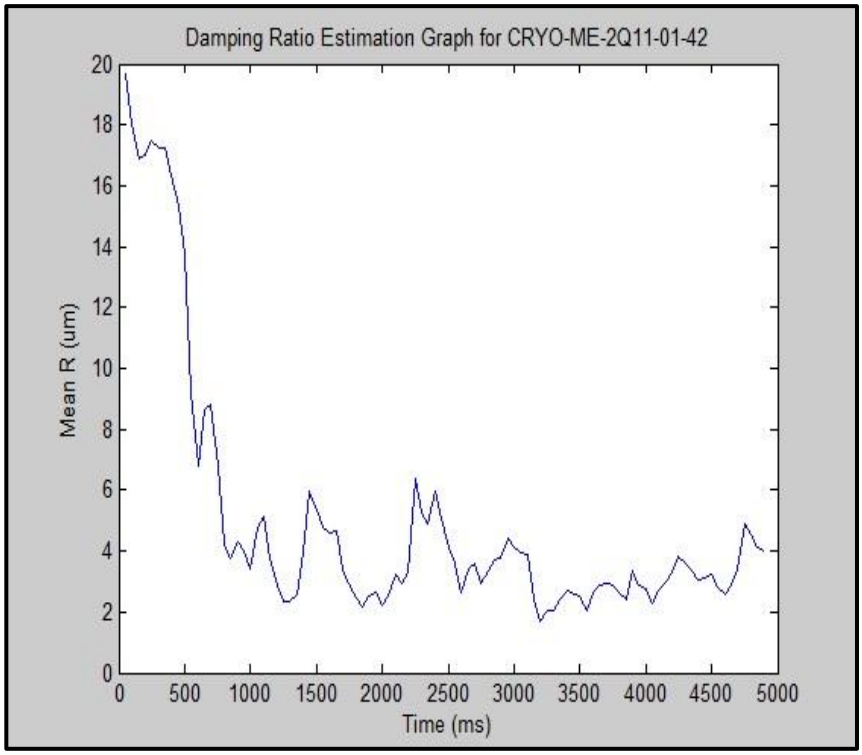

Fig. 8 Radial damping of cryogenic fusion target CRYO-ME-2Q11-01-42
This target damps to steady state motion within one to three seconds after excitation by the thermal shroud. Using the logarithmic decrement method with two points on this damping curve, a damping estimate of 0.38% was produced, which also implies a time for 1/e decay.

vibrational motion (which has a mean radius of approximately 3.3187 μm for CRYO-ME-2Q11-01-42). This is critically important in its potential for minimizing target vibration at the time of a laser shot. Designing a new routine for retraction of the thermal shroud which takes place over several seconds instead of approximately one second before the laser shot should, based on this work, be a successful way to address excessive target motion.

This data also lends further insight to the damping characteristics of targets under cryogenic conditions. It was found that the damping estimate actually decreases under the complex effects of the decreased temperature. This was demonstrated with the Type 1d target CRYO-ME-2Q11-01-42 with fundamental resonance frequency of approximately 207.5 Hz, where the damping estimate decreased from 0.90% of critical damping (half-power bandwidth method from a shaker test at room temperature) to 0.38% of critical damping (exponential decay method with target at 19 K). The half-power bandwidth method and exponential decay method have previously been found to give approximately equal damping estimates at room temperature [2].

3.2 Optimizing target design as a solution to excessive target motion

There is an alternative possibility for addressing excessive target motion, which considers targets that exhibit decreased amplitude of oscillation under excitation. Low frequency targets

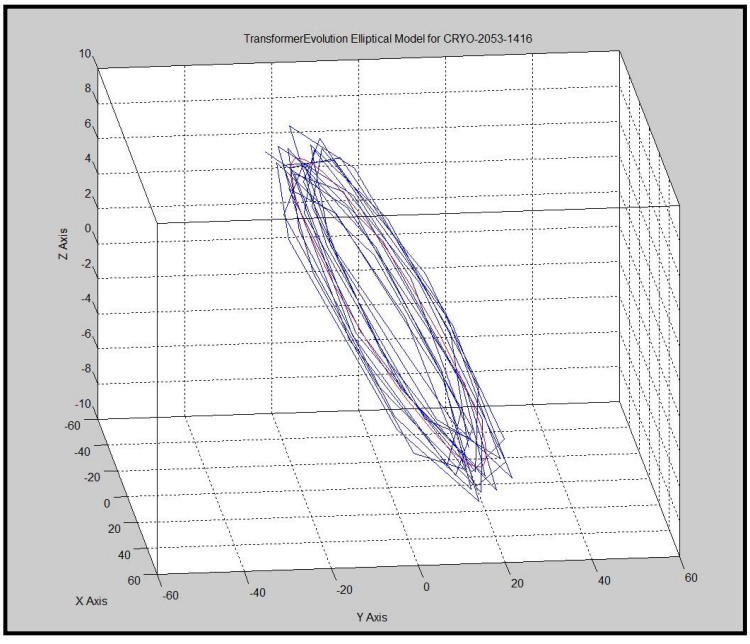

Fig. 9 Parametric elliptical model of the motion path of a low fundamental frequency target, CRYO 2053-1416
The red ellipse is the target motion path model created by the evolutionary algorithm *TransformerEvolution*, overlaid on the data plot (in blue). Low frequency targets such as this often exhibit a high radius of motion, around or greater than 30 μm.

with fundamental resonance frequencies around or below 200 Hz tend to feature regular elliptical paths which can be easily modeled as described above and shown in Fig. 9. However, both initial camera data and elliptical models clearly show a high average radius of motion for these targets which is detrimental to the efficiency of a laser shot.

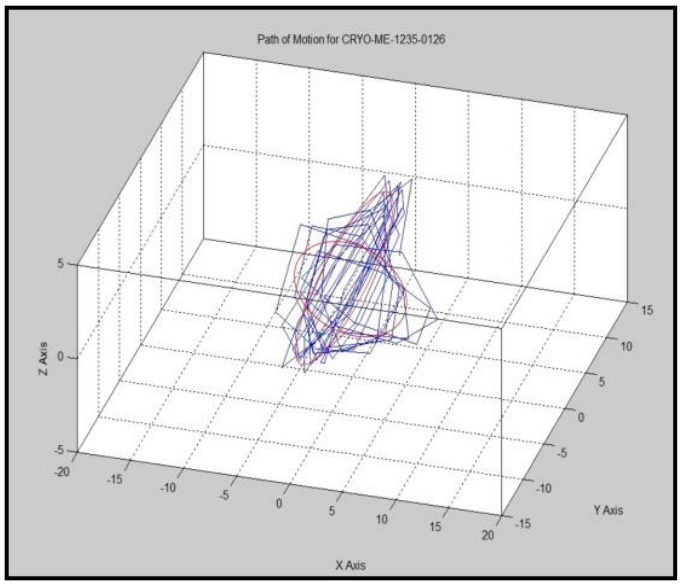

Fig. 10 Degeneration of distinct elliptical motion path around a threshold frequency of 300 Hz
Two separate elliptical motion paths are visible in this data as the phase angles of the motion components change about halfway into the time record. Average radius also significantly decreases.

When a target's fundamental resonance frequency is increased, the characteristics of a target's path of motion change drastically. Fig. 10 illustrates the path of motion of a Type 1c target, CRYO-ME-1235-0126, with fundamental resonance frequency of approximately 302.5 Hz. When the fundamental frequency of a target approaches 300 Hz, there is a distinct breakdown in the regular elliptical motion path into two ellipses. Since some targets change path very suddenly and may even increase their radius of motion, it is concluded that this effect is due to the higher fundamental frequencies of these targets. Higher frequency targets, above 400 Hz, do not exhibit a visible elliptical path at all. As shown in Fig. 11, a high

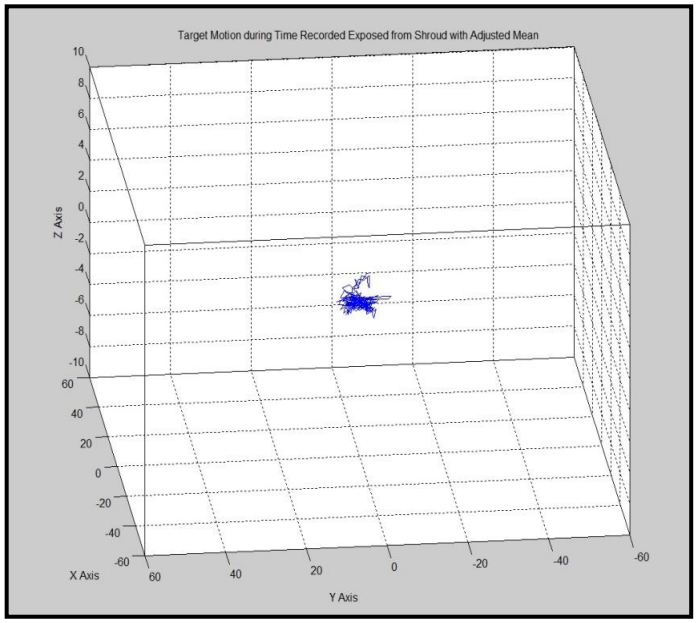

Fig. 11 Plot of motion path of a high fundamental frequency target
The target motion path exhibits a drastically decreased average radius of motion. Though the motion path appears noisy, tracing the curve shows the presence of periodic components.

fundamental frequency target's path of motion is extremely small as well as noisy. However, a program written in MATLAB to trace and highlight data points revealed significant periodicity to the target paths. The degeneration of the elliptical motion path around 300 Hz implies that these paths are unlikely to be elliptical. However, the path size approaches the sensitivity of the high speed camera data, limiting analysis. Nevertheless, this presents a second solution to excessive target motion. Using targets with high fundamental frequencies can minimize a target's motion simply because these targets do not exhibit high amplitudes of oscillation under excitation by the sources of vibration in the OMEGA target chamber. The average radius for these targets was calculated as an arithmetic mean of data, since 50-75 ms is not enough time for any significant damping to occur. A comparison of average radii for Type 1 (low fundamental frequency) and Type 4 and 6 (high fundamental frequency) targets measured is given below in Table 2 as an exact quantification of the potential of high frequency targets.

Table 2. Comparison of average radii for high and low fundamental frequency targets

	Average Radius	σ (Standard Deviation)
Type 1	33.30 μm	8.97
Type 4/6	3.98 μm	0.70

However, high fundamental frequency targets tend to be more fragile and are often lost during the process of filling the target with deuterium-tritium fuel and transporting it to the OMEGA target chamber for a laser shot.

4 Conclusions

Data from the OMEGA target chamber were used to analyze cryogenic target paths of motion and vibration characteristics. A time-domain parametric elliptical model was created based on this data to further characterize target behavior under excitation. Using this model, the damping ratio of cryogenic fusion targets at shot time was measured for the first time. It was

shown that a cryogenic mass equivalent target can damp under free vibration in one to three seconds. This model also has the potential to provide information about target position at the time of a laser shot. A new routine has recently been implemented on OMEGA which retracts the thermal shroud approximately four seconds before a laser shot, which has been numerically justified by this work. It is expected that the additional time after retraction will permit targets to damp fully and increase shot efficiency.

This data is also important in terms of helping to optimize target selection. Though targets with low fundamental resonance frequencies tend to follow a regular elliptical path, they have a greatly increased average radius from the origin. Targets with high fundamental resonance frequencies have decreased average radii, which suggests that these targets are superior in internal confinement fusion experiments because they permit greater uniformity of laser irradiation. The fragility of these targets makes them less desirable for practical laboratory use, however. Future work will build upon these models to design a target which is strong, stable, and less prone to vibrational motion. For future designs, the exponential decay method can be used in conjunction with the elliptical models described in this paper to calculate the necessary delay between thermal shroud retraction and time of the laser shot, with the ultimate goal of improving the efficiency and thus usable energy yield of internal confinement fusion.

Acknowledgements

I would like to thank Mr. L.D. Lund for being my research advisor and providing me essential information for my project and this report; Dr. R.S. Craxton for directing the research program at the Laboratory for Laser Energetics and reviewing this report; and Mr. M. Bonino for providing a walkthrough of the target fabrication laboratory as well as information about and images of the target.

Bibliography

[1] J. Nuckolls, L. Wood, A. Thiessen, and G. Zimmerman, “Laser compression of matter to super-high densities: thermonuclear (CTR) applications,” *Nature*, vol. 239, pp. 139-142, Sept. 1972.

[2] Zhang, Harvest. “Resonance and damping characteristics of cryogenic fusion targets.” *LLE Laboratory Report 306*. Rochester, NY: Laboratory for Laser Energetics, 2010.

[3] Harris, Cyril M. *Shock and Vibration Handbook, 3rd Edition*. New York: McGraw-Hill Company, 1988. pp. 2-5.

[4]. A.D. Nashif, D.I.G. Jones, and J.P. Henderson, *Vibration Damping*. New York: John Wiley & Sons, Inc., 1985, pp. 53, 117-154.

[5] Lay, David C. *Linear Algebra and its Applications, 3rd Edition*. Boston: Addison Wesley, 2003. pp. 160-162.

Photoaligned Liquid Crystal Wave Plate

Avery Gnolek
Webster Thomas High School

Advisor: Kenneth L. Marshall

University of Rochester
Laboratory for Laser Energetics
Summer High School Research Program 2011

Abstract

Liquid crystal (LC) wave plates were produced using a photosensitive polymer to generate alignment. Currently, alignment of liquid crystals is achieved through the use of mechanical buffing, although this process is relatively imprecise and inherently generates particulate contamination. Photoalignment of LC wave plates using a coumarin-based photopolymer resolves many of these fundamental problems with buffing. Because photoalignment of LC wave plates is a non-contact process, it provides high-quality LC alignment without introducing particulate contamination on to the substrate. For the low-birefringence LC materials used for wave plate fabrication, the alignment quality produced using coumarin-based photopolymers is most greatly impacted by the surface quality and optical uniformity of the substrates. When substrates with relaxed scratch/dig, wedge and flatness tolerances were used, LC alignment was poor with numerous disclinations (alignment defects). When substrate quality was improved, the number of disclinations was vastly reduced. Small-

aperture prototype photoaligned wave plates produced had retardance values well within the allowable specifications for buffed waveplates deployed in OMEGA.

Introduction

Wave plates are an important part of the OMEGA laser system. As a laser beam passes through the system, the high intensity and optical uniformity of the beam must be maintained. This is accomplished using a wide variety of lenses, amplifiers, and beam shapers that form and amplify the original beam. However, each of these devices will only operate correctly with a certain polarization state of light. Wave plates are used to change the polarization of the laser beams, ensuring that each element in the system receives the correct polarization.

The polarization shift in wave plates is accomplished using liquid crystals (LCs). This is possible because the observed properties of liquid crystals are dependent on orientation, making them anisotropic. Figure 1 shows the molecular orientation in an isotropic liquid. The molecules are arranged randomly, with a very low orientation order. An isotropic liquid has only one refractive index, which is independent of the direction in which the liquid is viewed. Liquid crystals are anisotropic, and are not arranged randomly but possess some orientation order. Anisotropic materials have different properties based upon the orientation in which they are viewed. This anisotropy allows them to shift the polarization of light. Rather than being aligned randomly, the molecules align generally in the same direction (Fig. 2). Because of this orientation order, liquid crystals have more than one refractive index, typically two. The difference between the two indices of refraction is called

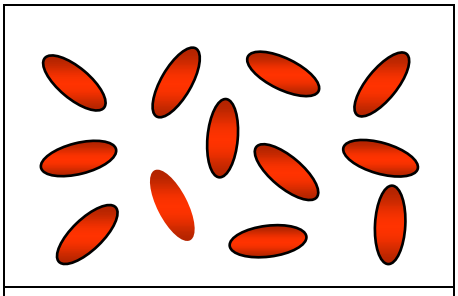

Figure 1: Molecular ordering in an isotropic liquid

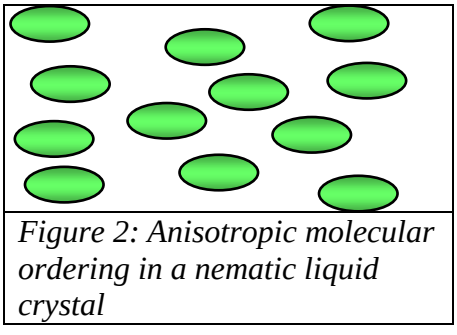

Figure 2: Anisotropic molecular ordering in a nematic liquid crystal

birefringence. It is birefringence that causes the change in polarization when light is passed through an anisotropic liquid.

When light enters a birefringent material, it breaks into two components with perpendicular directions of polarization. These are called the ordinary ray and the extraordinary ray. The refractive index is a measure of how fast light moves through the material. Because LCs are birefringent and have two refractive indexes, these components move through the LC at different speeds. The phase shift between the components caused by the difference in speed at which they propagate determines the polarization direction of the light. By varying the phase shift, different polarizations of light can be created. When the components are completely in phase, the light is linearly polarized. However, circular and elliptical polarizations can be produced by varying the phase shift. A phase shift of $\pi/2$ will convert linearly polarized light into circularly polarized light.

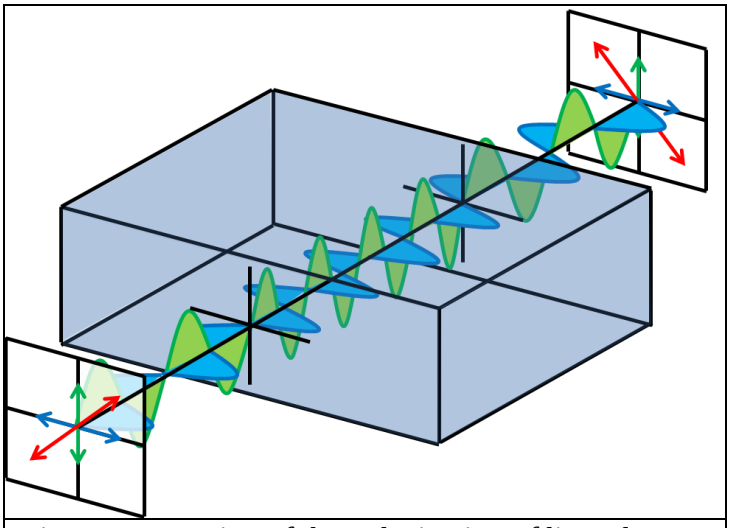

Figure 3: Rotation of the polarization of linearly polarized light through an anisotropic medium(e.g, a LC wave plate)

Figure 3 shows light passing through a half wave plate (shown as the blue box). Prior to moving through the wave plate, the light is linearly polarized. As the light passes through the wave plate, the ordinary and extraordinary ray, represented by the green and blue waves, gradually move out of phase, eventually rotating the polarization by 90°. The amount of phase shift is dependent on both the birefringence of the liquid crystal and the thickness of the wave plate, as governed by this equation:

$$\tau = \frac{2\pi\,\Delta n\,L}{\lambda} \qquad 1.$$

where τ is the phase shift (retardance), Δn is the birefringence, *L* is the thickness, and λ is the wavelength of light passing through the plate. By varying the thickness of the wave plate, the retardance can be adjusted.

However, in order to produce a viable wave plate, the LC molecules must be uniformly aligned in the cell. This can be accomplished in two different ways. Previously, liquid crystal alignment was generated using mechanical buffing. In this process, the glass substrate is first coated with a polymer alignment coating, then placed under a rotating cylinder, which gradually moves across the entire substrate. The rotation of the cylinder creates microscopic ridges along the surface of the polymer. The liquid crystals then align themselves along these ridges. If both substrates are buffed and positioned correctly, the LC molecules will be aligned parallel to each other (Fig. 4). Although the buffing process works well for information display and other low incident energy applications, it has many drawbacks for high peak power laser applications.[1] Because the buffing cylinder is physically scraping over the coated substrate, it can leave many embedded particles behind. These particles not only disrupt the LC alignment, but can also act as sites for laser-induced damage. Furthermore, it becomes more difficult to scale up the buffing process as the substrate size increases.

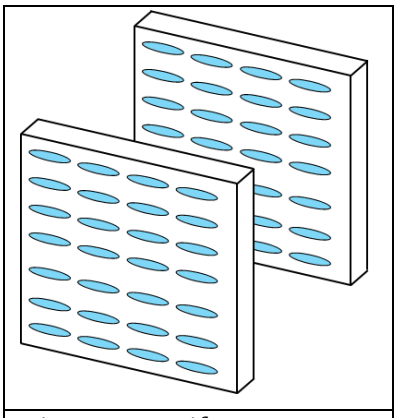

Figure 4: Uniform molecular alignment in an LC waveplate containing a molecular alignment layer on the substrate surfaces

Photoalignment can be used instead of buffing to generate LC alignment by coating the substrate with photo-reactive coumarin monomers and exposing it to linearly polarized UV light. This UV exposure causes the coumarin monomers to dimerize and align themselves

perpendicular to the polarization direction of the UV light[2,3] (Fig. 5). When the LC molecules come into contact with the photo-dimerized coumarin layer, the LC molecules will then align themselves parallel to these dimers, producing uniform alignment[4]. Because the photoalignment process is non-contacting and leaves no scratches or embedded particles, it is inherently clean-room compatible and readily scalable to much larger substrate sizes. As a result, photoaligned devices have a much higher damage threshold (30-60 J/cm^2 at 1054 nm, 1ns, than do buffed LC devices with the upper damage threshold of the device limited primarily by the LC material.

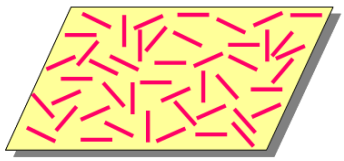

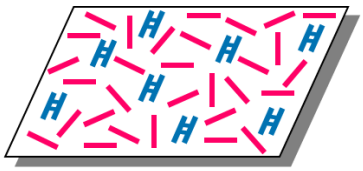

Figure 5: Representation of the coumarin photopolymer coating before and after UV irradiation. (Red lines are monomers, double blue lines are dimers)

Experimental

For most experiments, either 1" dia. BK7 round substrates with a surface flatness of one quarter-wave at 1054 nm or 1" x 1" Borofloat squares were used. The 1" x 1" Borofloat squares were used for early process development experiments, as they are much less expensive due to their poorer scratch-dig and wedge specifications. The higher quality BK7 round substrates were used for the final wave plate prototype fabrication.

Both the substrates and the synthetic wipers used to clean the substrates were rinsed with deionized (DI) water, to remove any large particles. The substrates were then scrubbed with the synthetic wipers using 0.05 µm Masterprep® Polishing Suspension, and rinsed again with DI water. The substrates were inspected using a water break test to reveal surface contaminants. In this test, substrates were rinsed with water and tilted. If the surface is sufficiently clean, water will stay spread as a continuous film on the substrate surface and not bead up or be pulled to the

edge of the substrate. Substrates that passed the water break test were placed in an ultrasonic bath filled with DI water and detergent at 69°C for 60 minutes. After the ultrasonic bath cleaning, the substrates were rinsed with DI water, then visible water droplets were removed from the substrates using a nitrogen air gun. The cleaned substrates were then placed on a hotplate at 130°C for 30 minutes to ensure that all absorbed water was evaporated.

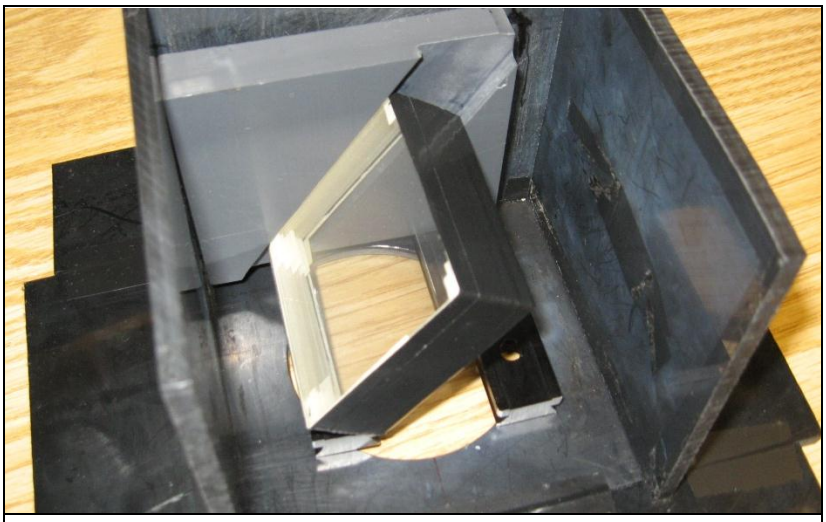

Figure 6: "Pile of plates" polarizer and polarizer holder

After drying, the substrates were placed on a spin-coater and covered with approximately 0.3 mL of chloroform. The spin-coater was covered with a glass crystallizing dish to prevent evaporation and ensure that the air was saturated with chloroform. Excess chloroform then was spun off at 4000 rpm for 60 seconds. Using a 0.45 μm PTFE 13 mm dia. hydrophobic syringe filter and glass syringe, approximately 0.3 ml of 0.1wt% coumarin Polymer 3 in chloroform was

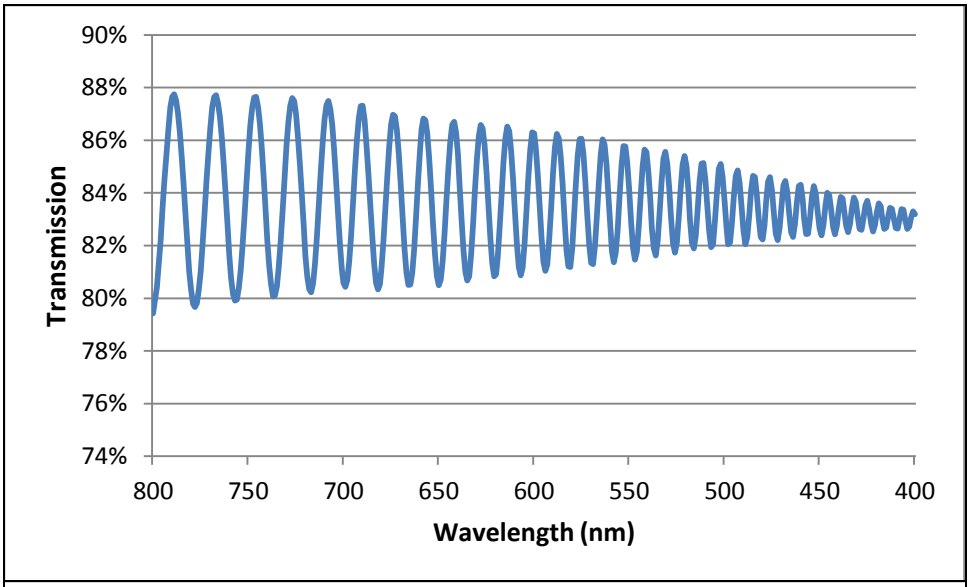

Figure 7: Interference fringes measure on an empty LC wave plate device. This data is used to accurately determine the cell gap before filling with LC.

deposited on the substrate. The substrate was immediately spun at 4000 rpm for 120 seconds. The substrates were then removed from the spin-coater to air-dry before being irradiated.

Photoalignment was achieved by irradiating the substrates for one minute with a broad-band 500-watt mercury xenon UV lamp equipped with a dichroic mirror and lenslet array to produce collimated UV light at 325 nm. To polarize the UV light, the substrates were placed under a "pile of plates" polarizer oriented at Brewster's angle (Figure 6). To assemble the cell, a capillary tube was first dipped in OG-142-13 UV-curing epoxy. The tip of a metal spatula was used to pick up a very small amount of 14 μm glass fiber spacers, which were mixed with the epoxy and applied to the corners of the substrates. The substrates were then assembled so that the alignment direction of the photoalignment layers was parallel to each other. The substrates were placed under a 365 nm low-intensity UV lamp to cure the fiber-filled epoxy spacers for 5 minutes. The cell gap (distance between the substrates) was measured using a Lambda 900 spectrophotometer. As shown in Fig. 7, the transmission of the empty cell followed a damped sinusoidal pattern as the wavelength of light being passed through the cell was decreased from 800 to 400 nm. This pattern could be used to calculate the cell gap[6] from the following equation:

$$t = \frac{\lambda_1 \lambda_2}{2n(\lambda_2 - \lambda_1)} \qquad 2.$$

where t equals the cell gap, λ_1 equals a wavelength of peak transmission, λ_2 equals the next wavelength of peak transmission, and *n* equals the refractive index of the material between the substrates (air). Once the cell gap was calculated, the LC material could be correctly blended and added to the device.

Using equation 1, the required birefringence of the LC mixture could be calculated after the cell gap was known. In order to obtain this birefringence, a blend of two commercial low-birefringence LC fluid mixtures (BDH 18523 and 14627) was prepared. These fluids were mixed at room temperature, then placed on a hot plate set at 60° C. The mixture was stirred with a magnetic stir bar at 500 rpm for two hours. Because the two LC mixtures have different

birefringence values, the birefringence of the final mixture could be adjusted by varying the percentages of 18523 and 14627. Although the exact proportion of LC used varied in each cell, the mixture consisted of between 49% to 52% 18523 by weight. Once this mixture was made, the cell was placed on a hot plate set to 80°C. The LC was drawn into a 1 mL plastic syringe, and a 0.45 µm PTFE 4 mm hydrophobic syringe filter was fitted on the end of the syringe. A small syringe needle was fitted to the end of the syringe filter and the cell was filled slowly with the needle tip contacted to the space between the two substrates. Once filled with LC and partially sealed with epoxy, the cells were cooled at 10°C per hour until they reached room temperature. This slow cooling rate avoids rapid LC fluid contraction that could cause alignment defects.

Discussion

Small-aperture prototype photoaligned wave plates had retardance values well within the allowable specifications for buffed waveplates already deployed in OMEGA. To meet this specification, a wave plate must have a high uniformity and contrast, as well as a retardance that

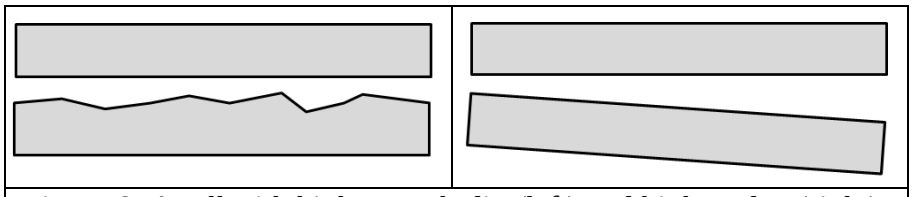

Figure 8: A cell with high scratch-dig (left) and high wedge (right)

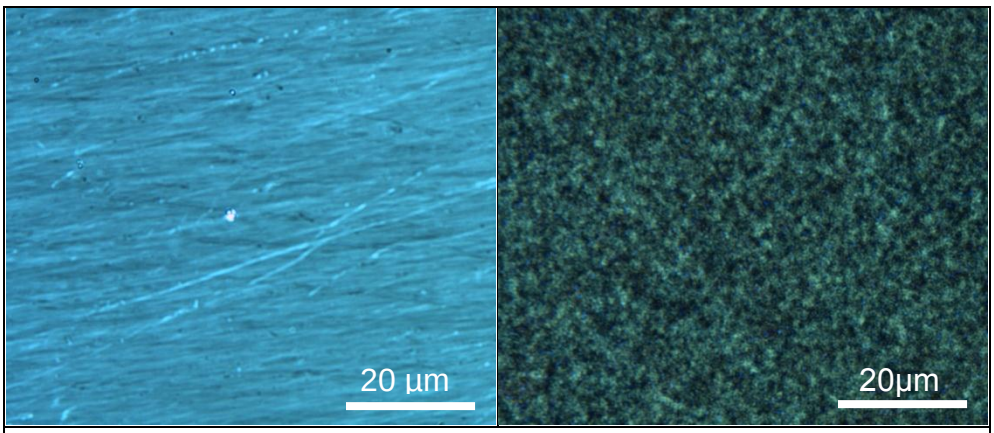

Figure 9: Comparision of liquid crystal alignment of buffed (left) and photoaligned (right) wave plates as viewed in transmission using a polarizing microscope with crossed polarizers.

deviates < 5% from the OMEGA device specification. It was determined that the most important factors impacting the quality of the photoaligned waveplate prototypes were the scratch-dig specification of the substrates and the wedge of the completed cell. A substrate with a high scratch-dig will have numerous alignment defects, while a cell with high wedge in its cell gap will cause the retardance to vary across the device clear aperture (Fig 8). Such a device would be unsuitable for use in operation in OMEGA, as a consistent retardance across the entire clear aperture is necessary to maintain beam uniformity. Photoaligned devices employing substrates with low scratch-dig and a small variance in cell gap thickness can produce waveplates with properties superior to those of buffed devices. As shown in Fig. 9, the buffed wave plate has multiple scratches and embedded particles, and readily visible buffing lines, while the photoaligned wave plate is free of embedded particles and has a more uniform alignment. This uniform alignment and cell gap allows cells to be created with nearly ideal retardances (Table 1).

Cell	**Thickness**	**Retardance**	**% Error**
A	14.08 μm	522.7 nm	0.82%
B	13.87 μm	530 nm	0.57%
C	14.10 μm	540 nm	2.47%
D	14.14 μm	543 nm	3.04%

Table 1: Measured retardance values for the small aperture photoaligned LC wave plate prototypes. The error is measured relative to the ideal retardance of 527 nm

The quality of the cell was also impacted by the spacers used to separate the substrates. Originally, 10 μm or 8 μm glass spheres were mixed with the OG 154-1 epoxy and applied to the corners of the substrate. However, cells produced with this method had extremely variable cell gaps. This problem was eliminated by using 14 μm glass fibers mixed into the epoxy instead of the glass beads. A combination of higher quality substrates and fiber spacers produced the most accurate and precise cells.

Conclusions

Experiments have shown that photoaligned wave plates of equal or superior quality to buffed wave plates can be created if substrates with low scratch-dig and wedge are used along with precise photopolymer application.

If the quality of photoaligned waves can continue to be improved, there will be many applications for photoaligned devices. Photoaligned wave plates could be used on the OMEGA and OMEGA EP laser systems to replace the currently used buffed wave plates. The repeatability, precision, and inherent cleanliness of the photoalignment process will offer vast improvements over buffing. Experiments in the future will explore scaling up the photoalignment process to larger wave plates and apertures. This is a requirement for use on the OMEGA system and will ensure that photoalignment is successful on large scale devices. As part of the scale-up process, large-aperture photoaligned waveplates will need to be tested for their laser damage resistance, both by small-aperture testing and on one OMEGA beamline to qualify then for full deployment in OMEGA or OMEGA EP as replacements for buffed LC wave plate technology.

Acknowledgments

I thank Dr. R. Stephen Craxton for overseeing the LLE high school program and selecting me for such an extraordinary research opportunity. I thank my advisor, Kenneth L. Marshall for all of his help throughout my project and for providing an opportunity to work in the Materials Lab. Finally, I thank the Materials Lab staff and students, especially Marisa Vargas for her help. I would additionally acknowledge Christophe Dorrer, Gary Mitchell and Kai Kao for helping to explain the properties of liquid crystals and the construction of waveplates.

References

[1] N. A. J. M. van Aerle, M. Barmentlo, and R. W. J. Hollering, "Effect of rubbing on the molecular orientating within polyimide orienting layers of liquid-crystal displays" *J. Appl. Phys.*, **74**, 3111 (1993).

[2] M. Schadt, H. Seiberle, A. Schuster, S. M. Kelly, "Photo-Induced Alignment and Patterning of Hybrid Liquid crystalline Polymer Films on Single Substrates," *J. Appl. Phys.*, **34,** 764-767 (1995)

[3] J. Chen, D.L Johnson, P. J. Bos, X. Wang, J. L. West, "Model of liquid crystal alignment by exposure to linearly polarized ultraviolet light," *Phys. Rev. E.*, **54**, 1599 (1996)

[4] J. M. Geary, J. W. Goodby, A. R. Kmetz, and J. S. Patel, "The mechanism of polymer alignment of liquid-crystal materials," *J. Appl. Phys.*, **62**, 4100 (1987).

[5] K. L. Marshall, J. Gan, G. Mitchell, S. Papernov, A. L. Rigatti, A. W. Schmid, and S. D. Jacobs, "Laser-Damage-Resistant Photoalignment Layers for High-Peak-Power Liquid Crystal Device Applications," in Liquid Crystals XII, edited by I. C. Khoo (SPIE, Bellingham, WA, 2008), Vol. 7050, Paper 70500L.

[6] K. H Yang, "Measurements of empty cell gap for liquid crystal displays using interferometric methods," *J. Appl. Phys.*, **64** (9), 1988

Designing a New Master Timing Generator

Dana Gretton
Honeoye Falls-Lima High School
Advisors: Robert Peck, Eryk Druszkiewicz

Laboratory for Laser Energetics
University of Rochester
Summer High School Research Program
Summer 2011

Abstract

At the Laboratory for Laser Energetics, a complex network of electronics serves to direct and monitor the operation of the OMEGA laser system. Some of these components, like the Master Timing Generator, are aging and incompatible with modern technology. The Master Timing Generator, or MTG, first introduced in the 1990s, is a logic device responsible for keeping all of the laser system triggers for diagnostic hardware such as computers, cameras, and sensors tightly synchronized to the laser pulse. To replace the present device's 20-year-old technology, a new MTG was designed on a modern Complex Programmable Logic Device chip known for its low power consumption and high reliability. An Ethernet interface was also developed so that the LLE network could communicate directly with the MTG, integrating with existing protocols and speeding error diagnosis. Oscilloscope traces verify that the up-to-date MTG faithfully reproduces all of the behaviors of its predecessor. Additionally, the device's new web page adds to its utility as LLE proceeds with its systems renewal.

1. Introduction

1.1 Master Timing Generator

The Master Timing Generator (MTG) is an input-output digital logic device that serves as a source of synchronizing signals for the thousands of laser system components in OMEGA, such as the video cameras, laser source, flash lamps, and shot diagnostics. Some of the MTG signals are generated continuously, to provide a time base or periodic reset for digital systems; others are generated in response to a stimulus from the Shot Executive to coordinate processes before, during, and after a laser shot. The Shot Executive is the computer system in the main control room responsible for coordinating all laboratory activities related to a laser shot according to the instructions from the Shot Director and other LLE staff. Located in the rear of OMEGA's Power Conditioning Office, the centrally located MTG distributes its signals via a series of cables, fiber optics and amplifiers throughout the laser bay and control room. The signals are accessible to technicians and equipment from standardized sets of ports at key locations. The MTG has four primary inputs and six primary outputs (Fig. 1), summarized below.

Continuous Inputs • 38 MHz **Gating Inputs** • T-10 Enable • T-0 Enable **Other Inputs** • Reset	**Continuous Outputs** • H-Sync • V-Sync • Five-Hz • Tenth-Hz **Gating Outputs** • T-10 • T-0

38 MHz. Known colloquially as the "heartbeat" of the LLE facility, the 38 MHz signal is an exceptionally stable sinusoidal signal used as a time base for all laboratory operations. Its actual

frequency is approximately 37.8 MHz. Its period is 26.46 ns. It is generated by a temperature-controlled, vibration-damped source, and distributed universally in the OMEGA system and the surrounding research laboratories.

T-10 Enable. The Shot Executive computer enables the MTG to assert a gated T-10 pulse with the T-10 Enable signal. The input is normally low, and is driven high by the Shot Executive for approximately 10 seconds so that it overlaps a single Tenth-Hz pulse, at which time the T-10 pulse is asserted (Fig. 2).

T-0 Enable. As for the T-10 Enable signal, the Shot Executive computer enables the MTG to assert a gated T-0 pulse with the T-0 Enable signal. The input is active high and is driven by the Shot Executive for approximately 10 seconds so that it overlaps a Tenth-Hz pulse, at which time the T-0 pulse is asserted. T-10 Enable and T-0 Enable allow the MTG to function as a synchronized intermediary between the Shot Executive and the OMEGA laser system.

Reset. The reset signal is issued by the Shot Executive, or by pressing the associated button on the MTG readout. It is active high. All outputs return to their default states for the duration of the reset pulse, and then resume normal operation on the pulse's falling edge.

H-Sync. H-Sync, or "Horizontal Synchronization," is an active-low, continuously generated periodic digital signal used exclusively by cameras. It has a frequency of approximately 58 kHz and a pulse width of 6.94 μs. The rising edges of H-Sync precede the rising edges of Tenth-Hz by 200 ns to make them coincident with V-Sync's rising edges. Because it is common to all LLE cameras, H-Sync ensures that all horizontal lines are synchronous. See Appendix A for details on analog video signals at LLE.

V-Sync. V-Sync, or "Vertical Synchronization," is an active-low, continuously generated periodic digital signal used exclusively by cameras. It has a frequency of approximately 60.2 Hz, significantly lower than H-Sync, and a pulse width of 569 μs, or 9 H-Sync cycles. The rising edges of V-Sync are always coincident with a rising edge of H-Sync. Because it is common to all LLE cameras, V-Sync ensures that all fields and frames recorded by LLE's imaging systems are synchronous. See Appendix A for details on analog video signals at LLE.

Five-Hz. Five-Hz is a continuously generated periodic digital signal primarily used to trigger human interfaces and displays to refresh at a rate comfortable for viewing. It has a period of 200 ms and a pulse width of 400 ns.

Tenth-Hz. Arguably the most important synchronization signal at LLE, the Tenth-Hz pulse is a continuously generated periodic digital signal used by instruments, computers and other equipment to trigger low-frequency tasks such as data dumps, resets and automatic self-diagnostic routines. It has a period of 10 s and a pulse width of 400 ns. The rising edges of the Tenth-Hz pulses are always precisely coincident with every 50^{th} Five-Hz pulse.

T-10. The sequence of events immediately before, during, and after irradiation of the target, occurring approximately once per hour at LLE, is known as a "shot cycle." During a shot cycle, exactly one T-10 pulse is asserted 10 seconds and 5 ms (one Tenth-Hz period and the shot delay) prior to irradiation, indicating that a shot is imminent. Upon receiving this signal, all laboratory devices initialize final preparation for the laser shot, including calibration, positioning and priming. Devices may also begin timing routines. With a pulse width of 422 ns, the T-10 pulse is identical to and occurs coincidently with a Tenth-Hz pulse.

T-0. During a shot cycle, exactly one T-0 pulse is asserted 5 ms prior to irradiation. Upon receiving this signal, laboratory devices initiate fine timing routines for triggering extremely time-sensitive instruments like streak cameras. With a pulse width of 422 ns, the T-0 pulse is identical to and occurs coincidently with a Tenth-Hz pulse.

Unlike a computer or microprocessor, the MTG does not have an internal clock signal; it is a purely combinational logic device. In general, the MTG utilizes digital counters to synthesize its continuously generated signals at integer multiples of 38 MHz. Its shot-cycle-related signals are derived from and synchronous with its continuous signals and are gated by the Shot Executive.

1.2 Rate Regenerator Modules (RRMs)

RRMs are complementary devices to the MTG in that they regenerate other relevant timing signals locally by monitoring the Tenth-Hz signal from the MTG and the laboratory-universal 38 MHz signal. RRMs are placed in strategic locations throughout OMEGA. All RRMs are slaved to the MTG, and are thus synchronized, but the signals they produce are more specialized for nearby applications and suffer from less noise due to long cabling. An RRM served as an important prototyping platform for the new MTG.

1.3 The Old MTG

The MTG currently installed in OMEGA, hereafter referred to as the "old MTG," was introduced in the 1990s (Fig. 3). At its heart is a Stamp microcontroller.

The old MTG is out of date in a variety of ways. While the industry standard for integrated circuit (IC) packaging has progressed to 0.5 mm pins or, even more recently, microdot array, the MTG continues to utilize components with tenth-inch-pin packaging. This discrepancy makes the parts difficult to replace because the ICs are no longer readily available. Its central logic device, the Stamp microcontroller, has its own set of limitations: microcontrollers have been replaced with combinational logic, such as Field Programmable Gate Arrays (FPGAs) and Complex Programmable Logic Devices (CPLDs), in applications such as this one; fewer programmers are now proficient with the Stamp's programming language, BASIC; and the microcontroller's development tools are no longer produced. Many newer devices in the OMEGA system, like RRMs, have a network interface and error reporting capability, features that the old MTG markedly lacks. These issues were addressed in the design of the new MTG.

In addition to the MTG inputs and outputs listed above, the old MTG has an "Incomplete Shot" indicator LED, which illuminates under any of the following circumstances:

- T-10 Enable is brought high, then low, without overlapping a Tenth-Hz pulse.
- A Tenth-Hz pulse occurs after T-10 Enable went low, without ever receiving a T-0 Enable.
- T-0 Enable is brought high, then low, without overlapping a Tenth-Hz pulse.

All of these conditions indicate that a shot was initiated by the Shot Executive, but was aborted short of completion. This functionality was considered when designing the new MTG.

1.4 Goals

The principal aim of the work undertaken was to replicate the old MTG on a new platform. The new platform was required to be modern, so that its replacement parts would be available in case of failure and maintenance would be simpler; flexible, so that any MTG behavioral changes required in the future would be implementable on stable hardware; and industry-standard, so that the hardware and corresponding backup hardware could be manufactured without the necessity of specialty fabrication services.

Secondary goals included safeguarding, error detection, and network communication capabilities for the MTG. Safeguards against noisy environmental conditions and incorrect shot cycle signaling were implemented. Several modes of error detection were pursued and evaluated, and two were implemented, in order to increase reliability and traceability of faults: shot error and clock error. Network communication was an objective because LLE is in the midst of a laser control system update and renewal in which older components are outfitted with the means to communicate over LLE's IP network. Networking allows the MTG to report its status and error messages to querying technicians and computer systems.

2. Designing a New MTG

2.1 Complex Programmable Logic Device

A Complex Programmable Logic Device, or CPLD (Fig. 4), was chosen as the platform for the new MTG. A CPLD is a medium-complexity digital logic device with non-volatile configuration memory constructed from an array of macrocells, each of which is a gate array that can be reconfigured arbitrarily. Whereas the old MTG utilized multiple interconnected discrete integrated circuits, the CPLD is a single 20-mm-square integrated circuit. All of the logic in the old MTG was condensed into one CPLD chip. Additionally, the CPLD-based MTG can be reprogrammed to add features in the future.

The Xilinx 256-macrocell CoolRunner-II-series CPLD was used because of its low propagation delay, low power consumption and high reliability. The OMEGA laser system, being by nature a light-speed arrangement, demands exceptional timing precision on the order of tens of nanoseconds from the MTG. The 256-cell CoolRunner-II pin-to-pin delay of 5.7 ns met the application requirements. Though power consumption is not itself a significant design parameter, heat production due to power dissipation should be minimized in each component

of the OMEGA system because of the environment's temperature sensitivity. The CoolRunner-II CPLD dissipates comparatively negligible heat during continuous operation. CoolRunner-IIs are more reliable because of their low heat production. A CPLD is an excellent choice of platform for redesigning the MTG.

2.2 Reverse Engineering

The first step in redesigning the MTG was full characterization of the old MTG. A backup old MTG was connected to the laboratory 38 MHz signal, and oscilloscope traces of its outputs revealed their characteristics. Analysis of the old MTG documentation, including wiring diagrams, was also utilized.

It was deduced that the signals produced by the old MTG that are named with Hertz numbers are in fact approximations, not precise frequencies; for example, Tenth-Hz was defined by the circuit architecture as 378,000,000 counts of the heartbeat signal, or 0.1003 Hz. Consequently, the LLE facility's equipment connected to the old MTG functions on an isolated, non-standard timebase that is similar to but divergent from the universal standard for time.

The results of the old MTG characterization are summarized in Table 1.

Table 1. Output Signal Characteristics of the Old MTG

Signal	Actual Frequency	Period	Period (38 MHz cycles)	Pulse Width	Pulse Width (38 MHz cycles)
H-Sync	60.2 Hz	63.3 µs	2400	6.94 µs	264
V-Sync	15.8 kHz	16.6 ms	630,000	569 µs	21,622
Five-Hz	5.01 Hz	199.2 ms	7,560,000	400 ns	16
Tenth-Hz	0.1003 Hz	9.97 s	378,000,000	400 ns	16
T-10	--	--	--	400 ns	16
T-0	--	--	--	400 ns	16

Had the MTG counted the 38 MHz signal to the precise number of cycles necessary to produce universally consistent Five-Hz and Tenth-Hz signals, its counters would seem to be arbitrarily configured; for example, the Tenth-Hz counter would need to count to 378,000,378, an unwieldy relatively prime number. Instead, the aforementioned approximations allow for significant architectural simplifications.

2.3 Counter Nesting

Rather than count each output signal independently, the MTG may produce its outputs more efficiently using a system of nested counters. The first tier in the nested-counter architecture divides its 38 MHz clock to a “greatest common factor” (GCF) for all of its signals, which is of much lower frequency; in this system, the GCF was found to be 1200, reducing the

GCF frequency to 31.5 kHz. Because there are four signals to be counted, every additional bit used in the GCF counter saves a bit from all four counters, a best case 1:3 space-on-chip optimization. Similarly, the Tenth-Hz count is an integer multiple of the Five-Hz count, so it may use the latter signal as its increment signal instead of the GCF, effectively nesting Tenth-Hz within Five-Hz and saving yet more bits. As such, the Tenth-Hz counter need only count to 50 Five-Hz cycles as opposed to 315,000 GCF cycles. Table 2 compares the number of bits necessary to count each continuously generated signal with and without counter nesting, showing significant improvement in total required bits. By nesting counters, an optimal arrangement with the smallest number of bits may be reached (Fig. 5).

Table 2. Comparison of Counter Sizes Before and After GCF Counter Nesting

Signal	Period (38 MHz cycles)	Period Counter Bits	Period with GCF (Period/1200)	Period Counter Bits with GCF
H-Sync	2400	12	2	1
V-Sync	630,000	20	525	10
Five-Hz	7,560,000	23	6300	13
Tenth-Hz	378,000,000	29	50*	6
GCF	--	--	1200	11
Total Bits		84		41

*actually Tenth-Hz period/(1200*6300)

2.4 Pre-Loaded Kick-Through

Counter nesting comes with its own drawbacks related to propagation speed. A raw counter, clocked directly by the 38 MHz signal, is limited in its input-rise-to-output-rise speed only by the string of logic gates in the threshold comparison operation that signifies the end of its count. On a device of the speed grade possessed by CoolRunner-II CPLDs, the combinational delay is a matter of a few tens of nanoseconds, but if the counters are nested, with each counter's output signal becoming the increment signal of the next, the propagation delay is compounded. With three layers of nested counters, the combinational delay reaches a magnitude approaching the leading-edge transition time of the old MTG's signals, altering the output measurably and rendering the approach unsuitable. However, further optimization solves the propagation delay problem.

The low-level logic of each counter was specialized to minimize propagation delay. The customized counters take advantage of the relatively long time between GCF counts to prime themselves for quick signal throughput upon reaching their counter thresholds. In this report, this counter alteration will be referred to as “Pre-Loaded Kick-Through” (PLKT). When the PLKT counter reaches a count preceding its threshold by one, it sets an internal flag that denotes that the next increment signal will be the threshold. The time-consuming threshold comparison operation is finished on the previous iteration. A single AND gate, taking the flag and the increment signal as inputs, is the only contributor to propagation delay. On CoolRunner-II CPLDs, AND gates have a standard delay of 1.2 ns, making counters implementing PLKT an

order of magnitude faster than standard counters. Combining nested counters with PLKT, it is possible to generate trigger signals of the correct frequency and with acceptably low delay.

2.5 Triggered Pulsers

In order to recreate the pulse widths of the old MTG, another logic component was developed. Though no OMEGA system device relies on the MTG pulses to be of precise duration, an effort was made to replicate this aspect of the old MTG in order to maximize compatibility. The component, here called a "Triggered Pulser," accepts a trigger input from one of the PLKT counters and outputs a signal that stays high for a specified number of 38 MHz cycles. These counter thresholds are hard-programmed to give precise, uniform pulse widths consistent with the old MTG. They are easily reconfigurable with each code download. Triggered Pulsers enhance modularity, ease of update, and similarity to the old MTG.

A variation on the Triggered Pulser, the Delayed Pulser, was also developed for V-Sync and H-Sync. It accepts a trigger input from a counter, waits for a specified number of 38 MHz cycles, and then outputs a signal that stays high for another specified number of cycles. Both V-Sync and H-Sync must be synchronized with the laser pulse, which occurs 5 ms after T-0. V-Sync was delayed the full 5 ms, since its period is longer than 5 ms, while H-Sync was delayed only enough to make it coincident with V-Sync.

2.6 Qualitative Plan

In summary, the qualitative circuit architecture for the continuous outputs is as shown in Fig. 6: the 38 MHz signal is divided by 1200 by a GCF clock divider. The divided clock becomes the increment signal for three counters implementing PLKT: V-Sync Trigger, H-Sync Trigger, and Five-Hz Trigger, which count to preset relatively prime thresholds of 6300, 2, and 525 respectively and reset continuously. The output of the Five-Hz trigger is directed to an additional PLKT counter, Tenth-Hz Trigger, with threshold 50. The first two trigger signals are inputs to two Delayed Pulsers for the actual V-Sync and H-Sync, which produce pulses of duration 264 and 21,622 38 MHz cycles, respectively. The second two trigger signals are inputs to two Triggered Pulsers for the actual Five-Hz and Tenth-Hz outputs, which both produce pulses of duration 16 38 MHz cycles. The T-10 and T-0 outputs are simply the Tenth-Hz pulses gated by T-10 Enable and T-0 Enable.

3. Implementation

3.1 Simplified Test Setup

The first steps toward implementation of the MTG took place on a Xilinx CoolRunner-II CPLD Demo Board (Fig. 7). The full architecture was implemented in VHSIC *(Very-High-Speed Integrated Circuit)* Hardware Description Language (VHDL) code. Unlike procedural programming languages, VHDL describes the way in which circuit elements in the macrocells of the CPLD will be physically connected. One attribute of VHDL, called "generic," allowed the design of modular logic components such as PLKT counters and Triggered Pulsers on general terms so that they could be reused with different thresholds, configurations, and relationships to other components.

All four continuous outputs were routed to LEDs embedded in the demo board. Reset functionality, which restarted the CPLD with cleared counters and reinitialized signals, was added and associated with a pushbutton on the demo board. For testing, a 1 MHz quartz crystal oscillator was used for a clock in place of the laboratory 38 MHz (slowed to 2.6% frequency) so that the signals would be observable. A few measurements with a stopwatch and a brief proportional calculation verified that the continuous signals had the correct frequencies, given their slow input clock.

3.2 RRM Test Setup

An RRM was chosen as the best test setup for the MTG because it contains a similar CPLD, it shares many of the MTG's I/O requirements, it is readily available, and it is convenient to reprogram. The VHDL code was migrated and mapped to the RRM's logic device, a CoolRunner-II 384-macrocell CPLD. A pulse generator set at 37.8 MHz was connected to the RRM's clock input to simulate the laboratory 38 MHz; its output pins were connected to a breakout board for oscilloscope probing (Fig. 8). Oscilloscope measurements of V-Sync, H-Sync, Five-Hz and Tenth-Hz were taken and compared with the specifications obtained through reverse engineering. The new MTG was found meet the specifications derived from the old MTG to an acceptable tolerance, as summarized in Table 3. In the table, the "expected" value is the specification value converted into the units of the measurement.

Table 3. Continuous Output Signal Test Results and Comparison with Specifications

Five-Hz Signal				
Characteristic	Specification	Expected	Measured	**% Difference**
Period	7560000 clks	199.2 ms	199.9 ms	**0.35%**
Pulse width	422 ns	422 ns	449.8 ns	**6.59%**

Tenth-Hz Signal				
Characteristic	Specification	Expected	Measured	**% Difference**
Period	378000000 clks	9.97 s	10.00 s	**0.30%**
Pulse width	422 ns	422 ns	449.8 ns	**6.59%**

H-Sync Signal				
Characteristic	Specification	Expected	Measured	**% Difference**
Period	2400 clks	63.3 µs	63.46 µs	**0.25%**
Pulse width	6.94 µs	6.94 µs	6.982 µs	**0.61%**

V-Sync Signal				
Characteristic	Specification	Expected	Measured	**% Difference**
Period	630000 clks	16.6 ms	16.66 ms	**0.36%**
Pulse width	569 µs	569 µs	571.9 µs	**0.51%**
Delay after T-0	5.00 ms	5.00 ms	5.00 ms	**0%**

Additionally, the Five-Hz and Tenth-Hz signals were shown to have coincident rise times within 1.3 ns, and V-Sync and H-Sync were shown to have coincident rise times within 1.2 ns (Fig. 9), both of which are tolerably low compared with the rise times of the pulses.

The RRM test setup allowed for an expanded testing scheme; its extra inputs allowed the gated signals to be tested as well. A Shot Cycle Simulator (SCS) device, which outputs the same sequence of T-10 and T-0 enable signals as the Shot Executive, was connected (Fig. 10). The MTG was verified to produce synchronous T-10 and T-0 signals correctly and reliably as it interacted with the SCS according to the description of the shot cycle: an active T-10 Enable was shown to produce one T-10 pulse, and an active T-0 Enable was shown to produce a T-0 pulse ten seconds later (Fig. 11). Additionally, T-10 and T-0 were each measured to have rise times coincident with Tenth-Hz within 2 ns.

3.3 Laser Shot Simulation Test

One integrated test was undertaken which would prove the correct operation of as many parts of the system as possible, short of installation at LLE. The MTG prototype was connected to a monitor, a camera, an LED, and an oscilloscope. V-Sync and H-Sync were routed to the corresponding inputs on a video signal generator. The video signal generator was in turn connected to a CRT monitor and an analog camera. It was verified that the video signal generator was synchronous with the MTG by slightly altering the setting of the frequency generator acting as a clock signal for the MTG and listening for the change in pitch of the hum produced by the CRT monitor. The camera was mounted on a workbench and connected to the monitor, where a live video feed was visible. An LED was spliced into the MTG's Five-Hz channel to simulate the laser flash. Five-Hz was chosen because it recurs quickly enough for easy observation and it had already been proven to be synchronous with T-0, the actual laser trigger, by earlier tests. The LED was pointed directly into the camera at close range, and the camera and LED were optically isolated with dark fabric (Fig. 12).

Simply capturing an image from the camera and displaying it on the CRT demonstrated that the video-related MTG signals were formed correctly. V-Sync, H-Sync, Five-Hz, and the camera output signal were probed with the oscilloscope (Fig. 13); the trace showed that the LED laser flash produced a large increase in the intensity of the camera output signal over the next two fields of video, constituting one frame (see Appendix A for details of analog video at LLE). Had the camera been asynchronous with the LED, at the incorrect frequency, the LED flash and the intensity spike would have exhibited a beat; had the timing of the LED flash been correct in frequency but incorrect in phase, the intensity spike would have been spread across two frames, or four fields. Neither of these indicators of error was apparent. Though the 5 ms delay between T-0 or, in this case, Five-Hz, and target irradiation was not included in this test, the delay between the LED pulse and the next camera blanking signal following V-Sync was measured to be 5.00 ms. The test demonstrates the correct phase and frequency relationships between the output signals of the MTG for practical use. The system was shown to be suitable for timing the OMEGA laser system.

4. Expanding the MTG

4.1 Shot Error

Though the functionality of the old MTG in the OMEGA system had been replicated and verified, the Incomplete Shot indicator LED on the old MTG had not been replaced. The Incomplete Shot represented only a small subset of possible errors, so the concept was generalized to Shot Error, including all plausible errors in the progression of the Shot Cycle. The process was tabulated using a Finite State Machine (FSM), which kept track of the Shot Cycle's state at any given time by monitoring the concerned signals: Tenth-Hz, T-10 Enable, and T-0 Enable. A correct path from state to state through the FSM was defined, and deviation from the correct path was considered error.

Five states were necessary to encode the entirety of the correct shot cycle path, as shown in the FSM state transition table (Fig. 14). In the Idle state, the MTG waits for a shot cycle to begin. When T-10 Enable becomes activated, the FSM enters T-10 Enabled. After Tenth-Hz has gone high and a T-10 pulse has been asserted, the FSM transitions to T-10 Finished. The same process recurs for T-0 Enabled and T-0 Finished, substituting T-0 Enable and T-0. Finally, when the T-0 Enable signal is no longer asserted, the FSM returns to the Idle state.

Transitions that violate the explicitly defined expected sequence trigger an error flag. For instance, it is possible that a malfunction in the Shot Executive system could cause T-10 Enable and T-0 Enable to be active simultaneously at the time of a Tenth-Hz pulse (Fig. 15), a very serious error. In order for this condition to come about, T-0 Enable must become active while the FSM is in the T-10 Enabled state, resulting in an error according to the state transition table.

Custom VHDL types were defined to implement the FSM on the CPLD, and reset-to-Idle capability was integrated with the usual reset for the MTG. The FSM does not interact in any way with the operation of the MTG; it is physically separated from the CPLD macrocells concerned with timing to improve resilience to failure. Its only output is the error information.

The Shot Error was successfully tested. An LED was used to indicate the error flag's state on the MTG prototype. The shot cycle simulator and oscilloscope were connected as in previous tests, and the LED did not light as correct shot cycles were executed. Then, each enable signal in turn was interrupted during the shot cycle, and the LED lit each time. The T-10 and T-0 Enable signals were also interchanged, which immediately caused the LED to light.

Because each FSM state is uniquely associated with a particular stage in the Shot Cycle, the errors are also unique to particular failures. This feature opens up the possibility of specific, cause-explicit error reporting. A half-byte error code was associated with each possible error in the FSM code in anticipation of this application, and cause-explicit error reporting was explored after the network interface was in place.

4.2 Clock Error

The 38 MHz signal is vital for all shot-related operations at LLE, and failure of this signal ought to be reported by the MTG because it is the hub of all timing processes. This functionality, Clock Error, was added to sense catastrophic loss of the signal and to report it to the Shot Executive. Sensing loss of 38 MHz with the MTG is non-trivial, because it acts as the

clock signal for the MTG. Combinational logic halts and the CPLD has no means of triggering self-diagnostics in the absence of its clock; it simply remains unresponsive. Nevertheless, the modular, flexible nature of CPLD macrocells provided a solution.

An external 10 kHz quartz crystal oscillator acted as both an external stimulus and a metric to which the 38 MHz signal was compared. Roughly 3800 cycles of the 38 MHz signal are expected to occur for each 10 kHz cycle; this count was checked using the "strobing" technique (Fig. 16). A counter for the 38 MHz signal was added in VHDL. Each rising edge of the 10 kHz signal caused the 38 MHz counter to pause momentarily. During the pause, the 38 MHz counter value was compared with the approximate expected value of 3800. If it deviated from 3800 too greatly, or if it was zero, a clock error was flagged. Then, the 38 MHz counter was reset in preparation for another comparison on the next 10 kHz rising edge. In this way, the 38 MHz counter was "strobed" for errors by the external oscillator.

Since the two timing signals are independently generated, the counter value at the time it is strobed must vary by at least one due to the lack of correlation between the signals. Noise can also introduce some variation in the count. To compensate, some tolerance was given to the count comparator by disregarding several of the least significant bits. Using a sequence of downloads and varying the number of disregarded bits between 1 and 10, a binary search was performed to find the minimum number of bits disregarded before stable, noise-resistant operation was achieved. The minimum was found to be four.

Like Shot Error, Clock Error sets an internal error flag when the strobe test fails. The error flag was routed to an LED on the MTG prototype. With four least significant bits ignored, the Clock Error ran for four hours continuously with no errors logged, but lit the indicator LED immediately upon disconnection of the 38 MHz signal.

4.3 Network Interface

LLE's IP network is a powerful tool through which its equipment is increasingly interconnected for ease of use and consistency of communication standards. Technicians may connect to any network-enabled device and check its status and error information from any LLE computer at will, and devices like the RRM modules have already proven the utility of such capability. The MTG was outfitted with a network interface in order to confer these benefits immediately upon installation. Error flags, error codes, reset commands, input-output information and a command line were made available over the network.

A NetBurner module was used as a communication engine for connecting the MTG to the LLE network (Fig. 17). The module is capable of both Ethernet and basic I/O communication. It can host its own webpage, and it comes with a device-specific C++-based software development kit. After assigning the NetBurner a unique LLE IP address, four bits of I/O were connected between the MTG prototype and the NetBurner. Three were assigned as inputs to the NetBurner: one to indicate Clock Error, and two to demonstrate a limited set of error codes from Shot Error. The last I/O bit was assigned as a NetBurner output, used for remotely resetting the MTG.

A webpage from an unrelated network-enabled LLE system component was adapted to display the error information and to interact with the remote reset. The two bits of Shot Error were interpreted together as a two-bit error code (range of 0-3 decimal), signifying three different sample errors (the fourth signifying no error), and formatted to display the

corresponding error messages on the webpage. The remote reset was implemented as a check-box. A command-line interface to the NetBurner was also made available for future expansion, should more sophisticated communication between the NetBurner and the MTG be established. All features are accessible in a single browser window (Fig. 18).

Using an LLE computer, the webpage was successfully accessed and displayed. Oscilloscope traces verified that the MTG underwent a reset as intended in response to the check-box interface. Using the SCS, shot errors were simulated by disconnecting the T-10 and T-0 Enable signals; the correct sample error message was displayed on the webpage each time.

5. Future Development

The work summarized herein represents only the initial stages of a longer process to update the MTG to meet new standards of reliability, interactivity and utility. Many concepts have been proven feasible, but few are ready for deployment. The LLE engineering staff will use this work as a foundation for further expansion as they prepare it for final packaging and installation. The network interface in particular has many more possibilities, such as automatic communication with the Shot Executive about status and errors, remote fine adjustment of the MTG's outputs for synchronization with OMEGA EP, and command-line routines for self-diagnosis and other functions. LLE can anticipate smoother operation, simpler maintenance, higher reliability, and tighter integration with the OMEGA system from its MTG in the future.

Acknowledgments

I would like to thank my advisor Robert Peck for obtaining for me the resources, in paper, files, electronics, and people, that I needed to pursue my project, and for his technical expertise in a wide array of electrical applications. He helped me overcome the insurmountable questions of where to begin and how to proceed as only experience can. I would also like to thank my other advisor Eryk Druszkiewicz, not only for his keen eye for effective applications of his problem-solving and data-manipulation skills, but also for his willingness to help me understand the solutions he found and his openness to my own ideas. I also owe gratitude to Jean Steve for masterfully organizing my schedule; to the engineering staff at the LLE Electronics Laboratory for being kind, pleasant, and helpful; and to Eugene Kowaluk, for his photographic and videographic expertise throughout the summer. Finally, I would like to thank Dr. Stephen Craxton for the opportunity to learn more in a summer than I could ever have hoped; for his recognition of the caliber of work of which high school students are capable; and for his continued dedication to bringing this excellent program to future high school students.

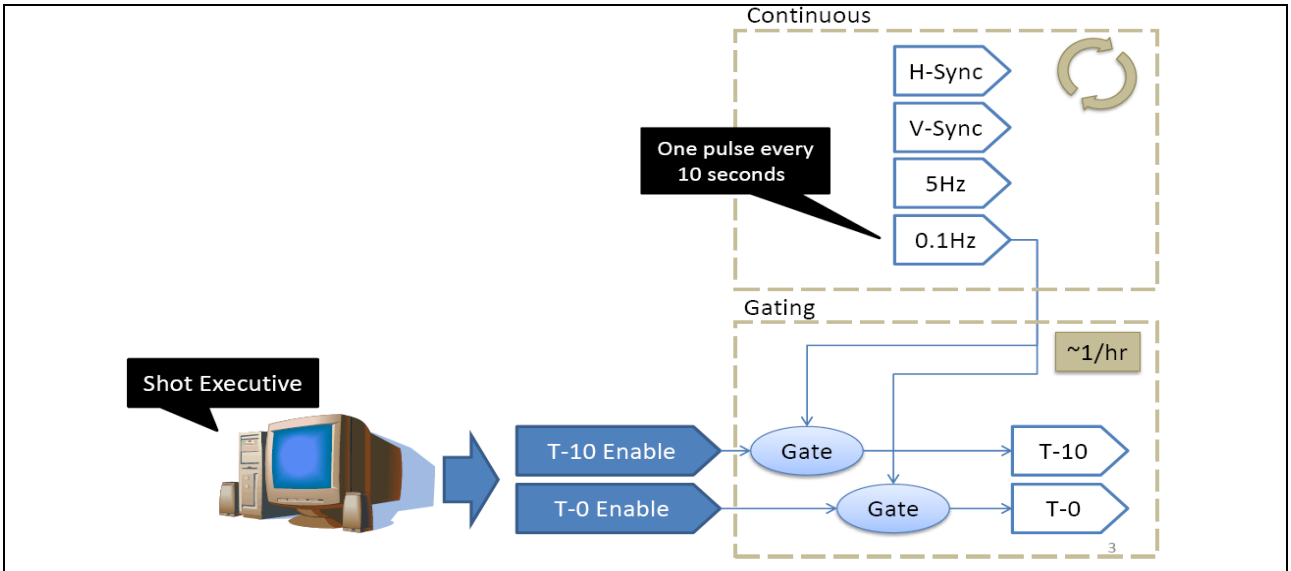

Fig. 1 Diagram of MTG Outputs: Outputs split into two groups: continuous and gating. Continuous outputs (H-sync, V-sync, Five-Hz and Tenth-Hz) are used to synchronize cameras and local timing for all devices in the OMEGA laser system. Gating outputs are only active approximately once per hour, on the OMEGA shot cycle schedule, when the Shot Executive computer system asserts T-10 and T-0 enables.

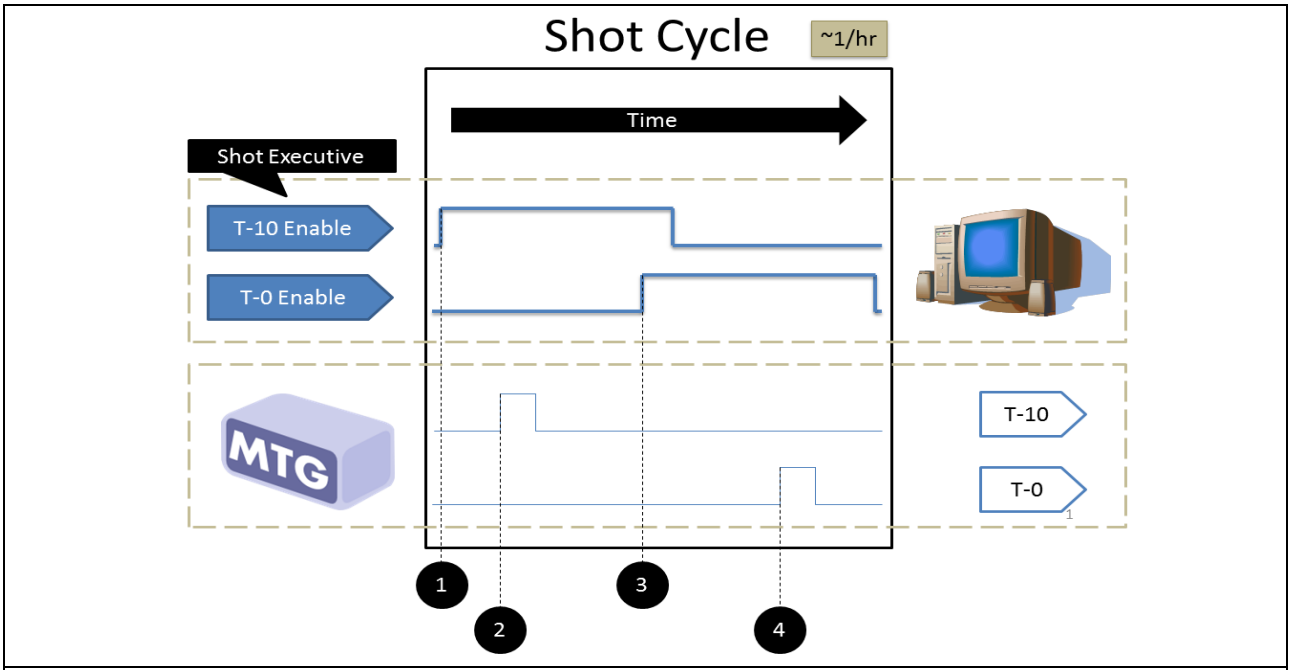

Fig. 2 Shot Cycle: In the seconds before a shot, the Shot Executive first asserts the T-10 Enable signal (1). The MTG waits for its own Tenth-Hz pulse, and then synchronously outputs the T-10 pulse (2). A few seconds later, the Shot Executive asserts the T-0 Enable signal and lowers T-10 Enable (3). The MTG again waits for its own Tenth-Hz pulse, and then synchronously outputs the T-0 pulse (4). *Pulse widths not to scale.*

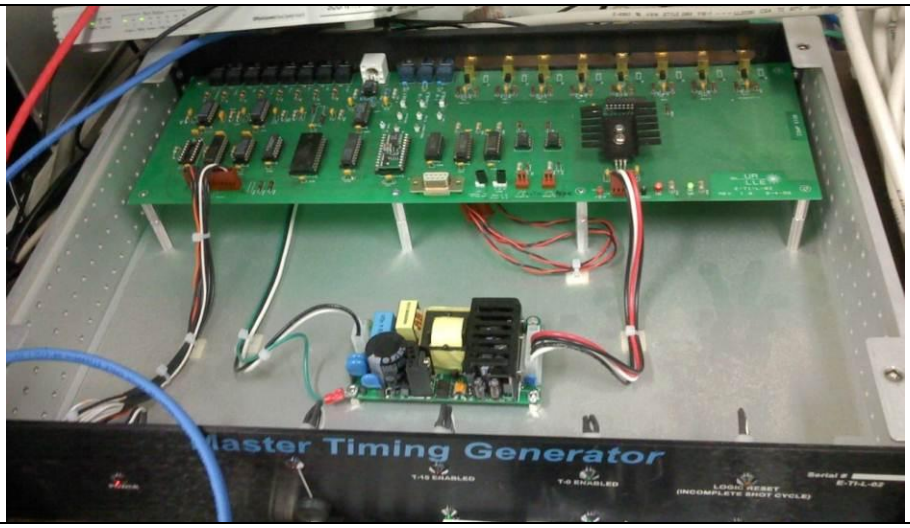

Fig. 3 Old MTG, internal view: Obsolete components and a sparse readout.

Fig. 4 CPLD: Made by Xilinx, this CoolRunner-II CPLD consumes very little power, has a very low pin-to-pin delay, and measures only 20 mm x 20 mm.

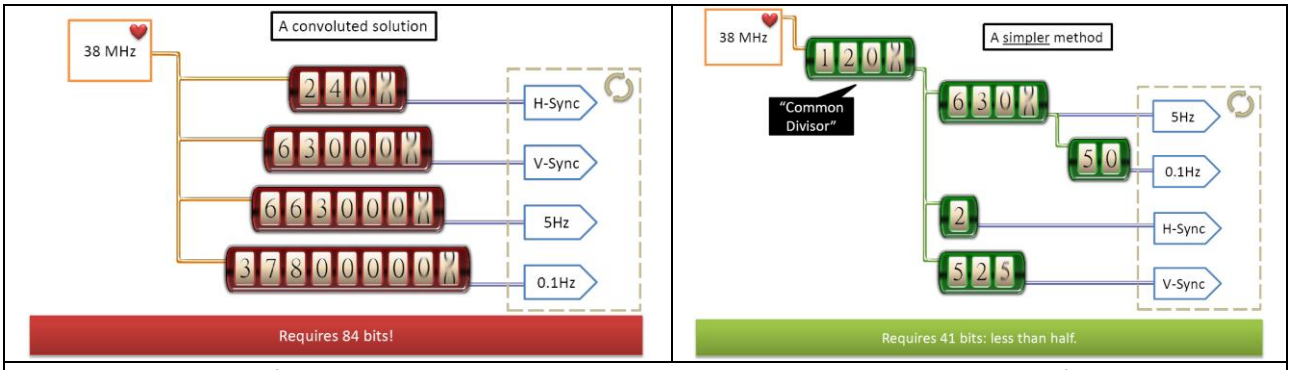

Fig. 5 Comparison of counter designs: Two possible counter arrangements are shown for dividing the heartbeat signal. The first uses one counter per signal. The second uses counters to count the outputs of others. By nesting counters, computing resources are saved.

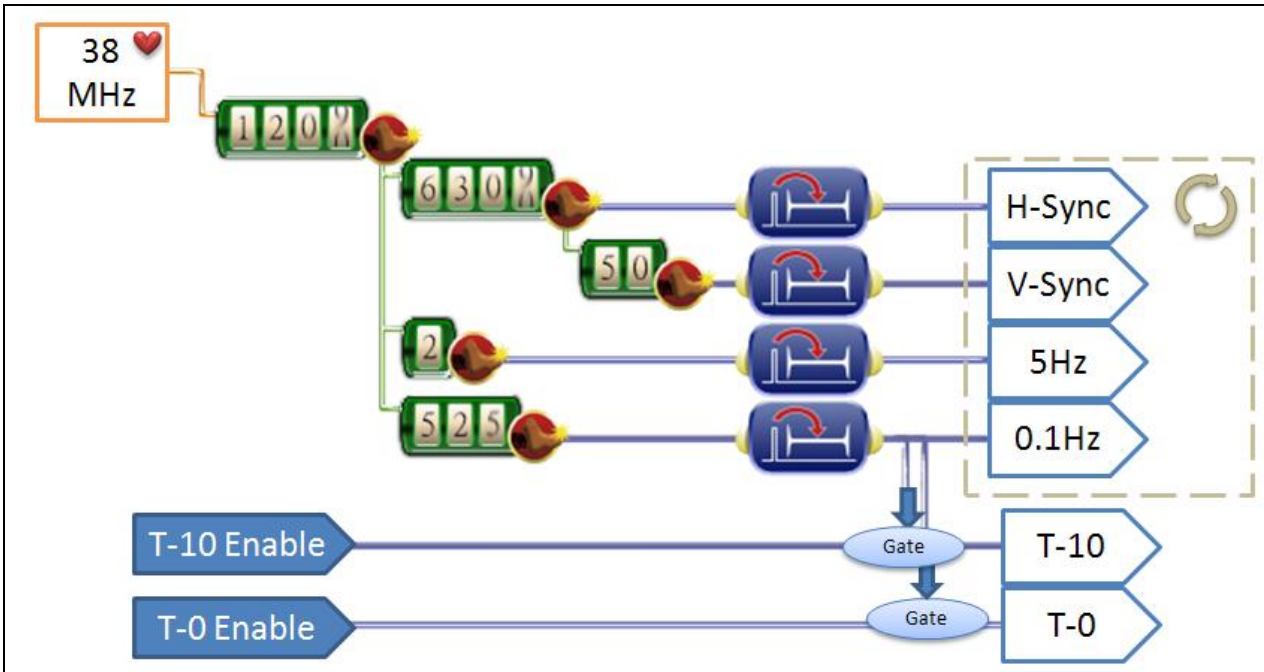

Fig. 6 Final schematic diagram: 38 MHz heartbeat divided by a cascade of nested counters, each implementing Pre-Loaded Kick-Through (red circles with boots). Triggered counters (rounded dark-blue rectangles) become outputs. Gated signals are created from Tenth-Hz output.

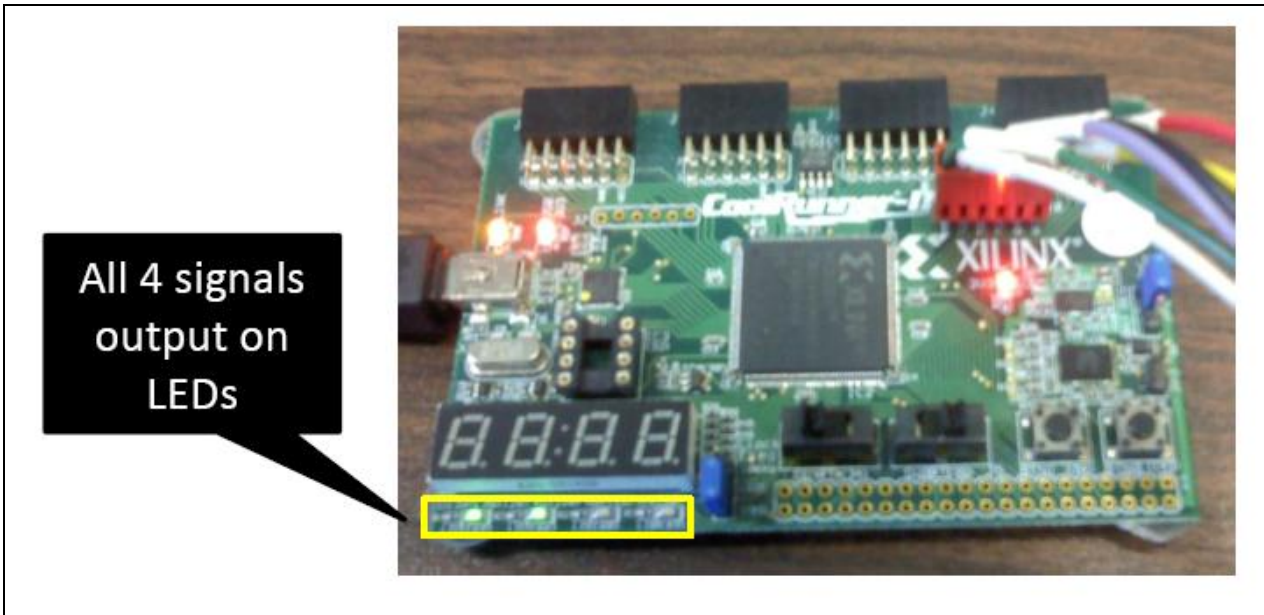

Fig. 7 Demo board with MTG program: The new MTG program was first implemented on a CPLD demo board. The four continuous outputs, V-Sync, H-Sync, Five-Hz, and Tenth-Hz, are routed to LEDs.

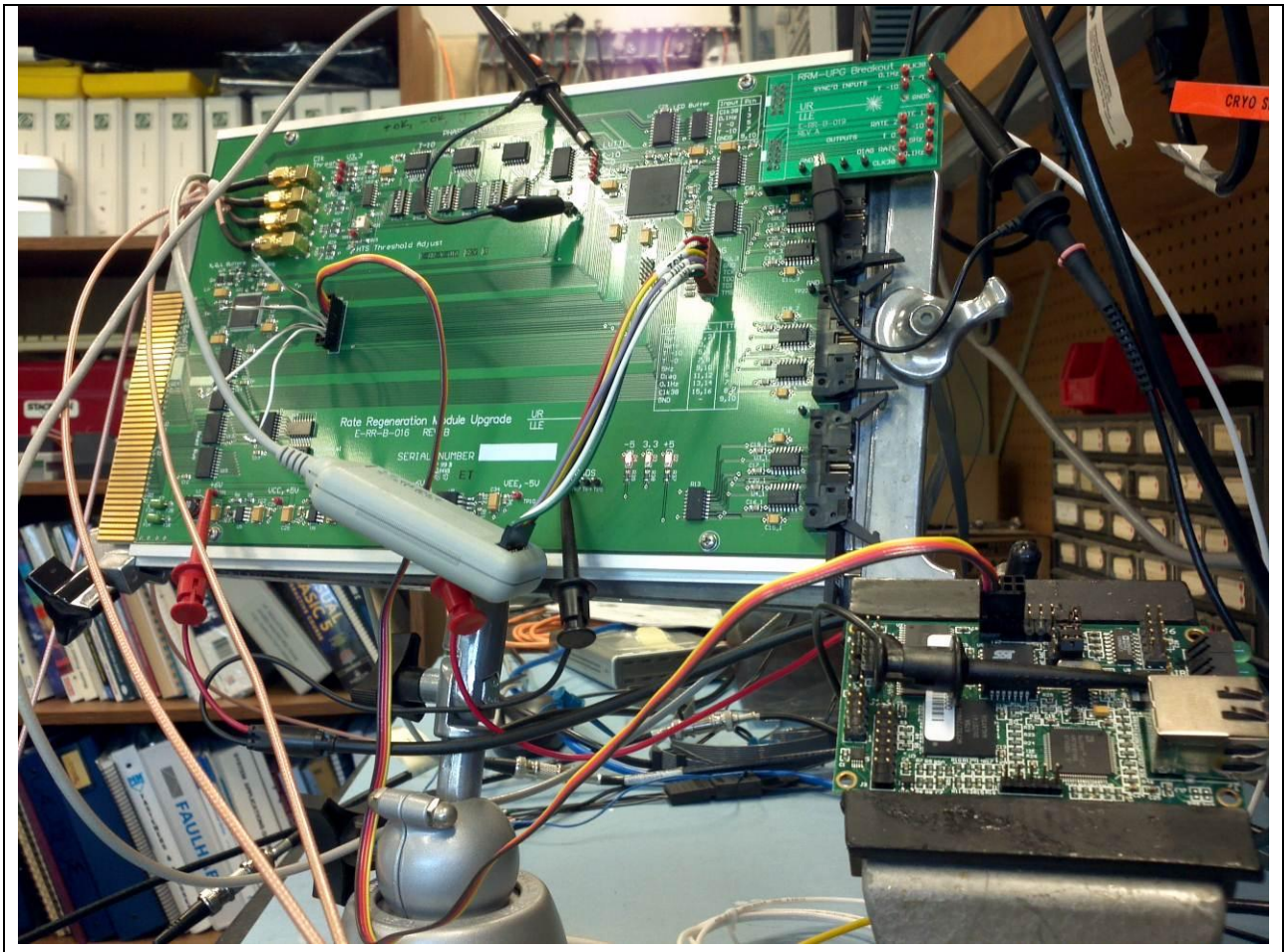

Fig. 8 Final test setup: The large circuit board is the RRM, adapted for MTG testing. Four RF-capable inputs are shown at the top left of the RRM, connected to gold-colored contacts. The V-Sync, H-Sync, Five-Hz, Tenth-Hz, T-10 and T-0 outputs are visible at the top right of the RRM, on a smaller green board, with an oscilloscope probe. The NetBurner module is shown in the lower right. The four-conductor ribbon cable (yellow, orange, red, black) is the I/0 for communications between the RRM and the NetBurner. The gray plastic device connected to the RRM via a bundle of colorful wires is the JTAG reprogramming interface for the CPLD.

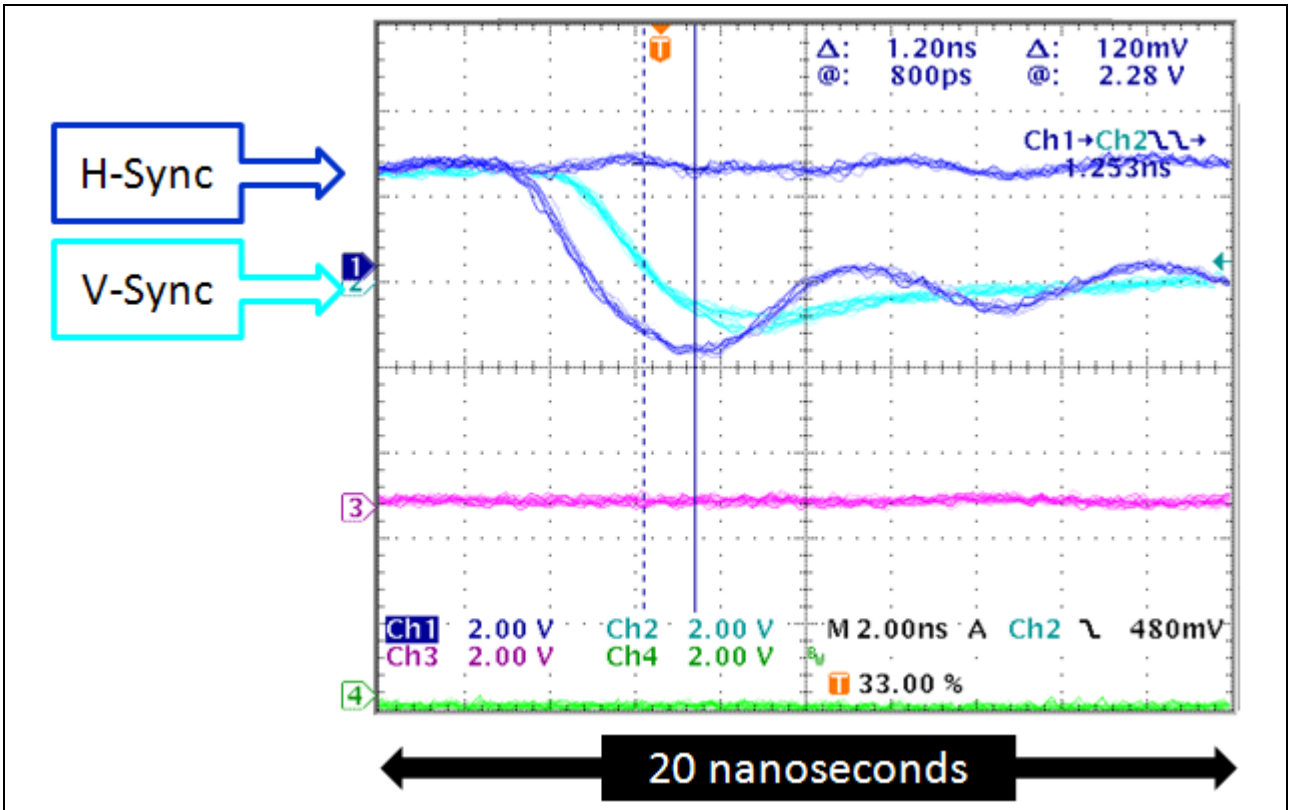

Fig. 9 Oscilloscope trace of Pre-Loaded Kick-Through results: V-Sync and H-sync were implemented using PLKT counters. V-Sync and H-Sync falling edges are shown on an extremely short time base. An exceptionally short delay of 1.253 ns is measured between edges. The result is significant because V-Sync follows H-Sync much more closely than would be possible using counters without PLKT. *Note: H-Sync appears to branch into two traces because interlaced video requires that the sync pulses only line up on every other V-Sync. Only the lower H-Sync trace is relevant.*

Fig. 10 Shot Cycle Simulator: Creates T-10 and T-0 enable pulses to imitate shot cycle progression. Connected to inputs of the RRM.

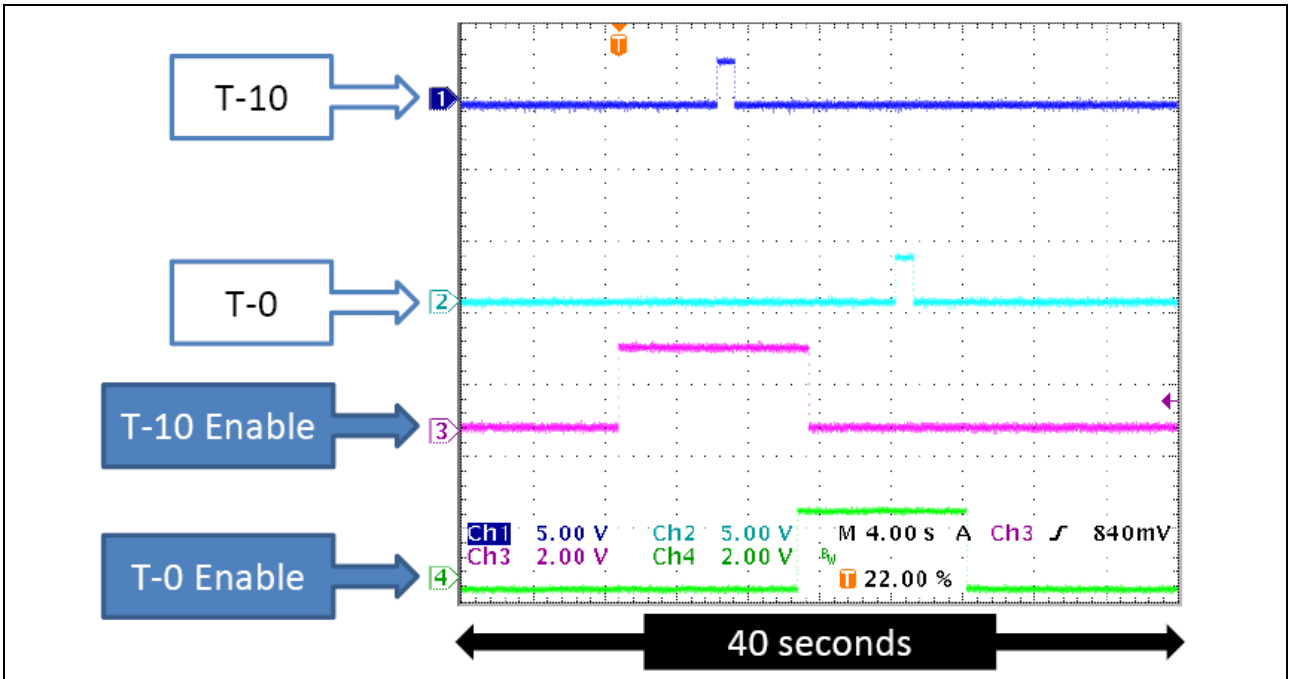

Fig. 11 Oscilloscope trace of shot cycle simulator: Correct T-10 and T-0 Enable cycle shown on channels 3 and 4, with corresponding T-10 and T-0 outputs from MTG on channels 1 and 2. T-10 and T-0 pulses were lengthened to 1.0 s in CPLD code for clarity.

Fig. 12 Synchronous camera test setup: Red LED, left image center, pulsed on T-0 to simulate the OMEGA laser. LED points directly into camera, synchronized by V-Sync and H-Sync. Setup is isolated from room light to create contrast with LED light.

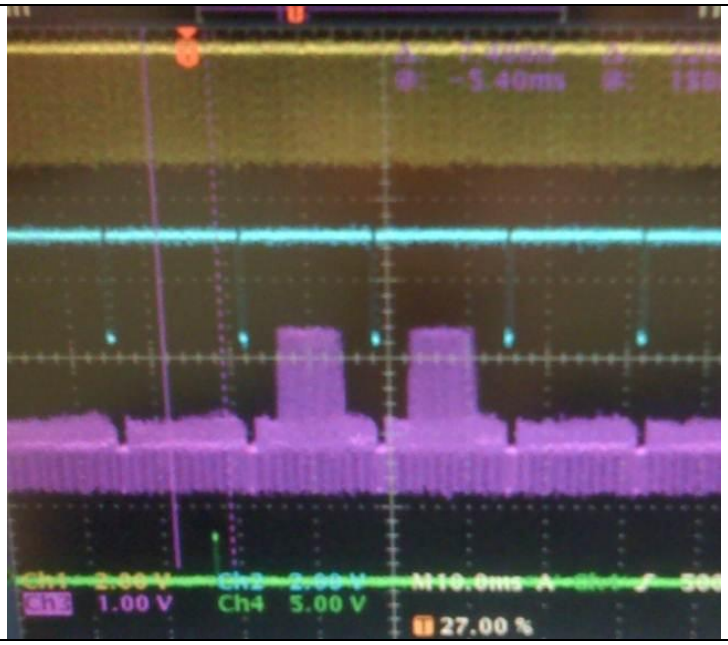

Fig. 13 Oscilloscope trace of synchronous camera test: Signals from top: H-Sync, yellow; V-Sync, blue; camera output, purple; T-0, green. The short LED pulse is shown in green near the bottom left. Since the camera uses interlaced video mode, each frame is represented by two V-Sync pulses. The next frame after the LED pulse shows spike in camera signal, or light intensity.

	T-10 Enable		T-0 Enable		0.1Hz	
state	enabled	disabled	enabled	disabled	high	low
"Idle"	Go to **"T-10 Enabled"**		error			
"T-10 Enabled"		error	error		Go to **"T-10 Finished"**	
"T-10 Finished"			Go to **"T-0 Enabled"**		error	
"T-0 Enabled"	error if 0.1Hz high			error	Go to **"T-0 Finished"**	
"T-0 Finished"				Go to **"Idle"**	error	

Fig. 14 Shot error state machine: As a shot progresses, the MTG advances through a Finite State Machine (FSM), evaluated on every clock cycle. States are shown on the left in order. The three signals relevant to the shot cycle process are shown at top: T-10 Enable, T-0 Enable, and Tenth-Hz. A white cell indicates no change, remaining in the current state. Each light green cell indicates an immediate switch to state shown. An error is flagged and an error code is logged whenever a red cell is encountered, allowing the mode of failure to be identified later.

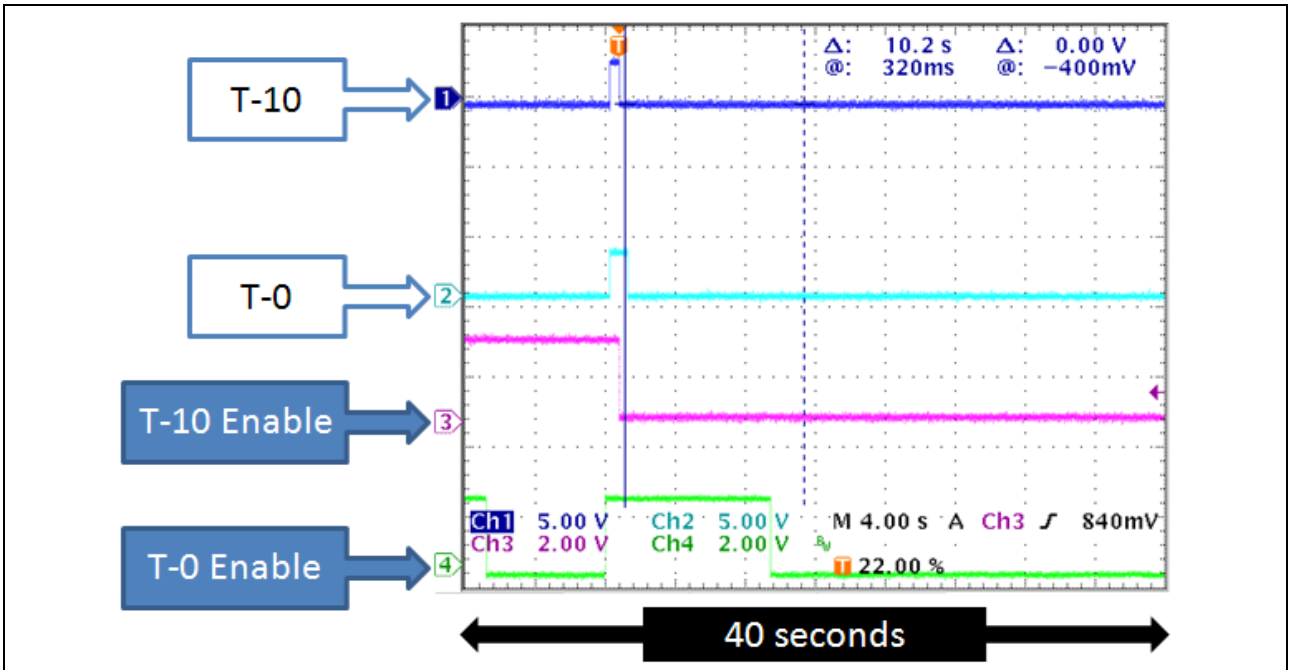

Fig. 15 Oscilloscope trace of a possible shot error: T-10 and T-0 enables overlap at the time of a Tenth-Hz pulse. T-10 and T-0 occur simultaneously as a result. An error code would be logged by the Shot Error FSM under the circumstances shown here.

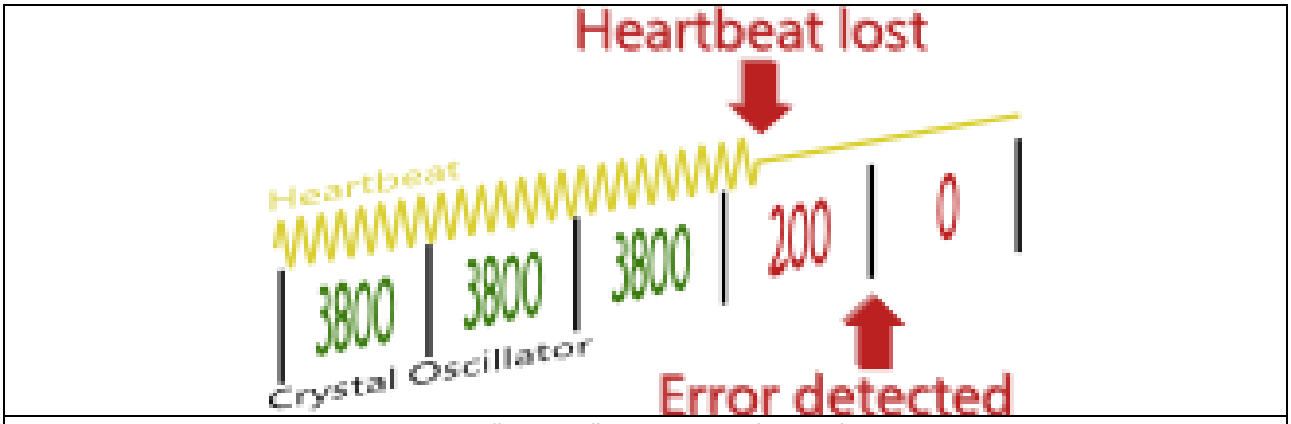

Fig. 16 Clock error: A crystal oscillator "strobes" the 38 MHz (yellow) counter on its rising edges and verifies that the counter's value lies within an acceptable range. If the counter reads too low, the clock is interrupted. If the counter reads too high, significant noise is present. In either case, the heartbeat experiences a failure, and a clock error is flagged.

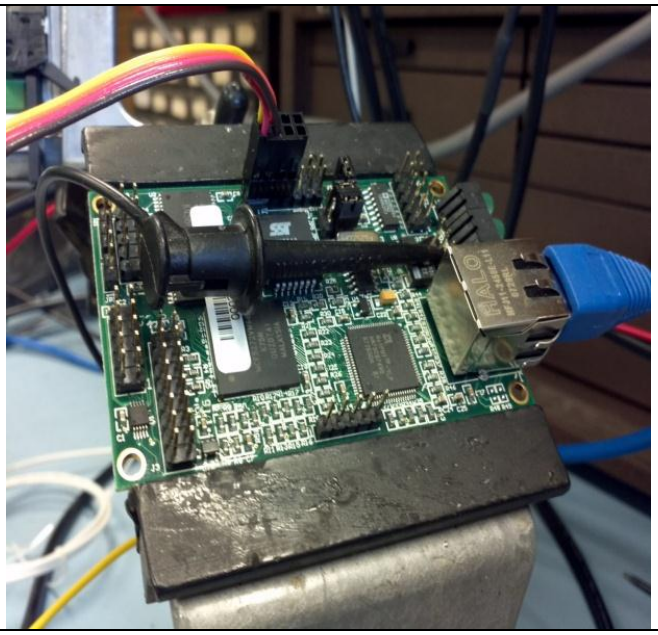

Fig. 17 NetBurner module: Shown clamped in vice. Black clip is oscilloscope probe. Ethernet port is visible in blue.

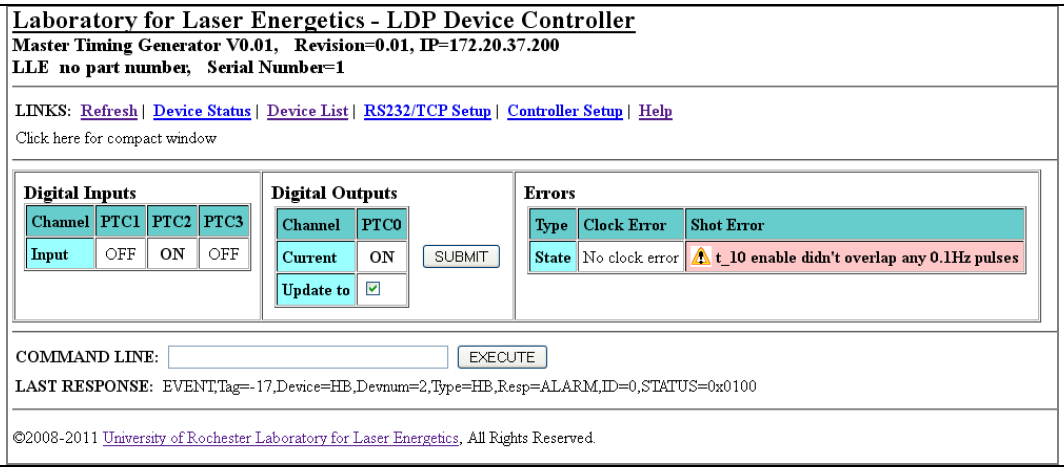

Fig. 18 MTG Webpage: Body elements, from left to right in table: digital inputs from the RRM to the NetBurner; digital output from NetBurner to RRM acting as a remote reset, shown in its default (enabled) state; error pane with formatted error messages, shown with an example error identified by the state machine: “T-10 enable didn’t overlap any Tenth-Hz pulses.” This error might occur in the case of a shot abort.

Appendix A: Analog Video at LLE

LLE makes use of analog cameras with interlaced video. These cameras output their image data serially on one conductor, one horizontal line of each field at a time. A field is all of the image data for every second horizontal line in an interlaced video feed; two consecutive fields make up a frame.

The image data are intended for use on cathode ray tube (CRT) displays. The cathode beam scans horizontal lines onto the display represented in the camera output by short (~30 µs) pulses of analog light-intensity data separated by equally short low periods (Fig. A). A "front porch," or a pause of duration equal to several horizontal line pulses, initiates transmission of a field. 525 horizontal lines are then transmitted for each field, followed by a brief "back porch," or pause at the end of the field. A "blanking period" follows, during which time the CRT display moves its cathode beam vertically to prepare for the next field.

Horizontal lines are triggered by an external "Horizontal Synchronization" pulse, and blanking is triggered by an external "Vertical Synchronization" pulse. The MTG generates these pulses, H-Sync and V-Sync. When multiple cameras are triggered by the same Horizontal and Vertical Synchronization pulses, their video feeds are synchronized and their image data are comparable in post-analysis because they were acquired simultaneously.

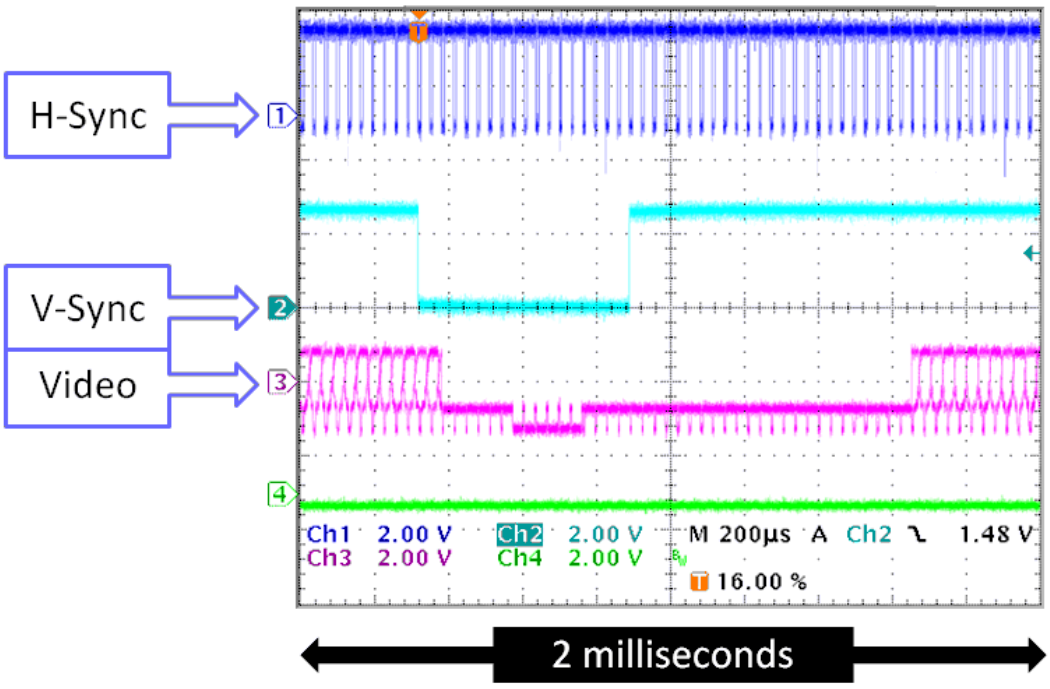

Fig. A Synchronized Video: The MTG test setup provides timing information to a camera. H-Sync is responsible for synchronizing the 525 lines in each video frame, visible at the right and left edges of the video signal. In order, the back porch, blanking, and front porch portions of the video signal take place in the lowered middle section. Synchronized by V-Sync, these features signify the transition to a new video field.

X-Ray Fluorescence as an Imploded Shell Diagnostic

Sean Hamlin

Fairport High School

LLE Advisor: Reuben Epstein

Laboratory for Laser Energetics

University of Rochester

Summer High School Research Program

May 2012

Abstract

When an imploded target shell is irradiated from within by hot-core x-ray emission, photoionization produces inner-orbital vacancies in atoms doped into the shell. Atomic electrons then fill these vacancies, resulting in characteristic K_α line fluorescence in the x-ray spectrum.[1] Due to the sensitivity of the amount of photoionization to the shell areal density, this fluorescence is a potential shell compression diagnostic. To explore this diagnostic concept, a simple model was developed to simulate the spectrum of a doped target shell.[2] The goal of this project was to compare this model with spectra from the detailed radiation-transport code Spect3D[3] for aluminum-doped target shells. The detailed simulation is a test of the assumptions of the simple model, such as optically thin K_α emission from the target shell. A discrepancy was found, suggesting most plausibly that the Spect3D atomic model is not consistent with the cold-metal fluorescence efficiency for aluminum used in the simple model. Further work is needed to determine whether the atomic physics model used in Spect3D is correct.

Introduction

At both the Laboratory for Laser Energetics and the National Ignition Facility (NIF), inertial confinement fusion (ICF) experiments are being carried out where targets are irradiated, causing them to implode.[4] NIF targets typically consist of an outer shell of germanium-doped plastic (CH) and an inner shell of cryogenic DT. Once peak compression has been reached, one obtains a compressed shell which is extremely high in density and a hot inner core which is low in density. With sufficiently high temperatures and densities achieved in NIF experiments, the target is expected to experience ignition, a condition where the energy production from fusion is substantial enough to be self-sustaining. One example of a diagnostic to measure the shell areal density, a measure of target shell compression implosion performance, is x-ray spectroscopic observation of the emission of x-ray fluorescence.

Shell fluorescence is the x-ray line emission that follows inner-shell photoionization of dopant atoms by x-rays emitted from the hot core.[1] This process is demonstrated in Figure 1. Typically, these appear as 2p-1s emission lines also known as K_α emission. The x-ray radiation emitted by the hot core of the target passes through the imploded target shell on its way to the spectrograph, creating an absorption spectrum at the detector. A relationship between the amount of measured K_α fluorescent emission and the amount of measured photoionization absorption seen in the target spectrum has been developed, based on a simple shell model.[2] If the model is upheld, this relationship can be used to infer the shell areal density. Complex radiation transfer codes can be used to validate this relationship between fluorescence and photoionization absorption and to ensure that the relationship between the amount of K_α fluorescence and the amount of photoionization absorption exhibited by the target shell is understood. Once this is

confirmed, this relationship becomes the basis of using photoelectric fluorescence as a diagnostic on future experiments on the NIF.

Overview of Fluorescence

In experiments currently occurring on the NIF,[4] the target consists of an outer shell of CH polymer, which is often doped with germanium. In order to investigate the atomic processes occurring inside the target shell using our detailed atomic model, it is necessary to use a simpler element as a surrogate for the germanium dopant, like aluminum because the Prism atomic model for germanium fluorescence is not yet complete.[1] Figure 1 shows schematically an imploded target similar to the ones used in NIF experiments, except that the shell is aluminum-doped hydrogen. When a target is irradiated, the target implodes, and the hot inner core emits x-rays which irradiate the outer shell of the target. This energy from the core interacts with the atoms of the dopant in the shell causing fluorescence to occur. The spectral distribution of the inner core emission is approximated by the expression

$$P_{core}(h\nu) = P_0 \frac{(h\nu)^3}{e^{h\nu/kT}-1}, \quad (1)$$

corresponding to a Planck or blackbody spectrum,[5] where $h\nu$ is the photon energy, kT is the core temperature, and P_0 is a constant. As this core emission passes through the target shell, some is absorbed and some is re-emitted as fluorescence.

The competition between various atomic processes, specifically spontaneous emission and autoionization, is a characteristic of the target dopant material and determines how much fluorescence occurs.[6] Photoionization absorption is the process by which some of the incoming x-ray photons from the hot core are absorbed when they photoionize K-shell electrons of the

atoms in the target shell (See Figure 2). Once the K-shell vacancy has been created, there are two possible atomic processes which can occur. First, the atom can be autoionized, which involves the internal emission of a photon that ionizes an outer shell electron. This can occur because the gap between the two energy levels in the transition is bigger than the energy required to ionize the electron. On the other hand, the vacancy can be filled by an outer shell electron along with the escape of a photon. If the vacancy is filled by an L-shell electron, by far the most likely of the possible radiative emission processes, then the emitted photon is a quantum of K_α fluorescence. The probability that the K-shell vacancy is filled by spontaneous K_α emission is expressed as the fluorescence efficiency, ω_{K_α}. Conversely, the probability that the vacancy is filled by autoionization is equal to $1 - \omega_{K_\alpha}$.

The fluorescence efficiency is the relative probability of spontaneous emission following the formation of a K-shell vacancy, which can be written in the form

$$\omega_{K_\alpha} = \frac{A_r P_{2p}}{A_r P_{2p} + A_a P_{2p}(P_{2p}-1)} . \quad (2)$$

In this expression, the probability that a 2p sublevel electron decays, $A_r P_{2p}$, is directly related to P_{2p}, the number of electrons in the 2p level. The competing probability that a 2p electron decays and transfers its energy to another 2p electron is equal to $A_a P_{2p}(P_{2p} - 1)$. The product $P_{2p}(P_{2p} - 1)$ represents the number of possible interacting electron pairs that can undergo the autoionization process after an inner shell vacancy is formed.[7] Figure 2 illustrates schematically the interaction between the atomic processes which are significant to fluorescence. Fluorescence appears as a measurable quantity of emission at the detector, and this emission is related to the quantity of photoionization absorption that occurs.

PrismSPECT and Spect3D

To study the conditions occurring during a target shell implosion, complex radiation transfer codes have been developed to model the irradiation of a compressed target shell by hot core radiation. One such program is Spect3D.[3] This code models the transfer of radiation and electrons between atomic sublevels by solving the implicit simultaneous rate equations which approximate the transition rates among the atoms of the target shell. These rate equations include all the atomic kinetics processes which are necessary to simulate fluorescence, including autoionization, photoionization, photoexcitation, and spontaneous emission. In addition, the codes include a large database of atomic levels and ionization species which permits the investigation to be as detailed as necessary. Another feature which is significant in demonstrating fluorescence is the ability to turn on and off certain atomic kinetics processes.

Figure 3 shows an x-ray spectrum produced by a Spect3D simulation. In this case of interest, a shell of 150 μm inner radius and 25 μm thick consists of a 1 g/cm^2 mixture of hydrogen with a 1%, by atom, concentration of aluminum. At the center is a small blackbody source of temperature 3 keV. It is made opaque enough to produce a blackbody spectrum, identical to Eq. (1), over the entire simulated spectral range, up to $h\nu = 10$ keV. Figure 3 shows an x-ray spectrum which exhibits both K_α fluorescence and photoionization absorption. The other feature which appears on the spectrum is a set of 1s to 3p sublevel absorption lines. The spectrum also shows distinctive lines for each species of the dopant in the target shell. This represents a normal simulation where all relevant processes are considered. Figure 4 is another Spect3D spectrum; however, this spectrum was generated with a zero rate coefficient for photoionization. As seen on the spectrum, no clear fluorescence lines appear. This demonstrates that Spect3D models fluorescence as a direct result of K-shell vacancies created by

photoionization of K-shell electrons. The implication of this is that Spect3D can be used to investigate fluorescence.

Simple Spectrum Model

Although the complex spectra simulated by Spect3D are helpful, it is useful to develop a simpler model in order to better understand and to interpret the data. Such a model has been developed.[2] The emitted continuum spectrum can be modeled by the equations

$$P(h\nu) = P_0 \frac{(h\nu)^3}{e^{h\nu/kT} - 1} e^{-\tau_L (\frac{h\nu_K}{h\nu})^3}; h\nu < h\nu_K$$

and

$$P(h\nu) = P_0 \frac{(h\nu)^3}{e^{h\nu/kT} - 1} e^{-(\tau_K + \tau_L)(\frac{h\nu_K}{h\nu})^3}; h\nu \geq h\nu_K \,, \quad (3)$$

where P_0 is the intensity coefficient from Eq. (1), $h\nu$ is the photon energy, kT is the core temperature, τ_K is the K-shell contribution to the opacity at the K-edge, τ_L is the L-shell contribution to the opacity at the K-edge, and ν_K is the photon energy at the K-edge, the energy threshold of K-shell photoionization. The Spect3D simulation output is provided as a set of spectral data points with the form ($h\nu, P$). We treat this synthetic spectral data as actual measured data. We fit the simple model to this data in order to estimate four unknown parameters, the core temperature, the initial intensity, the K-shell opacity and the L-shell opacity. Using four Spect3D data points, these four unknown parameters can be solved for, giving the user another set of information about the conditions occurring in the imploded target. Figure 5 demonstrates a Spect3D generated spectrum along with the four point model, showing in

particular the drop in the spectrum at the K-edge. The size of this drop is directly related to the shell areal density and to the amount of fluorescence. Therefore, a measurement of the fluorescence provides an independent measurement of the areal density.

Relating Fluorescence and Shell Areal Density

The shell areal density is a characteristic of an implosion which is vital to the success of the implosion. Fortunately, a relationship between spectrum and imploded shell parameters has been found[2] which allows the areal density to be inferred. This relationship can be expressed by the equation:

$$\frac{\int P(h\upsilon)_{K_\alpha} dh\nu}{\Delta P_{K-edge}\, h\nu_{K_\alpha}} = \omega_{K_\alpha} F(\tau, kT/h\nu_{K-edge}) \ . \qquad (4)$$

In Eq. (4), $P(h\upsilon)_{K_\alpha}$ is the spectral power of the K_α emission, ΔP_{K-edge} is the change in spectral power at the K-edge, ω_{K_α} is the fluorescence efficiency, and the function $F(\tau, t)$ is a slowly varying function of optical thickness τ and the core temperature t in units of the K-edge energy, $t = kT/h\upsilon_{K-edge}$. This equation says that the ratio of the number of K_α photons that are emitted to the number of photons that are absorbed creating K-shell vacancies is equal to the K_α fluorescence efficiency multiplied by a correction factor given by the function $F(\tau, t)$ of the dimensionless variables τ and t. This function is of order unity, and relates the number of photoionization events to the amount of energy absorbed by photoionization. It is primarily determined by the temperature of the core continuum spectrum and by the optical thickness of the shell. This function has been obtained for the case where the K_α photons escape freely and where the shell thickness is small, relative to its radius.

The function $F(\tau, t)$ is given by the expression

$$F(\tau,t) = \int_1^{\infty} \frac{(1-e^{-\tau/x^3})}{(1-e^{-\tau})} \frac{(e^{1/t}-1)}{(e^{x/t}-1)} x^2 dx \quad . \tag{5}$$

This was provided by Dr. Epstein[2] and has been plotted in Fig. 6 as a family of functions of τ for several values of t. The point corresponding to the case shown in Fig. 5 is indicated by the small circle. The detailed derivation of this expression was a "given" for the purposes of this project and is not repeated in this report. What it represents is the spectral integral of the photoionization probability for a photon passing through the shell, weighted by the photon spectral distribution obtained from the photon energy distribution given by Eq. (1). The integrand is normalized to unity at the K-edge, ($x = 1$ or $h\nu = E_{K-edge}$).

One relationship on which the above model is based is

$$\frac{(P_{K-edge} - \Delta P_{K-edge})}{P_{K-edge}} = e^{-\tau_K}, \tag{6}$$

where τ_K is the optical thickness at the K-edge due to K-shell photoionization, P_{K-edge} is the power at the top of the K-edge, and ΔP_{K-edge} is the drop in the flux at the K-edge.[5] The areal density $\rho\Delta R$ of the shell is related to τ_K according to

$$\tau_K = \mu\rho\Delta R \quad , \tag{7}$$

where μ is the contribution to the mass absorption coefficient due to the K-shell photoionization of the dopant in the target shell. Using the tabulated known value of μ for aluminum,[8] Eq. (7)

gives a result completely consistent with the simulated spectrum in Fig. 5, indicating that Spect3D is calculating the photoionization portion of the fluorescence process correctly.

An important goal of this project has been to validate Eqs. (4) and (5) using the simulated spectrum generated by Spect3D and shown in Fig. 5, with its K-edge continuum drop and K_α emission. We obtain $\int P(h\nu)_{K_\alpha} dh\nu = 1.37 \times 10^{16}$ erg/cm^2/sec from the spectrum by subtracting the continuum fit shown as the red line in Fig. 5 to isolate the K_α emission, which is then integrated numerically using the trapezoidal method in a simple computer program. The drop in the continuum at the K-edge $\Delta P_{K-edge} = 1.69 \times 10^{15}\ erg/cm^2/sec/eV$ was also measured directly from this simulated spectrum. The fluorescence efficiency of Al, $\omega_{K\alpha}$, is known to be 0.0387[6] and the photon energy of K_α, $h\nu_{K_\alpha}$, is 1487 eV. For these values, Eq. (4) is consistent with a value of F(τ,t) of 0.141, but one obtains from the model the value $F(\tau, t) = 0.720$ for kT = 3 keV and $\tau = 0.757$. The result, then, is that Spect3D predicts about 20% of the K_α emission expected by the model.

Even with the simplicity of the fluorescence model, its underlying assumptions are reasonable, so this factor-of-5 disagreement is larger than expected. The most plausible explanation for this discrepancy, and the most promising direction for future work, is that the cold-metal value for the fluorescence efficiency of aluminum, used by the model, is not being reproduced by Spect3D for the conditions of the experiment. There is no reason to doubt the completeness and accuracy of the Spect3D atomic model for Al, however. In retrospect, estimates by R. Epstein and B. Yaakobi[9] suggest that electron collisional and radiative recombination effects, which are included in the Spect3D atomic model, might reduce the effective fluorescence efficiency of lower-Z elements like aluminum, perhaps enough to account

for this discrepancy. The additional non-radiating processes would add to the denominator in Eq. (2). This disagreement is not encouraging, but it is a preliminary result that does not yet rule out using fluorescence as an areal density diagnostic for imploded targets and invites further work in that direction.

Conclusion

Fluorescence is the x-ray line emission which follows inner shell photoionization. This fluorescence emission is sensitive to the shell areal density, allowing a relationship to be formed between the amount of fluorescence and the amount of photoionization absorption. Spect3D provides a detailed model for the irradiation of an imploded target shell by emission from a hot inner core that includes all of the relevant atomic processes involved in fluorescence as a part of its atomic rate equations. Using this program, it is possible to demonstrate and study a simple model for the radiation from an imploded target shell. In particular, simple theoretical relationships which have been developed have been tested using simulated data provided by the Spect3D program. For one example, a factor-of-five discrepancy was found between Spect3D and the simple model. For now, the fluorescence of aluminum cannot be considered reliable without further simulation and without investigation into the underlying atomic physics.

The fluorescence from a germanium shell additive has been measured in several implosions on the NIF, however, and has been found to be consistent with the measured continuum spectra, according to the simple model, including Eq. 4 and Eq. 5, modified for the core emission spectrum at the much higher energies where germanium is photoionized. A proof-of-principle calculation for germanium fluorescence, similar to the one for aluminum carried out

in this project, would provide valuable insight into the ongoing implosion experiments on the NIF.

Acknowledgements

I would like to thank my advisor, Dr. Reuben Epstein, and the director of the program, Dr. Stephen Craxton, for their hard work to have made this experience possible. I would also like to express my appreciation for Michael Charissis and all of his technical help throughout the program.

References

1. J.J. MacFarlane, I.E. Golovkin, P.R. Woodruff, "Modeling of Inner-Shell Line Emission from Cu Targets Heated by Short Pulse Lasers," Prism Computational Sciences, Inc. Madison WI.
2. R. Epstein, private communication; R. Epstein *et al.*, Bul. Am. Phys. Soc. **56**, No. 12, 67 (2011) ; S. Regan et al., Phys. Plasmas.
3. Prism Computational Sciences, Inc., Madison, WI; J. J. MacFarlane *et al.*, HEDP **3**, 181 (2007).
4. Lois H. Gresh, Robert L. McCrory, and John M. Soures. *Inertial Confinement Fusion: An Introduction*. Laboratory for Laser Energetics: Rochester, NY. 2009; S.H. Glenzer et al., Plasma Phys. Control. Fusion 54, 045013 (2012).
5. S. Chandrasekhar, *Radiative Transfer*, Dover Publications, New York, 1960; R. Epstein, "The Equation of Transfer," personal manuscript - private communication, 2011.
6. J. H. Hubbell et al., J. Phys. Chem. Ref. Data, **32**, 339 (1994).
7. E. J. McGuire, Phys. Rev. **185**, 1 (1969).

8. J. H. Hubbell and S. M. Seltzer, on-line NIST Physical Measurement Laboratory report NISTIR 5632, www.nist.gov/pml/data/xraycoef/index.cfm.

9. R. Epstein and B. Yaakobi, Phys. Rev. **A 44**, 5111 (1991).

Figures

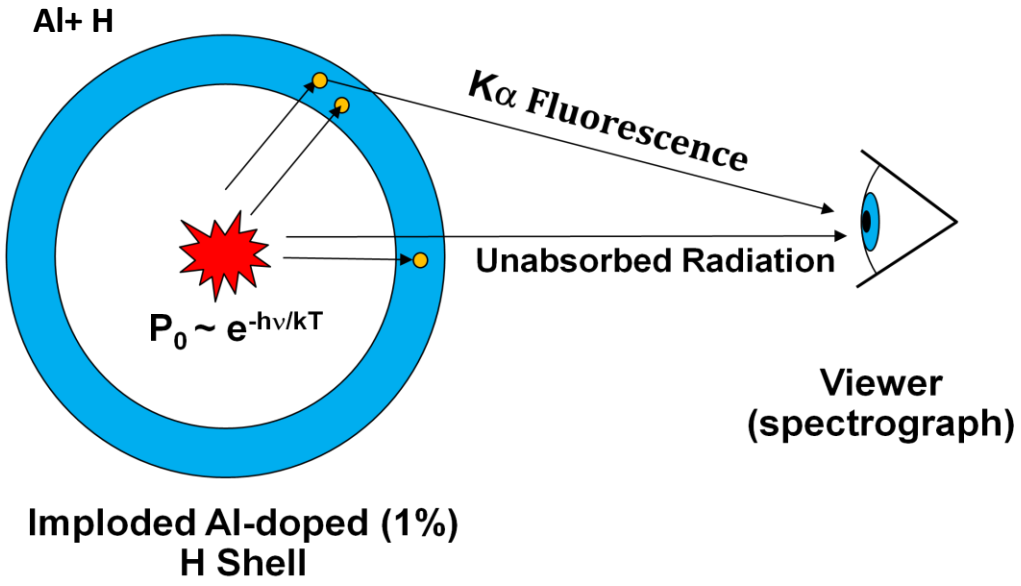

Fig. 1. An imploded target shell doped with aluminum. The target shell is being irradiated by x-rays from the hot core. These x-rays interact with the atoms in the target shell as they make their way to the detector.

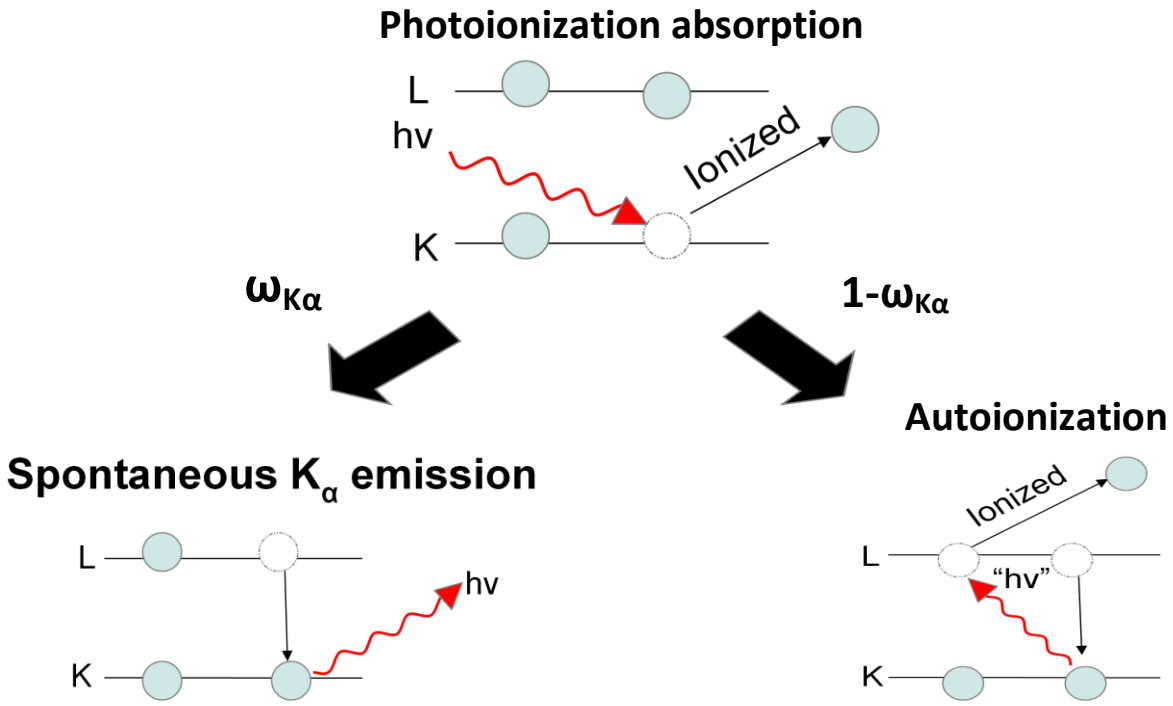

Fig. 2. Diagrams of the simple atomic processes involved in fluorescence. Photoionization, spontaneous emission, and autoionization are all shown. The probabilities, $\omega_{K\alpha}$ and $1-\omega_{K\alpha}$, of each process occurring after photoionization are also shown. The L shell has a higher electron energy level than the K shell.

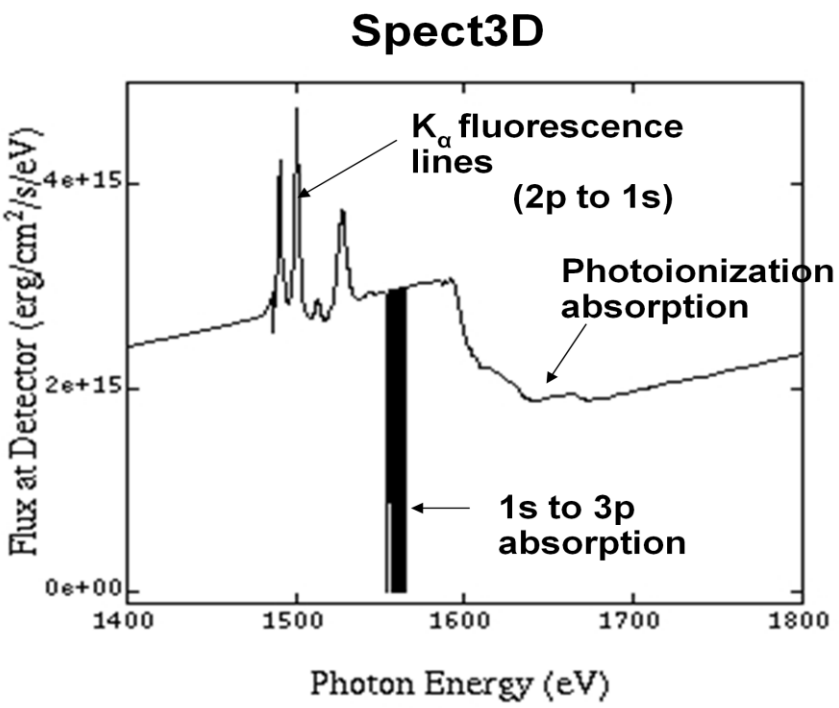

Fig. 3. A Spect3D simulated spectrum. The spectrum graphs photon energy vs. flux at the detector. The spectrum exhibits fluorescence lines, photoionization absorption, and 1s to 3p absorption lines.

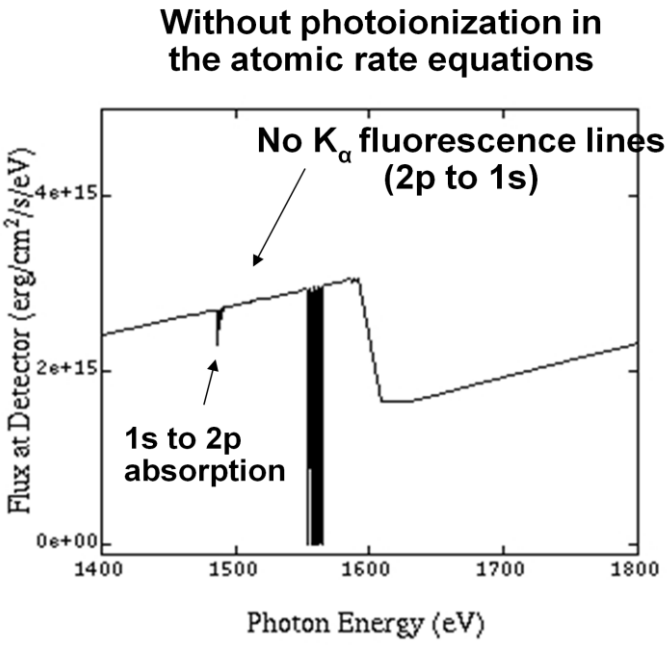

Fig. 4. A Spect3D simulated spectrum. This simulation was done without photoionization in the atomic rate equations which are solved by the complex radiation transfer code.

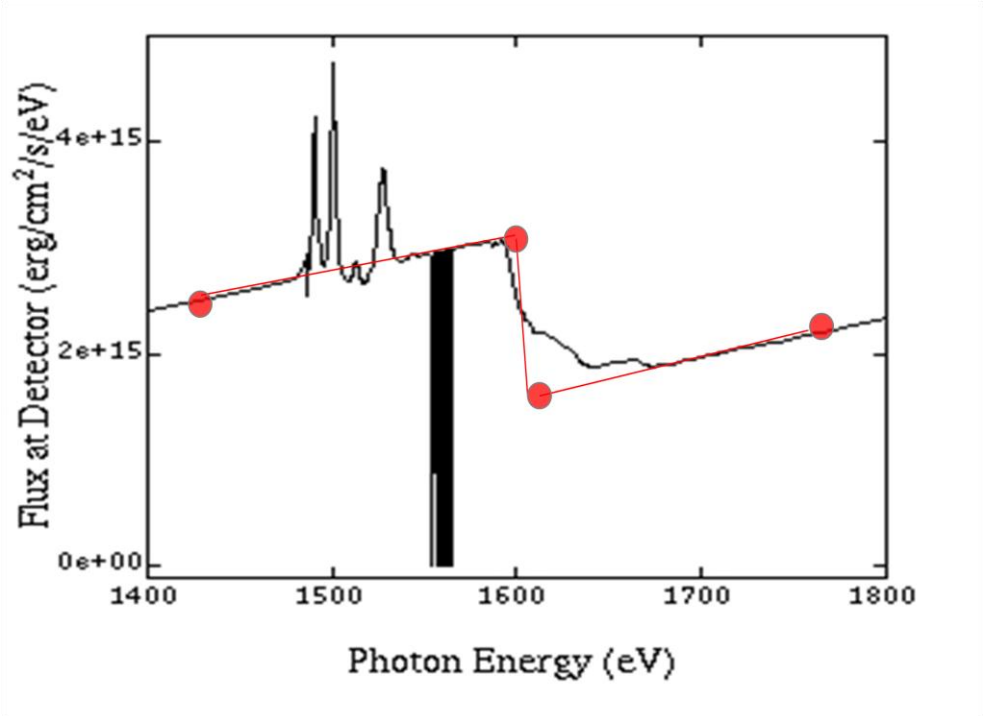

Fig. 5. A spectrum demonstrating the four-point model. This spectrum demonstrates the way in which a model of the emitted spectrum can be developed by extrapolating four data points from the Spect3D data.

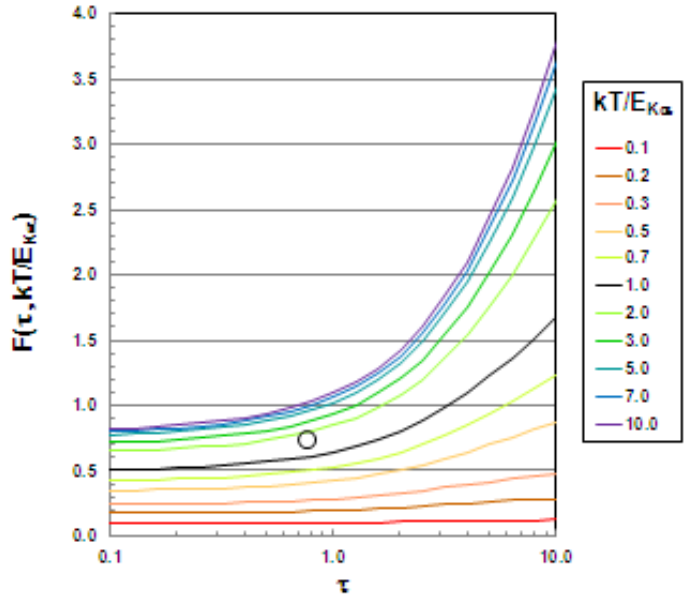

Fig. 6. The fluorescence response function plotted as a function of the shell optical thickness for various values of the source temperature in units of the K-edge energy. These results were obtained for the Planck continuum source created in the Spect3D simulation. Near the point $\tau =$ 0.757 and $kT/E_{K\alpha} = 1.92$, indicated by the small circle, the value of the function 0.720 varies slowly with these parameters.

Characterization and Design of Magnetic Coils for the Magneto-Inertial Fusion Electrical Discharge System (MIFEDS)

Felix Q. Jin

Brighton High School
Rochester, NY

Advisor: Dr. Gennady Fiksel

Laboratory for Laser Energetics
University of Rochester
Rochester, NY
November 2011

Abstract

The Magneto-Inertial Fusion Electrical Discharge System (MIFEDS) is used to provide a strong pulse of magnetic field required for a broad range of nuclear fusion and astrophysical applications. A dual-coil system currently used for MIFEDS was characterized, and a better single-coil design was developed. First, a mathematical formula was derived, and the dynamics of the coil resistive heating, including the current skin effect and temperature diffusion, was calculated. The results show that the coil heating is small. Second, a diagnostic method using a quadratic approximation of current waveform peaks was developed, which can determine when coil arcing occurs based on frequency analysis of the coil current waveform. Third, two computer programs were written to calculate and map the magnetic field and the coil inductance, respectively. Results from these theoretical calculations indicate that the existing dual-coil design for MIFEDS could be improved and a single-coil design could provide a stronger and more uniform field. A single coil based on this new design was fabricated and experimentally tested, and results reveal that the magnetic field generated by the single coil is much stronger than that of the dual-coil design. This will result in better energy confinement for laser inertial fusion and thus higher fusion efficiency.

1. Introduction

Nuclear fusion energy is the energy generated through nuclear fusion processes, in which two light atomic nuclei fuse together to form a heavier nucleus. Unlike energy generated by fossil fuel and nuclear fission power, nuclear fusion is sustainable and environmentally clean. However, nuclear fusion energy remains under research and development stages in the United States and other countries. The Laboratory for Laser Energetics at the University of Rochester is one such facility that focuses on nuclear fusion studies, specifically inertial confinement fusion, which uses the 60-beam OMEGA laser system to initiate fusion by heating and compressing a cryogenic target.

The Magneto-Inertial Fusion Electrical Discharge System (MIFEDS) is used to provide a strong pulse of magnetic field required for magneto-inertial fusion (MIF) and for other applications such as astrophysics and high-energy-density plasmas.[1] MIFEDS uses strong magnetic fields to confine fusion fuel while the fuel is heated into a plasma. A strong magnetic field confines the plasma and reduces thermal loss. In MIF, magnetic fields are used to slow down plasma losses, and inertial compression is used to heat the plasma. One of the challenges for MIF is the need to form high-strength magnetic fields at the focus of the reaction. MIFEDS can be flexibly added to the OMEGA Laser System when MIF or other experiments involving strong magnetic fields are planned. Currently a dual magnetic coil design is used in MIFEDS to generate magnetic fields for high-energy-density plasma studies with the OMEGA Laser System at the University of Rochester. However, the physical characteristics of this dual magnetic coil device have not been fully investigated.

In this work, a mathematical formula, a diagnostic method and two computer programs were developed and used to determine the dynamics of the coil resistive heating, the time of coil

arcing, the strength of the magnetic field, and the coil inductance. Results from these theoretical calculations indicate that the current dual-coil design for MIFEDS could be improved by using a single-coil design. Furthermore, a single-coil device was fabricated and experimentally tested, and results reveal that the magnetic field generated by a single coil is much stronger and more uniform than that of the dual-coil design.

2 Mathematic Models and Experimental Methods

2.1 *The MIFEDS device*

MIFEDS is a system which produces a strong magnetic field in the target zone. A pulse of electric current travels through a coil at the end of the transmission line to produce this magnetic field. High-voltage (HV) capacitors are used to store the energy before firing, and a laser trigger beam is aimed at a spark gap. When the laser fires, it initiates the electrical discharge, which dumps the current through the transmission line and coil before returning through the reverse side of the transmission line. The other end of the transmission line is reconnected with the HV capacitors. MIFEDS is inserted into the OMEGA target chamber through one of the Ten-Inch Manipulator (TIM) ports.

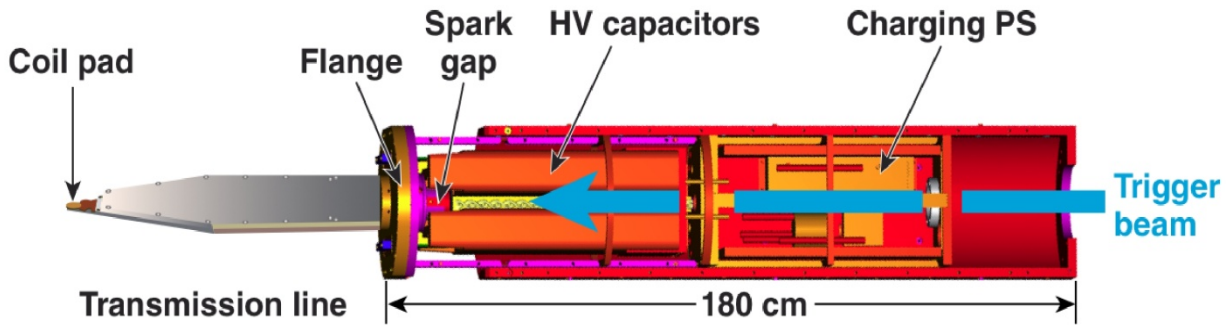

Fig. 1. Diagram of the MIFEDS assembly
High-voltage capacitors are charged, and then discharged by a spark gap, which is triggered by a laser trigger. Current travels down the transmission line and through the coils, generating a high magnetic field.

The MIFEDS system behaves like an LRC circuit with most of the capacitance being part of the HV capacitors and most of the inductance part of the coil and transmission line. The natural frequency depends on the exact coil that is used. However, in general, the initial period of the current is about 600 ns and the discharge current peaks at around 40 kA. The coil itself is fabricated out of high-purity sheet copper and insulated with kapton. The transmission line is composed of two parallel plates of aluminum also insulated with kapton.

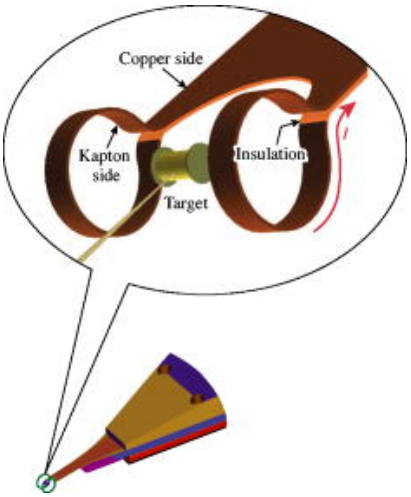

Fig. 2. Diagram of MIFEDS coil
As current flows through the coils, a strong magnetic field is created in the area around the target.[2]

2.2 The magnetic field-measuring apparatus

A Faraday rotation setup was used to measure the strength of the magnetic fields produced by MIFEDS. A Faraday probe was placed in between the two coils, and polarized light from a dedicated probe laser was passed through the probe. The probe's crystal rotates the polarization of light in proportion to the external magnetic field due to the Faraday effect. By measuring the amount of rotation, the magnetic field strength can be determined. The rotation angle θ is given by the expression $\theta = Blk$, where B is the magnetic field strength parallel to the light, l is the length of the crystal, and k is the Verdet constant of the crystal, which for our probe was 100 rad/T m. The test chamber and magnetic field-measuring apparatus are shown in Fig. 3.

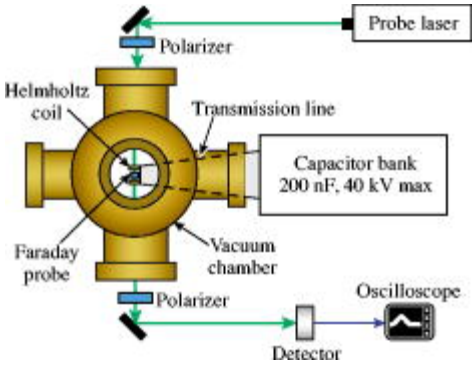

Fig. 3. Diagram of the magnetic field-measuring apparatus
A Faraday rotator was used inside the testing chamber to determine the magnetic field strength.[2]

The light intensity is measured by a detector and the data is collected with an oscilloscope. The field is then determined using Eq. (1) and Malus's law,

$$I = I_0 \cos^2 \theta \tag{1}$$

which gives the detected light intensity I as a function of the angle of rotation θ and the initial full intensity I_0. The second polarizer is configured so that without a magnetic field, the measured angle would be $\pi/2$ radians as this allows for maximum sensitivity in both field directions.

The current going through the system can also be measured and analyzed. This is done through a Rogowski pickup coil, a device which measures high-speed electrical current pulses. This coil is placed around the internal portion of the transmission line, near the HV capacitors.

2.3 Temperature of magnetic coils

The temperature of the MIFEDS magnetic coils was of importance because previous experiments and calculations suggested that some copper may be evaporating during discharge.[2] An equation was developed to model the temperature of the coils, taking into account skin effect current, temperature-dependant resistance, and resistive heating. The first, basic model considered only resistive heating and treated current density as uniform. According to Joule's law, the power P of resistive heating of the circuit is equal to the rate of energy transferred as heat to the coil. This primary expression is

$$P = \frac{dW}{dt} = I^2 R = C \frac{dT}{dt} \tag{2}$$

where I is the current, R is the resistance, C is the heat capacity of the material, and T is the temperature. The current becomes a function of time since the circuit is an oscillator, and the resistance becomes a function of the temperature of the coil.

Heat-dependent resistance follows the equation $R(T) = R_0[1 + \alpha(T - T_0)]$, where α is the temperature coefficient of resistance for copper, and R_0 is the initial resistance at some temperature T_0.

The skin effect current creates a non-uniform current distribution within the coil, and the current is mostly concentrated close to the outside of the coil. In order to determine a maximum bound for temperature, only the surface of the coil was considered, and radiative cooling was ignored. For an infinitely thick slab where x=0 is the surface and where the slab extends in the positive x-direction, skin effect calculations for the surface yield the following equations:

$$\delta = \sqrt{\frac{2}{\omega\mu\sigma}} \tag{3}$$

$$\frac{\partial j}{\partial x} = \frac{\mu_0\sigma}{P}\frac{\partial I}{\partial t} \tag{4}$$

$$j(x,t) = j_0 e^{-x/\delta} e^{i(\omega t - x/\delta)} \tag{5}$$

where δ is the skin depth, ω is the frequency, μ is the magnetic permeability of copper, μ_0 is the vacuum permeability, σ is the electrical conductivity, I is the total current entering the system, j is the current density, and j_0 is the maximum current density which occurs at the surface. Solving equations 3, 4, and 5 gives

$$j(x,t) = \frac{I_0}{\delta P} e^{-x/\delta} e^{i(\omega t - x/\delta)}, \tag{6}$$

which, at the surface (x=0), simplifies to

$$j(0,t) = \frac{\sqrt{2}I_0}{\delta P}\sin(\omega t + \frac{\pi}{4}). \tag{7}$$

Thus, the maximum current density at the surface of the coil is $\frac{\sqrt{2}I_0}{\delta P}$. Since the model sets t=0 when MIFEDS first fires, the current waveform at the surface can be approximated by

$$I(t) = \frac{\sqrt{2}I_0}{\delta P}\sin \omega t. \tag{8}$$

The heat capacity C is equal to the mass times the specific heat c. The final equation should evaluate current density instead of current, so the expression is divided by ρ, the density of copper. The final differential equation for temperature is

$$\frac{dT}{dt} = \frac{j^2(t)R(T)}{C\rho} = \frac{2I_0^2 \sin^2(\omega t)R_0[1 + \alpha(T - T_0)]}{\delta^2 P^2 C\rho}. \tag{9}$$

2.4 Frequency measurement and arcing analysis

Because the MIFEDS circuit is connected in a loop, it behaves like an LRC circuit. The natural frequency is inversely proportional to the square root of the inductance and the capacitance. This frequency can be determined from magnetic field or current measurements. In some tests, the magnetic field only oscillates for one period before collapsing. An increase in frequency is also observed after the field collapses, which indicates that arcing occurred because the inductance of the arc is much lower than that of the coil. Due to a phenomenon not yet fully explored, the first period of magnetic field is much weaker when there is an arc. Ensuring that arcing does not occur too soon allows it to be confirmed that a magnetic field is generated. A quadratic-regression method was used to estimate the peaks of the current waveform and determine the period. When the period drops, arcing is predicted to have happened.

2.5 Magnetic field mapping

The magnetic field generated by MIFEDS was of interest to examine field properties and to determine the location and strength of the maximum field produced. The general equation for the magnetic field generated by a current is given by the Biot-Savart law:

$$\vec{B} = \int \overrightarrow{dB} = \int \frac{\mu_0}{4\pi}\frac{I\overrightarrow{dl} \times \vec{s}}{|s|^3}. \tag{10}$$

Two parallel circular loops of coil were used as an approximation for the actual case. Fig. 4 is a sketch of the geometry and the variables used in the following derivation. A cross sectional contour diagram of the field sliced through the center was desired, so the point of interest was fixed in the yz-plane, with its x-coordinate equal to 0.

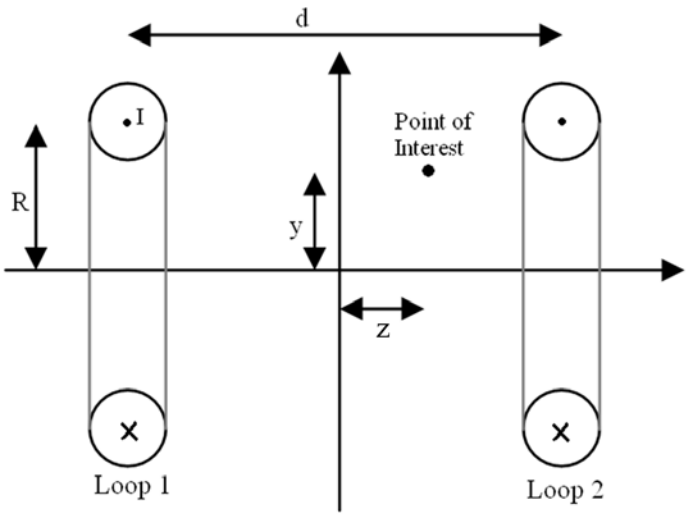

Fig. 4a. Cross-section of dual MIFEDS coils
This diagram shows the names of the variables assigned to the various properties of the coil configuration. The **i**(x) direction is into the page, **j**(y) direction is to the top, and **k**(z) direction is to the right.

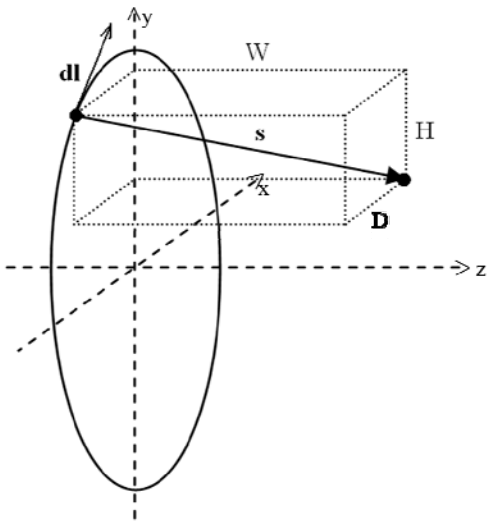

Fig. 4b. Diagram of single loop
The integral is evaluated along the path of the current (the circle), and **s** is the vector from the circle to the point of interest.

The variables D (depth), H (height), and W (width) are the components of the s-vector from the loop to the point of interest such that $\vec{s} = D\hat{\imath} + H\hat{\jmath} + W\hat{k}$. The D variable corresponds with the x-axis, H corresponds with the y-axis, and W corresponds with the z-axis. The magnitude of **s** is therefore $\sqrt{D^2 + H^2 + W^2}$. The integration starts from the top of the loop and goes around so that $\overrightarrow{dl} = dl\cos\theta\,\hat{\imath} - dl\sin\theta\,\hat{\jmath}$, where θ is the angle around the loop starting at the top. The cross product is $\overrightarrow{dl} \times \vec{s} = -Wdl\sin\theta\,\hat{\imath} - Wdl\cos\theta\,\hat{\jmath} + (H\cos\theta + D\sin\theta)dl\,\hat{k}$.

Analysis of the geometry yields the equations, $D = R\sin\theta$ and $H = R\cos\theta - y$, where y is the **j**-component of the distance from the center of the circle to the point (see Fig. 4a). The

identity $\theta = l/R$ is used to convert from the angle around the circle to the circumference traveled.

The equation for the magnetic field at a point (0, y, z) for a coil centered at the origin is

$$\vec{B} = \frac{\mu_0 I}{4\pi}\int_0^{2\pi} \frac{-z\sin\frac{l}{r}\hat{\imath} - z\cos\frac{l}{r}\hat{\jmath} + R\,\hat{k}}{\left[\left(R\sin\frac{l}{r}\right)^2 + \left(R\sin\frac{l}{r} - y\right)^2 + z^2\right]^{3/2}} dl. \tag{11}$$

To model two coils, the initial current I_0 is divided by 2, and an additional term is added. The W variable for the first coil is z-d/2 and for the second coil is z+d/2, where d is the distance between the two coils:

$$\vec{B} = \frac{\mu_0 I}{4\pi}\int_0^{2\pi} \left(\frac{-(z-\frac{d}{2})\sin\frac{l}{r}\hat{\imath} - (z-\frac{d}{2})\cos\frac{l}{r}\hat{\jmath} + R\,\hat{k}}{\left[\left(R\sin\frac{l}{r}\right)^2 + \left(R\sin\frac{l}{r} - y\right)^2 + (z-\frac{d}{2})^2\right]^{3/2}} \right. \tag{12}$$

$$\left. + \frac{-(z+\frac{d}{2})\sin\frac{l}{r}\hat{\imath} - (z+\frac{d}{2})\cos\frac{l}{r}\hat{\jmath} + R\,\hat{k}}{\left[\left(R\sin\frac{l}{r}\right)^2 + \left(R\sin\frac{l}{r} - y\right)^2 + (z+\frac{d}{2})^2\right]^{3/2}} \right) dl.$$

2.6 A new coil design

Initial calculations from the development of the magnetic field mapping suggested that a single magnetic coil could produce a stronger magnetic field than the dual-coil design that was used. However, a single coil does have a much higher impedance. In order to reduce this, a flatter coil was suggested because it would have similar impedance to that of the dual-coil design while possibly providing a stronger and more uniform magnetic field. To model a flat coil, multiple terms were added to the equation, with the

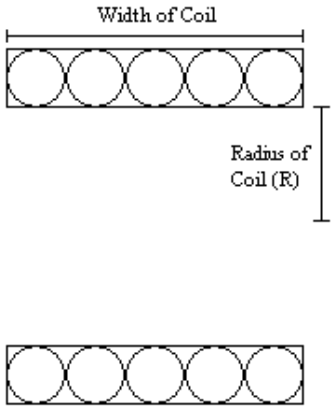

Fig. 5. Cross section showing how a flat single-coil was modeled
Circular coils stacked on each other approximate the flat coil.

loops being adjacent to each other. Using magnetic field mapping and calculations of inductance and impedance, it was determined that a coil 3 millimeters in width would be ideal.

3 Results

3.1 Solving for temperature

To solve the coil-temperature differential equation, a fourth-order Runge-Kutta-method program was written in MATLAB. The differential equation the program used was the previously derived Eq. 9. The average amplitude of the first period is 40 kA, so a value of 20 kA was used to model one of the two coils.

To approximate the perimeter of a cross section of the coil, a thickness of 0.25 mm and a width of 1 mm were used. The heat capacity C was calculated by multiplying the specific heat of copper by the mass per unit length, which was determined using the cross-sectional area and the density of copper.

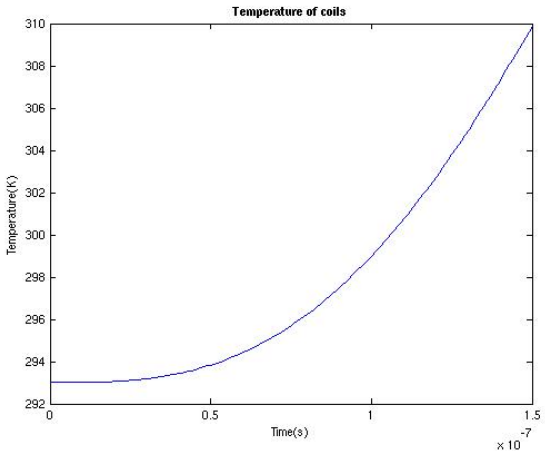

Fig. 6. Plot of the predicted temperature of MIFEDS coil during the first 150 ms
The initial temperature was set to room temperature. The coil theoretically sees an increase in temperature of about 17 Kelvin.

MIFEDS is fired 150 milliseconds before the laser shot because the peak of the magnetic field strength occurs 150 ms after the initial discharge. Fig. 6 shows the plot generated by the program. Based on these results, it was determined that the coil heating was minimal, and the copper was not evaporating before the laser shot.

3.2 Analysis of Arcing

Current data collected from the Rogowski coil in MIFEDS (Fig. 7a) was used for analysis. The data for the peaks of the current were then isolated. The peak of the quadratic regression for the data was used to approximate the actual peak. Fig. 7b shows one such analysis in which arcing clearly occurred. However, it was late enough to not have affected the magnetic field

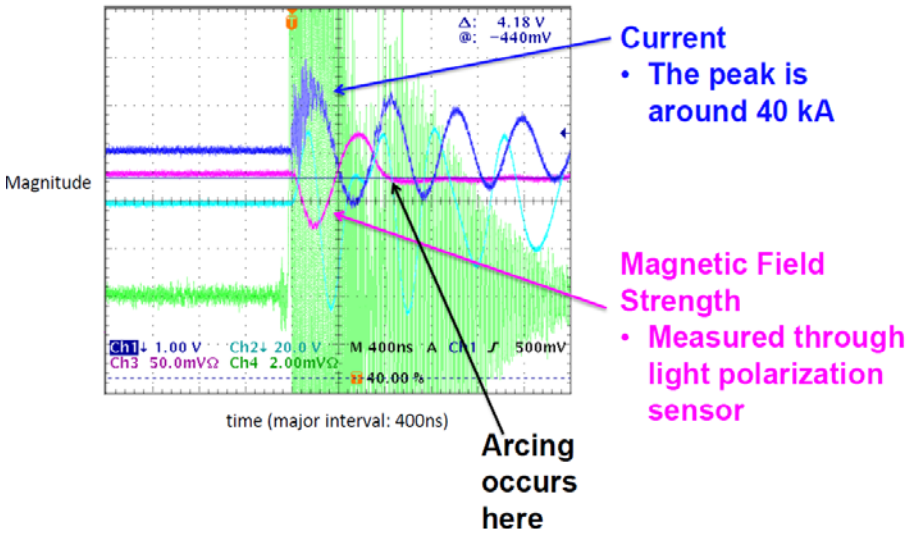

Fig. 7a. Data from the oscilloscope demonstrating arcing When arcing occurs, there is a slight change in frequency, and the magnetic field is no longer produced. The green and teal lines are from two other diagnostic tools not used for this experiment.

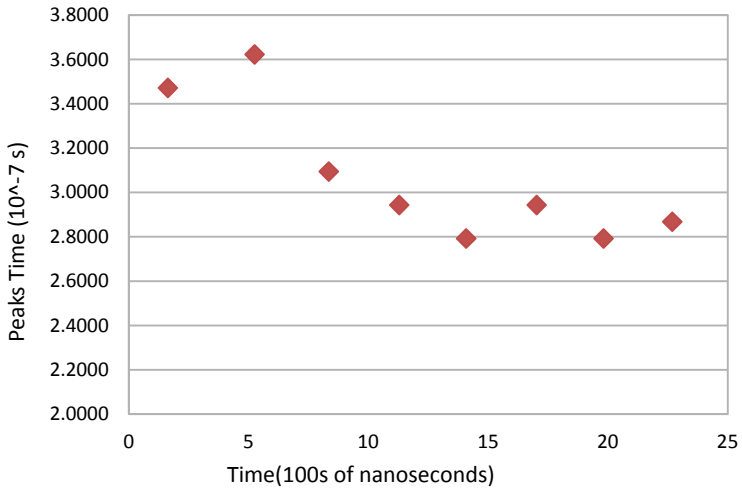

Fig. 7b. Analysis of the period of the waveform At the second period, arcing occurs, indicated by the drop in the period.

strength of the first half-period, which is when the laser would fire. On August 3 2011, an astrophysics experiment was conducted with the OMEGA laser and MIFEDS to study the effect of strong magnetic fields on certain particles. As shown in Fig. 8 frequency analysis was used to

confirm that the magnetic field did not collapse too early. Results indicated that the magnetic field was most likely stable, but may have been weaker in a few cases due to the arcing effect.

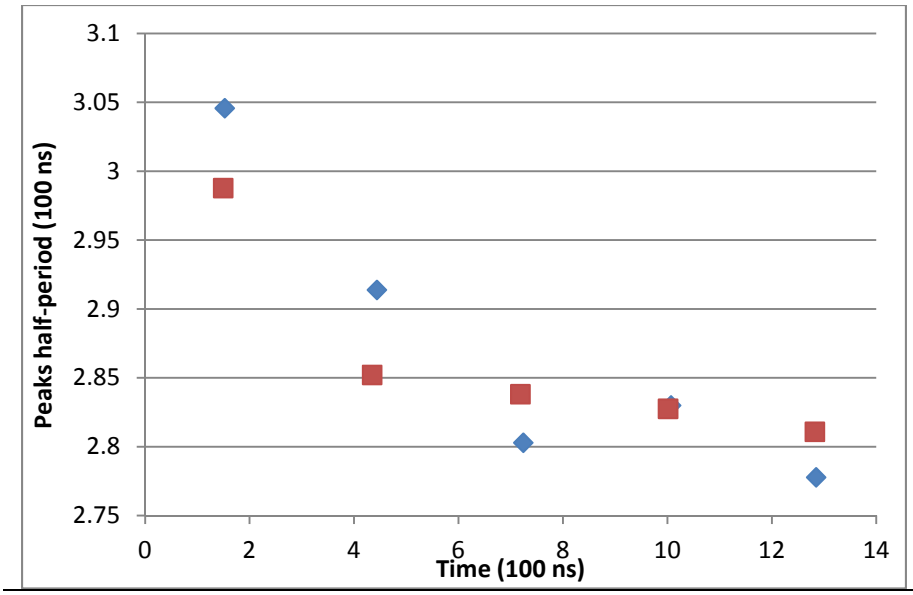

Fig. 8. Frequency analysis results from the 8-03-11 experiment
Arcing most likely occurred after the first half-period. This may have reduced the magnetic field strength during the shot.

3.3 Magnetic field maps

Code written in MATHEMATICA was used to numerically integrate equations (11) and (12) for the magnetic field and to create the contour plots. For the dual-coil map, a radius of 6 mm and a separation between the coils of 13 mm was used. Fig. 9 represents the result of these calculations. These results show that most of the magnetic field is concentrated at the center of each coil instead of between the coils. Additionally, the field is only uniform at the center, not near the edges.

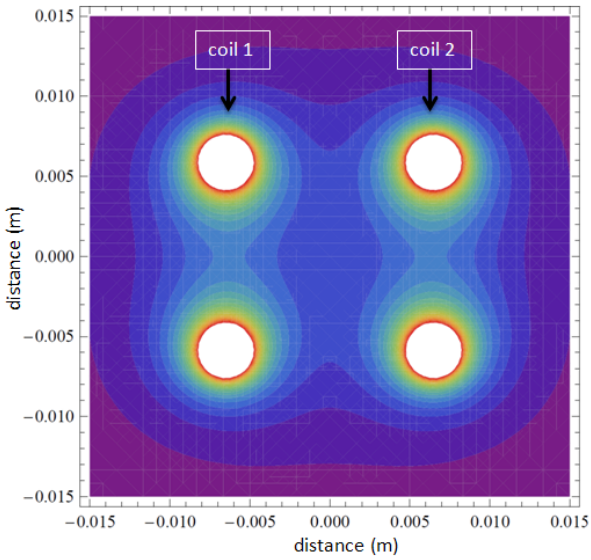

Fig. 9. Magnetic field contour plot for the standard dual-coil design
The outermost area represents a field strength of 0 to 0.5 T and the contour interval is 0.5 T.

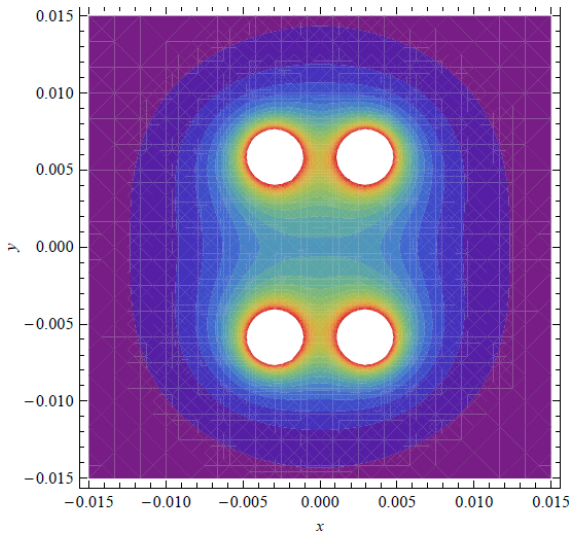

Fig. 10. Magnetic field contour plot for a Helmholtz coil
A Helmholtz arrangement produces the smoothest field at the center and in between the coils.

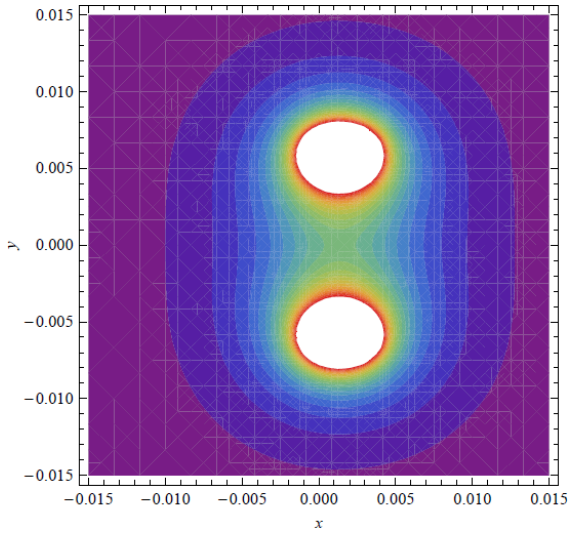

Fig. 11. Magnetic field contour plot for a flat single coil
The single coil design generates a much stronger and concentrated magnetic field at the center.

A Helmholtz coil arrangement is one where there are two coils and the distance between them is half the radius of a coil. As shown in Fig. 10, a Helmholtz coil produces the most uniform field at the center. A flat single-coil design was suggested to produce stronger and more uniform magnetic fields than the dual-coil design. Results (Fig. 11) indicate that the magnetic field for a single flat coil is much stronger than for a dual coil. Although the field is not extremely smooth, the single-coil field is closer to the Helmholtz field than is the field of the dual-coil design that was originally used (Fig. 9).

3.4 Experimental testing of the new coil design

A MIFEDS coil consisting of a single loop with a width of 3 mm was cut and bent out of a 0.25 mm-thick copper stock. Because of certain limitations of the viewing geometry, the Faraday probe could not be placed at the center of the loop. Instead, the probe was placed to the side of the coil, and the measurement at the edge would be converted to a value for the magnetic

field at the center. The new coil was placed into the test chamber, and MIFEDS was charged and fired. Fig. 12a shows the data collected from the oscilloscope for this test. The dark blue line is current, and the purple line is magnetic field strength. Although arcing occurred quickly since the magnetic field stopped oscillating after the peak, the field was still strong.

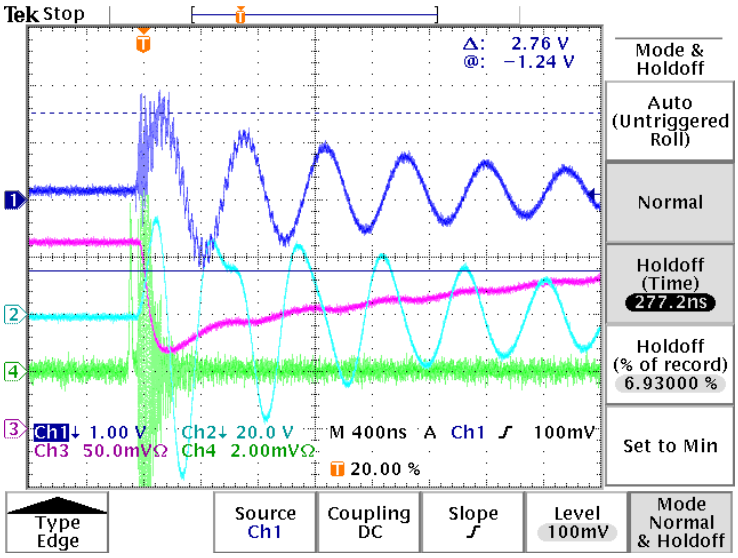

Fig. 12a. Current and magnetic field data for flat coil test
Arcing occurs very early on in this test, but the single flat coil produced a much stronger field.

Fig. 12b. Image of the Faraday probe location
This picture was used to determine the distance from the probe to the center. Coil width is 3 mm

The measured magnetic field strength was 3.15 T, which is the strength at the location of the probe, placed besides the coil. The image shown in Fig. 12b was used to find how far the probe was from the center. Using calculations from the magnetic field maps, a conversion ratio was determined to find the field strength at the center. The probe was about 1.5 mm from the center, so the maximum field strength at the center was predicted to be 4.37 T, much stronger than the dual-coil design, which produced a field strength averaging about 1.6 T.

4 Conclusions

Calculations and mathematical models were produced to characterize the magnetic coils used for the MIFEDS. A model of coil heating was produced, which predicted that the coils were not evaporating. Frequency-analysis methods were used to predict coil arcing and to confirm the successful generation of a magnetic field for experiments involving MIFEDS. The magnetic field produced by the coil was analyzed and mapped. Based on these results, a new single-coil design was proposed, fabricated, and experimentally tested; the results of the test confirmed that this design produced stronger magnetic fields.

Future research will improve upon both the temperature and magnetic field models. The goal is to produce new designs and modifications to MIFEDS that will improve efficiency, field strength, and field uniformity. These improvements and the increased productivity will ultimately allow MIFEDS to meet the requirements of and be used in more experiments and applications requiring strong magnetic fields.

Acknowledgements

I would like to thank Dr. Gennady Fiksel for being my research advisor and helping me with the project, Po-Yu Chang for his teaching and technical assistance, the program director Dr. R. S. Craxton for providing me this research opportunity, and Dr. Anatoly Spitkovsky at the Department of Astrophysics, Princeton University for providing me the opportunity to work with him and help conduct a laser shot experiment at the Laboratory for Laser Energetics, University of Rochester.

References

[1] Gotchev *et al*., "Laser-Driven Magnetic-Flux Compression in High-Energy-Density Plasmas, *Physical Review Letters,* **103**:215004, 2009.

[2] Gotchev *et al*., "Seeding magnetic fields for laser-driven flux compression in high-energy-density plasmas," *Review of Scientific Instruments*, **80**:043504, 2009.

Modeling Tritium Removal from Metal Surfaces

Jefferson Lee

Canandaigua Academy
Canandaigua, NY

Advisor: W. T. Shmayda

Laboratory for Laser Energetics
University of Rochester
Rochester, NY
September 2011

Abstract

A program was written to numerically model the diffusion of tritons throughout a metal bulk. The program uses Fick's diffusion equation to follow the time evolution of a concentration profile. It has been used to accurately model how particles will flow out of a system with a concentration of zero at the surface. It has also been used to model how a change in diffusion constant, such as the one between the metal oxide layer and the metal bulk, affects the diffusion of particles. Using this model for the concentration profiles within a substance, the outgassing rate of tritons from a surface as a function of time has also been modeled. The outgassing rate model accurately models the outgassing rate from experiments at longer times, but at earlier times it is less accurate. This is believed to be due to the fact that only diffusion through the solid is accounted for in the outgassing rate model, and surface equations are ignored. This would suggest that at earlier times, the removal of tritons is governed by surface equations, while at later times it is governed by diffusion. Work on a more complex program to model the removal of tritons from the surface of the metal has been started, and will be used in conjunction with the diffusion model.

Introduction

Tritium, (H-3) is a radioactive isotope of hydrogen that occurs naturally, and has a half life of 12.32 years. It can often replace hydrogen in a molecule containing hydrogen. For example, a hydrogen atom in water (H_2O) can be replaced by a tritium, forming tritiated water (HTO). Due to this characteristic and its small atomic size, tritium can often remain in a substance after multiple swabs to remove it.

Tritium has many applications. Due to its radioactive nature, it is often used as a tracer in biological, chemical and environmental studies. Tritium is used in radio-luminescent sources relying on decay betas to make scintillant deposited on the inner surfaces of tubes to fluoresce. Tritium is a fuel in the production of fusion energy. Tritiated water is also useful for studying the effects of water absorption to surfaces.

The removal of tritium from metal surfaces is important because the tritium can diffuse through the metal that is used to handle it or that comes in contact with it. Removing this radioactivity is important in insuring safety. Due to the composition of the metal substrate, the removal of tritium is not uniform and consists of a number of different movements, as seen in Figure 1.

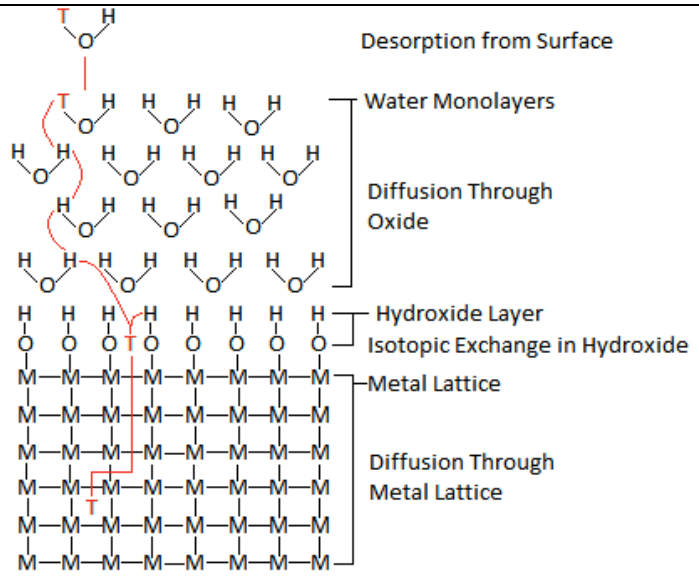

Figure 1. Removal of tritium from a metal bulk

Tritium from the bulk diffuses through the metal lattice, undergoes isotopic exchange within the hydroxide layer and water monolayers, and is desorbed from the surface into the gas stream

Figure 1 shows that tritium undergoes a multi-step removal process; it must diffuse through the metal lattice, undergo isotopic exchange into the hydroxide layer and the water monolayers forming the oxide layers, diffuse through the oxide, and then desorb from the surface or be removed from the surface by a flow of helium over the surface of the metal. As tritiated water is removed from the surface by the gas stream, new particles will diffuse through the oxide layer under a concentration gradient, causing more particles to diffuse to the oxide layer from the metal lattice under a concentration.

Experimental Setup

In testing my model for accuracy, we will use data from collected in experiments performed at the Laboratory for Laser Energetics over the past 2 years. The experimental setup of these experiments has been described in the reports written by these experimentalists [1,2,3]. The setup is illustrated in Figure 2.

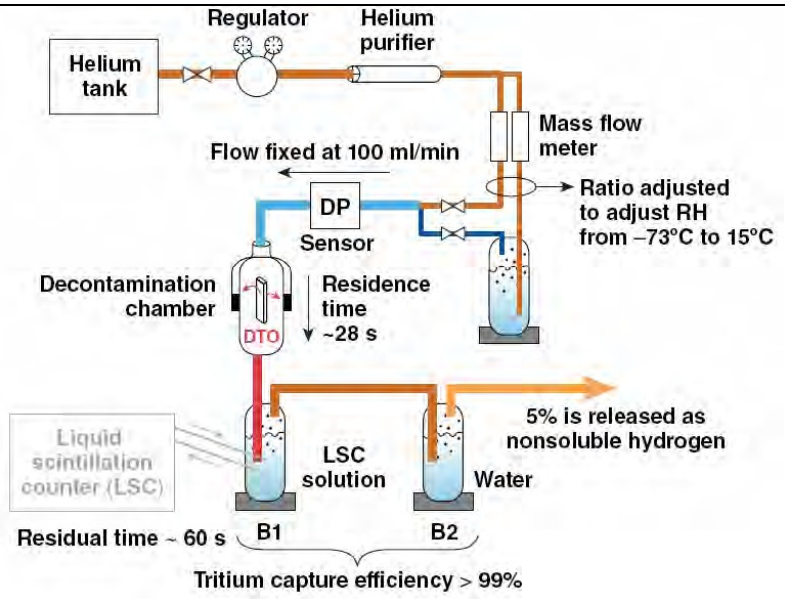

Figure 2. Experimental setup for the measurement of tritium desorption from metal coupons

Metal coupons that are contaminated with tritium are placed within the decontamination chamber. Helium is decompressed from the helium tank with the regulator, purified to remove trace contaminants, and split into two streams. Both streams are metered. One

stream flows directly towards the chamber; the second stream is humidified by bubbling the gas through water. The two streams are combined before entering the decontamination chamber. The relative humidity of the combined streams is adjusted by adjusting the ratio of the wet stream to the dry stream. The gas stream then flows through a dew point sensor (DP) to verify that the relative humidity is consistent with calculations. The decontamination chamber can be set to various temperatures to study the removal rate dependence on temperature and stream humidity. Tritium is removed from the surface of the metal as tritiated water. This water is collected in the liquid scintillation cocktail in the first bubbler (B1), where activity is counted by the liquid scintillation counter (LSC) as the tritiated water is collected. The gas then moves to the second bubbler (B2), where tritium that is not captured in the first bubbler can be removed. Two bubblers are used in series to confirm that the liquid scintillation cocktail in the first bubbler is removing at least 95% of the incoming tritiated water. Between the two bubblers, over 99.5% of the tritium transported to the bubblers is removed from the gas stream. Data from a number of previous experiments have been compiled, with variables including the type of metal, the relative humidity, and the temperature of the coupon. The liquid scintillation counter collects data in the form of activity, which can then be converted to an outgassing rate, which is what we will be using for our purposes.

Theory

Fick's laws of diffusion[4] state the following;

$$\frac{\partial c}{\partial t} = -\frac{\partial F}{\partial x} \tag{1}$$

$$F = -D\frac{\partial c}{\partial x} \tag{2}$$

where c is concentration, t is time, F is flux, x is distance into the metal, and D is the hydrogen diffusion coefficient in the medium of interest. Equations 1 and 2 lead us to equation 3.

$$\frac{\partial c}{\partial t} = \frac{\partial}{\partial x} D \frac{\partial c}{\partial x} \tag{3}$$

Since we are searching for a numerical solution, we must construct a numerical grid dividing the distance into *N* cells. If we define x_L as the left boundary and x_R as the right boundary, we can define the space between cells, Δx, as in the equation 4.

$$\Delta x = \frac{(x_R - x_L)}{N} \tag{4}$$

Using equation 4, we can define x_i, or the value of distance at the center of the "*ith"*cell.

$$x_i = x_L + (i - \frac{1}{2})\Delta x \tag{5}$$

It is important to note that for our purposes, x_L will be 0 for all equations and models. The next step is to define the diffusion coefficients. In our model, there will be two diffusion coefficients. One defines diffusion through the bulk and the other diffusion through the oxide layers. However, there are two layers of oxide; one on the left and one on the right. The left oxide layer will have diffusion constant D_A, the bulk D_B, and the right oxide layer D_C. We will then define the distance at which the diffusion constants change as x_s and x_t respectively. If we consider D_i as the diffusion constant within the "*ith*" cell, we have

$$D_i = D_A \text{ if } x_i < x_s \tag{6}$$

$$D_i = D_B \text{ if } x_s \le x_i \le x_t \tag{7}$$

$$D_i = D_B \text{ if } x_t < x_i \tag{8}$$

We can then define the diffusion constant at the interfaces between cells. With $D_{i+\frac{1}{2}}$ being the diffusion constant at the interface between the "*ith*" and the "*i*+1"th cell.

$$D_{i+\frac{1}{2}} = \frac{D_i + D_{i+!}}{2} \tag{9}$$

The next step is to solve Fick's equations. The subscript notation denotes the cell the value refers to. The next equations are equation 2 recast in finite difference form. $F_{i+\frac{1}{2}}$ is the flux at the interface between the "*ith*" and the "*i*+1"th cell. c_i refers to the concentration within cell *i*.

$$F_{i+\frac{1}{2}} = -D_{i+\frac{1}{2}} \frac{c_{i+1} - c_i}{\Delta x} \tag{10}$$

$$F_{i-\frac{1}{2}} = -D_{i-\frac{1}{2}} \frac{c_i - c_{i-1}}{\Delta x} \tag{11}$$

The next step is to write equation 1 in finite difference form[5]. Δt refers to the time-step to be used between each concentration profile that the program generates; i.e., assuming that the concentration c_i within cell i is known at time t, we need to find c'_i the concentration at a time $t + \Delta t$.

$$\frac{c'_i - c_i}{\Delta t} = \frac{-(F_{i+\frac{1}{2}} - F_{i-\frac{1}{2}})}{\Delta x} \tag{12}$$

Combining equation 11 and equation 12, we find equation 13.

$$\frac{c'_i - c_i}{\Delta t} = \frac{-1}{\Delta x}(-D_{i+\frac{1}{2}} \frac{c_{i+1} - c_i}{\Delta x} + D_{i-\frac{1}{2}} \frac{c_i - c_{i-1}}{\Delta x}) \tag{13}$$

The only problem with this equation is that it uses past values of F to generate future values of c. By including F', or the flux at the new time, in our equation, we can make it more stable and more accurate. We also include a degree of implicitness, θ, to control the amount of weight that is given to the two times. The degree of implicitness must be between 0 and 1, inclusive. We therefore replace equation 12 with

$$\frac{c'_i - c_i}{\Delta t} = -\theta(\frac{F'_{i+\frac{1}{2}} - F'_{i-\frac{1}{2}}}{\Delta x}) - (1-\theta)(\frac{F_{i+\frac{1}{2}} - F_{i-\frac{1}{2}}}{\Delta x}) \tag{14}$$

Expressing F' in a similar way of expression as equation 13, we find equation 15;

$$\frac{c'_i - c_i}{\Delta t} = -\theta(-D_{i+\frac{1}{2}}\frac{c'_{i+1} - c'_i}{\Delta x^2} + D_{i-\frac{1}{2}}\frac{c'_i - c'_{i-1}}{\Delta x^2}) - (1-\theta)(-D_{i+\frac{1}{2}}\frac{c_{i+1} - c_i}{\Delta x^2} + D_{i-\frac{1}{2}}\frac{c_i - c_{i-1}}{\Delta x^2}) \quad (15)$$

To simplify the notation;

$$\alpha_i = \frac{D_{i-\frac{1}{2}}}{\Delta x^2}$$

$$\beta_i = \frac{D_{i+\frac{1}{2}}}{\Delta x^2}$$

$$P_i = -\theta\alpha_i$$

$$Q_i = \theta\alpha_i + \theta\beta_i + \frac{1}{\Delta t}$$

$$R_i = -\theta\beta_i$$

$$S_i = (1-\theta)\alpha_i c_{i-1} + (-(1-\theta)(\alpha_i + \beta_i) + \frac{1}{\Delta t})c_i + (1-\theta)\beta_i c_{i+1}$$

$$P_i c'_{i-1} + Q_i c'_i + R_i c'_{i+!} = S_i \quad (16)$$

It is important to remember that these equations are only being applied for the interior points of the concentration profile. For cells 1 and *N*, different boundary conditions will be used and applied. If we compile these equations into a matrix, we find that we have an almost complete tridiagonal matrix.

$$\begin{bmatrix} ? & ? & 0 & 0 & 0 & 0 & 0 & 0 \\ P_2 & Q_2 & R_2 & 0 & 0 & 0 & 0 & 0 \\ 0 & P_3 & Q_3 & R_3 & 0 & 0 & 0 & 0 \\ 0 & 0 & \ddots & \ddots & \ddots & 0 & 0 & 0 \\ 0 & 0 & 0 & P_i & Q_i & R_i & 0 & 0 \\ 0 & 0 & 0 & 0 & \ddots & \ddots & \ddots & 0 \\ 0 & 0 & 0 & 0 & 0 & P_{N-1} & Q_{N-1} & R_{N-1} \\ 0 & 0 & 0 & 0 & 0 & 0 & ? & ? \end{bmatrix} \times \begin{bmatrix} c'_1 \\ c'_2 \\ c'_3 \\ \vdots \\ c'_i \\ \vdots \\ c'_{N-1} \\ c'_N \end{bmatrix} = \begin{bmatrix} S_1 \\ S_2 \\ S_3 \\ \vdots \\ S_i \\ \vdots \\ S_{N-1} \\ S_N \end{bmatrix} \tag{17}$$

To complete the matrix equation, we must consider the boundary conditions. The boundary condition used in the model is one of specified concentration. A concentration is specified, and the program uses a linear extrapolation between c'_2 and the specified concentration to solve for c'_1. c_L is the specified concentration at the left boundary.

$$\frac{c'_1 - c_L}{x_1 - x_L} = \frac{c'_2 - c_L}{x_2 - x_L} \tag{18}$$

$$Q_1 = \frac{1}{x_1 - x_L}$$

$$R_1 = \frac{-1}{x_2 - x_L}$$

$$S_1 = C_L\left(\frac{1}{x_1 - x_L} - \frac{1}{x_2 - x_L}\right)$$

$$Q_1 c'_1 + R_1 c'_1 = S_1 \tag{19}$$

Similarly, we can arrive for the boundary condition on the right, where c_R is the specified concentration at the right boundary.

$$\frac{c'_N - c_R}{x_R - x_N} = \frac{c'_{N-1} - c_R}{x_R - x_{N-1}} \tag{20}$$

$$P_N = \frac{-1}{x_R - x_{N-1}}$$

$$Q_N = \frac{1}{x_R - x_N}$$

$$S_N = C_R\left(\frac{1}{x_R - x_N} - \frac{1}{x_R - x_{N-1}}\right)$$

$$P_N c'_{N-1} + Q_N c'_N = S_N \tag{21}$$

By using the coefficients from these boundary conditions, we now have a completed tridiagonal matrix equation. We do this by attempting to satisfy equation 22 for values of *i* between one and *N*-1, and by setting equations 23 and 24.

$$c'_i + X_i c'_{i+1} = Y_i \tag{22}$$

$$X_1 = \frac{R_1}{Q_1} \tag{23}$$

$$Y_1 = \frac{S_1}{Q_1} \tag{24}$$

Matrix algebra yields equations 25 and 26, for values of *I* between 2 and *N*.

$$X_i = \frac{R_i}{Q_i - P_i X_{i-1}} \tag{25}$$

$$Y_i = \frac{S_i - P_i Y_{i-1}}{Q_i - P_i X_{i-1}} \tag{26}$$

After solving through each row of the matrix, we solve for c'_N, which is equal to Y_N. We then use this to substitute backwards in equation 22, solving for *c'* along the way. After solving for all c'_i, these are then treated as c_i and the process is repeated to solve for the concentration profile at the next time-step. Using equation 2 again, these concentration profiles can then be used to solve for the flux exiting the system from both sides.

Results and Discussion

Concentration profiles were generated to test the validity of the model. Activity was calculated from the experimental data, which was then converted into the number of particles. The diffusion constant was chosen from the literature for the type of metal and the temperature of the coupon in the experiment. The initial concentration was assumed to be constant through the metal.

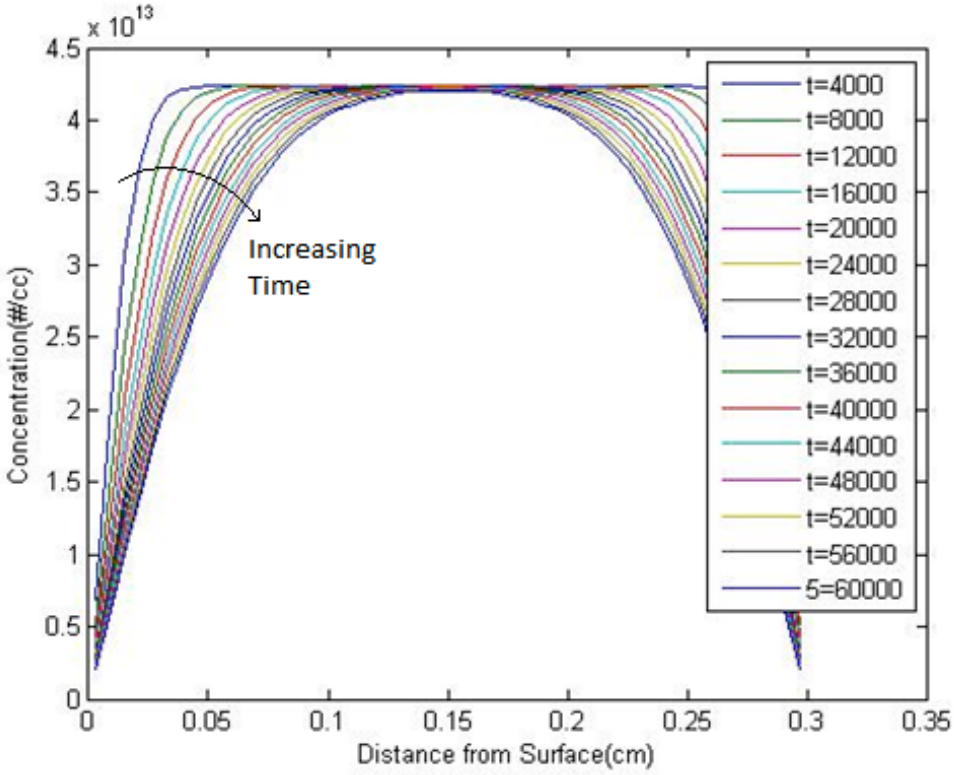

Figure 3. A Series of Concentration Profiles Generated by Model
Plotting concentration vs. distance from surface, the model generated concentration profiles modeling stainless steel at 200°C with constant diffusivity throughout the bulk. The profile develops as expected.

The profile develops according to expectation; as particles move outward the region of large concentration gradient expands inward. This was a test using constant diffusivity throughout the bulk, and therefore did not account for the oxide layer that is known to develop on the surface. The diffusivity through the oxide was chosen to be 20 times larger than the diffusivity through the bulk and another set of concentration profiles were

generated, as can be seen in Figure 4. The actual diffusivity through the oxide is unknown.

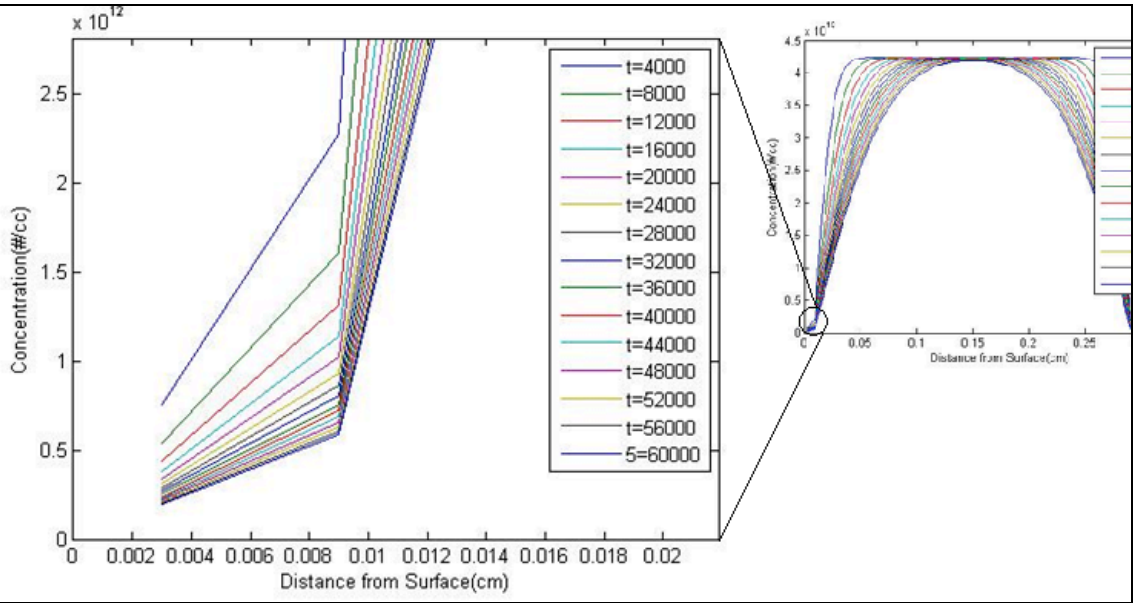

Figure 4. Concentration Profiles Modeling with Oxide
Plotting concentration against distance from the surface, the model shows that an oxide layer with a higher diffusivity than the bulk (20x) would cause a lower concentration gradient in this layer. The thickness of this layer was 90 µm.

Due to the higher diffusivity in the oxide layer, particles are removed at a quicker rate and the concentration gradient is therefore lower, as we see on the graph.

Concentration profiles were then developed at parameters to reflect an experimental run of a stainless steel coupon at 150ºC. The diffusion coefficient in the oxide layer was varied, and the data[(1)], converted from outgassing rate to flux, was compared to the model as seen in Figure 5.

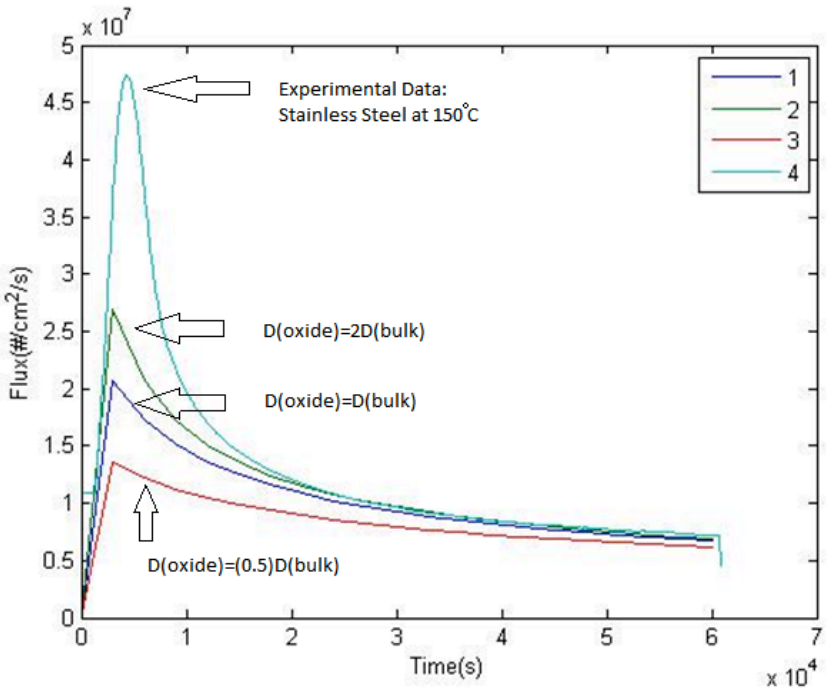

Figure 5. Comparing Model with Experimental Data
Plotting flux against time, the model suggests the outgassing rate is determined by diffusion at later times, but by surface reactions at earlier ones.

The comparison between the data and the model suggests that the outgassing rate of tritium is determined by diffusion at later times, but that the initial peak in outgassing rate is due to surface processes not modelled. The actual concentration profile of a metal coupon is not entirely uniform; within the oxide layers, concentrations actually tend to build to higher levels. The model suggests that this happens within the first 25,000 seconds, and that the outgassing rate is then determined by particles diffusing from the bulk outward. The comparison also seems to suggest that the diffusivity within the oxide layer is at least equal to if not greater than the diffusivity in the bulk; this can be seen by the fact that the models for the higher diffusivities come far closer to accurately modeling the curve.

Summary and Future Work

A numerical model was developed to describe the diffusion of particles through a solid, allowing for three regions of distinct diffusivity. The model suggests that while diffusion through the bulk and oxide is what determines the outgassing rate at later times, surface processes account for the removal of tritium at earlier times. It also suggests that the diffusivity within the oxide layer is at least equal to that of the bulk.

Tritium removal is a three-step process, involving desorption from the surface, diffusion through the bulk, and diffusion through the oxide. The last two have been accurately depicted through this model. Future work would involve extending this model to include equations for the surface processes.

References

1. Ryan Shea, "Tritium Desorption from Stainless Steel Surfaces at Variable Temperatures", 2010 Summer Research Program at the University of Rochester's Laboratory for Laser Energetics
2. Ben Petroski, "Water Desorption from Metallic Surfaces at Room Temperature", 2009 Summer Research Program at the University of Rochester's Laboratory for Laser Energetics
3. Andrew Boyce, "Water Stimulated Tritium Release from Metals", 2011 Summer Research Program at the University of Rochester's Laboratory for Laser Energetics
4. E. L. Cussler, "Diffusion, Mass transfer in Fluid Systems", Cambridge University Press, 2008.
5. R.S.Craxton, Unpublished notes and private communications, 2011

Acknowledgments

I thank Dr. Craxton for allowing me to participate in this truly rewarding program. Furthermore I thank him for providing guidance in formulating the finite difference equations in this model. I thank my advisor, Dr. Shmayda, for his support while I conducted this project. I thank Ben Petroski, Jefferson Lee and Matt Sharpe for their assistance in the project. Lastly, I thank all of my fellow high school students in the program for their support and advice.

Optimization of Beam Configurations for Shock Ignition Experiments on the NIF and OMEGA

Patricia Olson

Brighton High School

Rochester, New York

Adviser: Dr. R. S. Craxton

Laboratory for Laser Energetics

University of Rochester

Rochester, New York

November 2011

1. Abstract

Beam configurations were optimized for shock ignition experiments at both the National Ignition Facility (NIF) and the OMEGA Laser Facility. Shock ignition involves two different laser pulses, one to compress the target, and the other to ignite it. On the NIF, to compensate for the configuration of the laser quads, the beams are repointed towards the equator of the target in a method known as polar drive. The NIF experiment uses 96 out of 192 beams for the compression pulse, and the other 96 for the ignition pulse. The compression beams were optimized to provide a deviation of 3.5 microns, or 0.74% rms in the center of mass radius after implosion through 465 microns. The pointings used for the compression beams can be remapped and scaled to be used for the shock beams. The OMEGA experiment delivers the compression pulse to 40 of the 60 beams, and the shock pulse to the other 20. Adjustments to the compression beams led to an energy deposition uniformity of 1.2% rms, while adjustments to the shock beams resulted in uniformity of 3.9% rms. These results were achieved by running numerous 2-D hydrodynamic simulations using the code *SAGE* in which various parameters were adjusted.

2. Introduction

Nuclear fusion is a possible source for clean, renewable energy. One approach for achieving nuclear fusion is to irradiate a small spherical target made of a glass or plastic shell filled with deuterium and tritium, isotopes of hydrogen, with high power lasers.[1] The outside of the shell ablates outward while the inner part of the shell implodes, compressing the deuterium and tritium gas and causing it to reach an extremely high temperature and pressure. The high temperature of the gas allows the positively charged nuclei to overcome their repulsion forces, and the high pressure ensures a large number of fusion reactions before the target explodes. The deuterium and tritium nuclei fuse to create a helium nucleus and a high energy neutron. These energetic neutrons comprise most of the energy

released by the fusion reactions. If the product of the density of the fuel and the radius of the target is great enough, the energy of the helium nucleus will be deposited in the fuel. This is known as ignition. When ignition occurs, the energy released by the fusion reactions will be greater than the energy input by the lasers, an event known as breakeven. Laser fusion will be useful as an energy source once high energy gain is achieved: when the energy produced is one hundred times the energy put in.

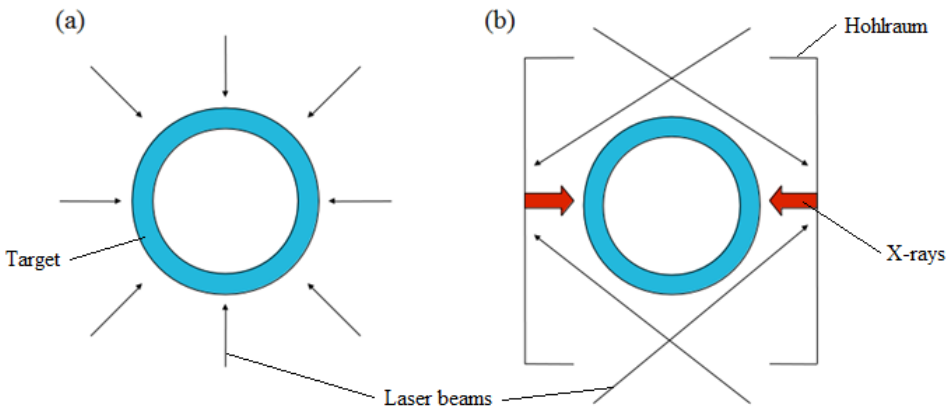

Figure 1: The two main approaches to inertial confinement fusion. (a) Direct drive involves pointing laser beams directly at the target in order to irradiate it. (b) Indirect drive involves pointing the laser beams at the inside of a cylindrical hohlraum, generating X-rays which irradiate the target.

There are two different approaches to laser fusion: direct drive and indirect drive. Direct drive involves pointing laser beams located all around the target at the center of the target so that they hit it at normal incidence [Figure 1(a)]. This is the approach for which the Laboratory for Laser Energetics OMEGA laser is configured. High uniformity is very important to achieving high compression and therefore high energy yields. In indirect drive, the target is surrounded by a hohlraum, a metal cylinder made of gold or another heavy metal [Figure 1(b)]. The laser beams are aimed at the inner walls of the hohlraum, entering through holes at the top and bottom. When the laser beams strike the inside of the hohlraum, they create X-rays which then irradiate the target, compressing it. Nearly all the initial energy from the laser beams is absorbed by the metal of the hohlraum, and nearly 80% is emitted in the

form of X-rays, but only 20% is absorbed by the target. The rest of the energy is lost as the X-rays are absorbed by the walls of the hohlraum or pass through the openings in the top and bottom. Though this method of laser fusion is far less efficient, it may result in more uniform irradiation of the target than is possible in direct drive. The National Ignition Facility (NIF) located at the Lawrence Livermore National Laboratory is configured for indirect drive. The NIF is currently the most powerful laser in the world. It has 192 beams divided into 48 quads, or sets of four beams, that deliver a total energy of 1.8 MJ to the target.

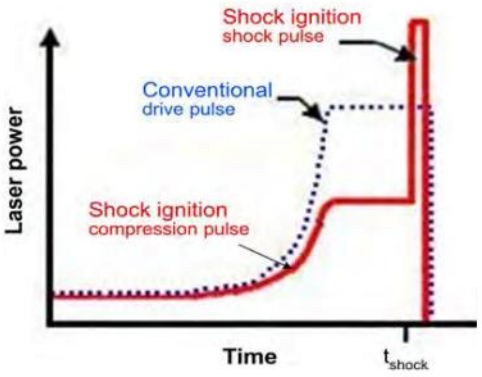

Figure 2: Graph comparing a conventional drive pulse and the compression and shock pulses of shock ignition. The dotted line depicts the conventional drive pulse, while the solid line shows the initial compression pulse and the final high power shock pulse.

Shock ignition is a concept for achieving maximum energy gain fusion. Traditional direct drive fusion experiments use a single long, high-intensity laser pulse which simultaneously compresses and ignites the fuel. Shock ignition splits the laser beams into two sets to deliver two pulses, which compress and ignite the fuel in two steps.[2] The first set delivers the compression pulse: a low intensity, long pulse used to compress the target as much as possible. This allows a greater mass of fuel to be compressed without having to reach the high temperature required for ignition. The second set of laser beams delivers the shock pulse: a short, high intensity pulse designed to achieve ignition. Figure 2 compares a traditional drive pulse to the shock pulse design. Experiments on both the NIF and OMEGA are planned to implement shock ignition.

OMEGA has a total of sixty beams which are positioned so that they form the vertices of a

truncated icosahedron. These beams originate from a single beam which is split into three beams, each of which is each split into twenty beams, adding up to the total of sixty beams. It is possible to put a separate pulse into one of the original three beams, creating twenty beams with one pulse shape and forty with another. This makes shock ignition experiments possible. A compression pulse can be delivered by forty of the sixty beams, and the other twenty can be used to deliver a shock pulse, but the sets of forty and twenty beams are not spaced uniformly around the target. If either set of beams were pointed at normal incidence at the target, energy deposition would be extremely non-uniform. The same problem occurs on the NIF, where it is desired to use half the beams for the compression pulse and half for the shock pulse. This is only compounded by the lack of beams at the equator of the target.

The goal of this work was to produce experimental designs for beam orientations to be used in experiments to be performed on both the NIF and OMEGA laser systems. Laser beams were shifted horizontally and vertically to optimize uniformity of energy deposition over the target surface. Optimized designs with high uniformities have been found for both systems that should allow for high energy yields.

3. Experimental Design for the NIF

There are 192 laser beams on the NIF, and laser beam ports are arranged in eight rings around the target, with four rings at angles of 23.5°, 30.0°, 44.5°, and 50.0° from vertical in both the upper and lower hemispheres. These angles allow the beams to hit the inside of the hohlraum at ideal angles. The beams are arranged such that there is a four-fold symmetry azimuthally. Laser beams are arranged in groups of four called quads. There are 48 quads, each occupying a single port in the target chamber. Each beam measures 35 cm by 35 cm square. The NIF was designed with another ring of ports at 77.45° from vertical in each hemisphere for possible future direct drive experiments, but reconfiguring

the laser beams to these ports would be very expensive and time consuming.

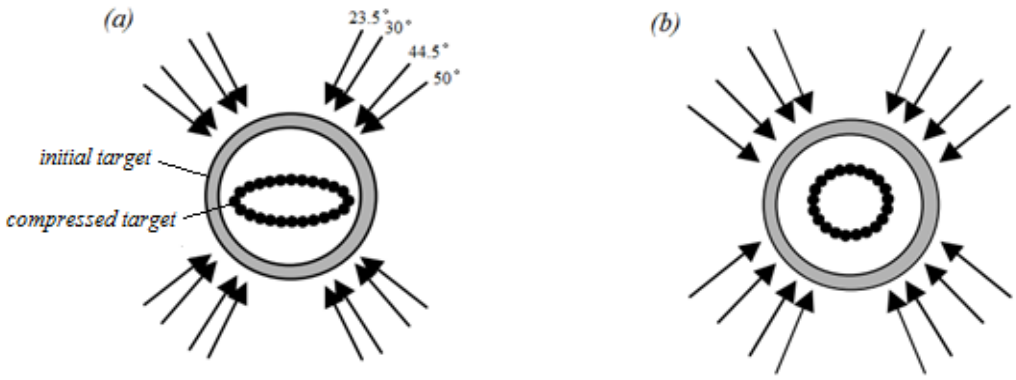

Figure 3: Drive without repointings versus polar drive on the NIF. (a) Pointing the laser beams directly at the center of the target results in very low uniformity of the compressed target. (b) Using polar drive, shifting the beams towards the equator allows for maximum implosion uniformity.

In order to begin direct drive experiments on the NIF as soon as possible, the method of polar drive is being developed. Polar drive was proven to be a viable technique on OMEGA,[3] and it has been explored theoretically for the NIF.[4,5] If the beams are merely aimed at the center of the target, the target will receive much more drive on the poles than at the equator [Figure 3(a)]. The shell velocity at the poles in this scenario would be approximately three times as large as the shell velocity at the equator.[6] If the beams are repositioned towards the equator the target will be driven much more uniformly, and direct drive experiments become possible on the NIF [Figure 3(b)].

Design limitations on the NIF mean that it is impossible to deliver the compression and shock pulses from beams in the same quad. Therefore, quads must be split so that each quad only carries one pulse or the other. In the designs reported in this paper, half of the quads deliver the compression pulse, while the rest are reserved to deliver the shock pulse. Parameters were adjusted in order to achieve maximum uniformity in compression of the target.

The experiment on the NIF implements the two step shock ignition process using polar drive.

Since only half of the quads are to be used for each pulse, not only must the beams be repositioned towards the equator to compensate for the lack of beams in that location, but they must be adjusted azimuthally to compensate for the lower number of beams available to irradiate the target.

Tucker[7] developed an experimental design for the compression beams. Using the two-dimensional hydrodynamics code *SAGE,*[8] she optimized beam pointings azimuthally and in the polar direction, and adjusted other parameters described in Section 3.1 below. Her design, seen in Figure 4, has a uniformity of 1.81% (8.1 microns) rms in center of mass radius after implosion through 465 microns. The goal of this work was to improve upon Tucker's design by continuing to adjust these parameters, taking advantage of increased freedom allowed in development of the experimental design.

The variation in radius of the target from the average radius using Tucker's design can be seen in the profile in Figure 4. Shaded quads represent the locations of the quads used for the compression pulse, while the quads that are not filled in represent the locations of the quads that will eventually be used for the shock pulse. The areas of high and low compression over the target surface follow a clear pattern. Areas of high compression, represented by a gradient from yellow to red, occur mostly in areas close to the quads used for the compression pulse. Areas of low compression, represented by a gradient from green to blue, occur mostly in areas without quads used for the compression pulse. This design is a great improvement over a design with center pointed beams, but it still has areas of non-uniformity, especially near the equator. There is a clear repeating pattern of high and low compression areas on either side of the equator.

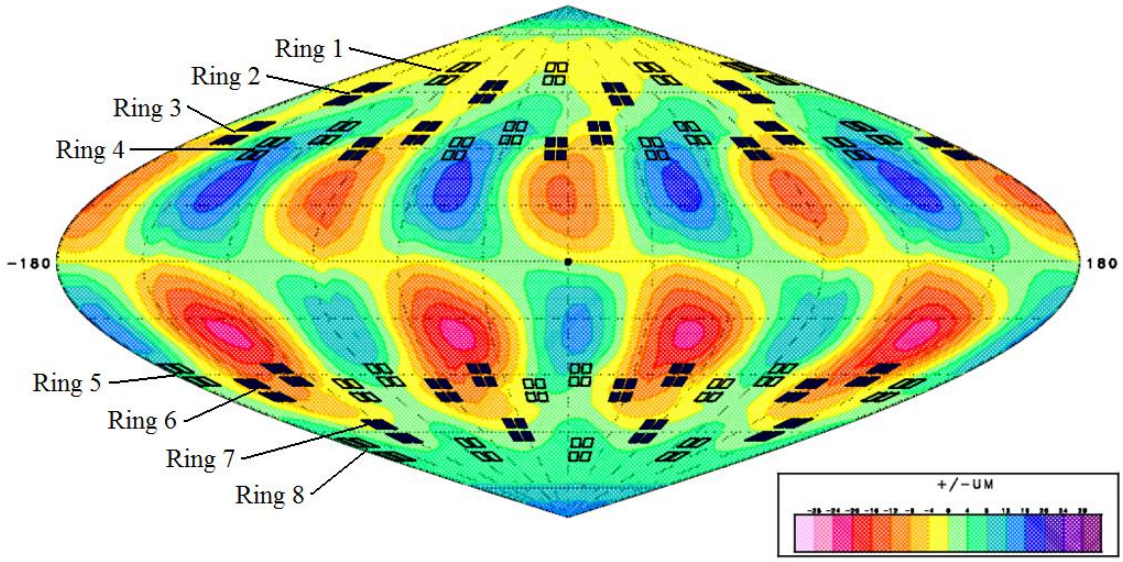

Figure 4: 3-D center of mass profile depicting non-uniformity over the target surface at 4 ns in Tucker's design (Ref. 7). Yellow and red areas represent the locations on the target shell that have a lower than average center of mass radius, while the green and blue areas depict locations with higher than average center of mass radius. The filled in quads represent the beams that are used for the compression pulse. This design had an rms of 1.81%. Beam rings are labeled in the top hemisphere.

3.1. Parameters for Optimization

In order to provide maximum uniformity in target compression, a number of parameters had to be adjusted. Figure 5 shows the optics in the laser system that control beam shift and defocus. Beams are shifted by moving the mirror that reflects the laser beam onto the target. The beam moves a specified distance perpendicular to its axis to cause the center of the beam to hit the target at a different location. Beam spots are defocused by moving the focus lens towards the target. The beam spot on the target increases in size and the maximum intensity decreases. The defocus of the beams must be changed to allow beams to overlap and irradiate the target as uniformly as possible. It is also a way to adjust the relative intensities of the four rings of beams. Indirect drive phase plates, optics used to determine the best-focus laser beam spot size, can be used for polar drive experiments because of defocusing.[8] The defocus increases the size of the beam spots enough that they are suitable for direct

drive despite the smaller size of the indirect drive beam spots.[9]

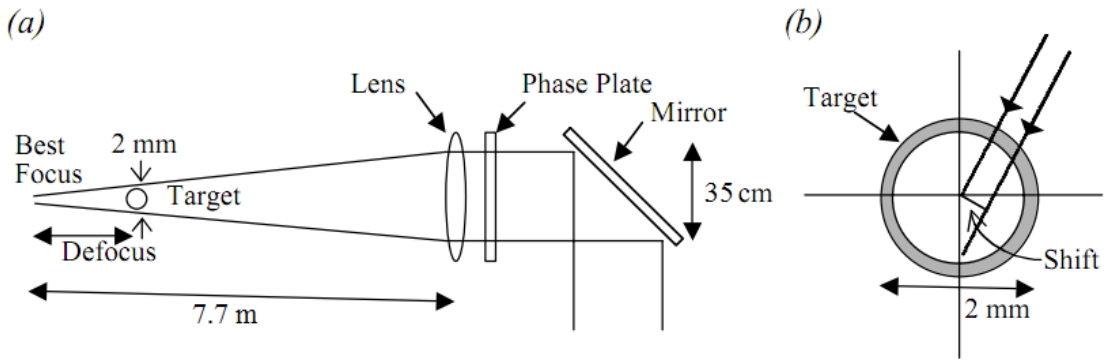

Figure 5: (a) Diagram (not to scale) depicting the components of the NIF laser involved in this work. (b) Diagram showing how beam shifts are measured perpendicular to the direction of the beam. This diagram depicts how a vertical shift is measured. [Ref. 9]

There were twelve different sets of beams in each hemisphere that could be shifted individually in the simulations. Each set of beams contained either four or eight beams spaced around the target surface in a ring. Rings are labeled in Figure 4. In the top hemisphere, there are two sets of beams in Rings 1 and 2 labeled from top to bottom: 1A, 1B, 2A, and 2B. Only beam sets 2A and 2B were used for the compression pulse, and all eight beams in each set were used. In the bottom hemisphere, sets 8A and 8B, corresponding to sets 1A and 1B in the top hemisphere, were used for the compression pulse. The top two beams in each quad (set 2A) could be moved the same amount vertically and horizontally, and the bottom two beams in each quad (set 2B) could be moved the same way. It was possible to choose whether to give each beam pair the same horizontal shift or opposite horizontal shifts [Figure 6]. The optimized design had all beams in set 2A moved one way and all beams in set 2B moved the other way, and included the same shifts in sets 8A and 8B in the bottom hemisphere.

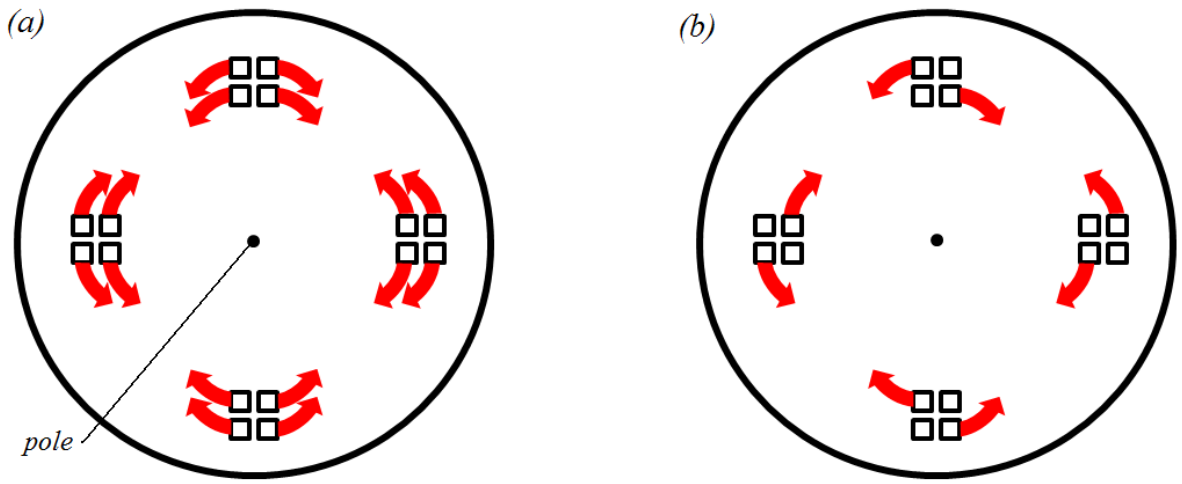

Figure 6: Depiction of two options for beam movement in Ring 2. Beam set 2A comprised of the inner eight beams in each diagram, and beam set 2B is comprised of the outer eight beams. (a) In the first option, beam pairs were moved with opposing horizontal shifts to spread out beam energy. (b) In the second option (and in the optimized design), beam pairs were given the same horizontal shift, but the inner pair was moved clockwise while the outer pair was moved counterclockwise.

There were four sets of beams in Rings 3 and 4, labeled 3A, 3B, 3C, 3D, 4A, 4B, 4C, and 4D. These beam sets can be seen in Figure 7. Each beam in a quad could be moved individually. This freedom was allowed by changes made to the *SAGE* code after Tucker's work. Tucker had the level of freedom shown in Figure 6(a) for every ring of beams. When shifts were given to these pairs of beams, they would always have the same vertical shift and opposite horizontal shifts. Energy from two different beams would often be deposited in the same location, as seen with sets 4B and 3C in Figure 7(a). This explains the pattern of high and low center of mass radii seen around the equator in Tucker's design [Figure 4]. In the optimized design, beams could be moved entirely independently of one another. Figure 7(b) shows how the problem with sets 4B and 3C was corrected using this increased freedom.

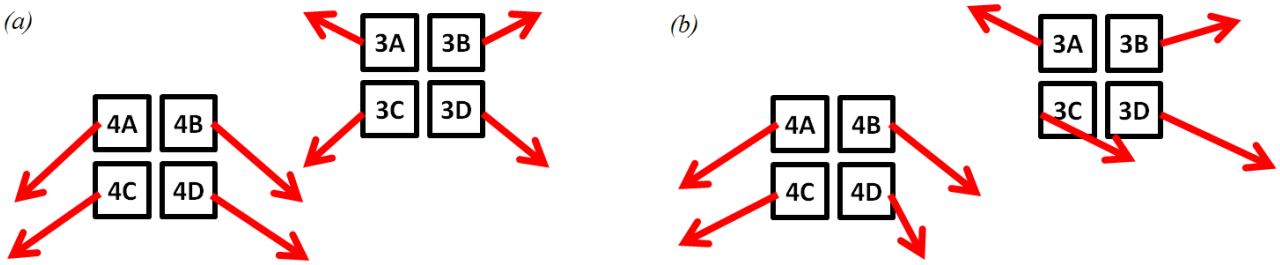

Figure 7: Approximation of beam pointings given to each beam in Rings 3 and 4. Beam sets are labeled. (a) In Tucker's design, beams were moved in pairs with the same vertical shift and opposite horizontal shifts. Note that beams 4B and 3C are shifted towards each other due to the nature of the shifting options, a phenomenon that decreases uniformity. (b) In the optimized design, each beam is given independent vertical and horizontal shifts.

The set of quads used in each ring could be changed. At the poles, it was possible to choose to use Ring 1 in both hemispheres, Ring 2 in both hemispheres, or Ring 1 in one hemisphere and Ring 2 in the other. At the equator, every other quad was taken in each of Rings 3 and 4. However, it was possible to choose which set of quads were taken, providing four different combinations of quad choices at the equator in each hemisphere.

3.2. Optimization Process and Optimized Designs

The goal of the optimization process was to develop a design, using 24 of the 48 of the quads on the NIF, that would result in as uniform an implosion as possible. A large number of 2-D hydrodynamic simulations were run using the code *SAGE* and then analyzed. These simulations used different variations of pointings, defocuses, and quad choices to determine the parameters for the optimum design.

Figure 8(a) shows the pulse that was put into the compression beams. The laser power increases to almost 90 terawatts, and the pulse ends just after 4 ns. Figure 8(b) is a ray trace plot for beam set 4A at 4 ns. The target has imploded from 900 microns to 465 microns. The critical surface can be seen in

this plot as the green contour line. Rays approach the target and deposit most of their energy at the critical surface as they refract away. The center of the beam shown in Figure 8(b) is aimed towards the equator of the target as is required for polar drive. 3-D ray tracing is used in the simulations.

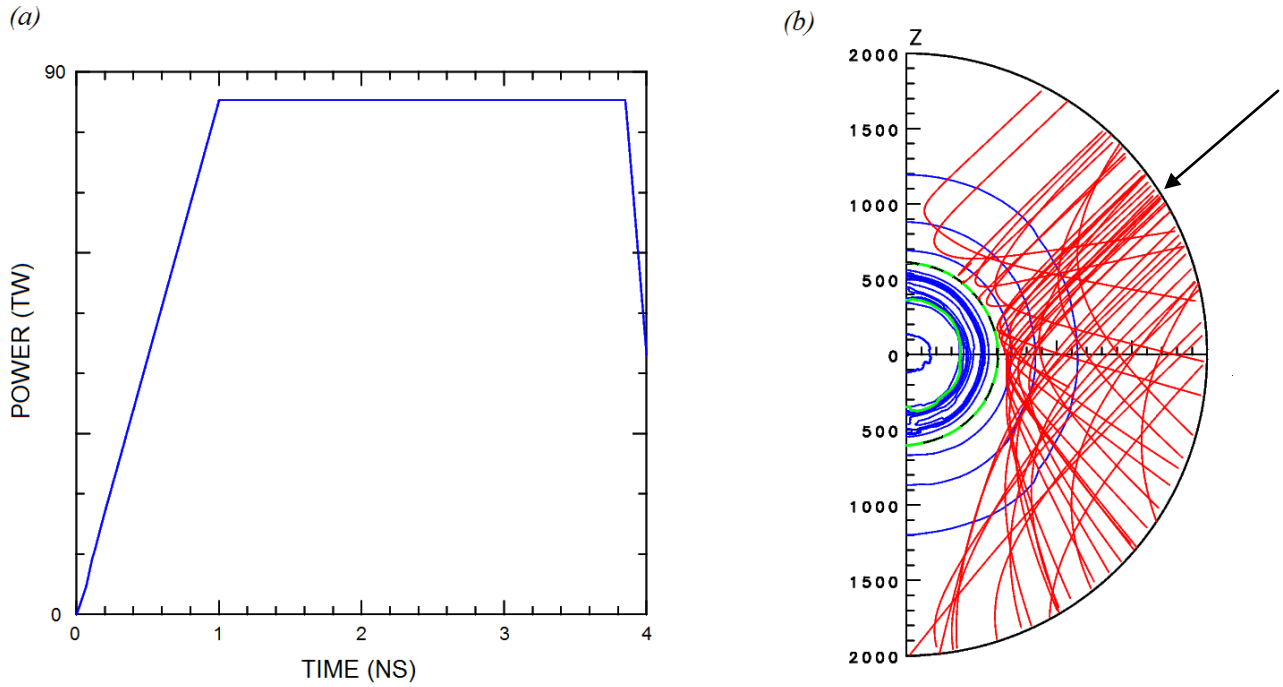

Figure 8: (a) Graph of power versus time of the compression pulse used in the NIF simulations. (b) Ray trace plot of a target after it has imploded from a radius of 900 microns to 465 microns. The critical surface is visible as the green ring. Beams refract away from the target close to the critical surface. The arrow indicates the direction of the laser beam.

Simulations were improved primarily through the use of sinusoidal projections of the target such as Figure 4 in Section 3 above. The effects of beam shifts and quad choice could be clearly seen on a projection depicting deviation in microns from the average center of mass over the target surface.

By adjusting the shifts of the beams and the quads used for the compression pulse, the optimum uniformity was reached. Energy deposition profiles for individual sets of beams, such as the one seen in Figure 9, were used to see where each beam deposits its energy. By comparing the individual energy deposition profile for each of the twenty four sets of beams to the center of mass profile of the target, it

was possible to see which beams were depositing their energy in areas of overcompression and which were depositing their energy in areas of undercompression. Each of the twenty four sets was then shifted simultaneously in the next simulation towards an area of undercompression to improve upon the uniformity of the design. This method of optimization does not follow a step by step progression attempting to improve each beam shift individually. This would have resulted in an optimal beam shift in relation to the position of the other beams, but as soon as the other beams were moved they might affect which areas are the least compressed, meaning that the former optimal position would no longer provide the best uniformity. Changing all the beam shifts simultaneously until no further improvements were made avoided this issue altogether. Once this point was reached, only one or a few of the beams would be moved at a time, sometimes by different amounts in several simulations so that the optimal beam shifts could be found.

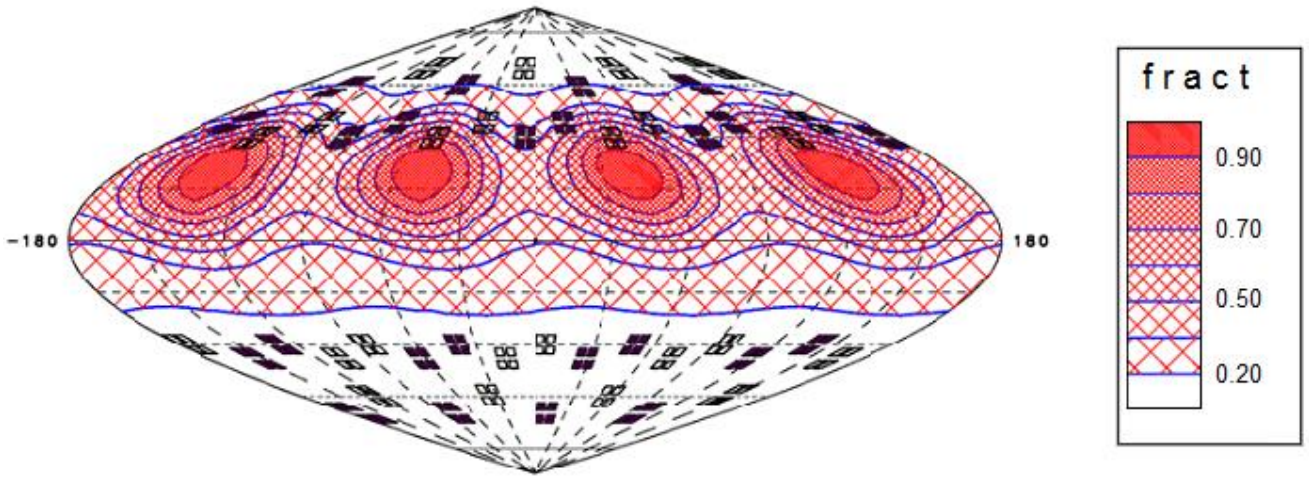

Figure 9: Energy deposition over the target surface by the beams in set 4A.

This method was pursued with several different choices of quads. Tucker's design had different patterns of quad choices in the top and bottom hemispheres. Both hemispheres in her design contained the same x and y shifts, but they were applied to different quad choices. This led to areas of more

significant overcompression in the bottom hemisphere and areas of more significant undercompression in the top hemisphere. Some simulations were run using different x and y pointings in the top and bottom hemispheres and the same quad choices in order to correct these issues. Others used the same patterns of quad choices in the top and bottom. The optimized design used the same quad choices as Tucker's design in the top hemisphere, but used the lowermost ring of beams in the bottom hemisphere, Ring 8 instead of Ring 7, in order to produce patterns in the top and bottom hemispheres that would overlap at the equator with a high uniformity.

The beam defocuses in Tucker's design provided a good level of uniformity without compromising the laser energy absorbed. Only minor changes to the beam defocuses were made.

Figure 10 shows the optimized design, which has an rms of 0.74%, or 3.5 microns, after the target has imploded to 456 microns, over a factor of two lower than the 1.81% rms of Tucker's design. This value is also well below the 1% rms thought to be required for ignition.[1] The parameters for the optimized design are listed in Table 1.

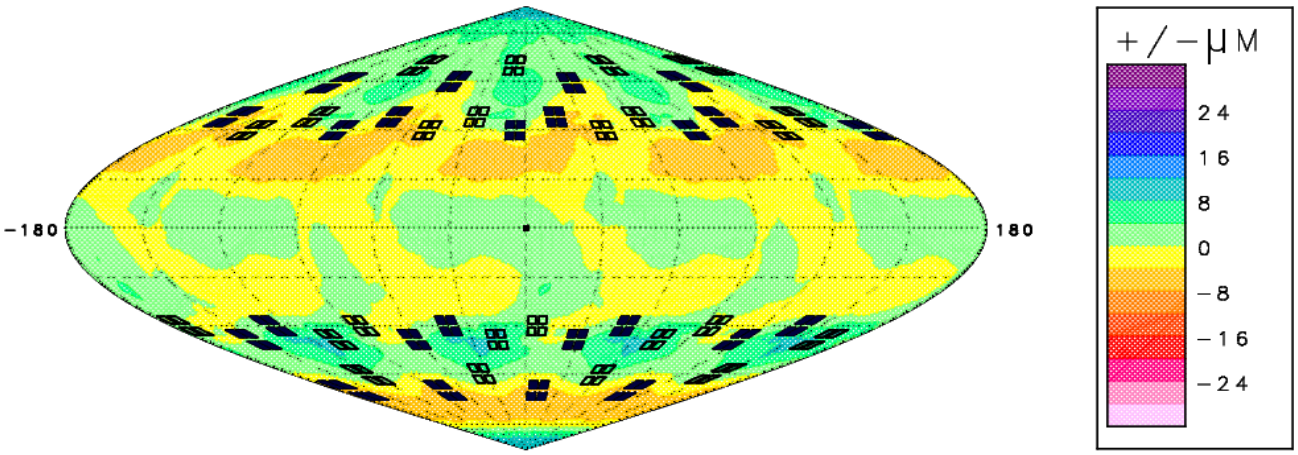

Figure 10: 3-D center of mass profile depicting non-uniformity over the target surface after 4 ns in the optimized design on the same scale as Figure 4. Yellow and orange areas represent lower than average center of mass radii, while green areas represent with higher than average center of mass radii. The non-uniformity in the center of mass has been reduced by a factor of two from Tucker's design, with an rms of 0.74%, or 3.5 microns, after the target has imploded past 435 microns.

This design has the advantage of being usable for the shock beam pointings due to the quad choices in the two hemispheres, namely the use of non-corresponding rings in each hemisphere: Ring 2 in the top hemisphere and Ring 8 in the bottom hemisphere. It is possible to map the parameters from the upper hemisphere for the compression pulse to the lower hemisphere for the shock pulse, and vice versa, and then to scale the pointings used for the compression pulse to the decreased size of the target after 4 ns. This should greatly simplify the development of the overall experimental design.

Set	θ	a, b (microns)	Defocus (cm)	Vertical Shift (microns)	Horizontal Shift (microns)	Number of beams used
1A	21.24	882, 631	–	–	–	0
1B	25.93	882, 631	–	–	–	0
2A	28.01	824, 590	2.9	36	-200	8
2B	32.70	824, 590	2.9	-24	300	8
3A	42.19	635, 367	2.6	182	-350	4
3B	42.19	635, 367	2.6	132	405	4
3C	46.89	635, 367	2.0	-318	270	4
3D	46.89	635, 367	2.0	-342	475	4
4A	47.68	593, 343	1.6	-397	-540	4
4B	47.68	593, 343	1.6	-487	415	4
4C	52.38	593, 343	1.4	-490	-545	4
4D	52.38	593, 343	1.4	-532	120	4

Table 1: Beam parameter specifications for the twelve beam sets in the upper hemisphere of the optimized design. Positive vertical shifts indicate shifts towards the poles, while negative values indicate shifts toward the equator. Positive horizontal shifts indicate rightward shifts, while negative values indicate leftward shifts. The values of a and b indicate the half-intensity focal spot radii of the phase plates currently installed on the NIF.

4. Experimental Designs for OMEGA

Before attempting shock ignition experiments on the NIF, experiments have been performed on OMEGA to investigate shock ignition on a smaller scale.[10] Preliminary experiments using forty beams for the compression pulse and twenty beams for the shock pulse were only partly successful due to non-uniform implosion of the target. To remedy this issue, beam pointing parameters were adjusted in order to increase the uniformity of energy deposition over the target surface. Optimization on OMEGA focused on compensating for the irregular beam arrangement. There was no ability to choose which beams would deliver the pulse due to the design of the laser system.

Figure 11 shows the shape of the laser pulse proposed for future experiments.[10] The lower power pulse is the compression pulse put into the forty beams. The higher power pulse which joins it at 2.6 ns is the shock pulse which is put into the twenty beams. The three pickets that come in the early part of the compression pulse launch shock waves that increase the compression of the target.

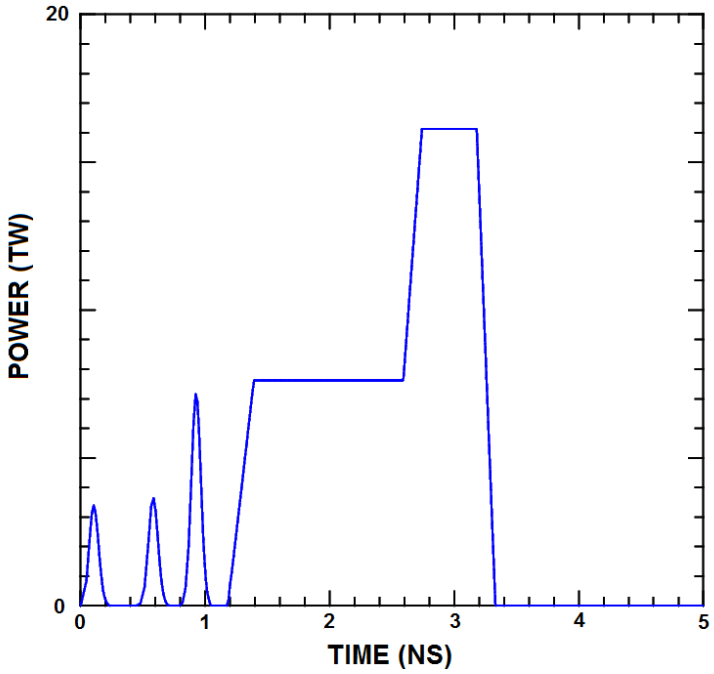

Figure 11: Graph of power versus time of the pulse used for OMEGA simulations. The compression pulse continues until 3.3 ns. The shock pulse turns on at 2.6 ns and ends at the same time as the compression pulse.

4.1. Optimized Design for the Compression Beams

The spacing of the forty compression beams leads to areas of high and low energy deposition. Figure 12 is an energy deposition profile calculated for beam pointing parameters used in preliminary experiments.[11] Shaded circles represent the beams delivering the compression pulse, and unshaded circles represent the beams that deliver the shock pulse later in the experiment. It is clear that there are areas of high and low energy deposition corresponding to areas where there are many compression beams and areas where there are few compression beams, respectively.

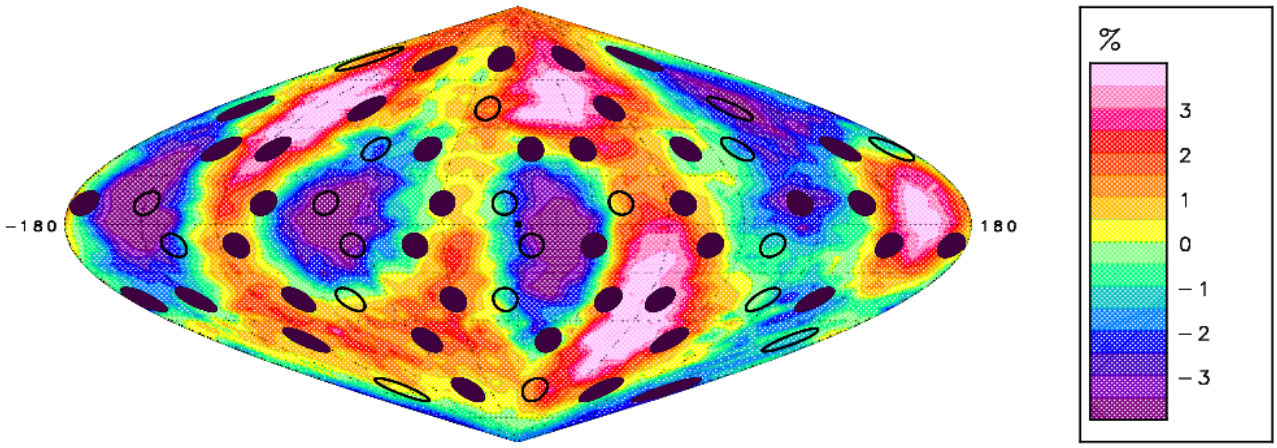

Figure 12: 3-D energy deposition profile showing non-uniformity on the target surface integrated up to 2.5 ns using Gotchev's beam pointings [Ref. 11]. The non-uniformity of the target is 2.11% averaged over the surface of the target. Yellow and pink areas indicate above average energy deposition, while green and purple areas indicate below average energy deposition.

The only parameters available to improve uniformity for the compression beams were beam shifts. These were optimized in much the same way as they were for the NIF design. Adjusting these shifts for OMEGA presented more of a challenge because each of the forty beams had to be shifted individually, rather than in symmetrical rings around the surface of the target. There were eighty different parameters to optimize, two per laser beam. The optimized design is shown in Figure 13. It has a uniformity of 1.19% rms, almost a factor of two better than the previous design.

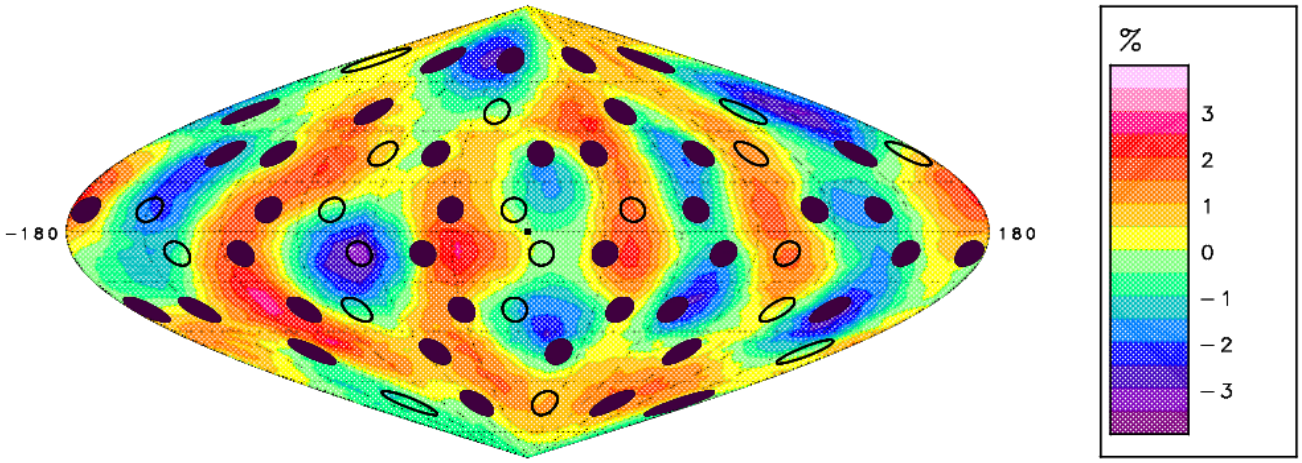

Figure 13: 3-D energy deposition profile showing non-uniformity on the target surface after 2.5 ns in the optimized design for the forty compression beams on OMEGA. This profile is on the same scale as Figure 12.

4.2. Optimized Design for the Shock Beams

The previous design[12] used for the shock beams assumed that pointing each of the twenty beams directly at one of the vertices of a dodecahedron on the initial target surface would be optimum. A simulation run on *SAGE* [Figure 14] showed that this design produced a non-uniformity of 6.7% rms.

The method for optimizing uniformity used for the shock beams was the same as the method used for the forty compression beams, though the smaller number of beams available made optimization more difficult. In areas with a high concentration of beams, such as the group of three beams seen in the center of the target in Figure 14, it was extremely difficult to lower the energy deposition. Similarly, it was extremely difficult to increase energy deposition in areas without many shock pulse beams in the vicinity.

These difficulties achieving uniform energy deposition can be explained by the way energy is deposited as beams travel past the target. Beams do not deposit all their energy in the one spot on the target at which they are pointed; instead they travel through plasma around the target and then refract

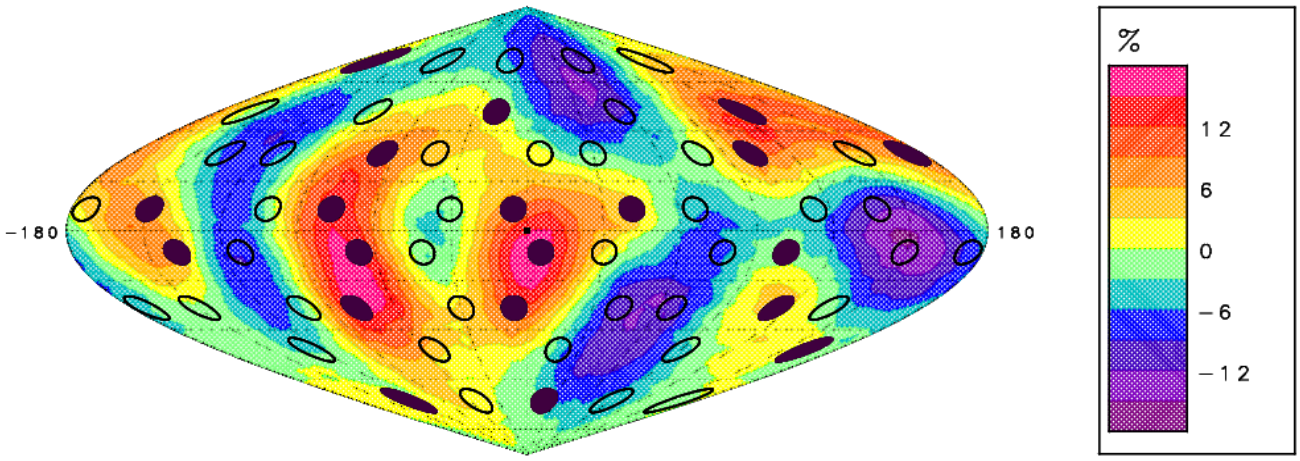

Figure 14: 3-D energy deposition profile showing non-uniformity on the target surface after 4 ns in the previous design for the 20 shock beams on OMEGA. This design has a non-uniformity of 6.7% rms averaged over the target surface. Yellow and pink areas indicate above average energy deposition, while green and purple areas indicate below average energy deposition.

away once they reach the critical surface as shown in Figure 8, with energy being deposited all the while. Beams are also nearly as large as the target, so even when they are shifted to provide greater energy to another part of the target, they still hit the same spot they would if they were pointed at the center of the target. A significant amount of energy is still deposited at that location because the rays at this point on the target are at normal incidence, allowing them to approach much closer to the critical surface and deposit more energy nearer to the center of the target. This makes it impossible to achieve anything but a higher than average energy deposition in these areas without repointing the beams so far that energy absorption by the target greatly decreases.

However, the optimized design did improve significantly upon the initial design. The optimized design can be seen in Figure 15. It has a non-uniformity of 3.9% rms, a significant improvement over the 6.7% rms of the previous design. It is also believed that the uniformity of the shock beams is less significant than for the compression beams since by the time the shock beams turn on, there will be a large plasma surrounding the target. Thermal conduction through the plasma will reduce non-uniformity caused by the shock beams.

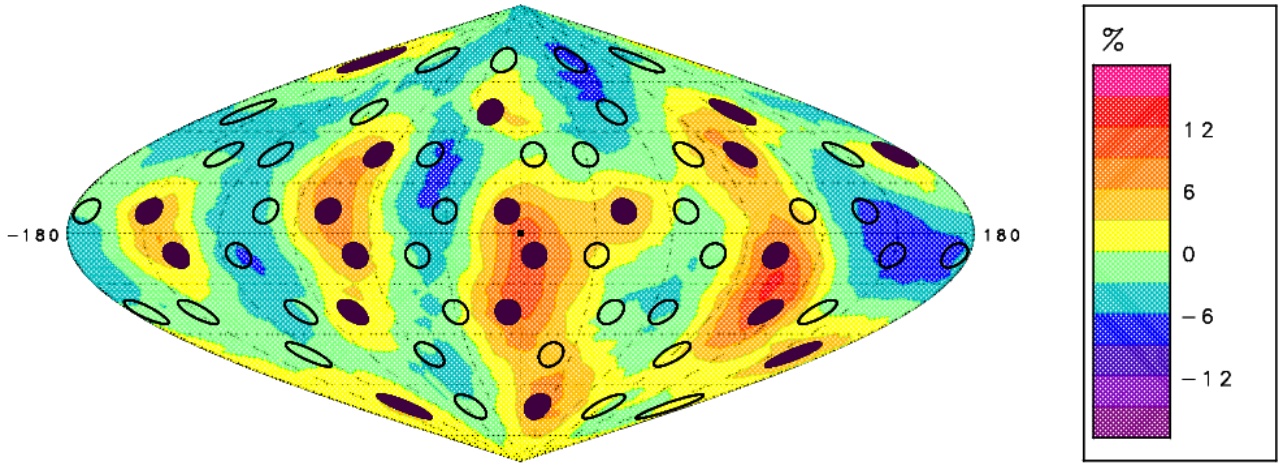

Figure 15: 3-D energy deposition profile showing non-uniformity over the target surface after 4 ns in the optimized design for the 20 shock beams on OMEGA on the same scale as Figure 14. This design has a non-uniformity of 3.9% rms.

5. Conclusion

Designs have been developed for shock ignition experiments on the NIF and OMEGA to provide optimum implosion uniformities. These were designed using 2-D hydrodynamic simulations with 3-D ray tracing. The experiment to be performed on the NIF utilizes polar drive to overcome the indirect drive setup of the laser facility, and the experimental design involves adjusting beam defocuses, quad choices, and beam shifts. The optimized design for the compression beams results in non-uniformity of 0.74% rms, which is more than a two-fold improvement over the previous non-uniformity of 1.81% rms. Due to the choice of configuration of the quads used for the compression pulse, the design can also be used for the shock beams by making some minor adjustments.

For OMEGA, beam shifts are required to account for the irregular arrangement of the forty compression beams and the twenty shock beams to be used in future experiments. The optimized design for the compression beams has a non-uniformity of 1.2% rms, nearly twice as small as the 2.1% rms non-uniformity in the previous design. The optimized design for the shock beams has a non-

uniformity of 3.9% rms, an improvement on the 6.7% rms non-uniformity in the previous design.

Using these designs, it will be possible to test the feasibility of shock ignition in experiments on OMEGA and the NIF.

6. Acknowledgments

I would like to thank Mr. Ted Kinsman for encouraging my interest in physics and encouraging me to apply to this program. I want to thank my parents for supporting me during my application and in my time at the laboratory. I would especially like to thank Dr. R. Stephen Craxton for advising me and for coordinating the program for all the students involved. Thanks also to the Laboratory for Laser Energetics for running the high school summer program.

References

[1] J. Nuckolls et al., "Laser Compression of Matter to Super-High Densities: Thermonuclear (CTR) Applications," Nature **239**, 139 (1972).

[2] R. Betti et al., "Shock Ignition of Thermonuclear Fuel with High Areal Density," Phys. Rev. Lett. **98** (15), 155001 (2007).

[3] R. S. Craxton et al., "Polar Direct Drive: Proof-of-Principle Experiments on OMEGA and Prospects for Ignition on the National Ignition Facility," Phys. Plasmas **12**, 056304 (2005).

[4] J. A. Marozas et al., "Polar-Direct-Drive Simulations and Experiments," Phys. Plasmas **13**, 056311 (2006).

[5] S. Skupsky et al., "Polar Direct Drive on the National Ignition Facility," Phys. Plasma **11**, 2763 (2004).

[6] R. S. Craxton and D. W. Jacobs-Perkins, "The Saturn Target for Polar Direct Drive on the National Ignition Facility," Phys. Rev. Lett. **94**, 095002 (2005).

[7] Laura A. Tucker, "A Design for a Shock Ignition Experiment on the NIF Including 3-D Effects," Laboratory for Laser Energetics High School Summer Research Program (2010).

[8] R. S. Craxton and R. C. McCrory, "Hydrodynamics of Thermal Self-Focusing in Laser Plasmas," J. Appl. Phys. **56**, 108 (1984).

[9] A. M. Cok et al, "Polar-drive designs for optimizing neutron yields on the National Ignition Facility," Phys. Plasmas **15**, 082705 (2008).

[10] K. Anderson, unpublished.

[11] O. Gotchev, unpublished.

[12] W. Theobald, unpublished.

The Use of Surface Grinding and Polishing to Remove Etch Induced Noise Pitting in CR-39 Samples

Sean Reid

Fairport High School

Fairport, NY 14450

Advisors: Michelle Burke, Robert Boni, Dr. Stephen Jacobs

Laboratory for Laser Energetics

University of Rochester

Rochester, NY

Summer 2011

Abstract:

A time-efficient surface grinding and polishing procedure was developed to remove noise pitting associated with the etching of CR-39. CR-39 is a solid-state nuclear track detector used to measure and analyze ions produced by fusion implosions on the OMEGA and OMEGA EP laser systems. Using CR-39 thickness measurements acquired during the grinding process, surface removal rates of 68 μm/min and 5 μm/min were determined for 15-μm and 9-μm-grade abrasive pads, respectively. Removing 3-4 μm of surface material eliminated noise pits, as well as shallow 1-MeV and 2-MeV proton-induced pits. Exposing a CR-39 sample to UV light before etching was investigated as a method to deepen shallow data pits. CR-39 exposure to UV light for 48 hours increased 1-MeV and 2-MeV proton pit depth. The combination of CR-39 UV exposure and surface grinding and polishing was shown to eliminate noise pits while preserving data pits.

Introduction:

CR-39 is a solid-state nuclear track detector used to measure ion yield from OMEGA and OMEGA EP inertial confinement fusion implosions. Charged particles emitted from laser fusion reactions are scattered radially from the target, uniformly striking the CR-39 detector as shown in Figure 1. Ions such as protons, deuterons, tritons, and alpha particles incident on the CR-39 disrupt the polymer's chemical bonds, scattering electrons and forming latent tracks in the material. These tracks are invisible to an optical microscope, and are typically 3 nm to 10 nm in diameter[1].

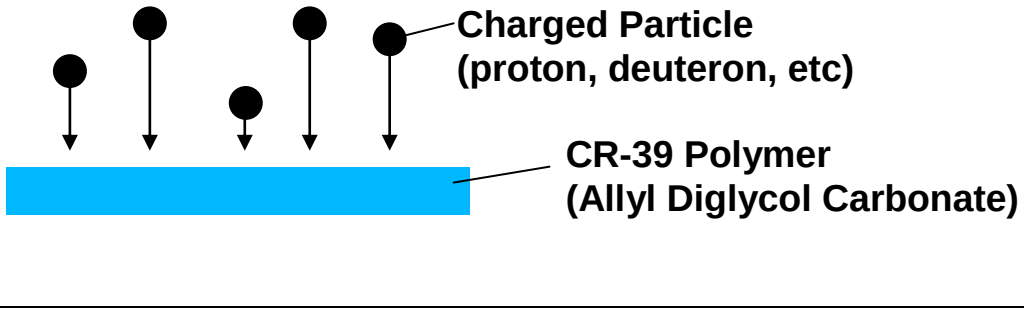

Figure 1:
CR-39 sample detecting ions emitted from inertial confinement fusion. The ions form latent tracks in the CR-39 polymer.

The irradiated CR-39 detector is exposed to a chemical etchant such as sodium hydroxide (NaOH) to establish latent track visibility. The etchant reacts with the polymer bonds of the detector, removing layers of material. The scattered bonds along the latent tracks of the CR-39 detector react faster than the bonds of the bulk material, resulting in conical-shaped pits as shown in Figure 2. These pits typically range from 5-25 μm in diameter, depending on particle type and etching conditions. A standard etch for the purposes of this experiment consists of a 6 hour exposure to 80°C, 6M NaOH.

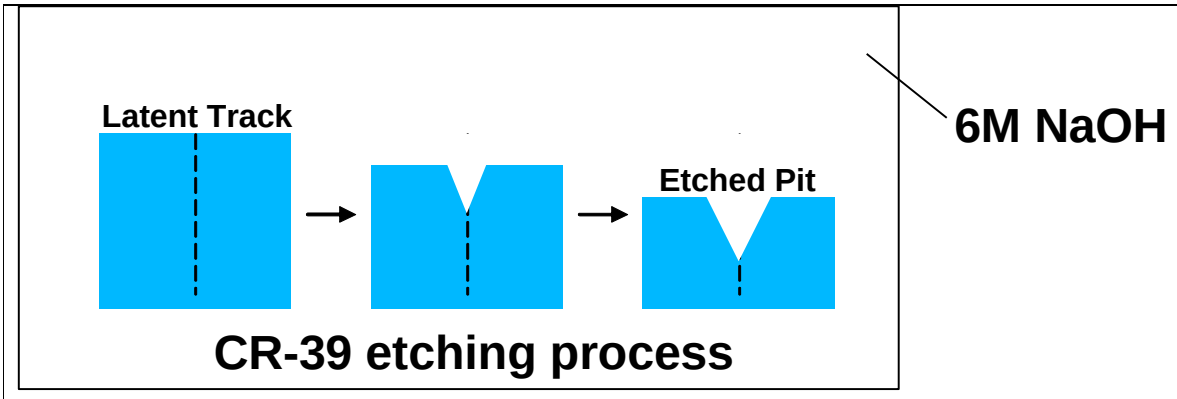

Figure 2:
The CR-39 etching process. NaOH etches along the latent tracks faster than the bulk material, forming visible conical pits.

The CR-39 is then scanned under an digital microscope to calculate ion yield from the etched tracks. A program developed by scientists at the Massachusetts Institute of Technology is used to facilitate this scanning process. The program analyzes images taken of the detector's surface to measure etched pit size and count, using contrast and eccentricity as parameters.

The Laboratory for Laser Energetics receives its shipments of CR-39 from Track Analysis Systems Ltd. Unfortunately, many of these shipments experience a noise pitting effect when exposed to NaOH, such that pitting appears on the CR-39 even in the absence of particle exposure. Other vendors such as Edmund Optics produce CR-39 samples which yield similar noise when etched, supporting the conclusion that noise pitting is not specific to Track Analysis Systems Ltd. Noise pitting differs from particle-induced pitting in formation and structure. It is not a result of particle irradiation, and therefore is not caused by latent particle tracks. Although MIT's scanning program is usually able to differentiate between noise and data, some noise may exhibit a similar contrast and/or eccentricity as charged particle-induced pits when analyzed, as seen in Figure 3.

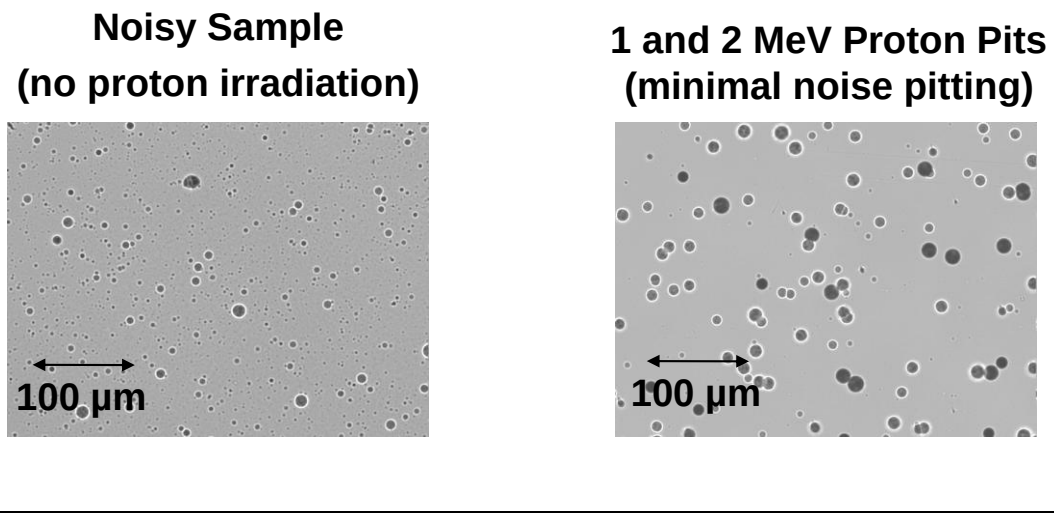

Figure 3:
Images of CR-39 samples at 40x magnification. CR-39 shows noise pitting, on the left, visually similar to data pits, on the right.

CR-39 Grinding and Polishing Procedures:

The majority of noise pitting is characterized by high eccentricity and low contrast, which prompted the CR-39 noise pitting experimental hypothesis that shallow noise pits could be easily ground and polished away while leaving the deeper charged particle induced pits remaining, as graphically represented in Figure 4.

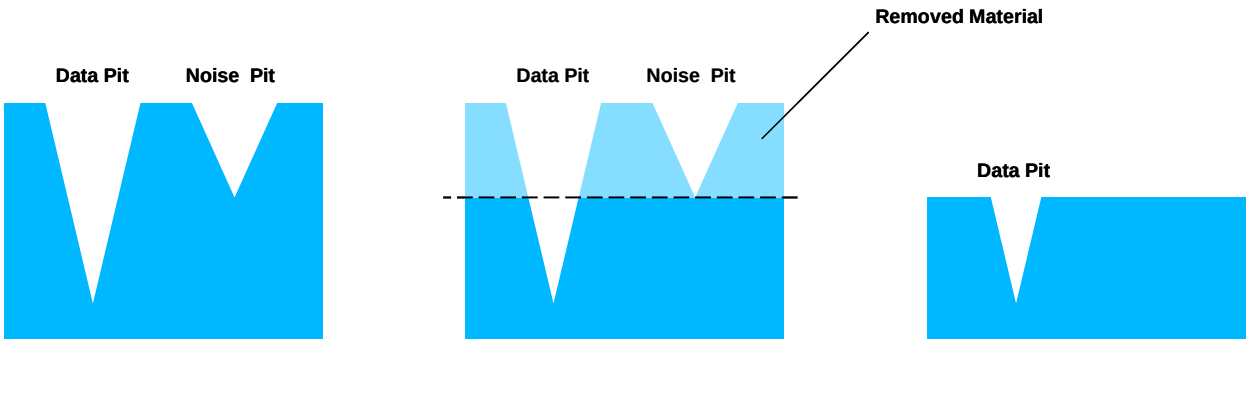

Figure 4:
The grinding and polishing method of noise pit reduction in CR-39. Surface material is removed, eliminating shallow noise pits and leaving deeper data pits.

Three types of abrasive pads were purchased from Universal Photonics Incorporated, for the purposes of grinding and polishing CR-39: a 15-μm rough-grade fixed abrasive pad for bulk removal, a 9-μm fine-grade fixed abrasive pad for surface smoothing, and a velveteen polishing pad to be used with an aluminum oxide solution for further surface smoothing.

A polishing rotating spindle was used to facilitate the grinding and polishing process. The CR-39 is mounted in a custom fabricated aluminum holder, with protective masking tape applied to the mounted side. An abrasive pad is then applied to the polishing spindle using the pad's adhesive backing. The polishing spindle and pad are moistened with water to flush residue during the grinding process; water must be continuously applied during grinding. To grind CR-39 on a moving spindle, the mounted sample is moved circularly on the surface of the abrasive pad, in the opposite direction of rotation of the spindle. The mounted sample is rotated often to create even abrasion.

To develop a time-efficient procedure for the grinding and polishing of CR-39, the grinding and polishing pads were tested for their surface removal rates. Each CR-39 sample used in the surface removal rate experiment was measured in ten invariant locations by a digital micrometer every minute during the grinding and polishing process. The average surface thickness was plotted against time to determine the rate of bulk material removal, as illustrated in Figure 5.

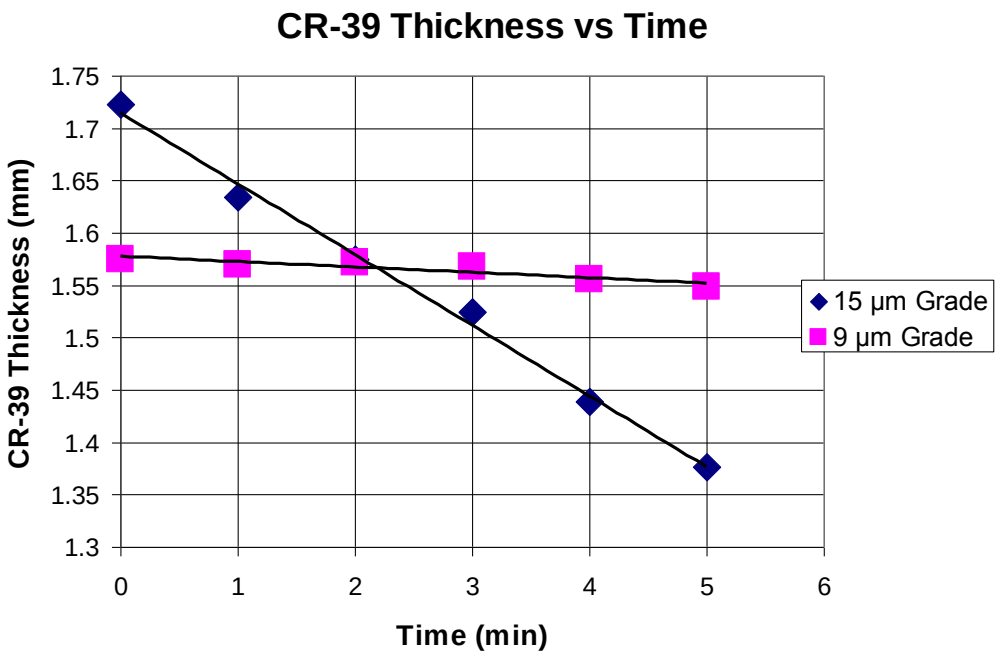

Figure 5:
The thickness of CR-39 samples plotted against time for two different fixed-abrasive pads. The slopes of the graphs represent the rate of surface material removal for the two pads: 5 µm/min for the 9 µm grade pad, 68 µm/min for the 15µm grade pad.

Rates of 68 µm/min and 5 µm/min were determined for the respective 15-µm-grade and 9-µm-grade pads. Due to its high rate of material removal, the 15-µm grade pad was removed entirely from the grinding process. The polishing velveteen with its aluminum oxide solution did not show any measurable rate of material removal, and was therefore not used for bulk removal estimates. Figure 6 shows this graphically.

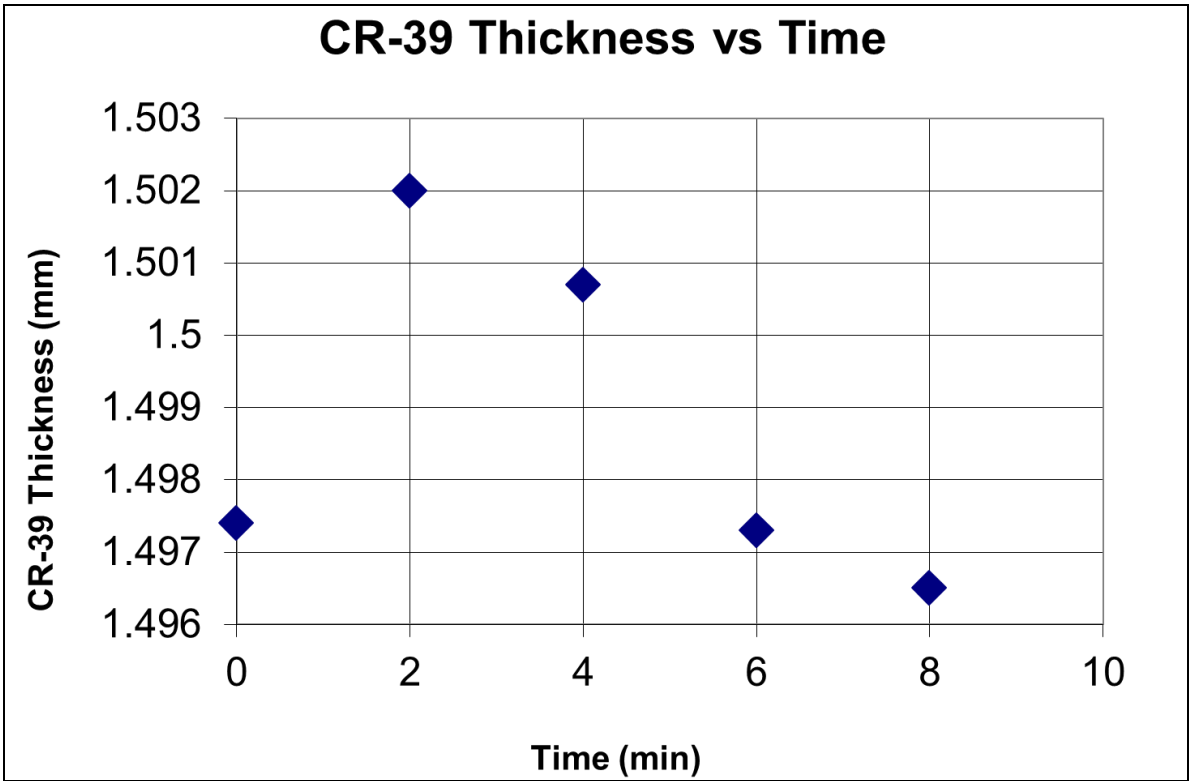

Figure 6:
CR-39 removal using a velveteen polishing pad and aluminum oxide polishing solution. The surface thickness could not be measured with sufficient accuracy to determine the material removal rate.

The order in which CR-39 etching occurs in the grinding and polishing process was also tested. A CR-39 sample was ground, polished, and then etched to determine the effects of CR-39 surface alterations on the etching process. Despite attempts to smooth the surface of the polymer with the polishing pad and solution, small scratches in the CR-39 surface were deepened during the etching process, becoming indistinguishable from noise as seen in Figure 7.

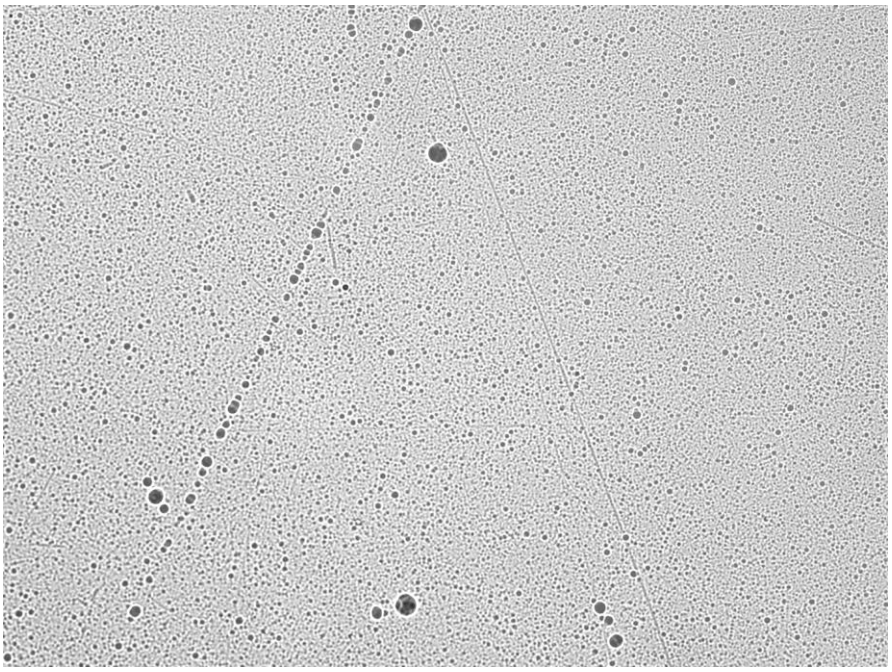

Figure 7:
CR-39 sample etched after grinding and polishing. Scratches and pits left by surface grinding are deepened during the etching process, creating etched noise.

Using the measured removal rates, a time-efficient procedure was developed to grind and polish noisy CR-39 samples. First, the etched sample is mounted in the aluminum holder with protective masking tape. It is ground for 30 seconds on the 9-μm-grade pad and spindle, removing approximately 3-4 μm of bulk material. Then it is moved to the polishing pad, where the surface is smoothed for 6 minutes.

After grinding, the surface of the CR-39 sample is scratched and unable to be scanned. The polishing pad and solution eliminate those scratches. The root-mean-square (RMS) surface roughness was measured every 2 minutes during the polishing process using a NewView 100 white-light interferometer to determine the most efficient polishing time. The results of this experiment are shown in Figure 8; after 6 minutes, the surface was smooth enough to be scanned.

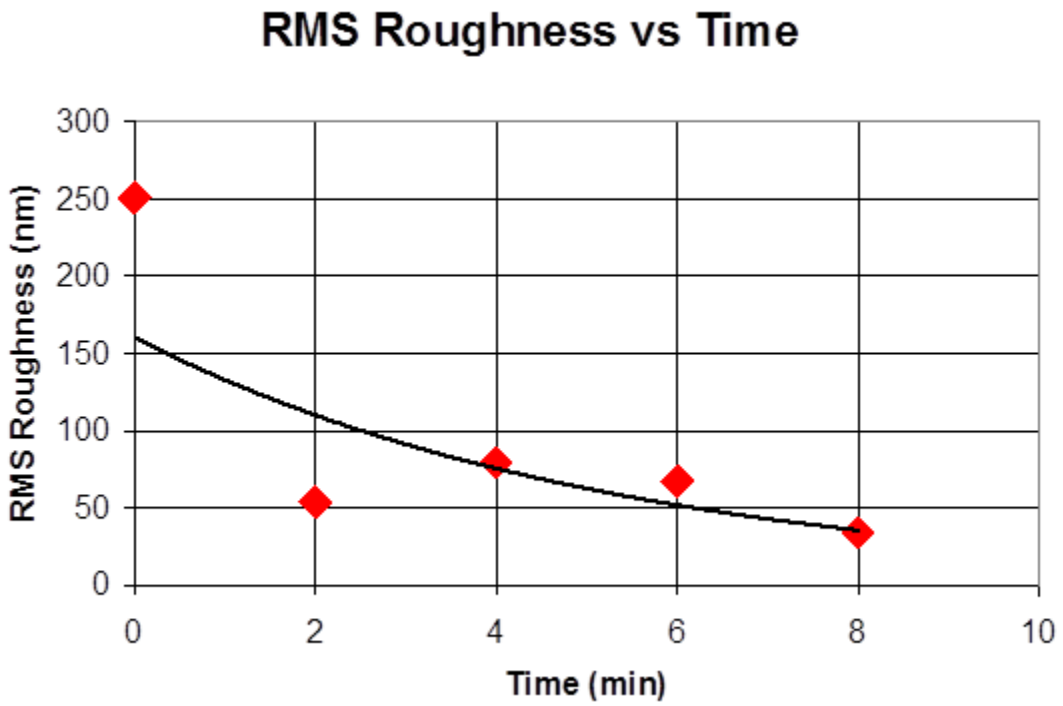

Figure 8:
RMS roughness deviation of a CR-39 sample plotted against polishing time. As the sample approaches the roughness grade of the polishing solution, the RMS roughness plateaus.

Etched CR-39 samples were observed after grinding and polishing, to establish a level of surface material removal that would eliminate noise and preserve the charged particle-induced etched pits. Images from an optical microscope in Figure 9 show that the grinding and polishing procedures remove shallow data pits, as well as noise pits. A method was therefore needed to increase the depth of the etched data pits without affecting noise pits.

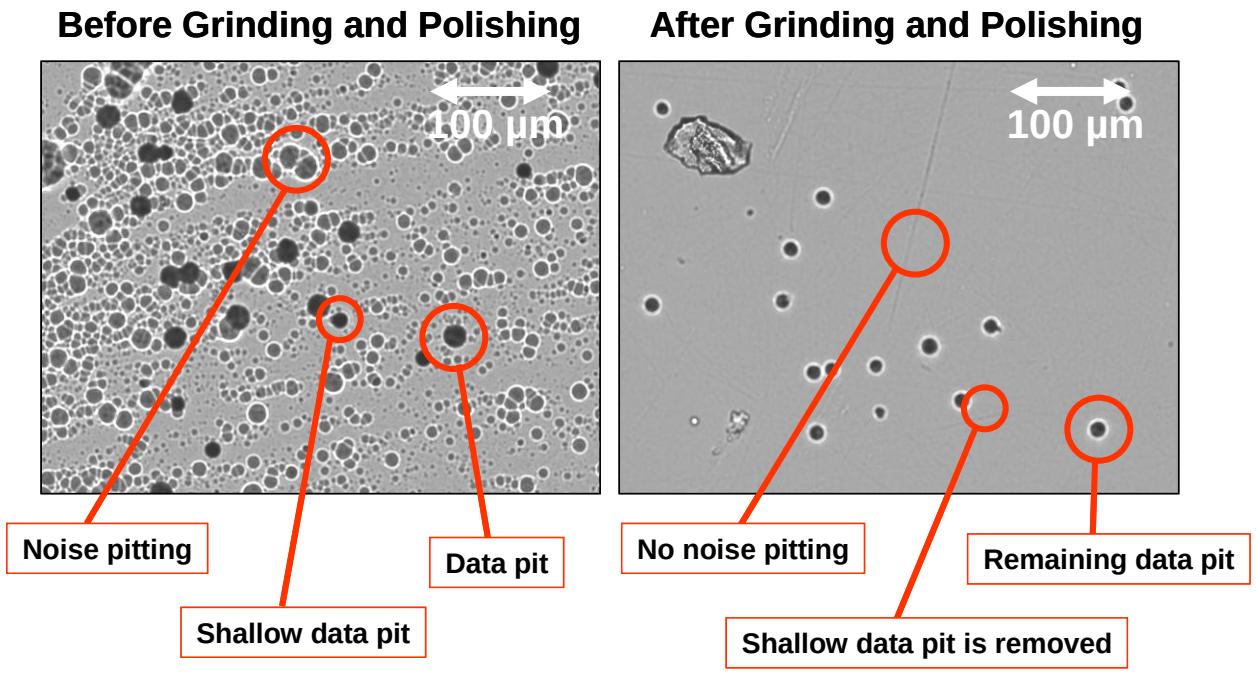

Figure 9:
CR-39 sample imaged at the same coordinates before and after grinding and polishing off 3-4 µm of surface material. Shallow data pits have been eliminated as well as noise pits.

Ultraviolet light exposure techniques:

When a CR-39 sample is etched, the NaOH etchant disrupts chemical bonds at the material surface, as well as along the latent tracks left by charged ions. The rate at which CR-39 is etched along the surface is known as the bulk etch rate. The rate at which material is removed from the latent tracks is called the track etch rate. The ratio of these rates, known as the track-to-bulk etch ratio, determines the resultant pit depth and diameter. Figure 10 shows how the etch ratio affects the pit shape. Exposure of CR-39 to UV irradiation has been confirmed to increase the track to bulk etch ratio of the polymer[2]. UV irradiation incident on a sample disrupts the broken chemical bonds of latent tracks such that, when etched, more track material in proportion to bulk material is etched.

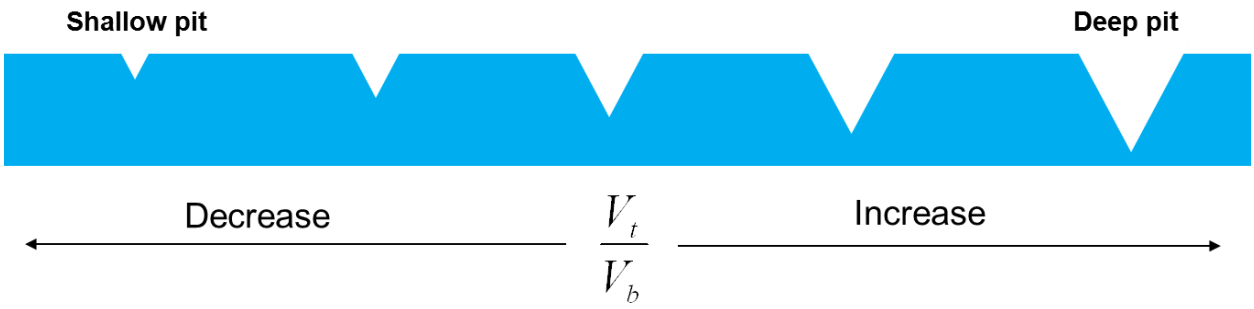

Figure 10:
The effect of the track-to-bulk etch ratio of CR-39 on the etched pit shape. UV exposure increases the track-to-bulk etch ratio, increasing the pit depth and diameter.

UV irradiation was therefore tested as a possible method for increasing the data pit depth and diameter in CR-39, such that data pits would not be removed as a result of grinding and polishing. Three light-emitting sources were tested for their effects on increasing the track-to-bulk etch ratio in CR-39. To optimize UV exposure, UV spectral emission was measured with a spectrometer. The spectra of the three tested sources are represented graphically in Figure 11.

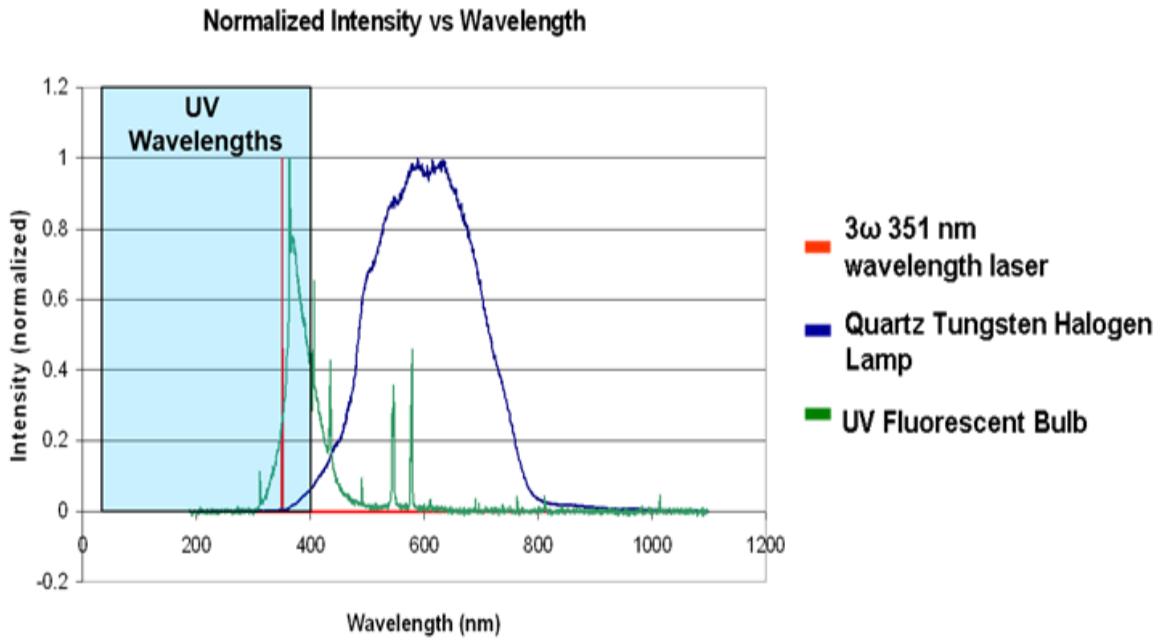

Figure 11:
The full spectral graphs of three tested UV sources, normalized intensity plotted against wavelength. The UV fluorescent bulb shows the broadest UV spectral emission, with 43.3% of its power in the UV spectrum.

A quartz halogen tungsten lamp with a power input of 150 W at 21 V and a power output of 0.87 W was determined to emit only 0.614% of its detected frequencies in the ultraviolet range. When exposed to the halogen source for six hours, alpha particle-induced latent tracks showed only a 10% increase in pit depth after etching. A UV fluorescent bulb array was also tested for its spectral output, and was determined to emit 43.3% of its detected frequencies in the ultraviolet range. As shown in Figure 12, 48 hour exposure to the UV fluorescent bulb array increased 1-MeV proton-induced etched pit diameters by 40.9%, indicating an increase in pit depth as well.

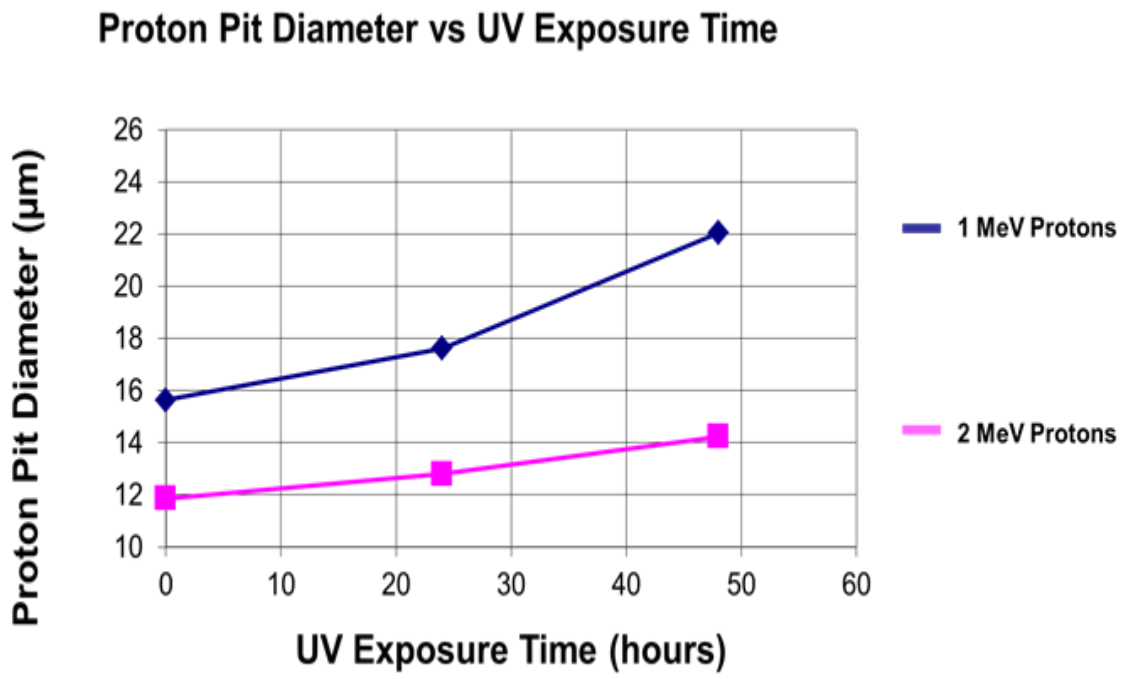

Figure 12:
Proton-induced etched pit diameters as a function of exposure to an ultraviolet bulb array. After 48 hours of exposure and a 6 hour standard etch, 1-MeV proton pits are 40.9% wider in diameter.

To expand upon the success of the UV bulb array, a 3ω 351-nm wavelength laser was tested for its effects on CR-39 etched pits. The 3ω laser was hypothesized to affect CR-39 latent tracks quicker and more efficiently than the UV fluorescent bulb array, due to its controlled, focused emission of a single wavelength of ultraviolet light as shown in Figure 11. However, as shown in Figure 13, CR-39 samples exposed to the 351-nm wavelength laser at intervals of 1, 10, and 100 minutes showed no discernable correlation between alpha particle-induced pit depth and exposure time. This suggests that the wavelength of the 3ω laser, 351nm, is not the optimal wavelength for UV exposure.

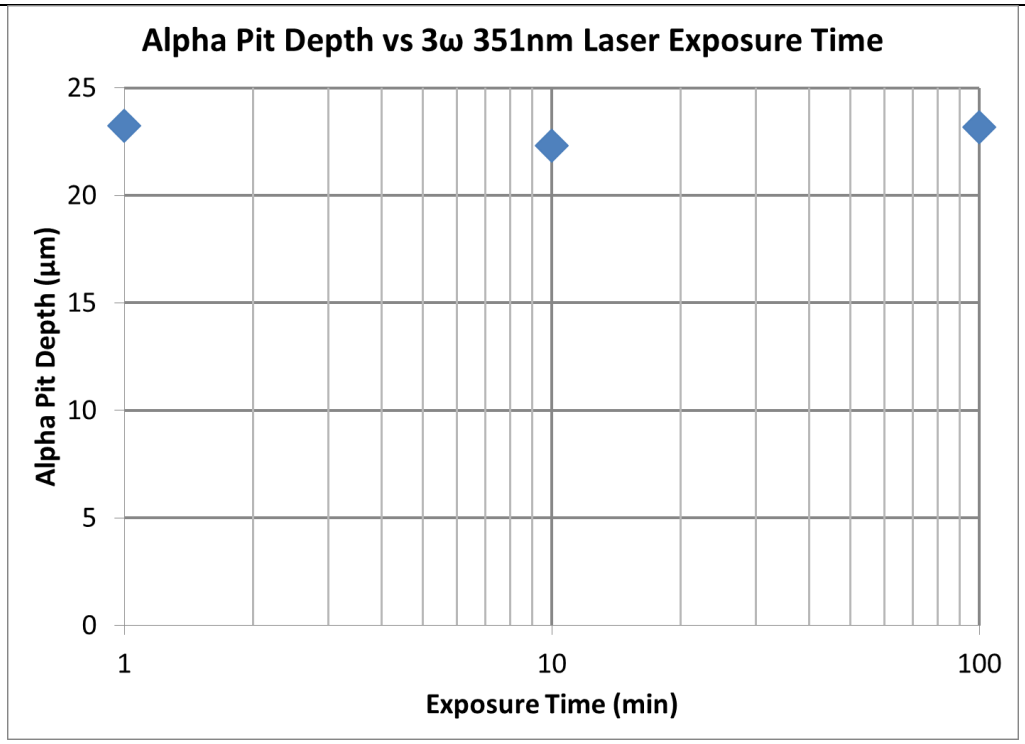

Figure 13:
Alpha particle-induced etched pit depth plotted against 3ω UV laser exposure time, with a logarithmic x-axis scale. The control CR-39 sample with 0 minutes of UV exposure had etched alpha pits averaging 22.5 µm in depth. As the pit depth remained relatively constant throughout each trial, it was concluded that there is no correlation between 351-nm wavelength UV and etched pit depth.

It was hypothesized that a wavelength exists at which the scattered particles in the latent tracks of CR-39 would resonate, such that the etching process would produce deeper, wider pits. The broad-spectrum halogen lamp did not include enough UV intensity in its spectrum to feasibly affect pit depth and diameter. The broad-spectrum UV bulb array included this wavelength in its spectrum, and therefore increased the resulting pit depth and diameter. Despite its high-powered UV emission, the 3ω UV laser did not emit the correct wavelength to create a discernable effect. Future experimentation, as shown in Figure 14, will determine the optimal wavelength for UV exposure. A broadband UV source will be refracted through a prism and onto an exposed sample of CR-39. Due to the refractive properties of the prism, the wavelength of light incident on

the sample will change with position. When etched, the position of the deepest pits on the sample will correspond to the optimal wavelength for UV exposure.

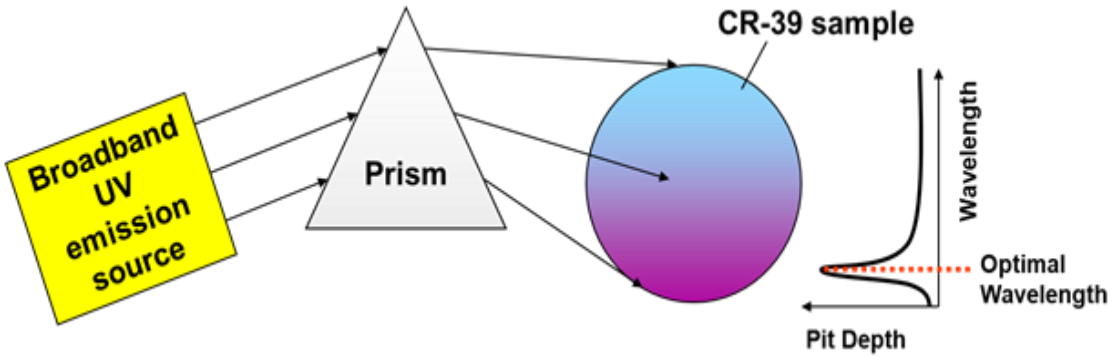

Figure 14:
Future schematic for optimization of UV exposure of CR-39. A broad spectrum of UV light is refracted through a prism such that the wavelength of light incident on a CR-39 sample will change with position. After etching, the deepest pits will correspond to the optimal wavelength.

Application of UV exposure:

A noisy CR-39 sample which had been irradiated with 1-MeV and 2-MeV protons was exposed to UV light for 24 hours from the UV fluorescent bulb array. This sample was etched under standard conditions, and successively ground and polished for 30 seconds and 6 minutes, respectively. To test the application of CR-39 UV exposure to the optimized noise removal process, the sample was imaged at the same place before and after grinding and polishing. As shown in Figure 15, most of the proton pits remain after grinding and polishing, indicating that UV exposure is valid as a technique to increase proton pit depth.

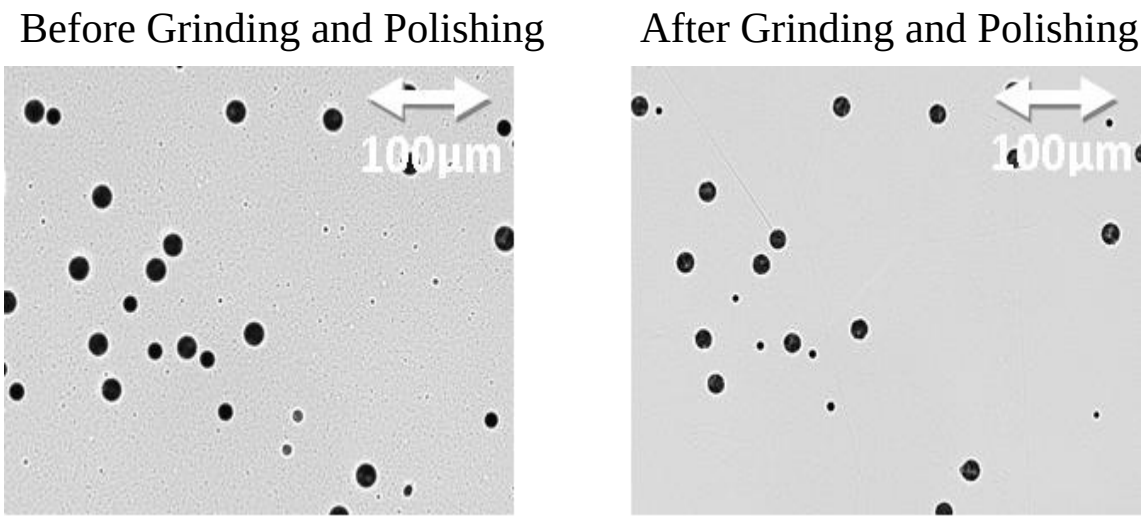

Figure 15:
Images of a CR-39 sample taken at 40x magnification before and after grinding and polishing. The sample was exposed for 24 hours under a UV fluorescent bulb to increase the pit depth. The majority of proton-induced data pits remain as a result.

Conclusions:

Grinding and polishing procedures were tested and confirmed as a feasible method to reduce noise in CR-39 diagnostics. The grinding and polishing process was established to remove noise pits in etched samples; unfortunately, the procedure also removed shallow data pits. To deepen the shallow data pits without affecting noise pits, UV exposure of CR-39 was investigated. When exposed to a broad-spectrum UV bulb array for 48 hours, CR-39 exhibited a 40.9% increase in 1-MeV proton pit diameter, indicating an increase in depth due to UV light. Future investigation of UV exposure will determine the optimal laser wavelength to increase data pit depth; the broad-band UV source is very inefficient. The time-efficient grinding and polishing process was used on a noisy CR-39 sample which had been exposed to 24 hours of broadband UV light; the noise was eliminated and most of the data pits remained. This confirms UV irradiation,

grinding, and polishing as a viable set of procedures to remove etch-induced noise pitting in CR-39 samples.

Acknowledgements:

I would like to express my gratitude to my advisor Michelle Burke for her persistent enthusiasm and support. Also, I would like to thank Robert Boni, Joe Katz, and Dr. Stephen Jacobs for their invaluable insight and guidance. Finally, I would like to thank Program Director Dr. Stephen Craxton for providing this unique research opportunity.

References:

[1] Hicks, Damien G. Charged Particle Spectroscopy: A New Window on Inertial Fusion. Ph. D. thesis, Massachusetts Institute of Technology (1999).

[2] Z. Arif, M. Saiyid-Uz-Zafar, G. Hussain, H. A. Khan, K. Jamil, I. M. Siddiqui. "Improvement in the sensitization of the plastic track detectors by ultraviolet irradiations." International Journal of Radiation Applications and Instrumentation (1985).

Abrasion Resistant Anti-Reflective Sol-Gel Coatings

Madeline Rutan
Penfield High School

Advisor: Kenneth L. Marshall

University of Rochester
Laboratory for Laser Energetics
Summer High School Research Program 2011

Abstract:

Anti-reflective sol-gel coatings are deposited on many of the optical surfaces in both the OMEGA and OMEGA EP laser systems. These coatings are responsible for yielding the maximum transmission of UV light as it passes from air into the glass optics. One issue with these coatings resides in their lack of abrasion resistance. An unmodified sol-gel coating will be scratched if subjected to a very small mass dragged across its surface (~ 6 g), making it necessary to handle optics containing these coatings with extreme caution during installation and alignment.

In an effort to increase the abrasion resistance of sol-gel coatings, organosilane modified sol-gel particles have been crosslinked with dithiols. This process increases abrasion resistance because the dithiol crosslinkers bond sol-gel particles to each other and to the coated substrate, resulting in a robust sol-gel network that can withstand greater abrasive forces. The most promising results have been demonstrated using a 15 mol% solution of the organosilane modifier 3-methacryloxypropyltriethoxysilane (MOTOS) in combination with the crosslinker pentanedithiol. A substrate coated with this solution demonstrated little to no damage after a mass of 36 g was dragged across its surface (simulating abrasive forces that the coating may endure during handling) while maintaining 96% transmission. A reduction in transmission of the coating was observed with increasing abrasion resistance

Introduction:

Optics in the OMEGA and OMEGA EP laser systems rely on sol-gel coatings to reduce transmission losses. Each time that the laser beam comes in contact with an air-glass interface, there is the opportunity for losses in transmission (called Fresnel losses) due to the difference in refractive indices of the air and glass**.** Fresnel loss accounts for roughly a 4% transmission loss for each air/substrate

interface. By depositing a coating on the substrate surfaces, the difference in refractive indices between the coating and the air is decreased, which helps to maintain maximum transmission. For a given wavelength range of light, the optimum refractive index of the coating is equal to the square root of that of the glass [(1)]. For the substrates used in this work, the glass has an index of refraction of 1.51, and therefore, the coating should have a refractive index of 1.26. While sol-gel coatings based on tetraethyl-orthosilicate (TEOS) have proven effective in maintaining high transmission, they are easily damaged through incidental, frictional contact with masses of only 6 g. To increase abrasion resistance, experiments involving the chemical modification of sol-gel coatings with organosilanes and crosslinking with dithiols have been performed. The chemical modification and crosslinking within the coating produces a robust network of bonds. This network provides for an increase in abrasion resistance because the crosslinked bonds not only join the particles to each other, but also help to adhere the coating to the glass substrate. A standard alkoxysilane, tetraethyl orthosilicate (TEOS), is used to create the sol-gel through a condensation reaction that is triggered by the presence of a base catalyst (ammonium hydroxide).

In previous work, difunctional aldehydes, specifically glyoxal and glutaraldehyde, were used as cross-linking agents to improve the abrasion resistance of TEOS-based sol-gel coatings [(2)]. The advantage of using organosilane modifiers and dithiol crosslinking agents resides in the ability to conduct the crosslinking reaction by UV irradiation at room temperature. Glyoxal and glutaraldehyde both require a 90 min baking cycle at 130˚ C to initiate crosslinking.

Experimental

To prepare the standard, unmodified sol gel solution, 23 mL of TEOS is mixed into 220 mL of ethanol and stirred constantly at room temperature. Water from the atmosphere triggers a hydrolysis reaction in the solution and ethanol is liberated from the TEOS leaving silicon with four hydroxyl groups. [(2,3)] This solution undergoes a base catalyzed polycondensation reaction once 7 mL of ammonium

hydroxide are added. The polycondensation reaction results in the formation of silica oxide (SiO_2) particles, which continue to grow in diameter as the solution ages for one week. This reaction continues until the ammonia in solution is refluxed out of the system at the conclusion of the week. At this point, the SiO_2 particles have grown to 20 nm and are left suspended as a colloid in the ethanol solution. Figure. 1 shows this series of reactions.

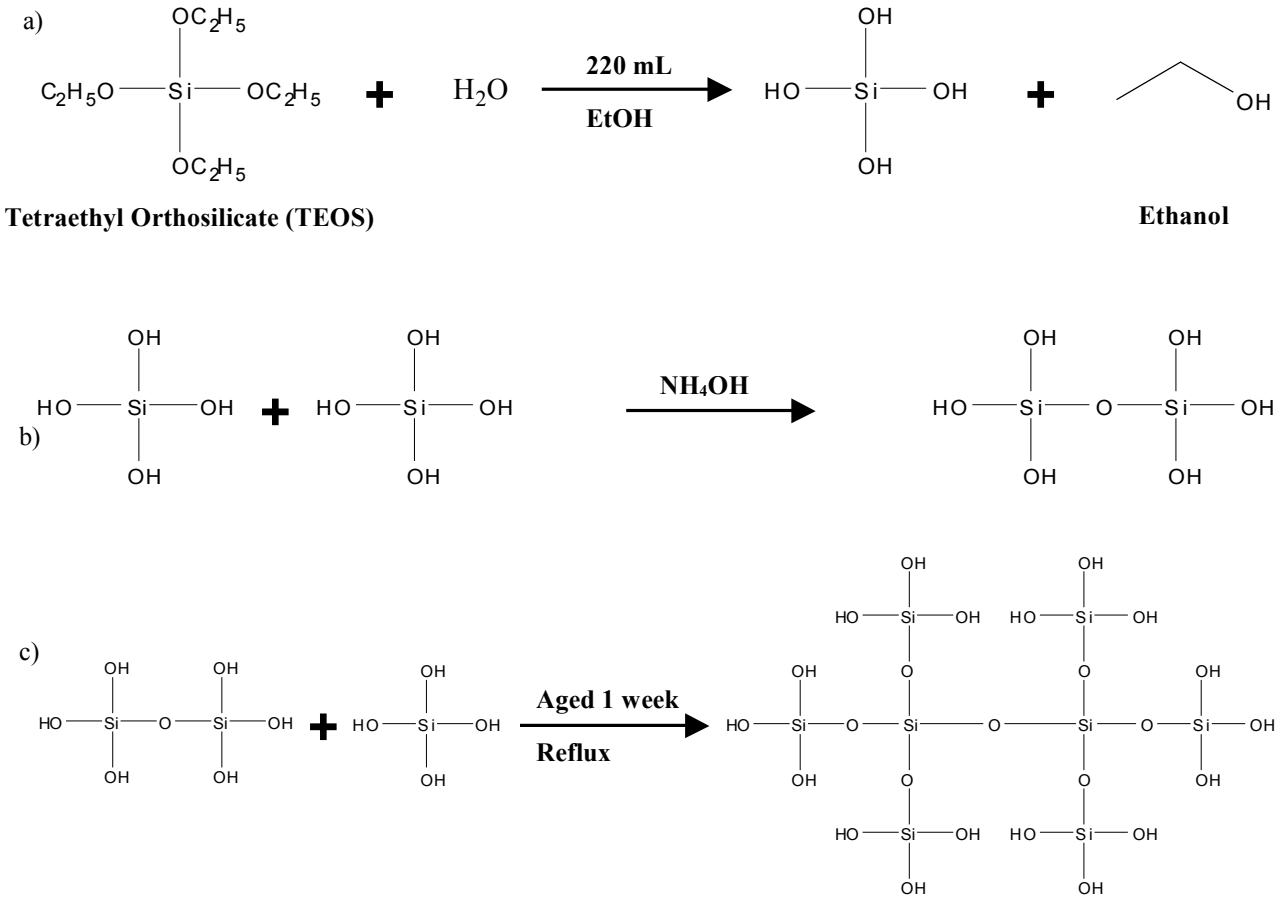

Fig. 1: Formation of silica oxide particles via the sol-gel process. a) TEOS is hydrolyzed, liberating ethanol. b) A polycondensation reaction occurs in the presence of a base catalyst (ammonium hydroxide). c) Polycondensation results in the formation of silica oxide particles after one week, at which point the ammonium hydroxide is removed from solution by reflux as ammonia gas.

The colloidal suspension of SiO_2 particles is modified using the organosilane 3-methacryloxypropyltriethoxysilane (MOTOS), which attaches to the surface of the SiO_2 particle. The modifiers allow for more bonds between particles as crosslinking agents can attack the carbon-carbon double bonds on the modifiers. Fig. 2 shows a MOTOS molecule, while Fig. 3 shows a schematic of a TEOS-based sol-gel particle modified by organosilanes reacted with cross-linking agents.

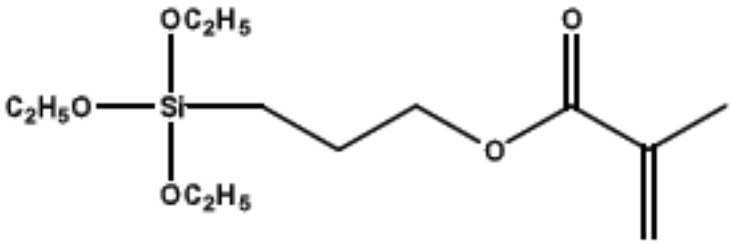

Fig. 2: 3-Methacryloxypropyltriethoxysilane (MOTOS). The carbon-carbon double bond (vinyl group) on MOTOS provides an opportunity for a crosslinking agent to create bonds between SiO_2 particles

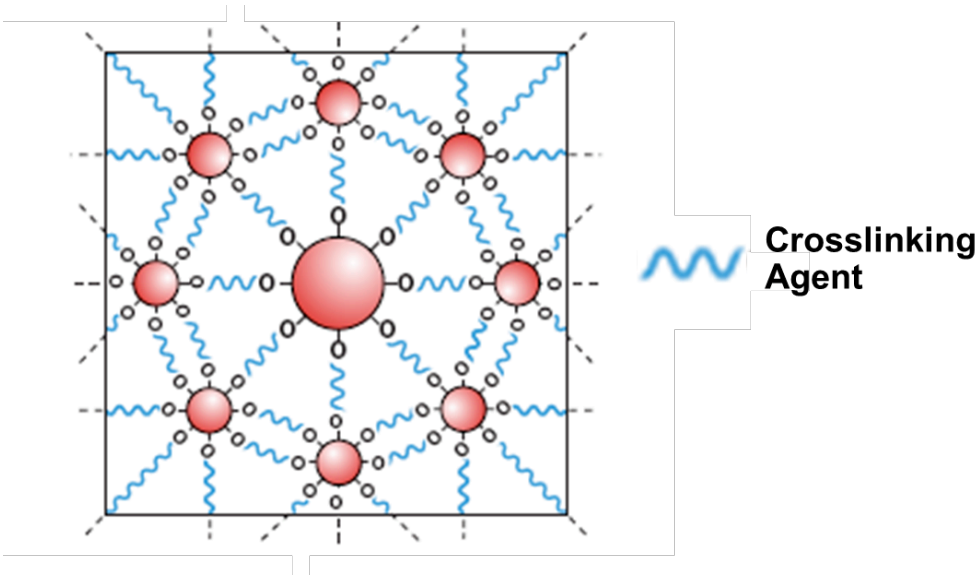

Fig. 3: Modified, crosslinked silica oxide particle. The silica oxide particles have been modified, allowing the crosslinking agent to create bonds between particles forming a robust network.

Dithiol crosslinking agents are added to the solution containing these organosilane-modified SiO_2 particles in a slightly less than a 2:1 molar ratio of organosilane to dithiol to ensure that cross-linking occurs between two SiO_2 particles Three dithiol crosslinking agents (propanedithiol, butanedithiol, and pentanedithiol) were initially used in this study. Crosslinking occurs when the nucleophilic dithiol attacks the electron-rich vinyl groups of the MOTOS organosilane molecules bonded to the SiO_2 particles, resulting in a network of bonds [4,5]. This reaction is triggered when the coating is exposed to 254 nm UV light for 30 min. Fig. 4 shows the photoinitiated reaction.

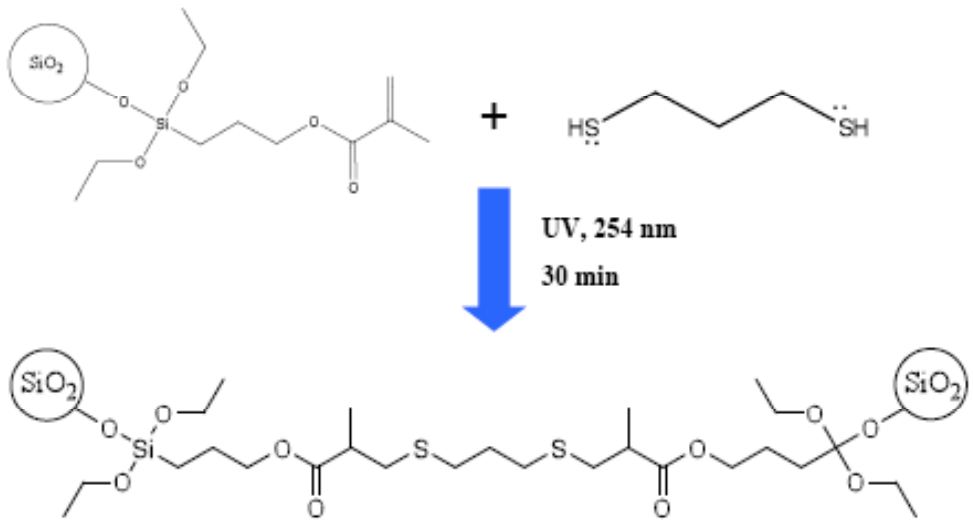

Fig. 4: Photoinitiated crosslinking reaction. The nucleophilic dithiol (propanedithiol) reacts with two different modified SiO_2 particles, forming a network of bonds between SiO_2 particles.

Solutions were prepared in a Class 100 vertical laminar flow exhaust hood housed inside a Class 10,000 clean room. After mixing the TEOS, MOTOS, and dithiol, the solutions were left to stir for several hours. Additional stirring was necessary prior to spin-coat deposition to ensure an even distribution of particles in the solution. The solutions were applied to the optics via a spin-coating process in the vertical laminar flow exhaust hood. The coating solution was deposited onto the optic in 0.5 mL quantities- or enough to cover the surface of the substrate- from glass syringes fitted with a

submicron particle filter and the substrate was spun at 3000 RPM for 40 seconds. After a two-day drying period in air, the substrates were placed under a 254 nm UV lamp for 30 minutes to complete the crosslinking reation before any tests were run.

Sol-gel coatings prepared from all three dithiols with MOTOS were evaluated for their transmission characteristics. Coatings prepared using propanedithiol and butanedithiol did not display any anti-reflection properties (i.e., showed little to no improvement in transmission as compared to the transmission of an uncoated optic). For this reason, only pentanedithiol was pursued further as a cross-linking agent for these coatings.

To test the abrasion resistance of the pentanedithiol-crosslinked coatings, the coated substrate was placed with the coated side up between two sheets of clean-room wipes as seen in Fig. 5. Square substrates (~6 g each) were stacked on top of clean-room wipes one at a time. Before the addition of each new substrate, the wipe carrying the applied mass was dragged across the surface of the coated substrate and then the mass of the stack of substrates was determined. The coating on the substrate was then observed by eye for any gross damage. If scratches could be seen, the dry wipe test was complete and the final mass of the stack of square substrates was measured. If there was no damage observed, another square substrate was placed on top of the stack and the procedure was repeated. Substrates with coatings that showed no observable damage when mass loads $\geq$100g were dragged across their surfaces were viewed under a microscope at 100x magnification for any small-scale damage. No damage was evident at this magnification.

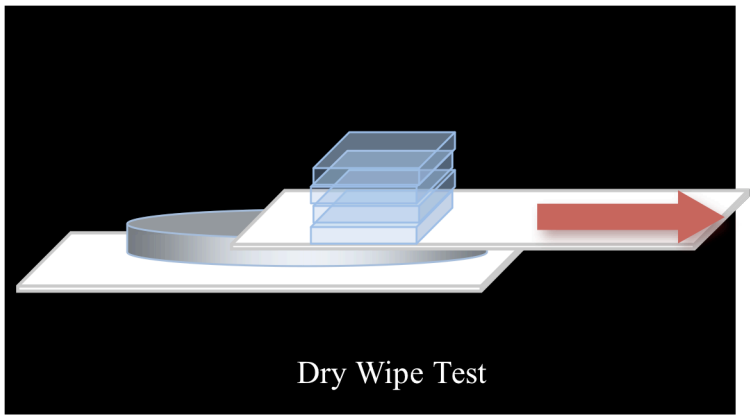

Fig. 5: Dry wipe test diagram for abrasion resistance of a coating. The top clean-room wipe carrying a stack of substrates was dragged in a straight line across the surface of the coated substrate, which was then observed with the naked eye for any scratches.

The abrasion resistance results for the pentanedithiol-crosslinked coatings are shown in Table 1, along with optical transmission data for each substrate tested. Coatings modified with 15 mol% MOTOS solutions and pentanedithiol exhibited transmission results that are comparable to those of the standard TEOS coatings currently employed in the OMEGA and OMEGA EP laser systems. These coated substrates also showed an abrasion resistance six times stronger than that of the TEOS coatings. When experiments were run using the 25 mol% concentrated MOTOS-pentanedithiol solutions, a higher abrasion resistance was achieved (100 g dragged across the surface did not scratch the coating), but there was also a large decrease in transmission as compared to coatings with a lower MOTOS/pentanedithiol concentration. Because an abrasion resistance of over 100 g would not be necessary for sol-gel coatings in OMEGA or OMEGA EP (where optics are routinely handled with considerable care due to their size, weight, and high replacement cost) it would be prudent to sacrifice some abrasion resistance for improvements in transmission.

When the abrasion and transmission results on MOTOS-pentanedithiol modified coatings are compared to those for the glutaraldehyde and glyoxal systems, it is evident that equivalent results can be obtained through the use of MOTOS-pentanedithiol solutions (Table 1). The crosslinking with dithiols achieves the same or better abrasion resistance at room temperature deposition as with elevated temperature using reactive dialdehydes, therefore enabling easier application of coatings onto the optics.

Sol-gel composition (mol%)	% Transmission at AR (λ_{max})	Mass required to scratch coating (g)
TEOS (100%)	96.641 (1073 nm)	≤ 7
MOTOS-pentanedithiol (15%)	96.175 (882 nm)	36
MOTOS-pentanedithiol (25%)	93.904 (1358 nm)	100+
Glutaraldehyde (50%)	96.120 (532nm)	30
Glyoxal (50%)	96.447 (660 nm)	37

Table 1: Transmission and abrasion resistance for various cross-linked sol-gel coating compositions. Data for standard TEOS sol-gel coatings is included for reference.

Figure 6 compares the transmission of an uncoated optic, an optic coated on one side with the 15 mol% MOTOS/pentanedithiol crosslinked sol-gel solution and the calculated transmission of an optic coated on both sides with the same solution. The calculated transmission was obtained by multiplying the magnitude of the difference in transmissions of the uncoated and single side coated optics by 2 and then adding the transmission of the uncoated optic.

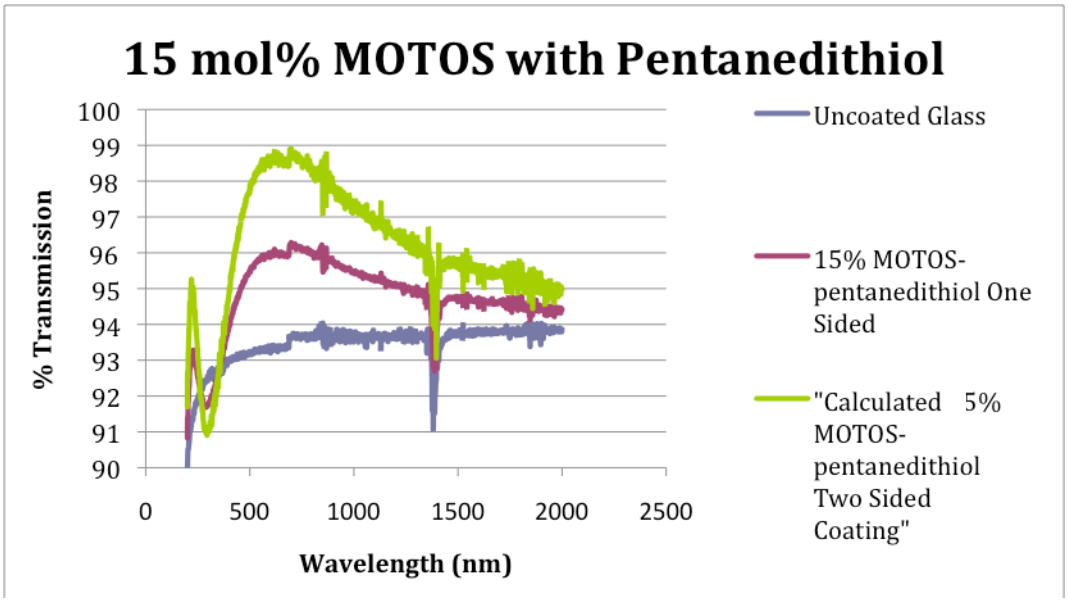

Fig. 6: Calculated transmission of a substrate with both sides coated compared to the measured transmission of uncoated and single-side-coated substrates. Transmission increases from the uncoated glass to the double coated glass as the coatings reduce Fresnel loss by narrowing the gap in refractive indices of the air and the glass.

Conclusion:

Optical elements were coated with sol-gel solutions containing 3-methacryloxypropyltriethoxysilane and crosslinking dithiols at concentrations of 15 mol% and 25 mol% via spin coating. Abrasion resistance of the coatings was tested using a dry-wipe protocol. The best results were obtained with coatings prepared from 15 mol% MOTOS-pentanedithiol solutions. These new coatings not only display excellent abrasion resistance but also provide the added benefit of a simple, room temperature deposition process. No high temperature bake is required as is needed for previously studied abrasion-resistant sol-gel coatings employing glutaraldehyde and glyoxal as cross-linking agents. Additional research remains to be done to determine the contamination resistance, hydrophobicity, and laser damage resistance of these new coatings (the latter is a key requirement for deployment in OMEGA and OMEGA EP), as well as to understand the mechanism driving the reduction in transmission with increasing abrasion resistance. Once these issues are better understood, work can progress toward

optimizing deposition parameters for application of these coatings to apertures suitable for future deployment in OMEGA and OMEGA EP.

Acknowledgements:

I am grateful to the University of Rochester Laboratory for Laser Energetics for this opportunity to conduct research at this facility. I appreciate the opportunity given to me by the director of the summer high school intern program, Dr. R. Stephen Craxton, and by my project advisor, Kenneth L. Marshall. For their additional help, I thank my project team Jason Lee, Andy Shulz, and Emily Jones, as well as Debbie Saulnier for assisting me in the completion of my project.

References:

1. Graham Woan. *The Cambridge Handbook of Physics Formulas*. Cambridge: Cambridge University Press, 2000. Print.

2. Leela Chockalingam. *Abrasion Resistant Anti-Reflective Sol-Gel Coatings.* Laboratory for Laser Energetics: Rochester, NY. 2009.

3. Gerald L. Witucki. *A Silane Primer: Chemistry and Applications of Alkoxy Silanes.* Journal of Coatings technology 63: 57-60. 1993.

4. Neil B. Cramer, Tanner Davies, Allison K. O'Brien, and Christopher N. Bowman. *Mechanism and Modeling of a Thiol-Ene Photopolymerization.* University of Colorado, Boulder, Colorado. University of Colorado Health Sciences Center, Denver, Colorado. 2003.

5. Neil B. Cramer, J Paul Scott, and Christopher N. Bowman. *Photopolymerizations of Thiol-Ene Polymers without Photoinitiators.* University of Colorado, Boulder, Colorado. University of Colorado Health Sciences Center, Denver Colorado. 2002.

6.

Generation of Radially Polarized Beams Using Optically Patterned Liquid Crystals

Michael Statt

School of the Arts

Advisors: Dr. Christophe Dorrer & Kenneth L. Marshall

University of Rochester

Laboratory for Laser Energetics

Summer High School Research Program 2011

Abstract

Radially polarizing liquid crystal (LC) devices aligned optically were investigated for applications in laser technology. Presently, radially polarized beams are generated through complex laser resonator configurations or buffing of LC alignment layers. Optically aligned LC devices offer several advantages over these methods, including their simple fabrication, low cost, high laser damage threshold, and scalability. This project researched the fabrication of the LC devices using a high-damage-threshold coumarin-based photopolymer irradiated with polarized UV light on a rotating stage coupled with a slit. Radially polarizing LC devices have been fabricated and characterized. This will lead to more research to improve the fabrication technique and make larger devices.

Introduction

Polarization is an important aspect of light. The polarization state locally describes the vibration of the electric field. This affects the propagation of optical beams and their interaction with matter. Laser beams are usually linearly polarized (the electric field is oriented in one particular direction across the entire beam) or circularly polarized (the electric field locally rotates at a rate given by the optical frequency at each point in the beam). However, new research has been done on the generation and use of cylindrical vector beams, such as radially and azimuthally polarized beams: the polarization is locally linear, but its orientation depends on the position in the beam. This leads to many interesting properties[1].

Radially polarized beams have many potential uses in laser technologies. In laser cutting, radially polarized beams have shown potential for large increases in efficiency. The orientation of the polarization to the plane of incidence heavily affects laser cutting efficiency. When the polarization is parallel to this plane it is called p-polarization. When the polarization is perpendicular to this plane, it is called s-polarization. For laser cutting, p-polarization is much more efficient. Presently, circularly polarized light is used for laser cutting because it is an average of s-polarization and p-polarization and therefore makes

uniform cuts. However, p-polarization yields a much higher absorption coefficient, meaning that the surface absorbs much more of the light of the beam when it is p-polarized than when it is s-polarized. The use of radially polarized light instead shows promise because it's p-polarized relative to the edge of the hole being drilled across the entire beam and could increase efficiency by 1.5 to 2 times.[1] Radially polarized beams can also be focused to a significantly smaller focal spot than linearly polarized light, 0.16λ compared to 0.26λ, due to the strong longitudinal component of the beam. This tighter focusing has uses in higher resolution microscopy.[1] Radially polarized beams also have uses in optical trapping due to the doughnut-shaped intensity distribution in the far field (i.e., when focused).[1] This intensity distribution is due to the destructive interference between the opposite polarizations on either side of the center of the beam.

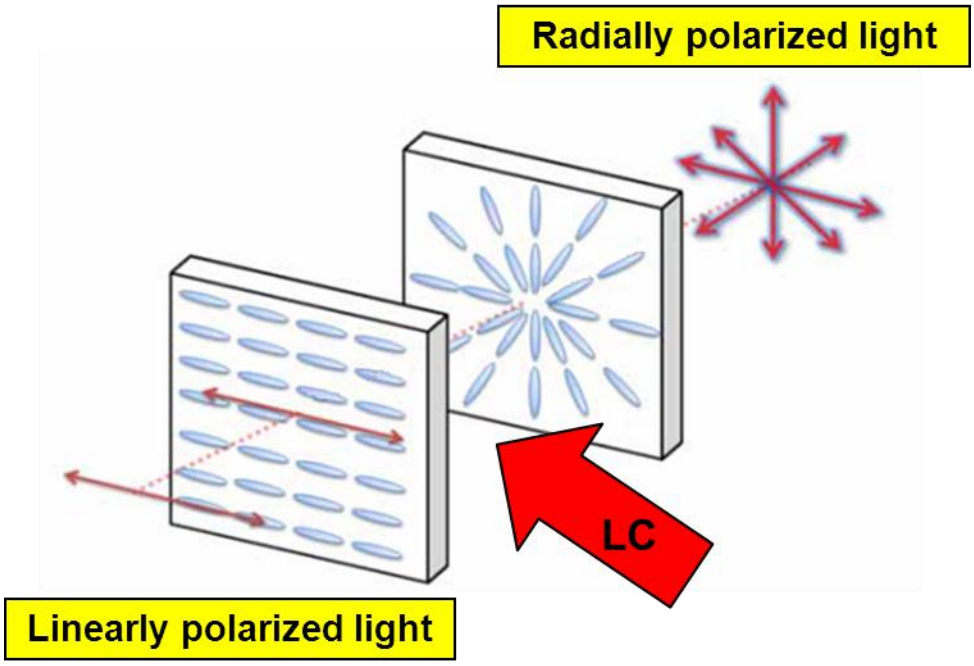

Figure 1: Schematic of a radially polarizing LC device. It consists of a linearly patterned substrate (left) and a radially patterned substrate (right), put together and filled with a twisted nematic liquid crystal

Presently, radially polarized beams are generated through complex resonator configurations or the superposition of Gaussian beam modes.[2] These methods, however, are cumbersome and not applicable to laser systems that cannot be specifically designed for radially polarized beams or where space is limited. Another method to generate radially polarized beams is with a segmented spatially variable λ/2 wave plate, but this method is not very accurate due to the distinct cuts between each segment.[3]

The generation of radially polarized beams using a radially patterned liquid crystal (LC) has been investigated as an alternative to the previously stated methods (Fig. 1). Liquid crystal devices are more advantageous than previous methods thanks to their simplicity, low cost, and ease of fabrication. Once fabricated, these devices are very easy to install into existing laser systems. As shown in Figure 1, all that is needed to convert incident polarized light to radially polarized light is to put the LC devices in front of a linearly polarized beam. They are also spatially continuous, unlike the segmented wave plate that consists of several pieces of glass put together. Finally, LC optical devices fabricated with patterned alignment layers generated by irradiation with polarized UV light have previously demonstrated a damage threshold higher than 30 J/cm^2 at 1053 nm in the nanosecond regime. Using such LC device technology allows the generation of radially polarized beams in high-energy and high-power laser systems.

There are two methods to align LC molecules: (1) by mechanical buffing of a polymer alignment layer and (2) by irradiating a photosensitive polymer layer with polarized UV light ("photoalignment".) The mechanical buffing process makes use of a polymer alignment layer deposited on a glass substrate and buffed by a machine so as to create a preferred direction for the LC molecule to align along. This process is inherently "dirty" in that it requires physical contact between the buffing roller and the coating, which generates particles and can produce large scratches in the alignment coating. Photoalignment, however, is a very clean, non-contacting process that uses polarized UV irradiation to align the LC molecules. Photoalignment was used to radially pattern the devices in this experiment. The UV irradiation causes a coumarin-based photopolymer, synthesized at the Laboratory for Laser Energetics, to dimerize

parallel to the polarization of the UV light. The LC molecules align themselves parallel to the dimers creating uniform alignment.[4] The radial pattern is possible through the use of a rotating stage coupled with a slit.

Experimental Device Fabrication

All processes except for cleaning and irradiation were done in Class 100 or better hoods inside a Class 10,000 clean room facility. Borofloat™ windows (25mm x 25mm, Edmund Optics® part number NT48-542) were used for the radially polarizing devices. The glass was wetted with deionized (DI) water, scrubbed with 0.05 μm Masterprep® Polishing Suspension micropolish and then rinsed with DI water. The substrates were subjected to a seven-second water break test where the surface tension of the water on the glass was examined: if a continuous sheet of water was unable to remain on the surface of the substrate for seven seconds without beading or pulling up from the surface (e.g. "breaking"), then more cleaning was necessary. If the substrates passed the water break test, they were placed in a substrate holder and then placed in a small glass container that was filled with DI water. This container was then placed in an ultrasonic bath at 69°C for 60 minutes with approximately 3 mL of Extran detergent added to the water in the container and just enough water added to the ultrasonic machine so as to not spill over the sides of the container. After cleaning in the ultrasonic bath the substrates were rinsed with DI water for approximately five minutes and dried with a nitrogen air gun. They were then placed on a hot plate set at 130°C for 30 min. to completely dry the substrates before depositing the photoalignment layer.

After cooling for 30 minutes, the substrates were placed one at a time on the circular stage of a spin-coater. A small crystallizing dish was then placed over the substrate; the dish had ventilation holes which were taped over prior to use. Covering the ventilation holes allows for the atmosphere which the substrate is in to become saturated with the vapor of the chloroform-based coatings. A 2-cc glass syringe fitted with a 0.45-μm PTFE 13-mm hydrophobic syringe filter and a syringe needle was used to deposit chloroform on the surface of one substrate to precondition the surface before coating (approximately 3

mL was used to completely flood one substrate.) The substrate was then spun at 4000 RPM for 60 seconds to spin off the chloroform. A second 2-cc glass syringe fitted with a 0.45-μm PTFE 13-mm hydrophobic syringe filter and syringe needle was used to deposit the photoalignment material (coumarin Polymer 3) as a 0.1 wt% solution in chloroform onto the substrate. It was then spun for 4000 RPM for 120 seconds. Each coated substrate was then air-dried under a Class 100 clean hood for 30 minutes.

Radial patterning of the dried photoalignment layer was achieved with a rotating-stage setup inserted in a photolithographic system emitting non-polarized UV light (Fig. 2). The setup consists of a 500-watt broad-band xenon light source equipped with a dichroic mirror and lenslet array configured to deliver collimated 325 nm UV light to a pile-of-plates polarizer set at Brewster's angle that produces linearly polarized UV light. The polarized UV light then passes through an adjustable slit set to restrict the width of the beam to 0.6 mm. A cylindrical lens reimages the beam onto a substrate previously coated with the photopolymer set on a rotating stage. During this irradiation process, the rotating stage was driven by a computer program that sets the rotation speed and the number of revolutions. The substrate was rotated at 10° per second for 30 minutes to align the dimer molecules in a radial pattern. Another substrate was then placed directly below the pile-of-plates polarizer on top of the closed slit and illuminated without rotation for 1 minute to induce parallel alignment.

The substrates were assembled into cells using an epoxy and spacer mixture prepared by mixing EPO-TEK® OG 154-1 UV-curing epoxy with a quantity of 10 μm glass microsphere spacers. A very small amount of the mixture was then applied to the corners of one linearly patterned substrate using a needle. A radially patterned substrate was then placed on top of this substrate and this resulting cell was irradiated under a 365 nm UV lamp for 5 minutes to cure the epoxy. The assembled cell was then heated to 100°C on a hot plate so as to raise its temperature above the nematic-to-isotropic phase transition temperature (or "clearing point") of the E7 LC (58°C). Filling the device above the clearing point of the LC material improves the final alignment quality of the device and speeds up the filling process due to the reduced viscosity of the LC material at elevated temperatures. A 1-mL plastic syringe fitted with a 0.45-

μm PTFE 4-mm hydrophobic syringe filter and syringe needle was used to fill the assembled cell with E7 LC (Manufactured by Merck.) Once filled, the cell was cooled at 10°C an hour until it reached room temperature.

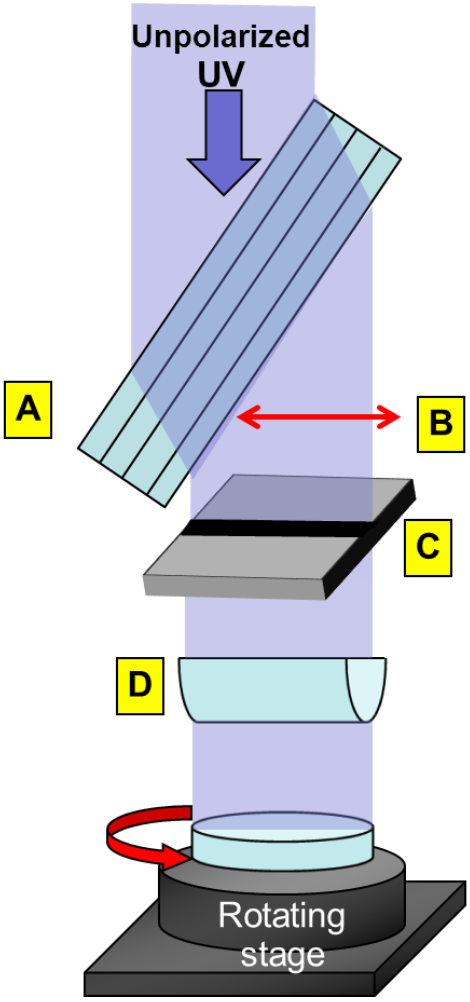

Figure 2: Schematic of the rotating-stage setup.

A) Pile-of-plates polarizer

B) Direction of polarization axis

C) Adjustable slit

D) **Cylindrical lens**

E) **Rotating stage**

The rotating stage was connected to a computer program that allowed the speed and number of revolutions to be controlled. Later, the rotating stage was put on a translation stage to allow movement perpendicular to the slit direction.

Experimental Results

Radially polarized beams were successfully generated through the use of an optically patterned LC device. The fabrication process and setup were optimized so as to align the slit with the rotation axis of the stage and to determine the speed of rotations that would yield the highest quality devices.

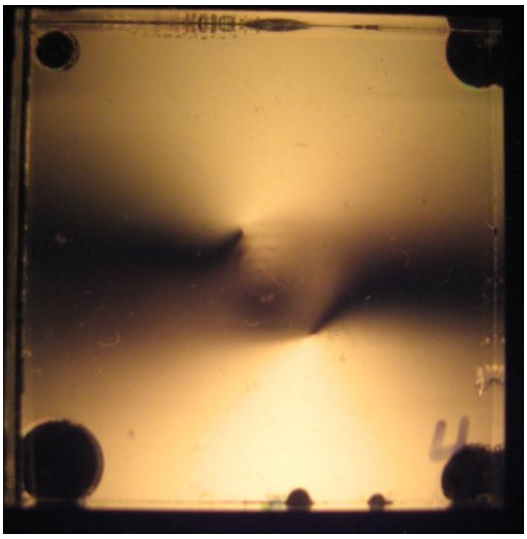

Figure 3: A LC device that was irradiated using one slow 180° turn, and incorrect relative alignment of the slit and rotation axis. Viewed through crossed polarizers.

The optimal rotation speed of the stage during irradiation was determined based on experimental trials. In early trials, inconsistencies in the width of the slit proved to be a major contributor to the poor quality of the devices. Devices that were irradiated with one 180° turn over a period of 15 minutes had large centers of undefined alignment (Fig. 3). After changing the rotation speed to 25 rotations over a period of 15 minutes, a much clearer and higher quality device resulted (Fig. 4a). The multiple rotation cycles produced by the increase in rotation speed helps to minimize the effect of the inconsistencies of the slit on LC alignment uniformity.

Even with multiple rotations, a large artifact in the center of the device that resembled a miniature radially polarizing device 90° out of phase with the rest of the device was produced (Fig. 4a). This artifact was found to be caused by the slit and rotation axis of the stage not being aligned. To correct this problem, the rotation stage holding the substrate was set on a translation stage to allow the position of the rotation axis to move relative to the fixed illumination from the slit. The alignment of the slit and the rotation axis of the stage were optimized using a calibration process. The process consisted of making an LC device by irradiating a substrate under the slit so as to make three lines at 45, 135°, and 225° when assembled and filled with LC material (Fig. 4b). If the slit and rotation axis were aligned properly, the 45°

(a) *(b)*

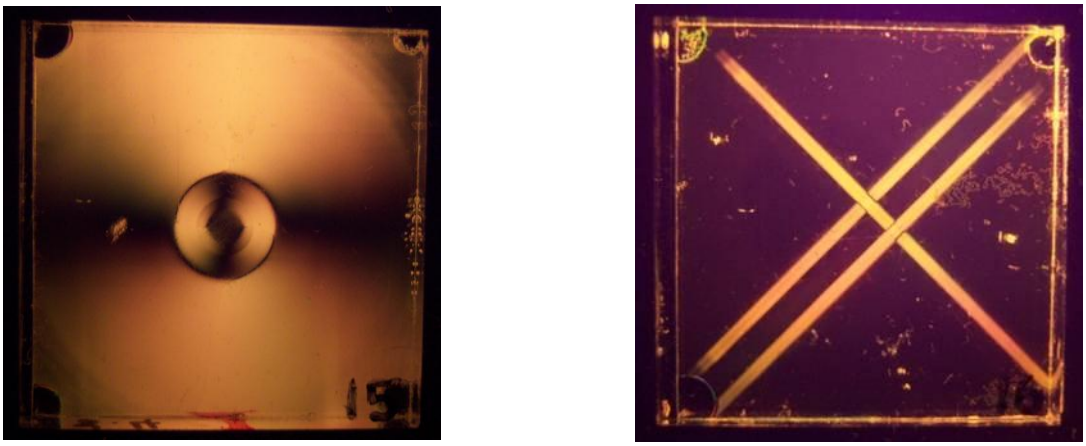

Figure 4: (a): Artifact found in center of devices with unaligned slit and rotating-stage. (b): A calibration cell. 3 lines at 3 discrete angles (45°, 135°, and 225°) were made using the slit in the rotating-stage setup. Proper alignment of the rotation axis and slit produces only two lines. Viewed through crossed polarizers.

and 225° lines would be indistinguishable; if misaligned, two separate lines were generated. The distance between the rotation axis and the illumination from the slit is half the distance between the centers of the two lines; this distance was determined using a *Leica*® DMRX polarizing microscope equipped with ImagePro microscope measuring software. The direction in which to move the stage was determined by

using the 135° line and the knowledge of the order in which the lines were irradiated. This calibration yielded a much better device and a significantly smaller artifact in the center that had a diameter that was approximately 0.6 mm (Fig. 5a). This device comes very close to a computer-generated image of an ideal device (Fig. 5b).

(a) **(b)**

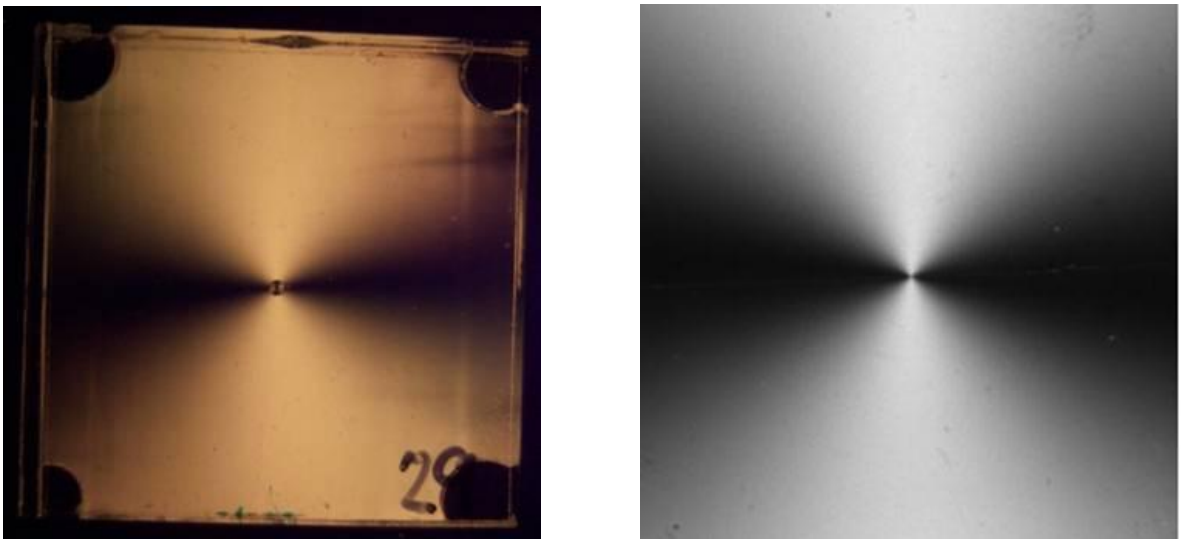

Figure 5: (a) -Fabricated device after alignment process (b) - Computer generated image of an ideal device. Viewed through crossed polarizers.

Another artifact found on all devices was a thin black line running straight up and down each device (Fig. 6). This disclination line, which is a region of undefined alignment of the LC, is caused by the LC twisting in opposite directions on either side of the line. These disclinations were measured, using ImagePro, to be 5-µm wide. Previous research into radially polarizing LC devices has obtained a similar disclination line, but in those devices the disclination lines were substantially larger (approximately 20 µm wide).[5]

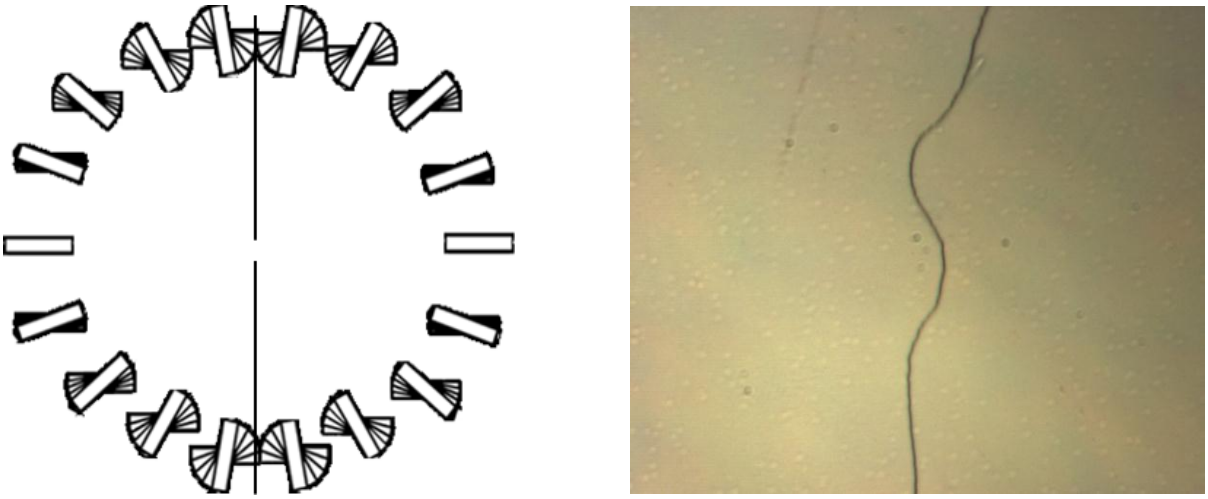

Figure 6: **Left- Twisting of the LC throughout the device. Right- Disclination line under 100X magnification (viewed with unpolarized light)**

The opposite twist directions also result in a π phase shift at the disclination line. This affects the focusing properties of the beams that pass through the devices, also called far-field properties. A transmission setup was used to characterize the devices. The setup included light passing sequentially through a polarizer, the device, and then a second polarizer that was rotated throughout the characterization. The light source used was amplified spontaneous emission around 1053 nm obtained from a fiber amplifier. The near field, or the properties of an unfocused beam, demonstrates the expected properties, as the polarizer selects a fraction of the beam polarized along its transmission axis (Fig. 7, first row). In the far field a radially polarized beam would be expected to yield a pattern that would rotate as the second polarizer rotated. However, when the radially polarized beams were characterized in the far field a pattern was observed that changed considerably as the polarizer rotated instead of simply rotating (Fig. 7, second row). A radial beam is expected to yield the desirable doughnut shaped beam in the far field, when no polarizer is present. The correct far field measurements were not observed due to the π phase shift at the disclination. This phase shift disrupts the destructive interference at the center of the beam that causes the doughnut-shaped intensity distribution. Investigation into this problem has yielded several promising methods of compensating for this phase shift, such as the use of an extra substrate to induce another π phase shift to cancel out the first one. The feasibility of this approach was demonstrated

later using a fused silica plate to induce the required phase shift on one side of the beam. After propagation through the LC device and this phase plate, the expected far field distribution patterns, without and with a polarizer, have been obtained for a radially polarized beam (Fig. 7, third row).

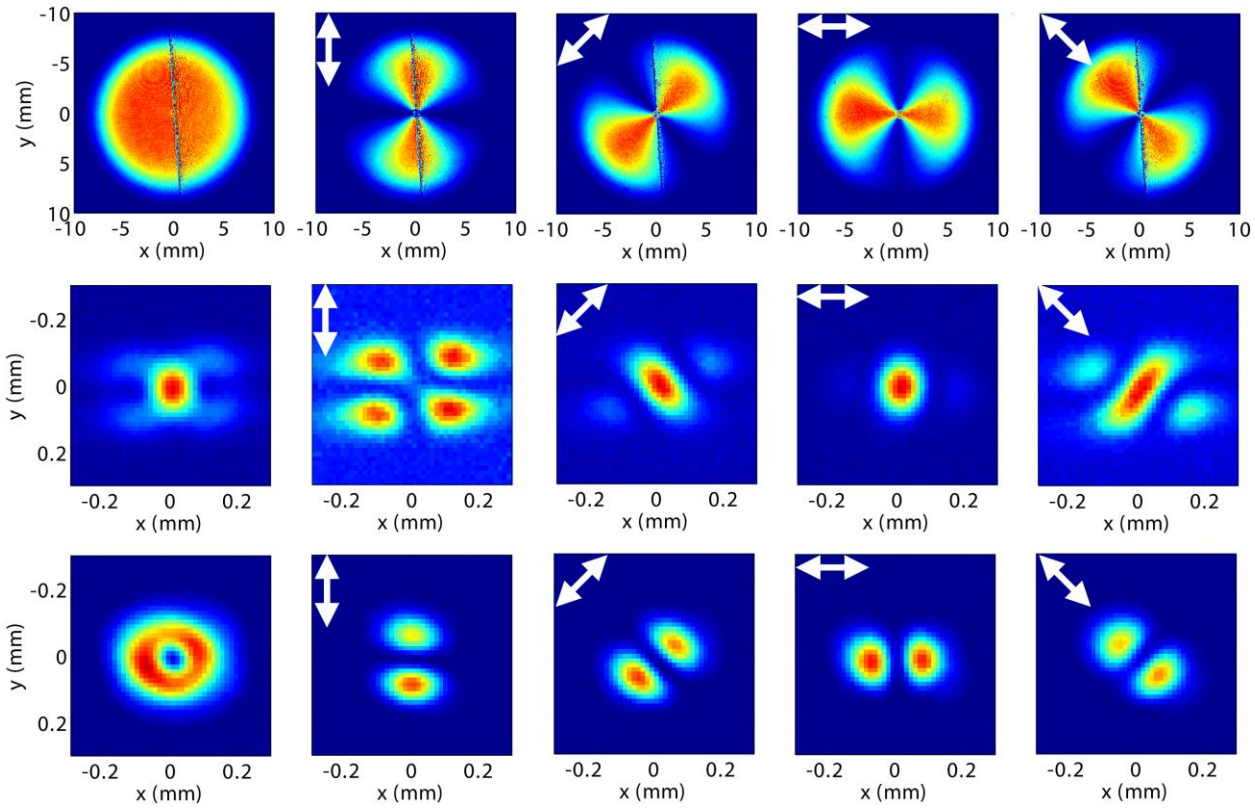

Figure 7: First row (from left to right): near field of the beam without a polarizer, and with a polarizer oriented in four different directions. **Second row** (from left to right): far field of the beam after the LC cell without a polarizer and with a polarizer oriented in four different directions. **Third row** (from left to right): far field of the beam after the LC cell and a corrective π phase plate without a polarizer and with a polarizer oriented in four different directions. In all cases, the white arrows indicate the transmission axis of the polarizer.

Conclusion

This investigation resulted in the successful fabrication and testing of radially polarizing LC devices. A setup was designed and constructed for radially patterning the photoalignment polymer layer used to generate the required LC alignment. Larger aperture devices for use in larger laser systems could be made in the future by scaling up the process and equipment used to fabricate the 25 mm devices reported here. More research could also be done to optimize methods aimed at compensating for the π phase shift without needing to add additional substrates or optical elements. These devices are a promising and simple way of generating radially polarized beams.

Acknowledgements

I thank Dr. R. Stephen Craxton for directing the high school summer research program at the Laboratory for Laser Energetics. I thank my advisors Dr. Christophe Dorrer and Kenneth L. Marshall for all their guidance, supervision, and instruction during my research. I also acknowledge Kai Kao and Dr. Simon Wei for their assistance and support. Finally, I thank the Materials Lab staff and students, especially Marisa Vargas and Avery Gnolek, for all their support throughout the program.

References

1. Qiwen Zhan. “Cylindrical vector beams: from mathematical concepts to applications”. *Advances in Optics and Photonics* **1**, 1-57 (2009).

2. Ram Oron, Shmuel Blit, Nir Davidson, Asher A. Friesem, Zeev Bomzon, and Erez Hasman. “The formation of laser beams with pure azimuthal or radial polarization”. *Applied Physics Letters* **77**, 3322-3324 (2000).

3. G. Machavariani, Y. Lumer, I. Moshe, A. Meir, and S. Jackel. “Spatially-variable retardation plate for efficient generation of radially- and azimuthally-polarized beams”. *Optics Communications* **281**, 732–738 (2008).

4. Vargas, Marisa C., “Laser Beam Shaping With Optically Patterned Liquid Crystals”; LLE Summer High School Research Program, 2010.

5. M. Stalder and M. Schadt. “Linearly polarized light with axial symmetry generated by liquid-crystal polarization converters” *Optics Letters* **21**, 1948-1950 (1996)

Optical Time-Domain Reflectometry for the Transport Spatial Filter on the OMEGA Extended Performance Laser

Troy Thomas
Webster Thomas High School
Advisor: Dr. Brian Kruschwitz

Laboratory for Laser Energetics
University of Rochester
High School Summer Research Program
2011

Abstract

An optical time-domain reflectometer (OTDR) is a diagnostic that measures light that has been reflected back towards the laser's origin. The transport spatial filter (TSF) OTDR is a device that measures these reflections in the latter half of the laser system, especially to monitor retroreflections from the target. A MATLAB computer program has been created that imports and analyzes OTDR data files. These data files contain information on the voltage of the return signal at specific times, the time scale used, and the shot type. The time that the light takes to return to the OTDR from specific optics has been determined through the use of ray trace charts. These charts have been used to trace the beam's path to the optic and back to the TSF OTDR. These times are used to create labels on the graph for the most important optics. The program then plots the data on a graph of voltage vs time. This graph allows easy interpretation of the data, allowing the user to diagnose any optic malfunctions or unexpected return signals.

Purpose

Optical time-domain reflectometry is used in the OMEGA EP (extended performance) system to identify and locate optics which have deformations or impurities, or optics that have another source of retroreflected light. To do this, it measures the reflected energy coming from each optic in the system. A small amount of energy is expected to come from each optic, but if a substantial amount is reflected, it may indicate that the optic is damaged. This excess energy can have various negative consequences. It can damage small optics in the beginning of the system that are only able to handle small amounts of energy. Some types of experiments also need a certain amount of energy, so if some is lost to reflection by damaged optics, the experiments can give flawed results. The OTDR measures the energy that is reflected back by optics. It can also

identify which optic is damaged by measuring the time that the energy took to reach the diagnostic. This is important because if we can identify which optic is damaged in a quick and precise manner, we can minimize the time it takes to replace the optic, and minimize the time the system is down.

The OMEGA EP laser can provide a plethora of shot types, not only by itself, but in tandem with the OMEGA laser. There are two OTDR diagnostics set up in the OMEGA EP laser system. The OTDR unit of interest for this work, the transport spatial filter (TSF) OTDR, is set up in the middle of the laser system, which allows it to diagnose problems with optics in the latter half of the system. In particular, the TSF OTDR was created to monitor the energy that is reflected back into the system by targets that passes by the safeguards installed in the OMEGA EP system. Until now, the TSF OTDR was aquiring shot measurements, but there was no way to read or use the data. If we could create a way to read and understand the data, it would be easier to monitor target retroreflections, identify failing optics, and keep the system running smoothly.

OMEGA EP Laser System

The OMEGA EP laser system was created to expand the range of experiments that can be carried out at LLE. It has its own target bay for independent experiments. The laser system uses a multi-pass architecture, which means the beam passes through optics multiple times in order to be amplified to higher energy levels. Figure 1 shows the path that the laser takes on its way to the target.

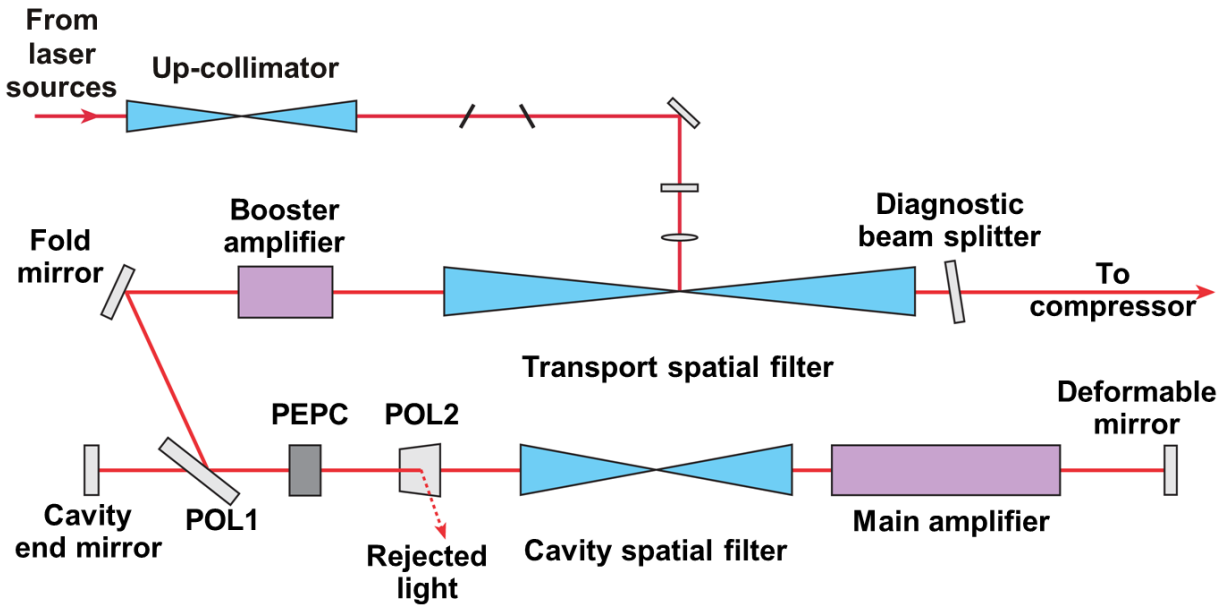

Figure 1 – OMEGA Extended Performance beam path. The OTDR records the signal at the center of the transport spatial filter, which includes retroreflections from all of the optical surfaces in the figure (except the injection path at the top of the figure from the laser sources), from the optical surfaces later in the system, and from the target.

The transport and cavity spatial filters (TSF and CSF) reduce modulation in the spatial beam profile, and allow the beam size and quality to remain intact over the long propagation distance required. The spatial filters focus the beam through a pinhole, then recollimate. However, there is more than one pinhole in each filter, in order to enable multiple passes. The CSF has 4 pinholes, because the beam normally passes through four times, and the TSF has two, corresponding to the first and fourth passes through the CSF. This means that the beam goes from the TSF first pinhole to the CSF first pinhole, and exits going through the CSF fourth pinhole to the TSF second pinhole. The OTDR measures the optical signal in the vicinity of the TSF pinholes, including retroreflections from all subsequent surfaces in the system.

The Plasma-Electrode Pockels Cell (PEPC) allows for the multi-pass architecture, by acting as an optical switch in conjunction with the cavity polarizer (seen in Figure 1 as POL1).

When turned on, the PEPC rotates the polarization of the laser. Then, when the beam comes back to the cavity polarizer, the polarizer can either pass through or reflect the beam, depending on the polarization. This complicates the OTDR analysis because each optic can provide multiple features on the OTDR, due to different paths to the optic, and different paths back through the system. In order to combat this, ray trace charts are used to determine all the possible ways and times that the beam can reflect off each optic. This allows for a more accurate diagnosis of the source of retroreflected energy.

Another important role of the PEPC is to isolate the laser system from light retroreflected from a target. Infrared light that is retroreflected from the target can propagate back through the beamline and become further amplified, which can create enormous fluences on the small optics in the front end of the system. This can greatly damage these smaller and more vulnerable optics. To protect the system, the PEPC is switched again when a target-retroreflected pulse would arrive back in the beamline. A short-pulse polarizer (POL2 in Figure 1) reflects this light, with its polarization rotated by the PEPC, into a beam dump where it can do no damage. However, due to imperfections in the PEPC switch and polarizers, a small amount of light is let through and reamplified. Most of this light is diverted into a beam dump in the TSF, but some can propagate back to the laser sources where it can damage optics if its energy is sufficiently high. The TSF OTDR is connected to the beam dump inside of the TSF in order to monitor the light reflected from target that leaks through the PEPC isolation system.

Optical Time Domain Reflectometry

There are two OTDR's built into the OMEGA EP laser system. Both were installed when OMEGA EP was created. The first is in the source of the laser system, so it is most effective for

the optics in the beginning of the system. This has been running for most of the laser's existence with a program that analyzes the data. The other OTDR is the TSF-OTDR, which is located at the TSF beam dump, previously described. Before now, it had never been utilized.

An OTDR is made up of an optical detector positioned to look forward into the system and detect light that reflects backwards. The optical detector, specifically a photodiode receptor, receives optical power and converts it into an electrical signal. The optical detector is connected to an oscilloscope, which records the electrical signal as a function of time to produce a voltage "waveform". By synchronizing the waveform with a reference time for the laser pulse, and calculating the time delay between the reference time and the reflected features, we can infer the path that the retroreflected pulse must have taken to reach the OTDR detector. In this way, the OTDR is like a radar system, which measures an object's distance by emitting radio waves and measuring the time required for reflections to return.

Development of Time Reference

In order to use the data acquired from the OTDR, we needed to create a time reference, in which to base the program off. This allows us to determine which optic has a defect. In order to determine a zero time, a lab procedure for the TSF OTDR time calibration was developed.

In the lab procedure, we used the deformable mirror (DM) to point the beam into the third pinhole instead of the second pinhole in the CSF. This caused it to reflect off the polarizer back into the TSF beam dump. This means that the OTDR will have one big voltage spike corresponding to the propagation of the beam to the DM and back. Then we turned the power

down to ten percent throttle, and gradually turned the throttle up until an accurate reading could be determined. Then we misaligned the DM so that we could be sure the spike was caused by the DM. Then we returned the DM to its original position.

With this information, the program could analyze OTDR data with an accurate time reference. Figure 2 shows the result of the experiment. The large spike around 600 ns is the reflected energy from the DM.

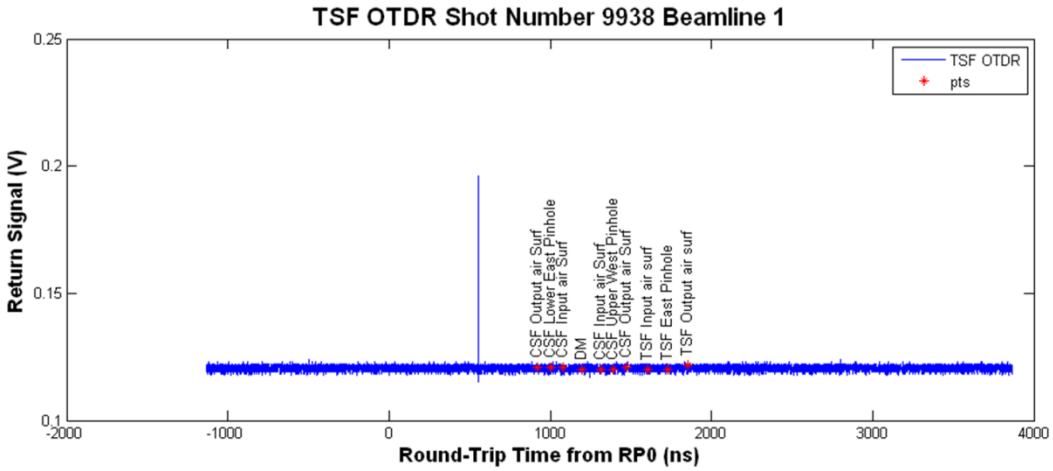

Figure 2 – Result of the time reference experiment on OMEGA EP Beamline 1. The voltage spike is a result of retroreflected light from the deformable mirror.

Software Development

A program was written in MATLAB which imports and analyzes the TSF OTDR information. MATLAB is an environment whose main objective is numerical computing and one that allows for matrix processing. It was chosen for this project due to its versatile matrix functions. The OTDR information includes long lists of times and voltages.

The user provides the shot number, and which beam line was diagnosed. Figure 3 shows the user input interfaces, which allow the user to feed information into the program. The program goes into the LLE database and searches for the corresponding shot. If the computer cannot find the shot, the user can manually select the file. Once the file is imported, the program displays a

voltage versus time graph of the information (such as Figure 2). There are labels that allow the user to identify which optic corresponds to which voltage peak.

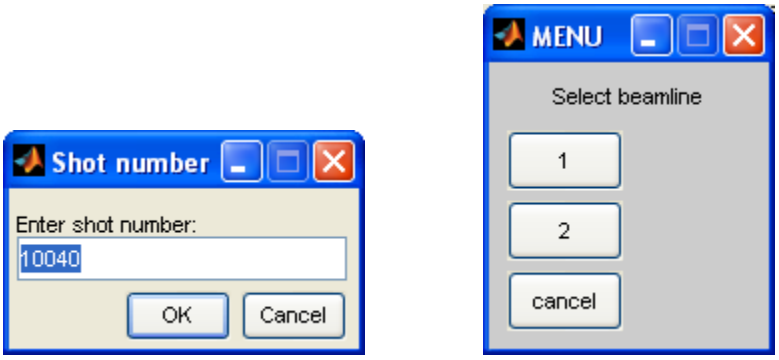

Figure 3 – User input interfaces for TSF-OTDR MATLAB program implementation

The program allows for easy user interpretation of the data, and allows the user to easily identify any optic malfunctions.

Software Implementation

The program is activated and runs for each OMEGA EP shot. The program then displays the graph and information with the other diagnostics. This helps make sure that there are no problems with the OMEGA EP laser system. When there is a defect, it is easy to identify.

Future Work

Future work includes calibrating the voltage along with the time. This way we could determine the energy of the retroreflected pulse, in addition to the location of its source. If it were calibrated, it would also be much easier to view and understand.

The OMEGA laser system could also implement this technology. It would be much more difficult to implement, because there are sixty beams instead of four, but it would be worth the investment, because it would cut down the amount of time required to identify and rectify defects in the optics of the system. In this way, the program and the OTDR technology could eventually help the OMEGA system as well as the OMEGA EP system.

Conclusion

The OTDR software provides a significant benefit to the OMEGA EP laser system, by helping to monitor target retroreflections and identify optic malfunctions. To do this, it records the energy that is reflected back through the laser system towards the source. By recording this and analyzing this data, we can monitor target retroreflection and identify damaged optics, allowing for efficient replacement. This minimizes the time it takes to identify and repair problems, allowing for more experiments and shots.

Acknowledgements

I would like to thank Dr. Brian Kruschwitz for advising me on the project and supervising me in this research. I would also like to thank Dr. Jack Kelly for stepping in for a short time during Dr. Kruschwitz's absence. Finally, I would like to thank Dr. R. Stephen Craxton for supervising the LLE High School Research Program, and for allowing me the opportunity to do this research.

Dynamic Defocusing in Streak Tubes

Harrison Xiao

Pittsford Sutherland High School
Pittsford, NY

Advisor: Dr. Paul Jaanimagi

Laboratory for Laser Energetics
Summer High School Research Program
University of Rochester
Rochester, NY

January 2012

1 Abstract

Streak cameras are used at LLE to measure the time histories of the laser pulse and the optical and x-ray emissions from OMEGA targets. A streak camera operates by applying fast-risetime voltage transients to a pair of parallel plates to deflect or streak electron trajectories across a phosphor screen. At high streak speeds, the foci of the electrons move behind the screen, thereby blurring the image on the screen. A program was written in C# to model electron deflection in streak cameras. The model uses the fourth-order Runge-Kutta method to integrate the Lorentz equation of motion and trace the path of electrons through the deflection plates as the voltages change. Data from the model was collected and extrapolated to calculate adjustments needed to refocus the electrons. A common-mode focusing voltage was applied to the deflection plates to shift the focal plane back to the screen.

2 Introduction

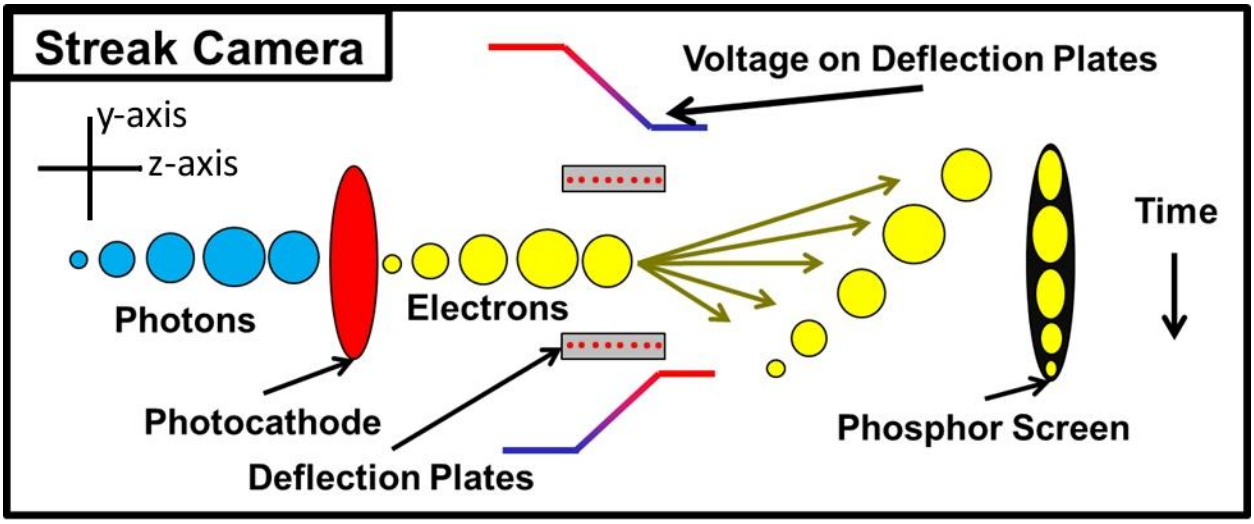

Figure 1: Simplified schematic diagram of a streak camera.
This 2-dimensional diagram illustrates electron deflection in a streak camera. The simplified schematic shows only the (y,z) plane and omits the input window and slit, the accelerating electrodes, and the focusing electrodes. Electrons produced by photons incident on the photocathode travel toward the right of the diagram and are deflected by the voltages on the deflection plates. The voltages change with respect to time according to their representations by the adjacent straight-line graphs of voltage.

The Laboratory for Laser Energetics utilizes streak cameras to measure the time histories of the laser pulse and the optical and x-ray emissions from OMEGA targets. A streak camera captures and records light pulse intensity with respect to time. As shown in Figure 1, photons entering a streak camera hit a photocathode after passing through a narrow slit. The photocathode emits electrons through the photoelectric effect, with the emitted electron current density linearly proportional to the incident photon intensity. These electrons are accelerated and focused by a set of electrodes in the streak tube.[1] The final section of the streak tube is a drift region where the electrons encounter the deflection plates. Initially the deflection plates are biased with one plate at a positive voltage and the other at a negative voltage. As the electrons pass through the deflection plates, fast-risetime voltage transients shift the voltage and reverse the polarity on the deflection plates, so that the last electron to pass through the deflection-plate field is deflected in the direction opposite to the first, with the middle electrons deflected at intermediate positions. The time at which any electron passes through the deflection field determines its angle of deflection, as shown in Figure 1. At the end of the streak tube, the deflected electrons hit a phosphor screen that emits light proportional to the number of electrons hitting a particular area.[2] To record the data, a charge-coupled device then captures a digital image of the phosphor screen from which a computer can read quantitative data. The photon intensity is transformed into a 2-dimensional image in which the temporal dimension is converted into a spatial dimension on the phosphor screen (Figure 1).

3 Dynamic Defocusing at High Streak Speeds

The rate of change of the voltage with time, $\frac{dV}{dt}$, on the deflection plates determines the rate of the electron beam deflection, i.e. the streak speed. This streak speed can be altered by adjusting the risetime and magnitude of the voltage transients applied to the deflection plates. Higher streak speeds allow for greater time resolution, as the temporal profile of the pulse is mapped to larger distances on

the phosphor screen. However, experimental evidence from streak cameras at high streak speeds have shown decreased temporal resolution due to beam defocusing. At slow streak speeds, the electron beam focuses at the phosphor screen. At high streak speeds, the focal plane of the beam begins to move behind the phosphor screen. Therefore the image of the pulse on the phosphor screen becomes blurred and is comparably wider. The degree of defocusing increases as $\frac{dV}{dt}$ is increased, since the electrons experience a greater change in voltage while passing through the deflection region.

4 Deflection model

4.1 Program Outline

The program *RungeKutta* was created in the C# programming language in order to further analyze and simulate dynamic defocusing in streak cameras. It is named after the algorithm central to the calculation of the electron trajectories in the program. The program models the drift region of the streak tube comprising the deflection plates and the phosphor screen, but excludes the accelerating and focusing electrodes. The electrons enter the deflection region through a small aperture. The model numerically solves the electron force equation to calculate the electron path, tracking the electrons in a rectangular coordinate system. The force and acceleration are calculated from a series of line charges representing the deflection plates, allowing the trajectories to be integrated through the Runge-Kutta method to track electron position. The program reads input data necessary for simulating dynamic deflection, including voltage, streak speed, deflection plate location, and initial electron positions and velocities from the accelerating and focusing electrodes. The data from the calculations is output to two ASCII files: one that contains detailed numerical data from the model, and another that contains data points that can be displayed in graphical form by a program named *Eoplot*.

4.2 Existing Code

Previously, a program for static electron deflection had been written by Dr. Paul Jaanimagi. This program models the deflection region on a numerical grid, solving the Laplace equation for the voltage at each grid point from which the electric fields and electron trajectories can be calculated.

To analyze dynamic defocusing, a program that included deflection plates with dynamic voltages and variable start times for the electrons was written. The previous code was modified to accommodate the new features required to model dynamic electron deflection.

4.3 Deflection Plate Modeling

The deflection plates in the program were modeled through a series of line charges arranged along the x-direction perpendicular to the plane of Figure 1, passing through the red dots shown in Figure 1. The electrons were given coordinates on a rectangular coordinate system. The electrons (travelling in the Y-Z plane) in the program were subjected to forces depending on their distances from the line charges on the deflection plates.

According to Coulomb's law, the force $\boldsymbol{F}$ acting upon two electrically charged particles is,

$$\boldsymbol{F} = k_e \frac{q_1 q_2}{r^2} \tag{1}$$

where k_e is the proportionality constant, defined as $k_e \approx 8.98755 \times 10^9\ N \cdot m^2/C^2$, q_1 and q_2 are the point charges, and r is the distance between the two points.

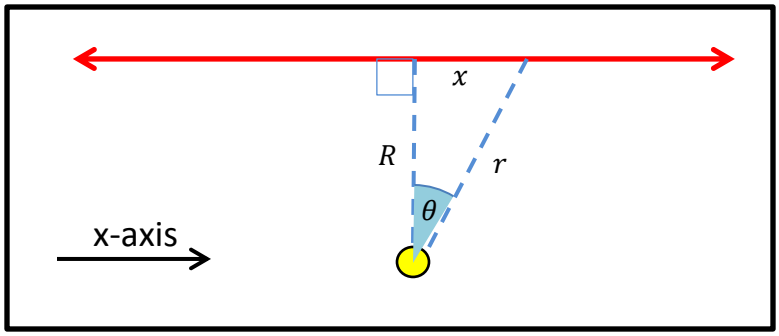

Figure 2: Electron distance from a line charge.
This diagram illustrates the variables involved in Eq. 2. The yellow circle represents the electron, the red line represents the line charge, and the blue dashed lines represent distance.

The force acting upon an electron due to a line charge can be obtained by integrating this equation along the line. Although the deflection plates in streak tubes do not extend to infinity along the X-axis of the rectangular coordinate plane in the model, it is possible to model deflection plates as line charges because the points on the line that are far from the center provide a negligible force on the electron, and thus can be ignored. The electric field for a line charge is radial from symmetry. The field at a distance R from the line (shown in Figure 2) can be derived through an integral of the point charge equation,

$$\boldsymbol{E_R} = 2\int_0^\infty k_e \frac{dq}{r^2}\cos\theta \tag{2.1}$$

where dq is an infinitesimal differential charge on the line, r is the distance from the point charge to the differential charge, and θ is the angle between R and r. Substituting into Eq. 2.1 λdx for dq, with λ as the charge density and dx as the differential distance on the line charge, (R/r) for $\cos\theta$, and $\sqrt{x^2+R^2}$ for r, with x as the distance on the line charge, results in,

$$\boldsymbol{E_R} = 2k_e\lambda R\int_0^\infty \frac{dx}{(x^2+R^2)^{3/2}} \tag{2.2}$$

and solving Eq. 2.2,

$$\boldsymbol{E_R} = \frac{2k_e\lambda}{R} \tag{2.3}$$

With this electric field, the Lorentz force equation is used to calculate the force acting on the electron based on its position relative to the field created by the point representing a line charge. The Lorentz equation is the following,

$$\boldsymbol{F} = q[\boldsymbol{E} + (\boldsymbol{v}\times\boldsymbol{B})] \tag{3}$$

where q is the particle charge, $\boldsymbol{E}$ is the electric field, and $(\boldsymbol{v}\times\boldsymbol{B})$ is the cross product between the instantaneous velocity $\boldsymbol{v}$ and the magnetic field $\boldsymbol{B}$ vectors. Because there are no static magnetic fields in the streak tube, $\boldsymbol{B}$ is set to zero. Substituting $\boldsymbol{E_R}$ from Eq. 2.3,

$$\boldsymbol{F} = \frac{2k_e\lambda q}{R} \tag{4.1}$$

where q is the charge of an electron. From Eq. 4.1, the force acting on an electron isn't determined by the inverse-square law, as Eq. 1 would show. Instead, the force is proportional to the inverse of the distance.

Because of the extreme speeds that the streak tube electrons move, ($\boldsymbol{v} \approx 0.2c$), where c is the speed of light, relativistic effects must be taken into account when calculating the movement of the electrons. As the electron's velocity approaches the speed of light, its kinetic energy is transferred into mass, decreasing the acceleration from the force caused by the deflection plates. The Newtonian formula for kinetic energy KE,

$$KE = \frac{1}{2}m_o\boldsymbol{v}^2 \tag{4.2}$$

where m_o is the electron rest mass, does not accurately account for the altered electron mass from relativistic effects. Therefore, a relativistic force equation is necessary to calculate electron acceleration. This can be derived from the derivative with respect to time of relativistic momentum $\boldsymbol{p}$ given by,

$$\boldsymbol{p} = \frac{m_o\boldsymbol{v}}{\sqrt{1-(\boldsymbol{v}^2/c^2)}} \tag{4.3.1}$$

$$\frac{d\boldsymbol{p}}{dt} = \boldsymbol{F} \tag{4.3.2}$$

Combining Eq. 4.3 with Eq. 3, an equation for instantaneous electron acceleration can be derived, by which,

$$\frac{m_o}{\sqrt{1-(\boldsymbol{v}^2/c^2)}}\frac{d\boldsymbol{v}}{dt} = q[\boldsymbol{E} + (\boldsymbol{v}\times\boldsymbol{B}) - \boldsymbol{v}\,(\boldsymbol{v}\cdot\boldsymbol{E})/c^2] \tag{4.4}$$

with $\boldsymbol{B} = 0$ in this work.

4.4 Electron Path Calculations

The electrons are each assigned an initial position, trajectory angle, and energy. These variables are gathered by the program from the input file, and are inserted into the equations of the program.

The instantaneous electric field acting on an electron from one line charge is calculated by inserting the distance between the electron and the line charge and the instantaneous charge of the line charge into Eq. 2.3 to give $\boldsymbol{E_R}$, which has Y and Z components. The process is repeated with the other line charges, which may have different distance and charge values, after which the field components are added and substituted into Eq. 4.4 to give the total instantaneous acceleration.

The program functions by repeating the calculations for the change in position and velocity over a time step based on the instantaneous acceleration. The code utilizes the fourth order Runge-Kutta approximation method to solve the differential equations,

$$X" = f(t, X, X') \tag{5.1}$$

$$X_{n+1} = X_n + h\left[X'_n + \frac{1}{6}(k_1 + k_2 + k_3)\right] + O(h^5) \tag{5.2}$$

$$X'_{n+1} = X'_n + \frac{1}{6}(k_1 + 2k_2 + 2k_3 + k_4) \tag{5.3}$$

$$k_1 = hf(t_n, X_n, X'_n) \tag{5.4}$$

$$k_2 = hf\left(t_n + \frac{h}{2}, X_n + \frac{h}{2}X'_n + \frac{h}{8}k_1, X'_n + \frac{k_1}{2}\right) \tag{5.5}$$

$$k_3 = hf\left(t_n + \frac{h}{2}, X_n + \frac{h}{2}X'_n + \frac{h}{8}k_1, X'_n + \frac{k_2}{2}\right) \tag{5.6}$$

$$k_4 = hf\left(t_n + h, X_n + hX'_n + \frac{h}{2}k_3, X'_n + k_3\right) \tag{5.7}$$

where $X"$ is the combined acceleration of the electron along the Y and Z axis, X' is the combined velocity of the electron, X is the position of the electron, h is the step size, n is the step number, and O is the error. The function $X" = f(t, X, X')$ used to calculate the k values is the acceleration equation from Eq. 4.4. The program repeats these steps for each electron, recalculating the acceleration, velocity, and change in position at each time step until they arrive at the phosphor screen.

4.5 Static Deflection Voltages

The initial conditions for the electron beam are set such that it converges on axis at the phosphor screen when no voltage is applied across the deflection plates (the middle group of trajectories in Figure 3). When the voltages on the deflection plates are set to a constant value, the electrons follow a static deflection trajectory, in which all the electrons are deflected in the same direction. For slow streak speeds, multiple code runs with static deflection at different voltages can be overlaid in order to model ideal dynamic deflection.

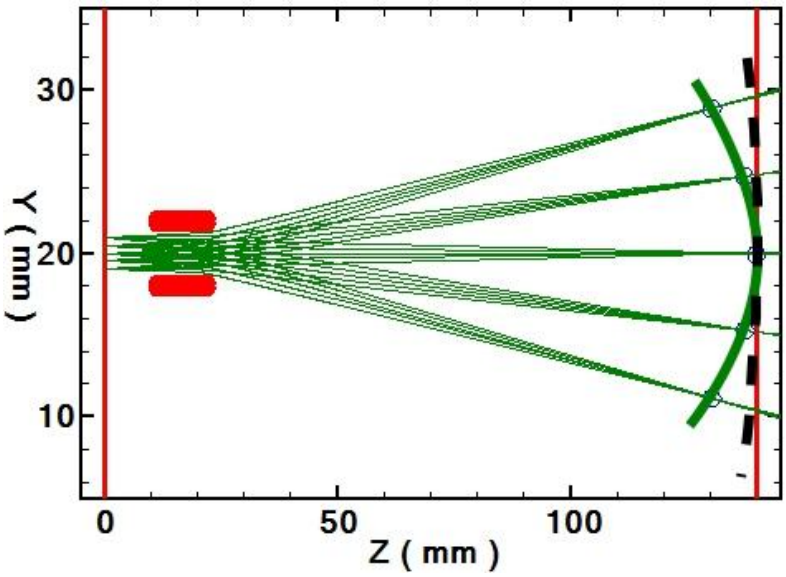

Figure 3: Static deflection focal plane.
The superposition of 5 code runs with different static voltages shows the parabolic focal plane. Graphical output of model data of a static deflection was displayed with *Eoplot*. The thick red lines represent deflection plates, the thin green lines are the electron trajectories, the thick green curve is the parabolic focal plane, and the dashed black line is a circular focal plane.

If the deflection angle for a certain deflection plate voltage remained constant regardless of electron height, the result would show a circular focal plane (the dashed black line in Figure 3), with its center at the deflection plates. However, the focal plane takes a parabolic shape tangent to the screen on axis, as seen by the thick green curve in Figure 3. The parabolic focal plane can be attributed to the fact that the impulse varies with electron height. Electrons passing between the deflection plates that are closer to the positive plate accelerate in the direction of electron propagation when approaching the deflection region, thus spending less time in the deflection region and resulting in a reduced deflection angle. On the other hand, electrons passing closer to the negative plate decelerate when approaching

the deflection region, spending more time between the plates and increasing the deflection angle of the beam.

4.6 Dynamic Deflection Voltages

For high streak speeds, a realistic model of the electron trajectories of streak cameras must include dynamic voltages since the deflection plates change polarity as the electron beam passes through. This allows for the sweep pattern of electron trajectories to be simulated in one run of the program, and also allows electron behavior and path in dynamic deflections to be analyzed.

In the dynamic model, the values of the charge on the deflection plates shift over time, with one going from a positive to negative potential and the other from negative to positive. The electron beam now consists of a sequence of time-delayed pulses synchronized to the maximal $\frac{dV}{dt}$ change at the deflection plates.

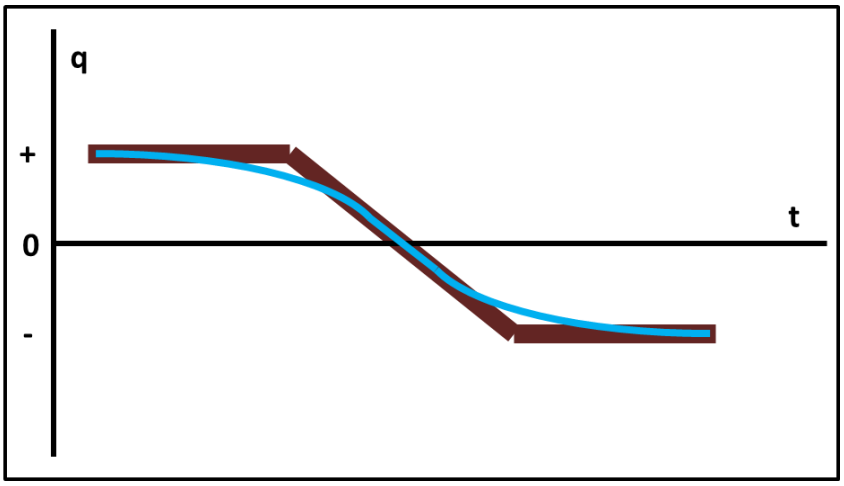

Figure 4: Sigmoid function and linear charge curve.
Curves model change in charge over time. The black represents a linear charge curve, and the blue, a charge curve modeled after a sigmoid function.

Ideally, the charge curves for streak cameras would be linear, with the potentials on each plate shifting at a constant rate. In reality, the charge curve is not so perfect, as it is limited by the capabilities of the equipment. To model the charge curve in *RungeKutta*, a sigmoid function was used (Figure 4):

$$q(t) = a + \frac{(b-a)}{1 + \mathrm{e}^{\frac{-(t-t_0)}{\lambda}}} \qquad (6)$$

where $q(t)$ is the charge of a point on the deflection plate at time t, a is the initial charge of the deflection plate, b is the final charge, t_0 is the time at which the curve reaches its midpoint, and λ is a value proportionate to the risetime.

Since electromagnetic waves can only travel at the speed of light, according to Maxwell's equations, it was necessary to include retarded potentials in the model. Therefore, because of the time it takes for the information to reach the electron, the electron experiences the force due to a previous charge on the plates. This delay of information is proportional to the distance of the electron from the deflection plates, as shown in the equation for retarded time,

$$t_r = t - \frac{r}{c} \tag{7}$$

where r is the distance between the electron and the line charge. This equation changes the charge that the electron encounters from each point on a deflection plate to the charge at the deflection plate point from an earlier distance-determined time.

5 Results and Approaches

5.1 Defocusing in the Model

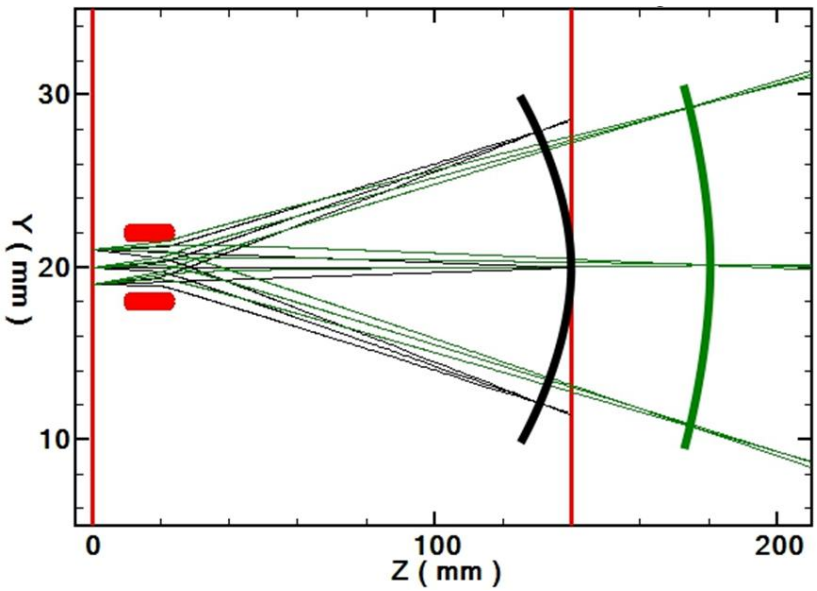

Figure 5: Overlay of static and dynamic deflection
A plot of the electron paths and focal plane from a static deflection is shown in black. The electron paths and focal plane from a dynamic deflection are in green. The shifted and defocused dynamic focal plane is due to a high streak speed.

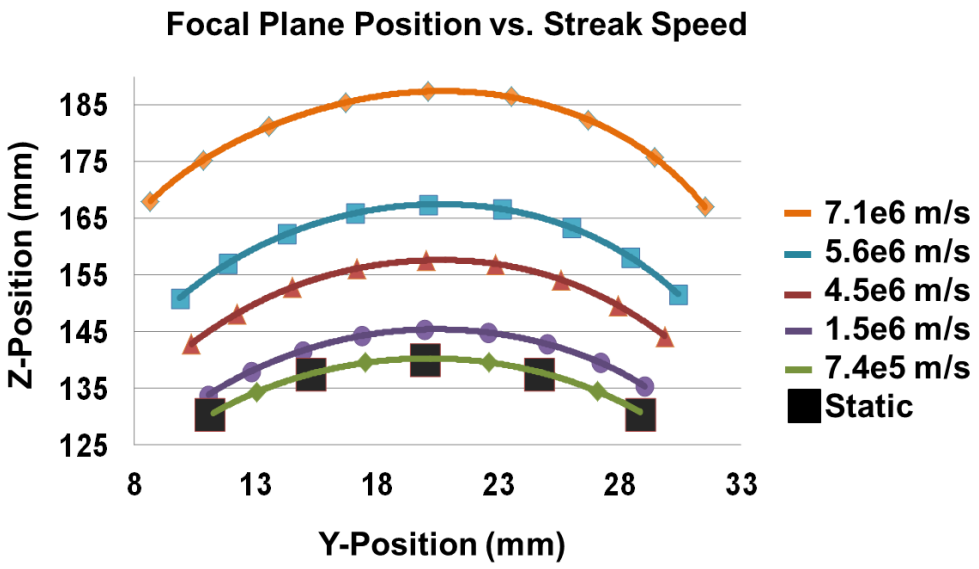

Figure 6: Focal plane position vs. streak speed from the dynamic deflection model. Graphs of the focal plane position at various streak speeds show the trend that focal plane displacement increases with streak speed.

Dynamic deflection code runs from *RungeKutta* demonstrate the same defocusing effects that streak cameras exhibit. At high sweep speeds, the simulated focal plane moves behind the phosphor screen, defocusing the image (Figure 5). Data from the model in Figure 6 show the dynamic defocusing increasing with sweep speed, following the same trend as the experimental data from streak cameras. At slower streak speeds, the focal plane is identical to that of a static deflection. It gradually moves further behind the phosphor screen as the streak speed increases. Data from dynamic deflection code runs indicate that the distance $D(s)$ the focal plane moves at each streak speed s can be fit to an equation of the form,

$$D(s) = As^B \tag{8}$$

where A and B are constants.

5.2 Common Mode Voltage

A common mode voltage (CMV) applied to both deflection plates adjusts the focus of the electron beam by altering the deflection path of the electrons. A negative CMV focuses the electron

beam (Figure 7). Using a negative CMV, it is possible to compensate for the dynamic defocusing created by the high sweep speeds and reposition the focal plane back at the phosphor screen.

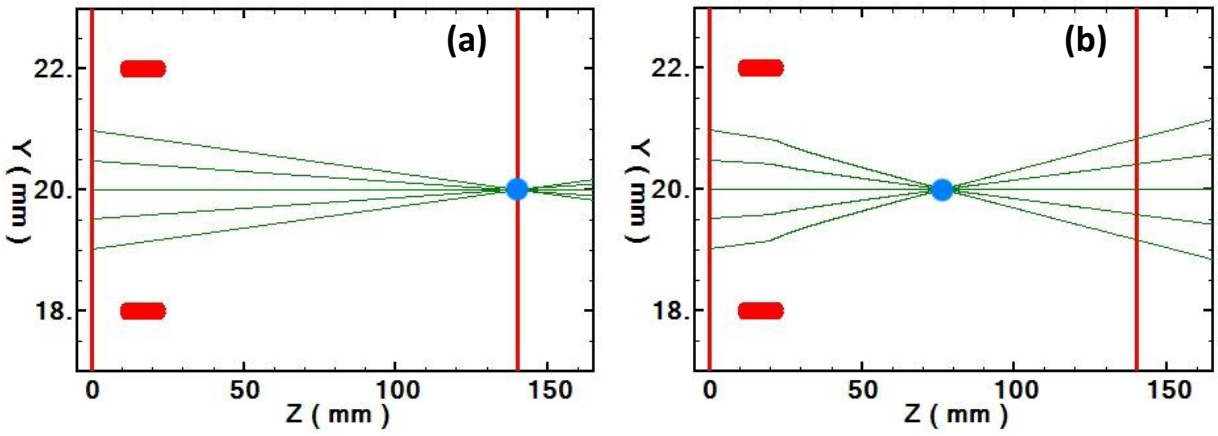

Figure 7: Effect of common mode voltage.
Graphs of (a) static shot with zero CMV and (b) static shot with a negative CMV demonstrate the focusing effects of a negative CMV.

5.3 Correction of Focal Plane

There are two main methods to achieve a negative CMV with the streak camera deflection plates. One method involves a time-shift of the voltage curve of one deflection plate, so that the voltage begins to decrease on the plate with the positive potential before the voltage on the other plate changes. The second method involves the addition of the CMV to the voltages on both plates.

The time-shift method creates a CMV that varies over time. Use of purely the time-shift method to compensate for extreme degrees of defocusing at high sweep speeds distorted the focal plane shape due to the inconsistency of the CMV. Drastic time shifts inverted the shape of the focal plane. Though this method wasn't further researched in this project, it may not be practical, due to the fact that the detailed risetimes of the voltage transients are very difficult to modify.

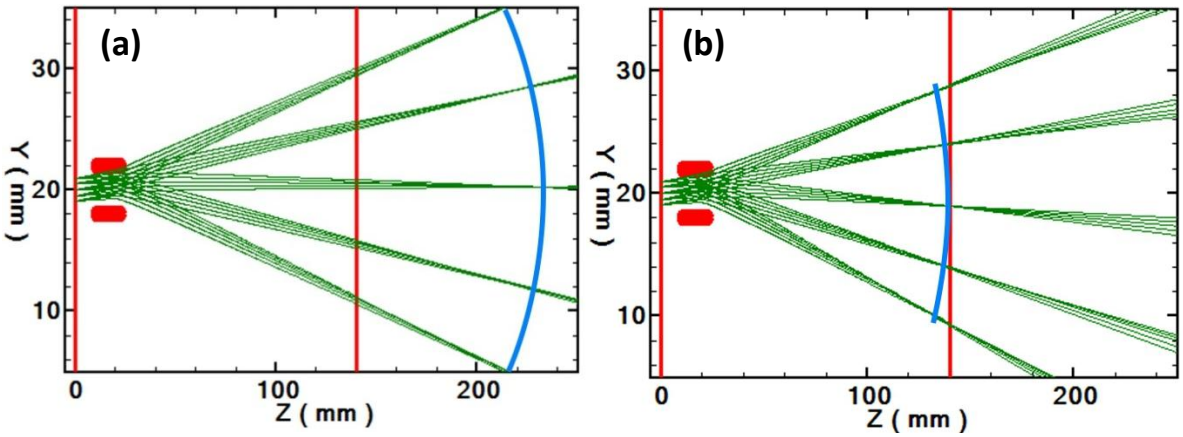

Figure 8: Correction for dynamic defocusing with a negative CMV.
Same as Figure 7, except applied to a dynamic shot with a high streak speed. The defocusing in (a) is corrected in (b) by a negative CMV.

The addition of a CMV to both plates was effective in preserving the shape of the focal plane as well as repositioning it back at the phosphor screen (Figure 8). Focal plane data with static deflection and a negative CMV can be fit to an equation in the form,

$$D(V) = Le^{KV} - L \tag{9}$$

where $D(V)$ is the distance the focal plane moves at negative CMV value V, L is the distance between the deflection plates and the phosphor screen, and K is a constant.

Using the equations,

$$\frac{1}{f} = \frac{1}{f_1} + \frac{1}{f_2} \tag{10.1}$$

$$\frac{1}{f} = \frac{1}{f_1} + \frac{1}{f_2} + \frac{1}{f_3} \tag{10.2}$$

with Eq. 10.1 being the double thin lens equation and Eq. 10.2 the triple thin lens equation, with f as the resultant focus of three lenses with foci f_1, f_2, and f_3, it is possible to calculate an equation so that a streak speed value corresponds to a correcting negative CMV value.

With the foci values of the model substituted into Eq. 10.2, the equation becomes,

$$\frac{1}{L} = \frac{1}{L} + \frac{1}{f_d} + \frac{1}{f_{cm}} \tag{11.1}$$

$$-\frac{1}{f_d} = \frac{1}{f_{cm}} \tag{11.2}$$

with L substituted for f, the intended resultant focus, and for f_1 as the focus of the focusing electrode, f_d as the focus of the defocusing lens, and f_{cm} as the focus of the negative CMV focusing lens. The foci f_d and f_{cm} in Eq. 11.2 can be found by using the double lens equation,

$$\frac{1}{f_{L+d}} = \frac{1}{L} + \frac{1}{f_d} \tag{11.3}$$

$$\frac{1}{f_{L+cm}} = \frac{1}{L} + \frac{1}{f_{cm}} \tag{11.4}$$

where f_{L+d} represents the resultant focus of the focusing electrode lens and defocusing lens, and f_{L+cm} the resultant focus of the focusing electrode lens and the negative CMV focusing lens. Substituting Eq. 11.3 and Eq. 11.4 into Eq. 11.2,

$$\frac{1}{f_{L+cm}} = \frac{2}{L} - \frac{1}{f_{L+d}} \tag{11.5}$$

and substituting Eq. 8 and Eq. 9 into Eq. 11.5 after adding L to both,

$$\frac{1}{Le^{KV}} = \frac{2}{L} - \frac{1}{As^B + L} \tag{11.6}$$

results in an equation with CMV and streak speed as variables.

6 Conclusion

A model for dynamic deflection in streak cameras, *RungeKutta*, has been written in C#. The model demonstrates the same defocusing effects that streak cameras exhibit. The effects of streak speed on dynamic defocusing in the model have been analyzed. Data from the model show the trend of the degree of dynamic defocusing increasing with streak speed. The data on dynamic defocusing from

the model can be fit into an equation and extrapolated to predict the effects of dynamic defocusing under various streak speeds.

A negative common mode voltage (CMV) was applied through two methods to correct the defocusing. The time-shifted voltage curve method proved ineffective in the model due to distortion of the focal plane. The model has shown that a constant negative CMV addition to the voltages of both deflection plates successfully corrected the focal plane. With a negative CMV, it is possible to run deflection shots with high streak speeds without sacrificing resolution.

Future work on dynamic defocusing in streak cameras may further improve the accuracy of *RungeKutta* or explore additional methods such as time-shifted voltage curves, modifying the focusing electrode, or a combination of methods to improve the efficiency of the correction.

7 Acknowledgements

I was supported by many individuals in this project, without which I wouldn't have been able to come this far. I cannot thank Dr. Paul Jaanimagi enough for the time and guidance he has given me in the project, as well as teaching me so much about streak cameras. I would like to thank Dr. Stephen Craxton for providing this research opportunity to high school students and for encouraging passion in physics through the program and its lectures, and express my gratitude toward Dr. Paul Jaanimagi, graduate student Steve Ivancic, and fellow interns Andrew Zhao, Kevin Mizes, and Felix Jin for helping me learn how to program, as well as instructing me on the specifics of C#.

References

[1] *Streak Tubes: Catalogue*. Photonis: Brive, France. 2010. Web. <www.photonis.com>

[2] *Guide to Streak Cameras.* Hamamatsu Photonics K.K.: Hamamatsu, Japan. September, 1999. Web. <www.hamamatsu.com>

Modeling and Testing Array Generation Techniques for Grid Image Refractometry on OMEGA EP

Andrew Zhao

Webster Thomas High School, 800 Five Mile Line Road, Webster, NY 14526

Kevin Mizes

Pittsford Sutherland High School, 55 Sutherland Street, Pittsford, NY 14534

Steve Ivancic, Advisor

University of Rochester - Laboratory for Laser Energetics, 250 E. River Rd, Rochester, NY 14623-1299

Robert Boni, Advisor

University of Rochester - Laboratory for Laser Energetics, 250 E. River Rd, Rochester, NY 14623-1299

Dr. Dustin Froula, Advisor

University of Rochester - Laboratory for Laser Energetics, 250 E. River Rd, Rochester, NY 14623-1299

March 29, 2012

Abstract

Grid imaging refractometry (GIR) is a method of measuring the density profile of a plasma region that is too large to be effectively measured using interferometry. A grid of beamlets generated by a laser is sent through the plasma and refracted. The refracted grid is imaged and the deflection of each grid point is measured to back calculate the plasma's density profile. GIR will be implemented onto the fourth-harmonic probe beam on the OMEGA EP laser. A GIR system was designed and built to test the effectiveness of array generation using a physical grid or a three beam interferometer. A three beam interferometer was built and produced a hexagonal pattern that could be used as a grid. Use of a three-beam interferometer allows arrays to be generated with substantially higher frequencies without facing detrimental diffraction effects.

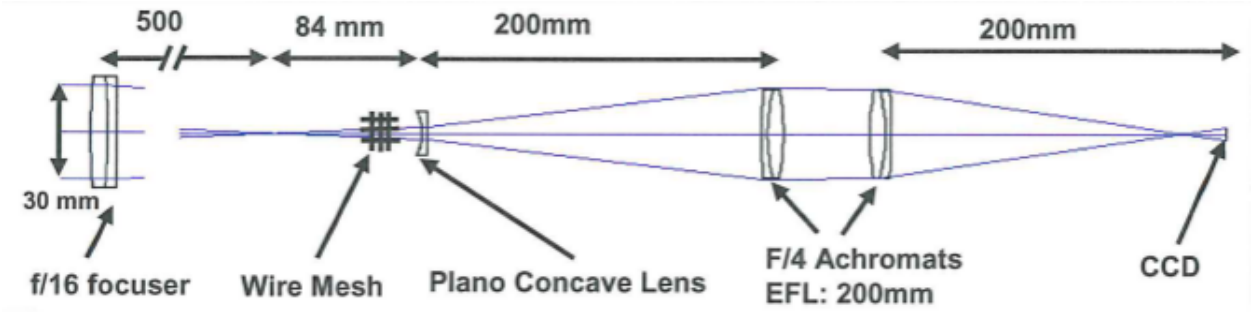

Figure 1: Model of the GIR setup. The plano-concave lens is used to represent the plasma

1. Introduction

In laser fusion, a plasma is produced when a laser is focused onto a target. The plasma is a hot, ionized gas that expands back towards the laser. The density of this plasma can be measured because the refractive properties of plasma at different densities are well known. Interferometry has been used to measure the density of the resultant plasma, but works only with smaller plasma volumes. Grid imaging refractometry (GIR)[1] is better suited for measuring larger plasmas, and will be implemented on the fourth-harmonic probe beam on the OMEGA EP laser at the Laboratory for Laser Energetics.

The basic setup of GIR is outlined in figure 1. This approach splits a collimated beam by sending it through a grid placed in front of a plasma. Each beamlet refracts differently with the varying refractive index of the plasma, which depends on plasma density. A collimating optic images the whole grid along different planes within the plasma. The deflection angle of each grid point is then calculated by subtracting the x,y coordinates of each corresponding grid point in different images. This process was automated using Matlab.

2. Optical Setup

A small scale GIR system was built to model the design for the OMEGA EP laser. The GIR system was built in stages to make modifying or testing a different stage easier. The system starts from a 30 mm collimated laser source to match the GIR design for OMEGA EP, and is put through an array generation assembly to create a grid of beamlets. The new grid is sent through a refractive target (the plano-concave lens in Figure 1) to simulate the plasma and finally through an imaging relay (the two f/4 achromats in Figure 1) to a CCD, where the image is saved and processed.

The setup tested two different methods of array generation, and gathered distorted images from different refractive targets. Instead of installing the GIR system in a real fusion system, the GIR system built used simulated plasma to make modifying the system faster, and limit the use of materials destroyed or consumed during the experiment[2].

2.1. Up-collimation and Refocusing

The system built for testing uses a laser produced at a 1.5 mm diameter. To match the fourth harmonic system, the beam was up-collimated to a 3.0 mm diameter. The input laser produces a beam with a Gaussian intensity profile. To eliminate the Gaussian intensity profile, a very fast aspheric lens is used to overfill the collimating lens. An achromatic lens is used as the collimating lens to help eliminate spherical aberration. The design was proposed and modeled in OSLO, and showed negligible amounts of aberration and intensity variation in the beam.

2.2. Imaging

The GIR system built uses two f/4 achromatic lenses to focus the refracted grid image onto a CCD. One lens samples the plasma region and the other lens focuses it onto the CCD. The focusing lens must be stationary at one focal length from the CCD, to prevent change in magnification while allowing the sampling lens to move. The sampling lens gathers grid images at its focal point. The lens can be moved to capture images at different distances along the imaging axis. The function of grid distortion relative to displacement along the imaging axis is needed to calculate the ray refraction.

A more advanced imaging system has been designed for implementation into the fourth harmonic probe. This system uses a semi-reflective beam splitter at an angle with a 100 m focal length mirror. Each time the beam is reflected between the beam splitter and mirror, it is shifted farther off axis, and the image of the plasma is moved farther along the optical axis. The system uses the first three beams that exit the system and images them onto a single CCD camera. This system allows for images at multiple planes to be captured simultaneously without the need for holography.

2.3. Array generation

The array is generated at some point before the f/16 lens in Figure 1 focuses the beam to the target region. It is necessary to focus the beam down from the original size of 30 mm in diameter

so it has enough energy to overcome plasma self-emission. The final grid image sampled is about 5 mm in diameter, the size of the plasma to be diagnosed. The beam is not initially started with a high enough power density to overcome plasma self-emission, because if it did, the beam would damage any optic it passed through. The beam sizes were chosen to effectively match the GIR plan for the fourth-harmonic probe beam.

2.3.1. Wire mesh

In the GIR system being implemented on OMEGA EP, the array is generated by placing a wire mesh along the beam path close to the sample region, held in place by a Ten-Inch Manipulator. The wire mesh will be destroyed on each shot, either by the plasma or by the probe beam.

Diffraction from a physical grid limits the imaging distance from the object plane. The diffraction effect is known as the Talbot effect. The Talbot effect occurs when light from evenly spaced sources diffracts and interferes. The Talbot effect causes the light to reform an array at regular intervals along the optical axis. The interval between successive reformations is called the Talbot length. At the half Talbot length, the image is reformed but phase shifted by the period. At the quarter Talbot length, the image is reformed but with double frequency. Figure 2 shows the Talbot carpet, an example of the interference effect across a plane. In this figure light is passed through the evenly spaced slits seen at 0 Talbot length. As the light propagates to the right, it diffracts and interferes. There is only a small range in the Talbot carpet where there is enough contrast, such that the interference peaks are less than 50% of the grid point's intensity peak, to be able to use a program to distinguish grid points that can be correlated with the original grid image.

The Talbot effect was studied by taking images across the Talbot length. The images (shown in relation to distance in Figure 2) determined the length of the usable region for imaging, based on contrast of the grid. The Talbot length was calculated with the formula:

$$L = \frac{2a^2}{\lambda} \tag{1}$$

where L is the Talbot length, a is the grating period of the mesh, and λ is the wavelength. For our setup, $a = 91$ μm, $\lambda = 543$ nm, so $L = 30.5$ mm. This Talbot length was convenient since, because in the optical setup used (Figure 1), we had around 40 mm of movement space before the grid image became two small for grid points to be distinguished.

Images were gathered by moving the imaging lens 1 mm away from the refractive medium from

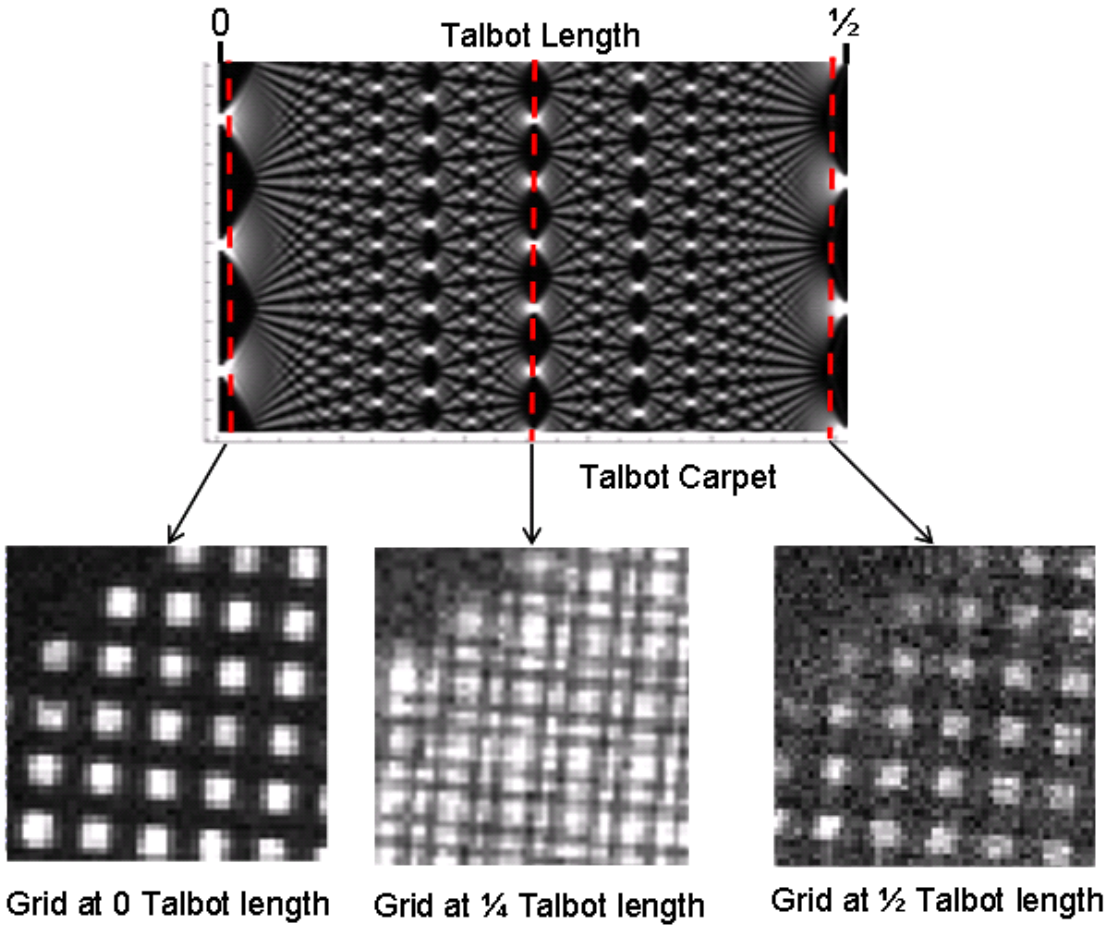

Figure 2: Talbot Carpet and three grid images, representative of their marked 1D section on the Talbot Carpet. The Talbot Carpet is an example of the Talbot effect, where light from evenly spaced sources diffracts and interferes. The images at the 0 Talbot length and the 1/2 Talbot length are usable, as determined by taking a lineout of intensity across grid points and showing interference peaks were less than 50% of a grid point's peak. These two images have grid points that can be correlated, while the 1/4 Talbot length image has no discernable grid points to correlate. This is due to the double frequency effect seen in the Talbot carpet at the 1/4 Talbot length.

its initial distance of 200 mm, the lens' focal length, until the grid points seemed distorted. The light intensity was averaged over three grid points for each grid image (Figure 2). An unusable grid image was determined to be where the modulation depth was less than 50% of the grid point's peak intensity. The range where usable images were produced was determined to be approximately 5% of the calculated Talbot length. At the quarter Talbot length, the double frequency image was not usable.

From Eq. (1), the Talbot length increases quadratically as the mesh period is increased.

2.3.2. Three beam interferometer

A second method of array generation was explored in response to the limitations of the physical grid.[3] An array was generated by interfering three beams together (Figure 3). Figure 3 (a) shows how the beams are interfered. MATLAB was used to simulate this interference based on the real part of the electric field equation. The intensity is found by summing each beam's electric field and multiplying the sum by its complex conjugate.

The azimuthal (ϕ) and zenith (θ) angles of the incident beams were then manipulated to show that the hexagonal grid generated by three beam interference could be controlled. Figure 3 demonstrates how the grid orientation and frequency change by θ and ϕ. In Figure 3 (b), the beams are interfered at $\theta = \pi/24$ and $\phi = 2\pi/3$. In image (c), one of the three beams' azimuthal angle, ϕ, was moved by $\pi/6$ distorting the grid. A frequency change is shown in Figure 3 (d), where θ was changed to $\pi/6$.

A three beam interferometer was built in the lab (Figure 3 (e)). A single beam was split into three using two-beam splitters, and the three three beams were recombined using two more beam splitters. To combine two beams, one is reflected and the other is propagated through. The azimuthal and the zenith angles of two beams can be changed by rotating a beam splitter using a gimbal mount. The three beam interferometer allows for a large range of azimuthal and zenith angles, giving complete freedom in the array frequency. The interferometer was tested to produce arrays with periods as small as 20 μm. Test images taken of the three beam interferometer's array showed high contrast up to 90% (Figure 4).

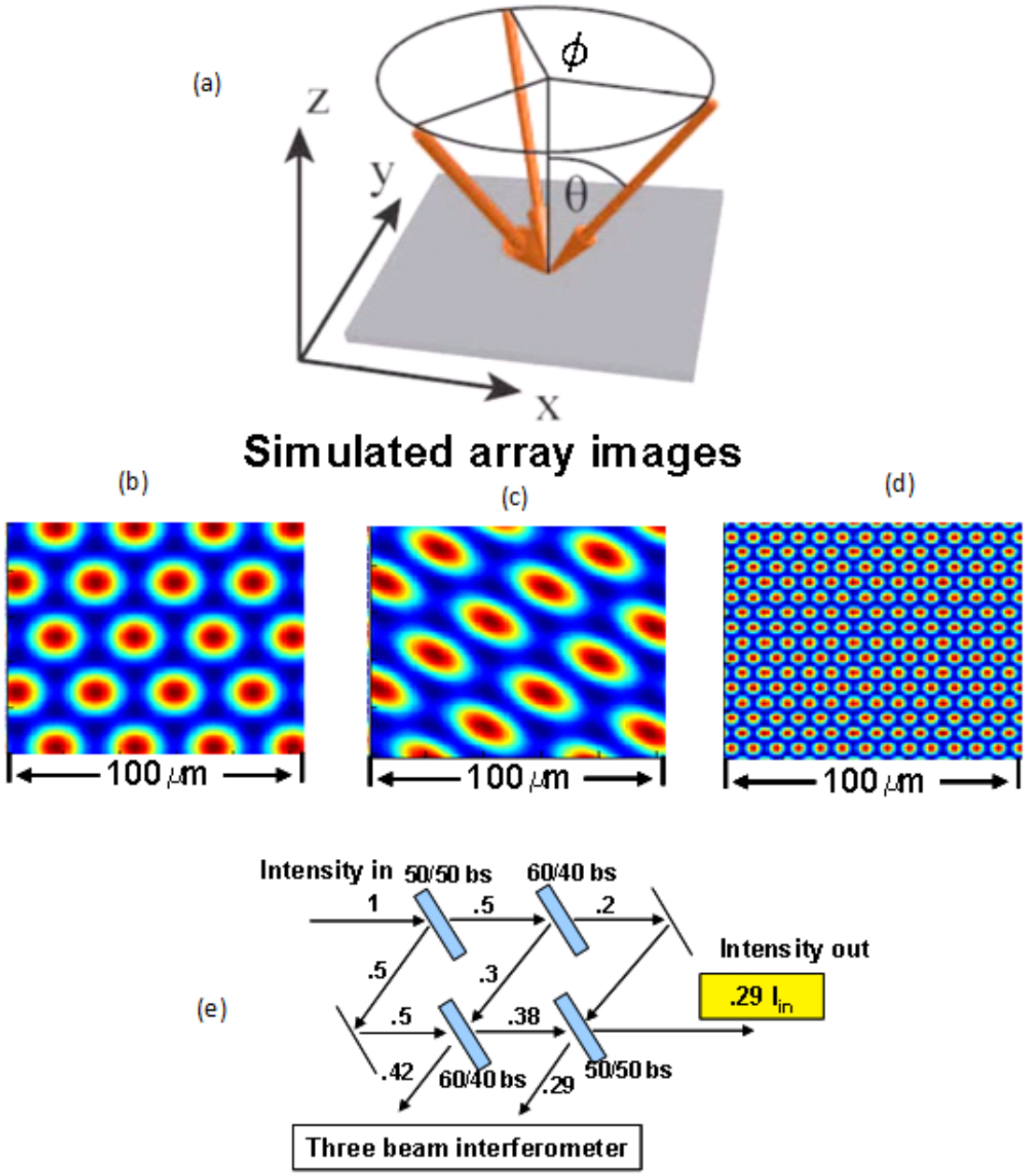

Figure 3: (a) Diagram of array generation using a three-beam interferometer. (b)-(d) Examples of simulated output light intensity. (e) Optical layout of the interferometer using 50/50 and 60/40 beam splitters. The top two split the beam and the bottom two recombine each beam to interfere. Notice the lost light through the recombiners. This accounts for the lower output intensity in the interferometer than the wire mesh.

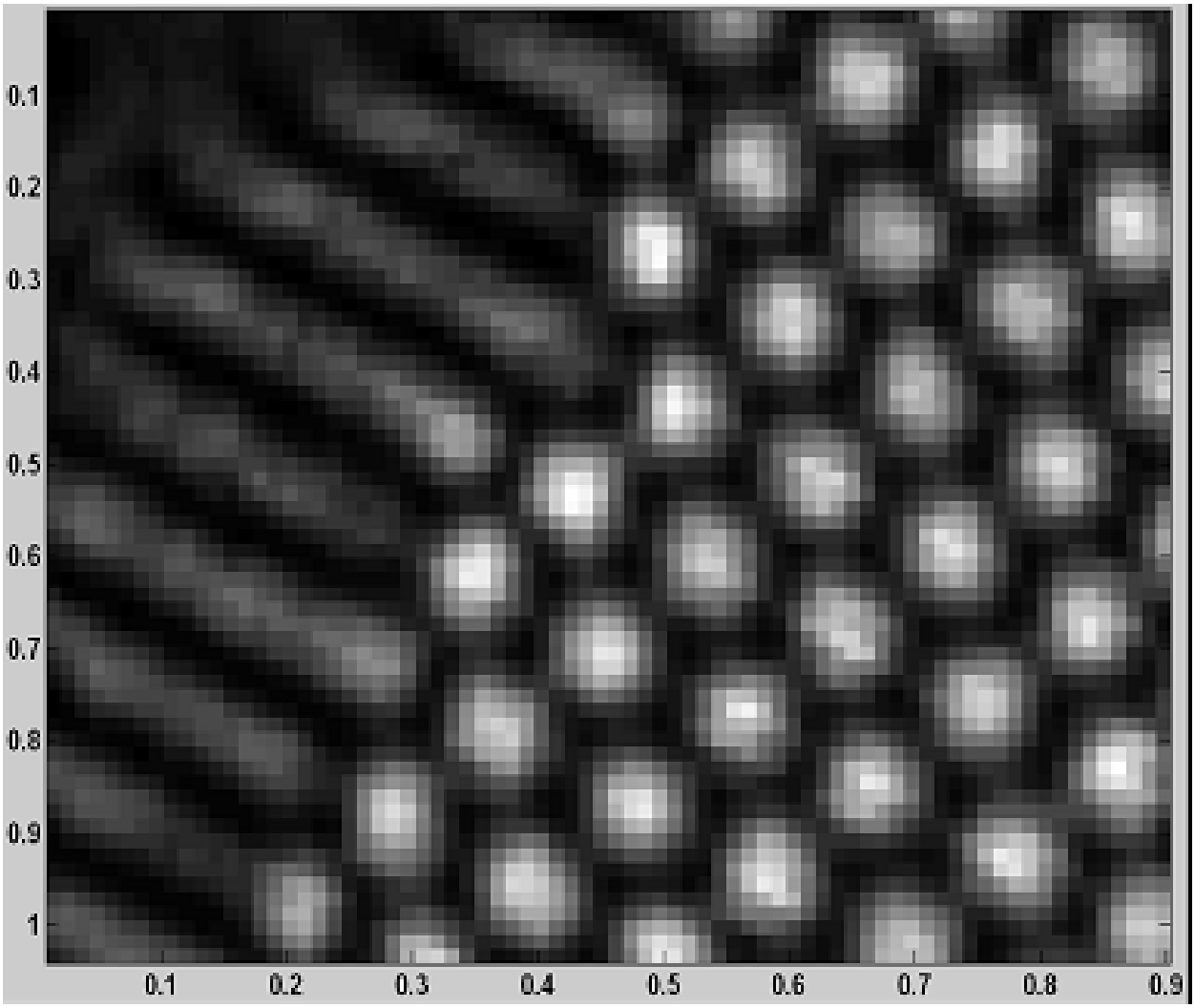

Figure 4: Grid image from three beam interference. The beam lines on the left of the image represent two beam interference fringes, due to the third beam not being combined completely. Very good contrast of 89% is seen around the grid points, usable for image processing.

3. Conclusion

The diffraction caused by the Talbot effect of a physical grid has been shown to match expected values. This level of diffraction adds a well defined and significant limitation to the frequency of a grid usable in GIR. The use of a grid with a spacing too small will result in unusable images.

A three beam interferometer has been constructed to form an array of hexagonal dots through interference. Because there is no diffraction, the hexagonal array is distinct and resolvable along the entire optical axis. The ability to precisely control the spacing and orientation of the grid has been demonstrated. Using this interferometer could allow the production of arrays of much smaller spacing than what was available using physical grids.

References

[1] R. S. Craxton, F. S. Turner, R. Hoefen, C. Darrow, E. F. Gabl, and G. E. Bush, "Characterization of laser-produced plasma density profiles using grid image refractometry," *Phys. Fluids B* **5**, p. 4419, 1993.

[2] D. D. Meyerhofer *et al.*, "Diagnostics for ep fourth harmonic probe beam (4wdiagn)," *Physics Requirements Document* , 2011.

[3] J. de Boor, N. Geyer, U. Gosele, and V. Schmidt, "Three-beam interference lithography: upgrading a lloyds interferometer for single-exposure hexagonal patterning," *Optics Letters* **34**, pp. 1783–1785, 2009.